Forschungszentrum Karlsruhe
in der Helmholtz-Gemeinschaft

Wissenschaftliche Berichte
FZKA 7263

Theoretical Synthesis and Experimental Measurements of Slotted Waveguide Feeding Systems For 2.45 GHz Industrial Microwave Heating Installations

S. Stančulović

**Institut für Hochleistungsimpuls- und
Mikrowellentechnik**

Dezember 2006

Forschungszentrum Karlsruhe

in der Helmholtz-Gemeinschaft

Wissenschaftliche Berichte

FZKA 7263

THEORETICAL SYNTHESIS AND EXPERIMENTAL MEASUREMENTS OF SLOTTED WAVEGUIDE FEEDING SYSTEMS FOR 2.45 GHz INDUSTRIAL MICROWAVE HEATING INSTALLATIONS

Sebastijan Stančulović

Institut für Hochleistungsimpuls- und
Mikrowellentechnik

Von der Fakultät für Elektrotechnik und Informationstechnik
der Universität Karlsruhe (TH) genehmigte Dissertation

Forschungszentrum Karlsruhe GmbH, Karlsruhe
2006

Forschungszentrum Karlsruhe GmbH
Postfach 3640, 76021 Karlsruhe

Mitglied der Hermann von Helmholtz-Gemeinschaft
Deutscher Forschungszentren (HGF)

ISSN 0947-8620

urn:nbn:de:0005-072630

THEORETICAL SYNTHESIS AND EXPERIMENTAL MEASUREMENTS OF SLOTTED WAVEGUIDE FEEDING SYSTEMS FOR 2.45 GHz INDUSTRIAL MICROWAVE HEATING INSTALLATIONS

Zur Erlangung des akademischen Grades eines

DOKTOR-INGENIEURS

von der Fakultät für Elektrotechnik und Informationstechnik
der Universität Fridericiana Karlsruhe

genehmigte

DISSERTATION

von

Dipl.-Ing. Sebastijan Stančulović
aus Bad Buchau

Tag der mündlichen Prüfung: 26.07.2006

Hauptreferent: Prof. Dr. rer. nat. Dr. h. c. M. Thumm

Korreferent: Prof. Dr. rer. nat. O. Dössel

Karlsruhe: 28.07.2006

ABSTRACT

In this work nonresonant slotted waveguide antennas have been theoretically synthesized and experimentally verified for feeding systems of industrial microwave applicators at 2.45 GHz. The application of the proposed slotted waveguides is particularly in the processing of carbon fibre reinforced plastics using microwave systems with hexagonal geometry (HEPHAISTOS technology). Implementation of the novel slot antenna arrays with minimized reflections enabled a direct coupling of cheap 2.45 GHz magnetrons to the feeds, without standard expensive microwave components such as isolators or circulators and tuners. Additionally, antennas with two different, mutually orthogonal, polarizations have been designed for suppression of undesired mutual cross coupling between neighbouring slotted waveguides. Further, the radiation characteristics of the nonresonant antennas have been calculated to allow the desired electromagnetic field homogeneity in the hexagonal microwave heating systems.

Using the commercial software package CST Microwave Studio various types of radiating waveguide slots were characterized. Normalized slot impedances and admittances have been numerically calculated as functions of different design parameters like slot length, width, displacement and shape. A novel banana slot geometry, which is optimized for the given flow of the currents in the inner waveguide wall, has been numerically investigated and compared to the conventional rectangular slots. The numerical calculations of the reflections, near fields and far fields of the synthesized nonresonant antennas have shown, that they are more convenient for the application in feeding systems than the standard slotted waveguide antennas having resonant distance between the slots. The new nonresonant antenna systems have an additional design parameter, the distance between the slots, and they provide better input antenna matching than the resonant feeding antennas, assuring a suppression of a standing wave (minimized reflections) in the feeding waveguide.

A new synthesis procedure for advanced slotted waveguide feeding systems has been developed using a linearization of the exponential attenuation function of the propagating fundamental TE_{10} waveguide mode. Additionally, the radiation characteristics of the antennas with transversal slots has been optimized by an optical method.

The synthesized slotted waveguide feeding systems have been experimentally verified performing measurements and tests in the low as well as in the high power range, for the cases that the antennas radiate into the free space, for a laboratory scaled applicator and for the industrial HEPHAISTOS CA2 applicator. The results of measurements confirmed that the designed slotted waveguide antennas meet all demands for simple feeding systems in high power microwave applicators.

THEORETISCHE SYNTHESE UND EXPERIMENTELLE VERMESSUNGEN VON SCHLITZHOHLLEITER-ANTENNEN ALS EINSPEISUNGSSYSTEME FÜR 2,45 GHz INDUSTRIELLE MIKROWELLEN-HEIZUNGSANLAGEN

KURZFASSUNG

Im Rahmen der vorliegenden Arbeit wurden nichtresonante Rechteckhohlleiterschlitzantennen als Einspeisungssysteme für großtechnische Mikrowellenapplikatoren bei der Industriefrequenz 2,45 GHz theoretisch berechnet und messtechnisch überprüft. Dabei steht die Prozessierung von Kohlefaserverbundstoffen mit hexagonalen HEPHAISTOS Mikrowellensystemen im Vordergrund. Die Realisierung von neuartigen, kostengünstigen und reflexionsarmen Schlitzantennen hat die direkte Kopplung von 2,45 GHz-Magnetrons, ohne die üblichen, teuren Mikrowellenkomponenten wie Isolatoren bzw. Zirkulatoren und Tuner, an die Einspeisungsantennen technisch günstig ermöglicht. Hierbei wurden Antennen mit gekreuzter Polarisation entwickelt, um die gegenseitige Verkopplung benachbarter Einspeisungssysteme zu minimieren und um die in den Speisehohlleitern rückwärtslaufende Leistung klein zu halten. Außerdem wurde die Abstrahlungscharakteristik der synthetisierten Hohlleiterschlitzantennen so bestimmt und optimiert, dass damit eine homogene Verteilung des elektromagnetischen Feldes in hexagonalen Applikatoren ermöglicht wird.

Verschiedene Schlitztypen in Hohlleiterantennen wurden mit Hilfe des kommerziellen Programmpakets CST Microwave Studio systematisch charakterisiert und normierte Schlitzimpedanzen und –admittanzen als Funktion der Schlitzparameter, wie Schlitzlänge, -breite und -form berechnet. Dabei wurden statt der üblichen Rechteckschlitze auch neuartige, an die Flussrichtung der Hohlleiterwandströme angepasste (Bananen-förmige) Schlitze behandelt. Die numerischen Berechnungen der reflektierten Leistung, des Nahfeldes und des Fernfeldes haben gezeigt, dass die neuen nichtresonanten Antennen für die Erfüllung der in der Aufgabestellung geforderten Kriterien besser geeignet sind als die üblichen Schlitzantennen mit resonantem Schlitzabstand. Die nichtresonanten Schlitzantennen haben einen weiteren Optimierungsparameter, den Schlitzabstand, und in diesem Fall, bei geeigneter Dimensionierung, existiert keine Stehwelle (reflektierte Leistung) im vom Magnetron herkommenden Rechteckhohlleiter.

Zur Synthese von optimierten nichtresonanten Rechteckhohlleiterschlitzantennen wurden neue Verfahren entwickelt. Für beide Antennen, mit Längsschlitzen oder mit Querschlitzen, beruht das neue Verfahren auf der Linearisierung der exponentiellen Dämpfungsfunktion der Grund-TE_{10}-Welle. Bei Antennen mit Querschlitzen erfolgt die Strahlungsoptimierung über eine optische Methode.

Die hergestellten Schlitzhohlleitersysteme wurden bei niedrigen und hohen Mikrowellenleistungen, im Freiraum, in Modellapplikatoren und im industriellen HEPHAISTOS-CA2-Applikator messtechnisch verifiziert. Die Ergebnisse der Messungen haben bestätigt, dass die synthetisierten Schlitzantennen alle Anforderungen für den Einsatz als einfache Einspeisungssysteme von Mikrowellenapplikatoren erfüllen.

CONTENTS

LIST OF ABBREVIATIONS

3-D	**T**hree-**D**imensional
ABC	**A**bsorbing **B**oundary **C**onditions
CFRP	**C**arbon **F**ibre **R**einforced **P**lastics
CST	**C**omputer **S**imulation **T**echnology
CW	**C**ontinuous **W**ave
DUT	**D**evice **U**nder **T**est
EM	**E**lectro**M**agnetic
FDTD	**F**inite **D**ifference **T**ime **D**omain
FITD	**F**inite **I**ntegral **T**ime **D**omain
FZK	**F**orschungs**Z**entrum **K**arlsruhe
HEPHAISTOS	**H**igh **E**lectromagnetic **P**ower **H**eating **A**utoclaveless **I**njected **ST**ructures **O**ven **S**ystem
IHM	**I**nstitut für **H**ochleistungsimpuls- und **M**ikrowellen Technik
IR	**I**nfra**R**ed
ISM	**I**ndustrial, **S**cientific and **M**edical
MW	**M**icro**W**ave(s)
MWS	**M**icro**W**ave **S**tudio
OSL	**O**pen, **S**hort and **L**oad
TE	**T**ransversal **E**lectric
TEM	**T**ransversal **E**lectro**M**agnetic
TL	**T**ransmission **L**ine
TM	**T**ransversal **M**agnetic
VNA	**V**ector **N**etwork **A**nalyzer
VSWR	**V**oltage **S**tanding **W**ave **R**atio

LIST OF SYMBOLS

a	inner width of a waveguide (*m*)
a_n	slot excitation amplitude
b	inner hight of a waveguide (m); normalized slot susceptance
$\vec{B}$	magnetic induction vector (*T*)
B	magnetic induction amplitude (*T*)
c	speed of light ($3 \cdot 10^8 \, m \cdot s^{-1}$)
c_P	specific heat capacity of a medium ($J \cdot kg^{-1} \cdot K^{-1}$)
C	constant
C’	capacitance per length ($F \cdot m^{-1}$)
d	slot displacement (offset) from the central waveguide line (*m*)
$d_{s,a}$	distance between waveguide short and a coupling antenna (*m*)
$\vec{D}$	electric flux density vector ($A \cdot s \cdot m^{-2}$)
D	antenna directivity (*dB*); distance between centers of neighboring slots (*m*)
D_P	penetration depth in dielectrics (*m*)
D_s	distance between last slot center and waveguide short (*m*)
$\vec{E}$	electric field vector ($V \cdot m^{-1}$)
E	electric field amplitude ($V \cdot m^{-1}$)
E_{max}	break down electric field for a dielectric ($V \cdot m^{-1}$)
f	frequency (*Hz*)
f_c	cut-off frequency (*Hz*)
F	antenna array factor (*dB*)
g	normalized slot conductance
G	antenna gain (*dB*)
G’	conductance per length ($S \cdot m^{-1}$)
h_a	antenna hight (*m*)
$\vec{H}$	magnetic field vector ($A \cdot m^{-1}$)
H	magnetic field amplitude ($A \cdot m^{-1}$)
I	current (*A*)
$\vec{j}_c$	free current density vector ($A \cdot m^{-2}$)
$\vec{j}_t$	total current density vector ($A \cdot m^{-2}$)
$\vec{j}_s$	surface current density vector ($A \cdot m^{-2}$)
j_s	surface current density amplitude ($A \cdot m^{-2}$)
j	imaginary unit
k	wave number in free space (m^{-1})
k_x, k_y, k_z	wave numbers in a waveguide in *x*, *y* and *z* direction, respectively (m^{-1})
l	distance (*m*); slot length (*m*)
L’	inductance per length ($H \cdot m^{-1}$)
m	waveguide mode number ; mass (*kg*)
$\vec{n}$	normal unit vector
n	waveguide mode number

N	number of slots in waveguide wall
p_{dis}	dissipated power density ($W \cdot m^{-2}$)
p_r	radiated power (W)
P_{array}	power pattern of an antenna array (dB)
P_{av}	average power (W)
P_{cc}	cross-coupled power (W)
P_{max}	maximum peak power (W)
P_l	lost power (W)
P_{ref}	reflected power (W)
P_t	transmitted power (W)
r	reflection coefficient; normalized slot resistance
r_a	antenna radius (m)
r_{in}	input reflection coefficient
R	distance (m)
R'	resistance per length ($\Omega \cdot m^{-1}$)
R_r	radiation resistance (Ω)
R_s	surface impedance of a conductor (Ω)
$\vec{S}$	Poynting vector ($W \cdot m^{-2}$)
S	scattering matrix
S_{11}, S_{12}, S_{21}, S_{22}	scattering parameters of a 2-port network
t	time (s)
T	temperature (°C)
V	voltage (V)
$VSWR$	voltage standing wave ratio
w	slot width (m)
x	space coordinate; normalized slot reactance
y	space coordinate; normalized admittance
y_{in}	normalized input admittance
Y_{in}	input admittance (S)
z	space coordinate; normalized impedance
z_{in}	normalized input impedance
Z_a	input impedance of an antenna (Ω)
Z_c	characteristic impedance (Ω)
Z_{dipole}	impedance of a dipole antenna (Ω)
Z_{in}	input impedance (Ω)
Z_L	load impedance (Ω)
Z_{slot}	impedance of a slot antenna (Ω)
Z_{TE}	characteristic impedance of TE mode (Ω)
Z_{TM}	characteristic impedance of TM mode (Ω)

GREEK SYMBOLS

α	attenuation constant (m^{-1}, $Np \cdot m^{-1}$ or $dB \cdot m^{-1}$)
β	phase conatant (m^{-1})
δ	penetration depth in a good conductor (skin depth) (m)
$\tan\delta$	dielectric loss tangent
$\tan\delta_{eff}$	effective dielectric loss tangent
ε	permittivity of materials ($F \cdot m^{-1}$)

ε_0	permittivity of vacuum ($8.85 \cdot 10^{-12} F \cdot m^{-1}$)
ε_r	relative permittivity of dielectrics
ε'_r	real part of relative complex permittivity (dielectric constant)
ε''_r	imaginary part of relative complex permittivity (dielectric loss factor)
ε''_{reff}	effective dielectric loss factor
φ	phase angle (*rad* or °)
γ	propagation constant (m^{-1})
η	antenna efficiency
λ	wavelength in free space (*m*)
λ_c	cut-off wavelength (*m*)
λ_g	wavelength in a waveguide (*m*)
μ	permeability of materials ($H \cdot m^{-1}$)
μ_0	permeability of vacuum ($4\pi \cdot 10^{-7} H \cdot m^{-1}$)
μ_r	relative permeability of materials
ν_G	group velocity ($m \cdot s^{-1}$)
ν_p	phase velocity ($m \cdot s^{-1}$)
θ	angle (°)
ρ	free charge density ($C \cdot m^{-3}$)
σ	electrical conductivity ($S \cdot m^{-1}$)
σ_{eff}	effective conductivity ($S \cdot m^{-1}$)
ω	angular frequency (*Hz*)
ξ	constant

1. INTRODUCTION

1.1 Aim of this dissertation

The main aim of this work is to design novel advanced energy feeding systems for high power microwave (MW) industrial applications, particularly for MW processing of materials. A device in which materials are processed by microwaves is called a microwave applicator and it is the main part of a MW heating installation. Industrial MW applicators are in general closed metallic structures, in which the workload is directly exposed to electromagnetic (EM) fields. Energy feeding systems transfer the MW energy from a source into the MW applicators. They determine the quality of EM power coupling into the MW ovens and in this function strongly influence the properties of a whole MW heating system. Hence, the design of energy feeding system presents a very important issue in the development of an industrial MW system.

EM waveguides, which are devices that transmit EM waves, are commonly used as feeding elements in MW heating systems. Today's MW heating technology requires highly efficient waveguide systems that additionally provide an appropriate EM field distribution in the MW applicators containing the processing sample. This leads to the definition of the primary design goals for the energy feeding elements as following: 1) total power transfer from the source to the workload and 2) the support of a desired EM field distribution inside the MW oven. Further, the costs of the proposed hardware have to be reduced in order to improve the existing economical benefits of the MW heating approach over the conventional heating techniques and make it market competitive. The MW energy feeding elements must show reliability and safety in high power operation, as well as an easy maintenance and a large flexibility at the same time.

Slotted waveguides (SW), which couple MW energy by means of slots in the waveguide walls, are used in this work for the feeding system. The slots offer many parameters for the optimization of a MW system, e.g. shape, length, width and position of the slots in the walls of the feeding waveguide. By proper optimization of the slots in directly coupled metallic waveguides several crucial issues are directly effected: one can improve the power coupling efficiency of the microwave system, tune the desired EM field distribution inside the MW applicator and decrease the system costs by avoiding expensive MW components. The strong design requirements for the SW feeds can be stated more precisely, such as:

- minimized reflections inside the feeding system, $P_{ref} \approx 0$ (see Fig. 1.1) ,
- very low level of cross coupling between neighbouring feeding parts in multi-sources fed MW applicators, $P_{cc} \approx 0$ (Fig. 1.1),
- constant EM energy radiation along the feed and
- direct coupling of the microwave sources into the feeding systems (avoiding high cost microwave components like tuners, isolators or circulators, as well as cooling devices).

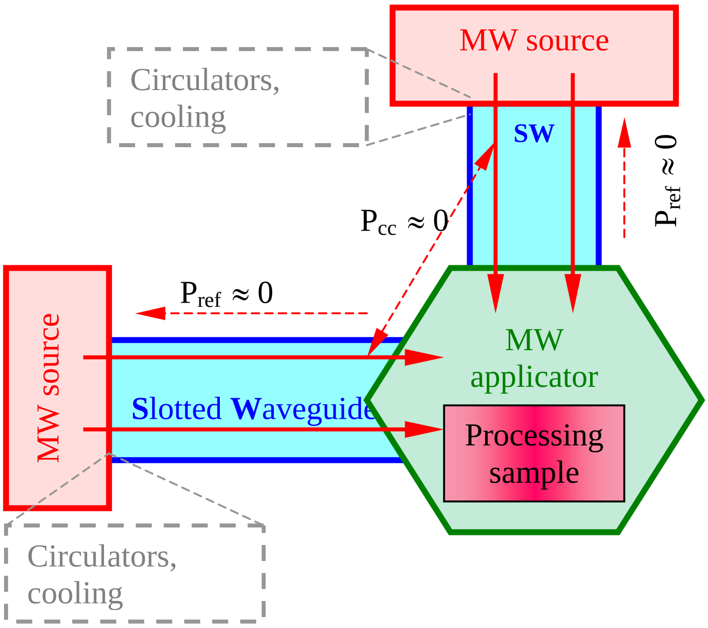

Figure 1.1 Schematic of a MW heating system with directly coupled slotted waveguide feeds

In order to fulfill these requirements, theoretical considerations on SW radiators have been done first. After that, the SWs were calculated using a new synthesis approach and numerical simulations, which have been preformed with CST MicroWave Studio (MWS) commercial software. Then, various experimental tests and measurements verified the proposed SW design and the calculated feeding elements were finely optimized.

1.2 Motivation - MW processing of materials at Forschungszentrum Karlsruhe

MW heating technology has been used in the field of industrial processing for many years [1]. Volumetric and selective heating and the opportunity of very high heating rates are the most prominent characteristics of the MW approach. In other words, the MWs instantaneously penetrate dielectric materials and they locally generate heat. That means, only the processed sample is heated, the oven and system components remain cold. These properties of MW material processing offer the main advantages with respect to the conventional heating technology, such as a shortening of processing time as well as energy savings.

At the Forschungszentrum Karlsruhe (FZK), Institut für Hochleistungsimpuls- und Mikrowellentechnik (IHM), Germany, research in the field of high frequency high power materials processing has been started more than a decade ago. In 1994 a compact system was established to develop technological applications in the field of high-temperature materials processing by means of millimeter-wave radiation. This system contains a high power generator operating at 30 GHz, a so-called gyrotron tube, providing 10 kW of millimeter-wave power [2]. It has been found that the heating at higher frequencies such as 30 GHz is, by a factor 10 – 100, stronger compared to the heating at the ISM frequencies of 915 MHz and 2.45 GHz (ISM: allocated for Industrial, Scientific and Medical applications) [3]. Further, with a smaller wavelength (higher frequencies), the problem of nonuniform heating for some specific samples is less critical. An industrial MW oven with hexagonal geometry that provides an improved uniform EM field distribution was successfully investigated and developed for production needs [4].

However, todays MW heating technology at 2.45 GHz, which uses magnetron tubes

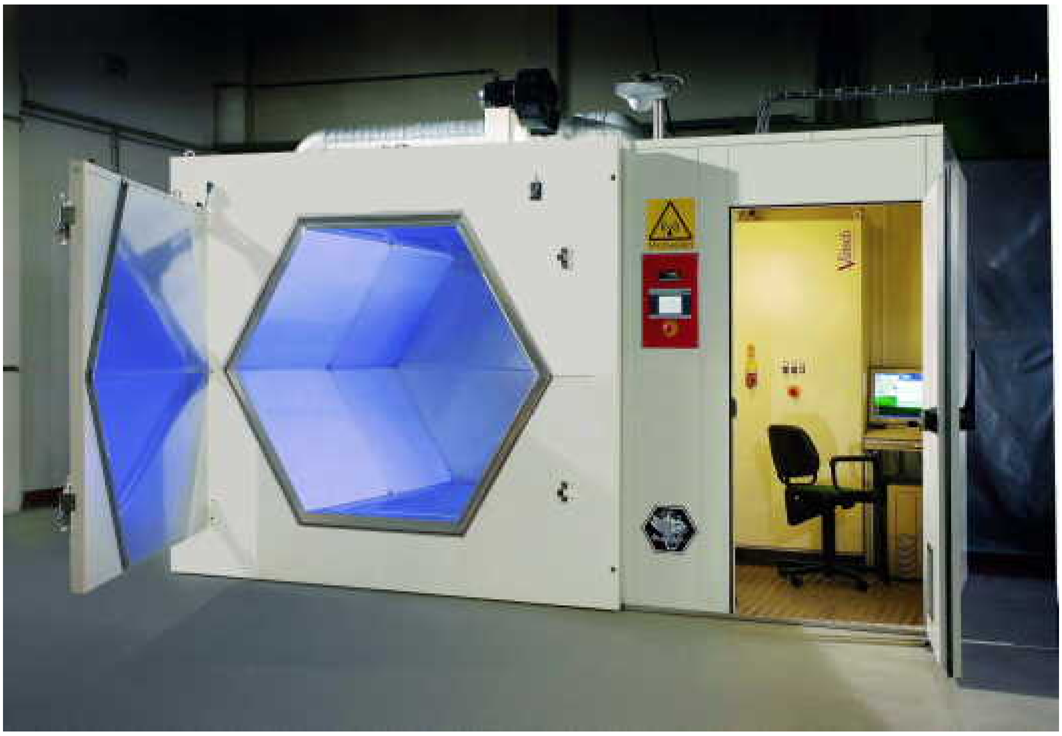

Figure 1.2 The new HEPHAISTOS-CA2 facility developed at FZK

for high power MW generation, instead the high-cost gyrotron source, has costs advantages in comparison with millimeter-wave heating systems [5]. Additionally, parametric investigations on the electrothermal behavior of materials have shown that the desired temperature homogeneity for some cases cannot be improved by increasing the frequency (e.g. 24 GHz) [6]. This factor launched additional research for 2.45 GHz systems and the conceptions of novel millimeter-wave technology have been transferred to 2.45 GHz technology to realize an economically more convenient approach.

A hexagonal prototype MW system HEPHAISTOS-CA1 (**H**igh **E**lectromagnetic **P**ower **H**eating **A**utoclaveless **I**njected **S**tructures **O**ven **S**ystem) at 2.45 GHz has been developed for the application in composite manufacturing [7]. Composites for aerospace applications have been successfully fabricated in the CA1 system and investigated for quality and certification issues [8]. Based on this system a novel modular and larger HEPHAISTOS-CA2 system (Fig. 1.2), which integrates advantageously all basic processing steps for carbon fibre reinforced plastics (CFRP), has been developed at FZK [9,10]. The developed MW installations are named after Hephaistos, who is the engineer and craftsman for the Greek gods and this name stands as well for the technological concept of this MW applicator approach. The modular HEPHAISTOS concept allows the processing of large structures. Further, due to the use of economically beneficial standard industrial 2.45 GHz components, the hardware-costs of the heating system were reduced compared to conventional systems (autoclaves). The system is now commercially available at the company of Vötsch, Reiskirchen, Germany (www.v-it.com).

Such an advantageous technology needs an improved design for the high power transfer from the MW sources into the applicators. This motivated a further research on the SWs and the development of advanced waveguide systems for the industrial HEPHAISTOS applicators. As it has been mentioned before, the proposed SW feeding systems should drastically reduce the reflected MW power to optimize the overall efficiency and costs of the HEPHAISTOS systems. Therefore, the main ambition of the PhD work that is presented here was to design sophisticated energy feeding systems according to the novel MW heating technology demands.

1.3 Design aspects and organization of the thesis

Intensive theoretical investigations on SWs were the first steps that have been taken in the developing process in order to successfully fulfill the defined design requirements. In the following chapter the basic theory of EM fields and EM waves in MW waveguides are given, which was needed for considerations and calculations of the SWs. Chapter 2 introduces the transmission lines (TL) and TL simulations of MW waveguides. Additionally, principles of high power MW coupling to the waveguides are presented in this chapter, as well as the magnetron source and other standard high power MW components.

The slots in the waveguides are basic antenna elements and as such they are described and considered in a separate chapter (chap. 3). Numerical calculations on waveguide slots have been performed to investigate the influence of various slot parameters on the slot radiating properties. Numerical models for simulations and the numerically obtained results are also presented in chapter 3. According the results of the numerical modeling appropriate radiating slot types have been selected for the SW design.

The calculations on SW are explained in more details in chapter 4. Two basic types of SW antennas are presented and compared particularly for the application in feeding systems. The textbooks SW design procedures are analyzed, highlighting the need for a novel design. Finally, new synthesis processes for SW antennas with two different polarizations of the radiated EM fields are described, as well as an optimization method for the radiation characteristics. Then numerical simulations of the synthesized SWs were performed for the purpose of first verifications of the new design procedures. They are also given in chapter 4.

Measurements and tests in the low power range as well in the high power range were performed in order to verify and optimize the new design. The set-ups for this experimental work are presented in chapter 5. The experimentally obtained results proved an optimized power transfer and the desired spatially uniform radiation along the developed SW feeding systems. Comments on these results are also given in chapter 5.

This dissertation ends with chapter 6, which includes the summary, conclusions and outlook.

2. MICROWAVE WAVEGUIDES

2.1 Electromagnetic Waves

2.1.1 Maxwell's equations

To describe the principles of high power microwave transmission and to calculate all important practical parameters for related problems, it is necessary to use the principles of electromagnetic wave propagation.

The theory of electromagnetic waves is based on the set of Maxwell's equations, due to James Clerk Maxwell (1832–1879), who formulated first a set of equations governing the behavior of macroscopic electromagnetic fields. In the years 1886-1888, Heinrich Hertz experimentally proved Maxwell's field theory in Karlsruhe, Germany. The today's well known differential form of Maxwell's equations is given by [11,12,13]:

$$div\vec{D} = \rho , \tag{2.1}$$

$$div\vec{B} = 0 , \tag{2.2}$$

$$rot\vec{E} = -\frac{\partial \vec{B}}{\partial t} , \tag{2.3}$$

$$rot\vec{H} = \vec{j}_c + \frac{\partial \vec{D}}{\partial t} , \tag{2.4}$$

where $\vec{D}$, $\vec{E}$, $\vec{B}$ and $\vec{H}$ are vectors of electric flux density, electric field strength, magnetic induction and magnetic field strength, respectively. The variables ρ and $\vec{j}_c$ present the sources in the Maxwell's equations system, and they are a free charge density and a free current density.

The constitutive equations interconnect the field vectors in cases that an electromagnetic field is applied to material media. In linear dielectric materials the relation between the electric flux density and the electric field strength is given by:

$$\vec{D} = \varepsilon_0 \varepsilon_r \vec{E} , \tag{2.5}$$

where ε_r is the relative permittivity of the dielectric material, which can be a tensor (anisotropic medium) or scalar (isotropic medium) for nondispersive and lossless media, and

$\varepsilon_0 = 8.85 \cdot 10^{-12}$ F/m is the permittivity of vacuum. The product $\varepsilon_0 \varepsilon_r$ is designated as ε and is called permittivity of the material.

For linear magnetic materials, the relation between magnetic induction and magnetic field strength is given by:

$$\vec{B} = \mu_0 \mu_r \vec{H} , \tag{2.6}$$

where μ_r is a material parameter, called the relative permeability of the magnetic media, and $\mu_0 = 4\pi \cdot 10^{-7}$ Vs/Am is the permeability of the vacuum. The magnetic permeability of a material is $\mu = \mu_0 \mu_r$.

In conducting media, the conduction current density is directly proportional to the electric field:

$$\vec{j}_c = \sigma \vec{E} , \tag{2.7}$$

where the constant σ is the electrical conductivity of the material in S/m.

On the boundary between two media the electromagnetic field has to satisfy the boundary conditions. Considering Maxwell's equation in integral form it can be easily found that the tangential components of the electric field vector and the magnetic field vector are steady on the interface between two dielectric materials. The normal components of $\vec{D}$ and $\vec{B}$ are also continuous in charge free, nonconducting dielectric regions.

Further, on the boundary between conductors and dielectrics, as in the important case of wave propagation inside dielectrically filled metallic waveguides, there is no electric field tangentially on the conducting media and only the normal component of the electric field exists outside the conductor. The magnetic field must lie entirely tangentially along this interface, i.e. the normal component of the magnetic field is zero on such a boundary.

2.1.2 Wave equations and plane EM waves

The wave equations give the space and time dependence of the $\vec{E}$ and $\vec{H}$ vectors and describe the wave nature of time-varying macroscopic electromagnetic fields. In a source-free nonconducting simple media, where ρ and $\vec{j}_c$ are zero, the wave equations for electromagnetic fields are directly derived from Maxwell's equations:

$$\nabla^2 \vec{E} - \mu\varepsilon \frac{\partial^2 \vec{E}}{\partial t^2} = 0 , \tag{2.8}$$

$$\nabla^2 \vec{H} - \mu\varepsilon \frac{\partial^2 \vec{H}}{\partial t^2} = 0 . \tag{2.9}$$

These are homogeneous 3-dimensional vector partial differential equations. To solve the wave equations 2.8 and 2.9, we can suppose that the vectors $\vec{E}$ and $\vec{H}$ depend only on one space dimension, e.g. z coordinate, and on the time coordinate. Now we can write $\frac{\partial}{\partial x} = \frac{\partial}{\partial y} = 0$ for both vector fields, and above equations will reduce to a set of scalar differential equations that describes the plane or transversal electromagnetic (TEM) wave. Plane waves are waves in which the surfaces of constant amplitude and phase (wavefronts) are everywhere parallel planes normal to the direction of propagation.

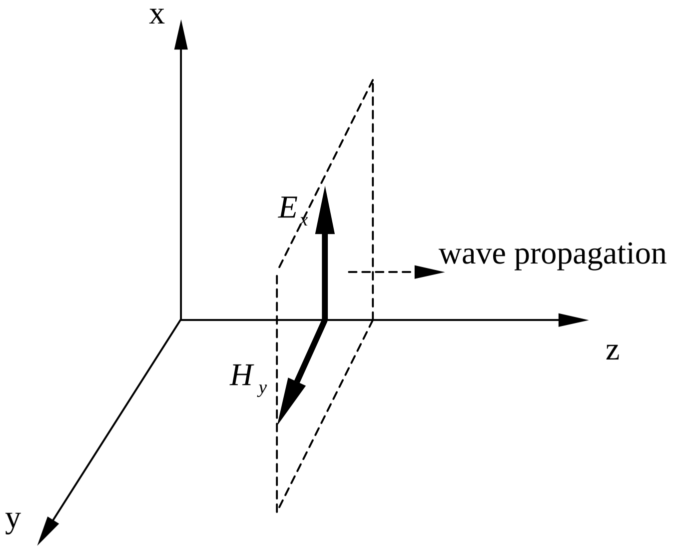

Figure 2.1 Transversal character of the plane EM wave field components

They are also the simplest practical approximation of the natural spherical EM waves at long distances from the wave sources. For the considered case, the vector fields have only transversal components and they are zero in the direction of wave propagation. They are mutually perpendicular also. Now, the scalar wave equations for $\vec{E}$ and $\vec{H}$ of the plane wave propagating along the +z direction are (Fig. 2.1):

(2.10) $$\frac{\partial^2 E_x}{\partial z^2} - \frac{1}{v_p^2}\frac{\partial^2 E_x}{\partial t^2} = 0,$$

(2.11) $$\frac{\partial^2 H_y}{\partial z^2} - \frac{1}{v_p^2}\frac{\partial^2 H_y}{\partial t^2} = 0,$$

where the constant $v_p = \frac{1}{\sqrt{\mu\varepsilon}}$ is the phase velocity in the medium described with the parameters ε and μ. In the free space v_p equals the speed of light $c = 1/\sqrt{\mu_0\varepsilon_0} = 3 \cdot 10^8$ m/s.

As a solution of above equations one can choose the function $\cos\left[\omega\left(t - z/v_p\right) + \varphi\right]$, which represents the wave propagating in +z direction. Now, the EM field components are:

(2.12) $$E_x = E_0 \cos(\omega t - \beta z + \varphi),$$

(2.13) $$H_y = H_0 \cos(\omega t - \beta z + \varphi),$$

where E_0 and H_0 are the field amplitudes that fulfill the relation $H_0 = \sqrt{\frac{\varepsilon}{\mu}} E_0$, ω is the angular frequency, $\beta = \frac{\omega}{v_p}$ is the phase constant and φ is the phase angle for $t = 0$ and $z = 0$.

The ratio $Z_c = \sqrt{\frac{\mu}{\varepsilon}}$ presents the characteristic or wave impedance. Here, the wavelength and frequency of the EM wave can be defined as $\lambda = \frac{2\pi}{\beta}$ and $f = \frac{\omega}{2\pi}$ respectively, and it is obvious that $\lambda = \frac{v_p}{f}$.

2.1.3 Complex notation of the EM fields

The sinusoidal time-harmonic fields of a plane EM wave can be represented using complex notation also, assuming that $\varphi = 0$:

(2.14) $$E_{xc} = E_0 e^{j(\omega t - \beta z)} = E_{0c} e^{-\gamma z},$$

(2.15) $$E_x = \Re(E_{xc}),$$

(2.16) $$H_{yc} = H_0 e^{j(\omega t - \beta z)} = H_{0c} e^{-\gamma z},$$

(2.17) $$H_y = \Re(H_{yc}),$$

where j is the imaginary unit, which is defined by $j^2 = -1$, $E_{0c} = E_0 e^{j\omega t}$ and $H_{0c} = H_0 e^{j\omega t}$ are the complex field amplitudes, and γ is a new complex quantity the propagation constant that is for lossless propagation pure imaginary $\gamma = j\beta = j\omega\sqrt{\varepsilon\mu}$. In the time-harmonic, loss free case, the wave equations in the frequency domain become the so-called Helmholtz's equations:

(2.18) $$\frac{\partial^2 E_{xc}}{\partial z^2} - \omega^2 \varepsilon\mu E_{xc} = 0,$$

(2.19) $$\frac{\partial^2 H_{yc}}{\partial z^2} - \omega^2 \varepsilon\mu H_{yc} = 0.$$

2.1.4 Poynting vector

The cross product of the electric field strength and magnetic field strength vectors has a dimension of a power flux density and it is called the Poynting vector:

(2.20) $$\vec{S} = \vec{E} \times \vec{H}.$$

The Poynting vector is always perpendicular to both field vectors and parallel to the direction of propagation. Its magnitude equals the rate of the power flow of the EM wave per unit area of a surface perpendicular to the propagation direction. For time-harmonic fields there is an alternative complex form $\vec{S}_c$ of the Poynting vector and for a plane EM wave from Fig. 2.1 it is [11]:

(2.21) $$\vec{S}_c = \frac{1}{2}\vec{E}_c \times \vec{H}_c^* = \frac{1}{2} E_{xc} H_{yc}^* e_z,$$

where * denotes the conjugate complex value and e_z is the unit vector in +z direction. The real part of the complex Poynting vector represents the time-averaged power flow density or the active component of the power flux density. The imaginary part of the complex Poynting vector is the reactive component of the power flow density.

Only the time harmonic fields will be considered in the following, the complex fields and their components will be denoted without subscript c, for example $E_x = E_{xc}$.

2.1.5 Complex dielectric constant

To calculate the loss in a conductive medium it is useful to define a complex dielectric constant:

$$\varepsilon_r = \varepsilon_r^{'} - j\varepsilon_r^{''}. \tag{2.22}$$

The real part of the relative complex permittivity is the dielectric constant of the material $\varepsilon_r^{'} = \varepsilon_r$ and the imaginary part $\varepsilon_r^{''} = \dfrac{\sigma}{\omega\varepsilon_0}$ includes conductive and dielectric losses and can be described as the dielectric loss factor. The phase of the ε_r denotes the dielectric loss tangent:

$$\tan\delta = \frac{\Im(\varepsilon_r)}{\Re(\varepsilon_r)} = \frac{\sigma}{\omega\varepsilon_0\varepsilon_r}. \tag{2.23}$$

So, the dissipated power density in a material can be calculated using:

$$p_{dis} = \frac{1}{2}\sigma\left|E_0\right|^2. \tag{2.24}$$

The theory of microwave heating is based on relation 2.24. Here it should be pointed out that the loss factor itself is a function of frequency and temperature.

Further, in a lossy material the plane waves are considered to be damped because of the presence of conductive or ohmic losses and dielectric or polarization losses. In this case, the propagation constant becomes a complex value $\gamma^2 = -\omega^2\varepsilon_r\mu$, where ε_r is defined by equ. 2.22. So, the propagation constant $\gamma = \alpha + j\beta$ has both, a real part that corresponds to the damping as an attenuation constant α, and the imaginary part, which is related to the phase constant β. Hence, in a lossy medium the field attenuates exponentially along the direction propagation, which can be expressed by:

$$\vec{E} = E_0 e^{-\gamma z} = E_0 e^{-\alpha z} e^{-j\beta z}. \tag{2.25}$$

2.1.6 Effective loss factor

Starting from Ampere's law (see equ. 2.4) and using the constitutive relations and the concept of the complex dielectric constant (equ. 2.22), one can derive $\vec{j}_t$, the total current density in the dielectric material for a sinusoidal time-harmonic electric field:

$$rot\vec{H} = \vec{j}_t = \left(\sigma_d + j\omega\varepsilon_0\varepsilon_r\right)\vec{E}, \tag{2.26}$$

where σ_d is the conductivity of the dielectric. Further, it can be easily shown that only the imaginary part of the complex dielectric constant contributes to the losses:

$$\vec{j}_t = \left[\sigma_d + j\omega\varepsilon_0\left(\varepsilon_r^{'} - j\varepsilon_r^{''}\right)\right]\vec{E} = \left(\sigma_d + \omega\varepsilon_0\varepsilon_r^{''}\right)\vec{E} + j\omega\varepsilon_0\varepsilon_r^{'}\vec{E}\ , \tag{2.27}$$

because it is related to the in phase current density component (Fig. 2.2). The real part of the complex relative permittivity contributes to the energy that is stored in the dielectric and it is related to the current density component which is normal to the electric field (Fig. 2.2). The disadvantage of the classical approach presented with equation 2.23, where a general conductivity σ stands for all losses, is that the loss mechanisms are not highlighted, and it is impossible to estimate their single contributions into the total loss.

Now the losses due to conduction and those due to dipolar polarization can be grouped together by defining an effective dielectric loss factor [14,15]:

$$\varepsilon_{reff}^{''} = \varepsilon_r^{''} + \frac{\sigma_d}{\omega\varepsilon_0}\ , \tag{2.28}$$

which is always a part of current component in phase:

$$\vec{j}_t = \omega\varepsilon_0\varepsilon_{reff}^{''}\vec{E} + j\omega\varepsilon_0\varepsilon_r^{'}\vec{E}\ . \tag{2.29}$$

The total losses can be represented defining the effective conductivity:

$$\sigma_{eff} = \sigma_d + \omega\varepsilon_0\varepsilon_r^{''}\ . \tag{2.30}$$

Using the effective conductivity concept, the other polarization losses, such as electronic, atomic and space charge polarization losses, can be easily taken into account, by addition of their contributions to σ_{eff}.

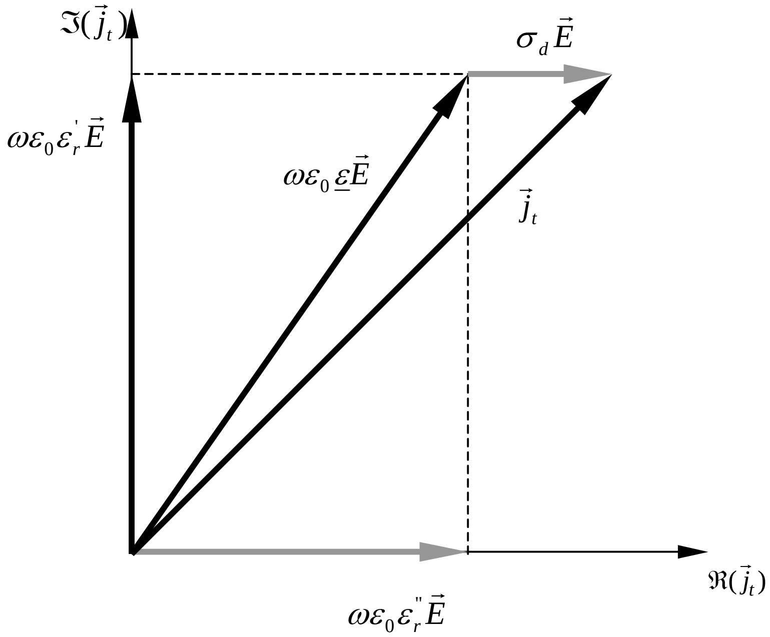

Figure 2.2 Phasor diagram of a dielectric material with ionic conduction

After introducing the effective dielectric loss factor, an effective loss tangent can be also defined as:

$$\tan\delta_{eff} = \frac{\varepsilon_{reff}^{''}}{\varepsilon_r^{'}} = \frac{\varepsilon_r^{''} + \frac{\sigma_d}{\omega\varepsilon_0}}{\varepsilon_r^{'}} = \tan\delta + \frac{\sigma_d}{\omega\varepsilon_0\varepsilon_r^{'}} . \tag{2.31}$$

The complex permittivity concept can be visually presented using the phasor diagram (Fig. 2.2).

2.1.7 Penetration depth and surface impedance in conductors

A plane EM wave will penetrate a conductor very weakly and the field will be concentrated near the conductor surface. Penetration is a function of the material properties and the frequency and can be characterized by the penetration depth δ, that is the distance from the surface at which the field is damped to the value $\frac{1}{e}$ from the value at the surface. From 2.25 it is obvious that $\delta = \frac{1}{\alpha}$. For good conductors the electric conductivity has very high values and satisfies the condition $\sigma >> \omega\varepsilon$. In this case, the attenuation and the phase constants are equal and they are a function only of the frequency, electric conductivity and permeability, $\alpha = \beta = \sqrt{\frac{\omega\mu\sigma}{2}}$. This relation leads to the well known equation for the penetration depth (skin depth) in conductors:

$$\delta = \frac{1}{\sqrt{\pi f \mu\sigma}} . \tag{2.32}$$

The losses on the surface can be calculated using the surface impedance R_s of a good conductor [12]:

$$R_s = \sqrt{\frac{\omega\mu}{2\sigma}} = \frac{1}{\sigma\delta} . \tag{2.33}$$

The penetration depths δ and the surface impedances R_s for silver, copper, aluminium, brass and stainless steel at the ISM frequency 2.45 GHz are calculated using equations 2.32 and 2.33 and are given in Tab. 2.1.

Material	δ at 2.45 GHz (μm)	R_s at 2.45 GHz (Ω)
Ag	1.282	0.0124
Cu	1.336	0.0129
Al	1.657	0.0160
Brass	2.822	0.0273
Stainless steel	3.469	0.0335

Table 2.1 Penetration depths and surface impedances at 2.45 GHz

2.1.8 Penetration depth in dielectrics

The penetration depth in dielectrics is determined by the absorption of EM power in the material. The field intensity and its associated power flux density fall exponentially with the distance from the surface. The penetration depth D_p in dielectrics is defined as the depth into the material at which the power has fallen to e^{-1} of its surface value, i.e. $D_p = \frac{1}{2\alpha}$ where α is the attenuation constant in the lossy material. In dielectrics the electric conductivity is much lower than for conductors and α is a function of both, the relative permittivity and the loss factor. Hence, the power penetration depth in dielectrics can be calculated using [14, 16]:

$$D_p = \frac{\lambda_0}{2\pi\sqrt{2\varepsilon_r'}} \frac{1}{\sqrt{\sqrt{1+\left(\frac{\varepsilon_r''}{\varepsilon_r'}\right)^2}-1}}, \tag{2.34}$$

where λ_0 is the wavelength in the free space.

2.1.9 EM wave polarizations

Depending on the spatial variation of the plane wave field components during one time cycle, different polarizations of a plane wave can be distinguished: linear, circular and elliptical. In the linearly polarized plane wave case, the field vector varies only along one direction, which is perpendicular to the propagation direction (Fig. 2.1). For the circular and the elliptical polarizations the top of the field vector draws a circle or an ellipse in the transversal plane, respectively, during one oscillation period T (Fig. 2.3).

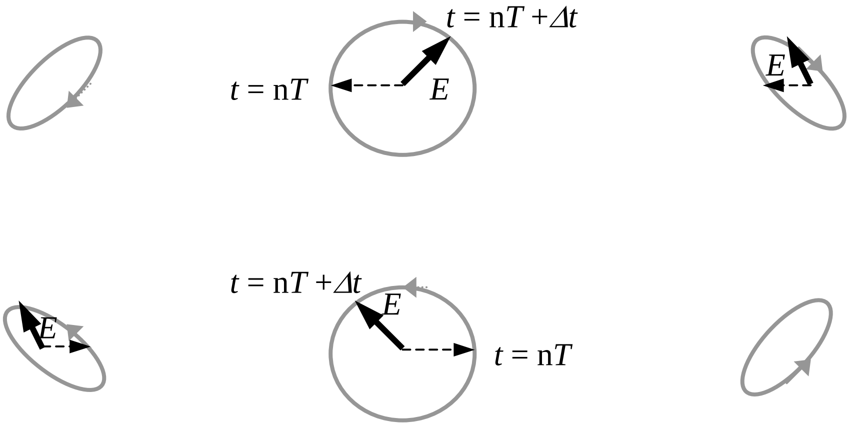

Figure 2.3 Elliptical and circular polarizations of a plane wave

2.1.10 EM wave reflection and refraction

It is also necessary to determine and describe the reflection and refraction of EM waves. If a plane EM wave propagates from one dielectric media 1 into another dielectric media 2, then it will be partially transmitted into the media 2 and partially reflected back into the media 1. This will occur under the well known Fresnel's law of reflection and refraction [11, 12]. It describes the spatial behavior of the incident, reflected and transmitted wave and gives the geometrical relations between the directions of these waves. The amplitudes of the reflected and transmitted waves can be calculated using the so called Fresnel’s coefficients of reflection and transmission, which are functions of the material parameters.

So, it is very important for efficient microwave heating to assure that only a small amount of the incident EM power will be reflected from the material, which means that the processing sample has to be matched to the processing EM fields. Additionally, the material parameters have to ensure a good absorbtion of the transmitted EM energy into the material at a given processing frequency.

2.2 Electromagnetic Waves in Rectangular Waveguides

2.2.1 Rectangular waveguides

High power high frequency electromagnetic waves can be transported very efficiently through waveguides. Waveguides are metallic hollow structures, usually with rectangular, circular or elliptical transversal geometry, filled with air or some other dielectric. Attenuation along the propagation in such waveguides is much lower than in the case of EM waves guided by wires or by coaxial waveguides, because the losses are only due to the ohmic dissipation in the highly conducting metallic waveguide walls. This dissipation is very low, making the waveguides comfortable for transmission of high power microwaves.

Starting from Maxwell’s equations and satisfying the boundary conditions, the EM fields inside waveguides with simple geometry can be well determined [11,12]. Knowing these EM field distributions in the waveguides, it is easy to calculate all important technical waveguide parameters, and design them appropriately for the application.

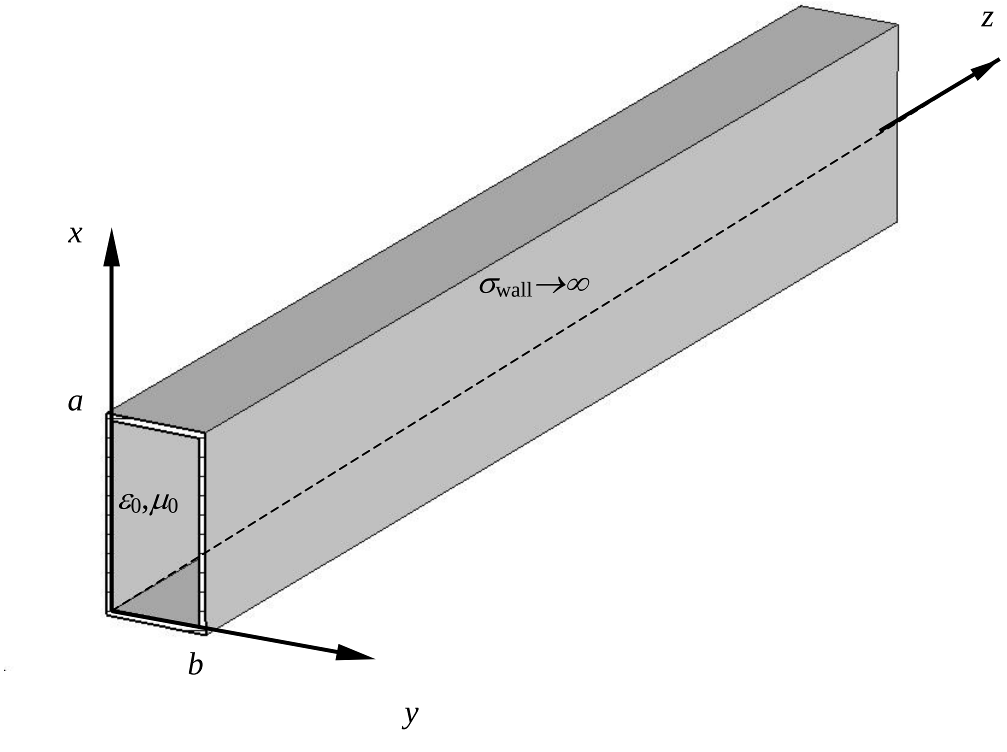

Figure 2.4 Rectangular air filled waveguide with perfectly conducting walls

For the propagation of time harmonic EM waves in z direction along a rectangular air filled waveguide with perfectly conducting walls (Fig. 2.4), the EM fields have to satisfy Maxwell’s equations:

$$rot\vec{E} = -j\omega\mu\vec{H}\,, \tag{2.35}$$

$$rot\vec{H} = j\omega\varepsilon\vec{E}\,. \tag{2.36}$$

The boundary conditions have to be also satisfied, i. e. on assumed perfectly conducting walls the tangential electric field and the normal magnetic field components have to vanish, which can be described by (using the Fig. 2.4):

(2.37) $$E_y = H_x = E_z = 0,\ \text{for}\ x = 0\ \text{and}\ x = a\text{, and}$$

(2.38) $$E_x = H_y = E_z = 0,\ \text{for}\ y = 0\ \text{and}\ y = b\,.$$

The propagating wave in z direction has an exponential $e^{-jk_z z}$ dependency on the z coordinate, where k_z is the wave number or the propagation constant along the waveguide axis (z direction). Hence, all z derivatives can be interchanged by multiplication of $-jk_z$. Now, after an elimination of the transversal field components from above frequency domain equations using the rules for *rot* calculations, the two dimensional homogeneous scalar Helmholtz's equation for the longitudinal field components can be written as:

(2.39) $$\nabla_t H_z + k^2 H_z = 0\,,$$

(2.40) $$\nabla_t E_z + k^2 E_z = 0\,,$$

where $\nabla_t = \frac{\partial}{\partial x} + \frac{\partial}{\partial y}$ is a transversal differential operator and $k^2 = \omega^2 \varepsilon\mu - k_z^2$. Using the method of variables separation and satisfying the given boundary conditions, the solutions of the above partial differential equations can be written as:

(2.41) $$H_z = H_0 \cos(k_x x)\cos(k_y y) e^{-jk_z z}\text{, and}$$

(2.42) $$E_z = E_0 \sin(k_x x)\sin(k_y y) e^{-jk_z z}\,,$$

where the constants H_0 and E_0 are the amplitudes of the magnetic field z component and the electric field z component. The constants k_x and k_y are the wave numbers of propagation in x and y directions. They also satisfy the relations: $k^2 = k_x^2 + k_y^2$, $k_x = \frac{m\pi}{a}$ and $k_y = \frac{n\pi}{b}$, where *m* and *n* are nonnegative integers. The different field solutions for different combinations of *m* and *n* are called EM waveguide modes and they present physically different field distributions of the propagating EM waves in the waveguides. Because of that, the integers *m* and *n* are also called the mode numbers.

2.2.2 Cut off frequency, cut off wavelength and waveguide wavelength

Now, the propagation constant in z direction k_z can be expressed as:

(2.43) $$k_z = \sqrt{\omega^2 \varepsilon\mu - \left(\frac{m\pi}{a}\right)^2 - \left(\frac{n\pi}{b}\right)^2}\,.$$

For wave propagation in z direction the propagation constant k_z must be purely real, or the wave will be highly attenuated along the waveguide and no propagation will be possible (evanescent modes). Hence, the transversal waveguide dimensions and the mode numbers must be chosen to satisfy the following condition:

(2.44) $$\omega^2\varepsilon\mu-\left(\frac{m\pi}{a}\right)^2+\left(\frac{n\pi}{b}\right)^2>0\,,$$

for a given frequency $f=\frac{\omega}{2\pi}$. In other words, for given a and b only the waves with frequencies higher than the following cut-off frequency f_c can propagate:

(2.45) $$f_c=\frac{c}{2\pi}\sqrt{\left(\frac{m\pi}{a}\right)^2+\left(\frac{n\pi}{b}\right)^2}\,,$$

and the waveguides are low pass filters. So, in waveguides it is possible to transfer only waves with wavelengths shorter than the cut-off wavelength:

(2.46) $$\lambda_c=\frac{c}{f_c}=\frac{2}{\sqrt{\left(\frac{m}{a}\right)^2+\left(\frac{n}{b}\right)^2}}\,.$$

Using the equations 2.43 and 2.45 the wavelength $\lambda_{g,z}$ of waves propagating in the waveguide in z direction can be calculated as:

(2.47) $$\lambda_{g,z}=\frac{2\pi}{k_z}=\frac{2\pi}{\sqrt{\frac{2\pi}{\lambda^2}-\left(\frac{2m}{a}\right)^2-\left(\frac{2n}{b}\right)^2}}=\frac{\lambda}{\sqrt{1-\left(\frac{f_c}{f}\right)^2}}\,.$$

From the last relation the wavelength in the waveguide $\lambda_{g,z}$ will be always longer than the wavelength in the free space λ. As it can be seen in the Fig. 2.5, for the special case that $f=f_c$ the $\lambda_{g,z}$ reaches approximately infinity and for frequencies much higher than f_c the wavelength in the waveguide is approaching the free space wavelength.

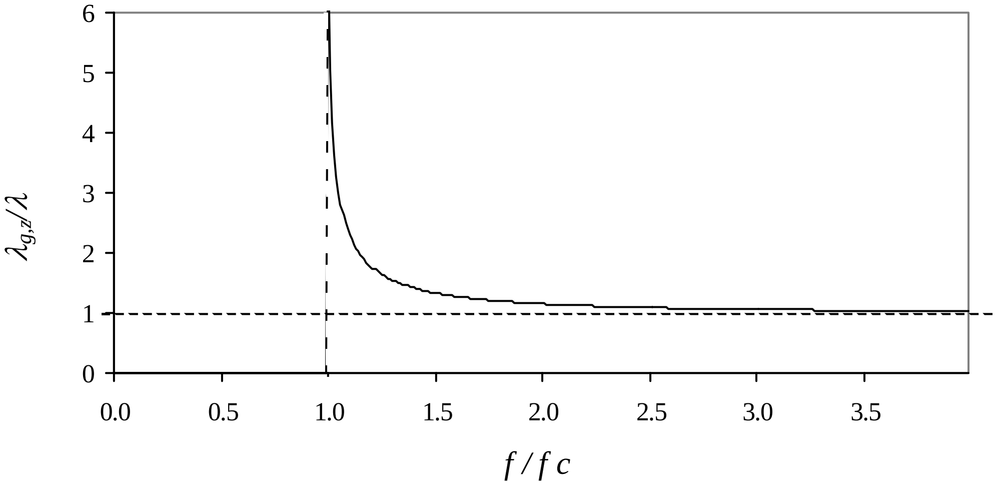

Figure 2.5 Normalized waveguide wavelength as a function of normalized frequency

2.2.3 Phase velocity and group velocity

Also the phase velocity v_P of the EM mode in the waveguide differs from the phase velocity in the free space *c* [13,17]:

$$v_P = \frac{\omega}{k_z} = f\lambda_{g,z} = \frac{c}{\sqrt{1-\left(\frac{f_c}{f}\right)^2}}. \tag{2.48}$$

The phase velocity is the velocity of phase propagation along the waveguide in z direction and as it can be seen from above equation, it is always larger than the speed of light in free space. However, EM signals carrying the EM energy propagate with the group velocity v_G through the waveguides:

$$v_G = \frac{d\omega}{dk_z} = \frac{c^2}{v_P} = c\sqrt{1-\left(\frac{f_c}{f}\right)^2}, \tag{2.49}$$

which is always lower than the speed of light *c*. The normalized group velocity is presented in Fig. 2.6 as a function of the normalized frequency. The group velocity at the cut-off frequency approaches zero (there is no wave propagation in the waveguide) and near the cut-off it shows strong frequency dependency, which is not desirable for practical use. So, in common applications the waveguides are used at frequencies above $\frac{5}{4} f_c$ (grey line in Fig. 2.6).

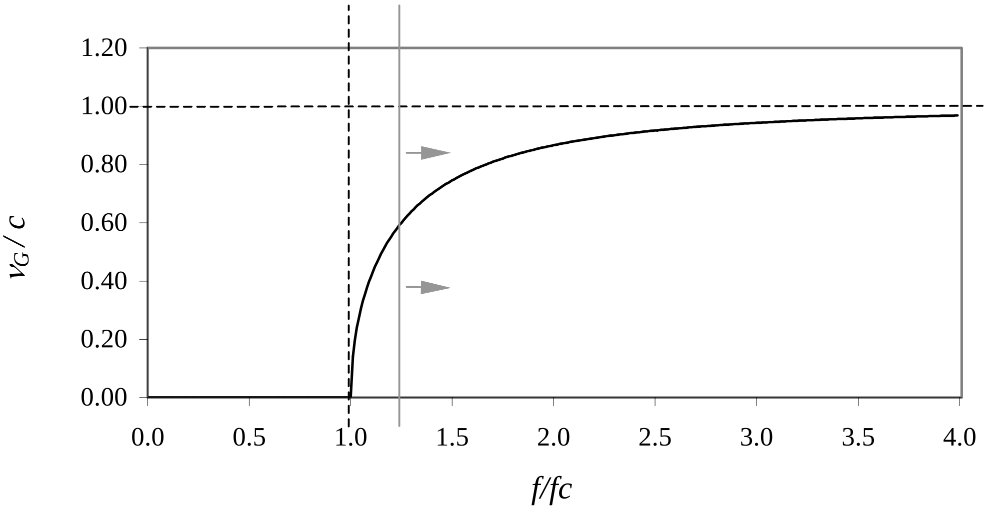

Figure 2.6 Normalized group velocity as a function of normalized frequency

2.2.4 Transversal electric modes

Using the expressions for axial field components (equ. 2.41 and 2.42) the transversal electric and magnetic field components can be calculated. For $E_z = 0$ (only the magnetic field has an axial component) the other field components are:

$$E_x = -\frac{j\omega\mu}{k^2}\frac{\partial H_z}{\partial y} = \frac{j\omega\mu}{k^2}\frac{n\pi}{b} H_0 \cos(\frac{m\pi}{a}x)\sin(\frac{n\pi}{b}y)e^{-jk_z z}, \tag{2.50}$$

(2.51) $$E_y = \frac{j\omega\mu}{k^2}\frac{\partial H_z}{\partial x} = -\frac{j\omega\mu}{k^2}\frac{m\pi}{a}H_0 \sin(\frac{m\pi}{a}x)\cos(\frac{n\pi}{b}y)e^{-jk_z z},$$

(2.52) $$H_x = -\frac{k_z}{k^2}\frac{\partial H_z}{\partial x} = \frac{k_z}{k^2}\frac{m\pi}{a}H_0 \sin(\frac{m\pi}{a}x)\cos(\frac{n\pi}{b}y)e^{-jk_z z},$$

(2.53) $$H_y = -\frac{k_z}{k^2}\frac{\partial H_z}{\partial y} = \frac{k_z}{k^2}\frac{n\pi}{b}H_0 \cos(\frac{m\pi}{a}x)\sin(\frac{n\pi}{b}y)e^{-jk_z z}.$$

This type of waves has only an axial magnetic field component, i. e. the electric field components are transversal and it is called transversal electric TE wave or H wave. The transversal magnetic and electric field components are mutually orthogonal, as in a plane wave. According the above notation it is obvious that the integers *m* and *n* cannot be zero at the same time, i. e. at least one of them must be different from 0.

Characteristic impedance of TE modes

The relation between the transversal electric and magnetic field components presents the characteristic impedance of a TE mode [18,19]:

(2.54) $$Z_{TE} = \frac{E_x}{H_y} = -\frac{E_y}{H_x} = \frac{\omega\mu}{k_z} = \sqrt{\frac{\mu}{\varepsilon}}\frac{1}{\sqrt{1-\left(\frac{f_c}{f}\right)^2}}.$$

2.2.5 Transversal magnetic modes

Similarly, for $H_z = 0$, the transversal field components are:

(2.55) $$E_x = -\frac{k_z^2}{k^2}\frac{\partial E_z}{\partial x} = -\frac{k_z^2}{k^2}\frac{m\pi}{a}E_0 \cos(\frac{m\pi}{a}x)\sin(\frac{n\pi}{b}y)e^{-jk_z z},$$

(2.56) $$E_y = -\frac{k_z^2}{k^2}\frac{\partial E_z}{\partial y} = -\frac{k_z^2}{k^2}\frac{n\pi}{b}E_0 \sin(\frac{m\pi}{a}x)\cos(\frac{n\pi}{b}y)e^{-jk_z z},$$

(2.57) $$H_x = \frac{j\omega\varepsilon}{k^2}\frac{\partial E_z}{\partial y} = \frac{j\omega\varepsilon}{k^2}\frac{n\pi}{b}E_0 \sin(\frac{m\pi}{a}x)\cos(\frac{n\pi}{b}y)e^{-jk_z z},$$

(2.58) $$H_y = -\frac{j\omega\varepsilon}{k^2}\frac{\partial E_z}{\partial x} = -\frac{j\omega\varepsilon}{k^2}\frac{n\pi}{b}E_0 \cos(\frac{m\pi}{a}x)\sin(\frac{n\pi}{b}y)e^{-jk_z z}.$$

These equations present the field components of so called transversal magnetic TM waves, because they have only an electric field component parallel to the propagation direction. They are also called E waves. For TM waves both mode numbers must be non zero in order to have non vanishing field components (equ. 2.55 – 2.58).

Characteristic impedance of TM modes

The characteristic impedance of TM modes is [19]:

(2.59) $$Z_{TM} = \frac{E_x}{H_y} = -\frac{E_y}{H_x} = \frac{\omega\mu}{k_z} = \sqrt{\frac{\mu}{\varepsilon}}\sqrt{1-\left(\frac{f_c}{f}\right)^2} .$$

In Fig. 2.7 both characteristic impedances are shown. For both, TE and TM modes, the characteristic impedance is pure imaginary for $f < f_c$, the phase difference between the transversal electric and transversal magnetic field component is $\frac{\pi}{2}$ and there is no energy transfer along the waveguide in the z direction. For frequencies higher than cut off the characteristic impedances are pure real, the transversal field components are in phase and EM energy transfer occurs in the z direction.

For the critical case of $f = f_c$ the characteristic impedance of TE modes is infinite and the waveguide can be presented as an open circuit. If the frequency of the wave is above the cut off, then Z_{TE} falls with increasing frequency to the amount of the free space characteristic wave impedance $Z_c = \sqrt{\frac{\mu_0}{\varepsilon_0}} = 377\Omega$, for frequencies much higher than f_c.

The characteristic impedance of TM waves is zero at the cut-off frequency and the waveguide is a short cut. With increasing frequency, Z_{TM} is also increasing and it approaches asymptotically Z_c.

2.2.6 Superposition of two TEM waves

TM or TE waves can be described by a superposition of two plane TEM waves [11], which virtually travel along the waveguide bouncing from the waveguide walls with a constant angle θ. In Fig. 2.8 the case of a TM wave with longitudinal electric field component

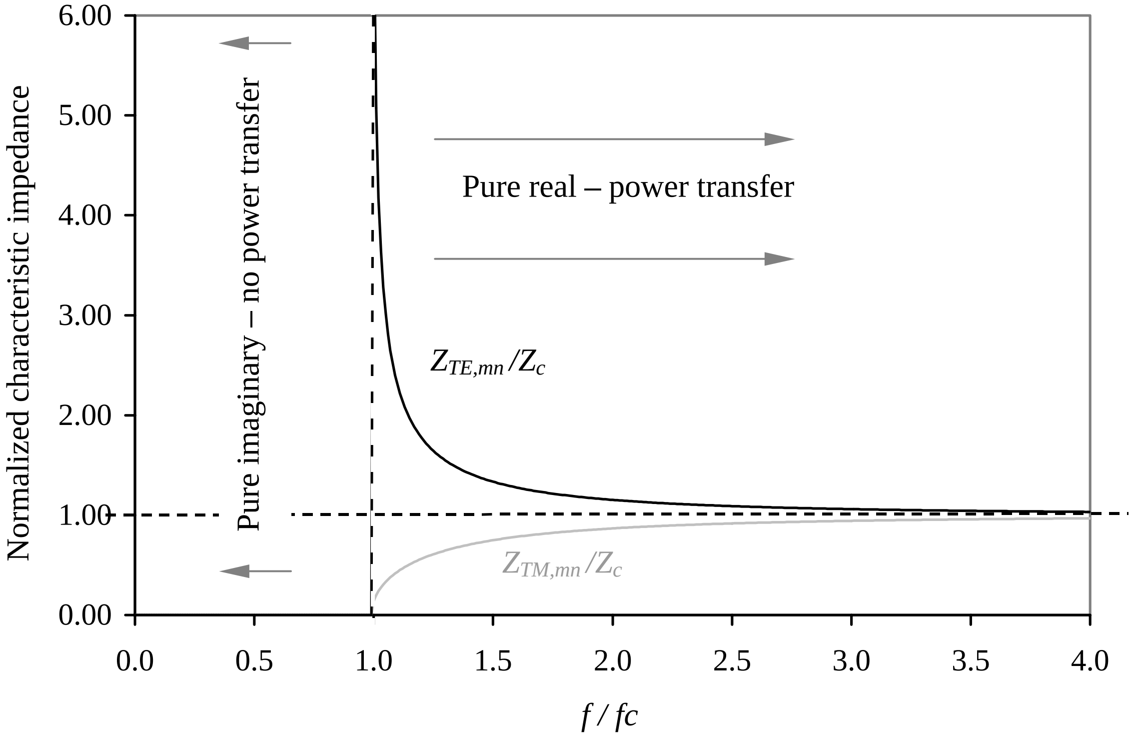

Figure 2.7 Normalized characteristic mode impedances as a function of normalized frequency

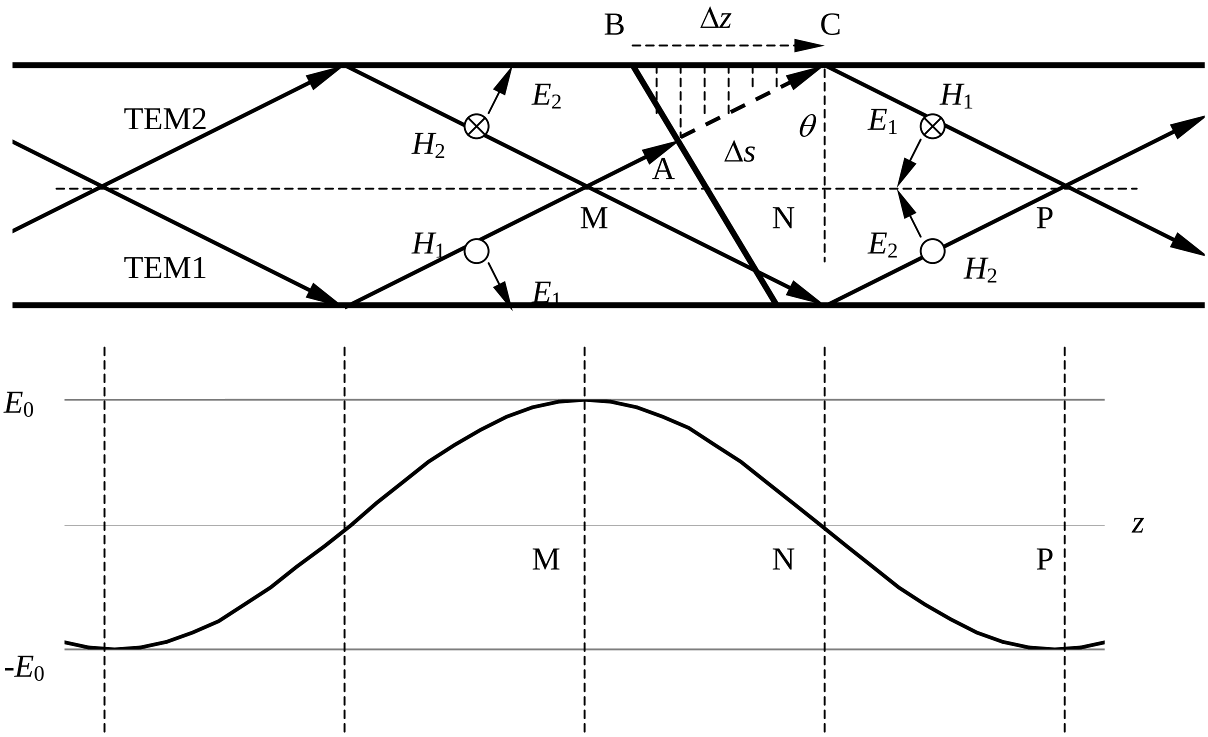

Figure 2.8 TM wave as a superposition of two plane waves

is shown. The plane waves are assigned as TEM1 and TEM2 with E_1, H_1 and E_1, H_2 transversal field components, respectively. It is obvious that a superposition of the H field components is always destructive and there is no resulting magnetic field component in the z direction. However, the summation of the E_1 and E_2 components gives constructive results in the points M and P and a destructive zero result in point N. So, the resulting electric field has a longitudinal component, which is sinusoidally dependent on the *z* coordinate, as for a TM waveguide mode.

Using this approach and Fig. 2.8, a more pictorial explanation for the rise of the phase velocity of the waveguide waves above the speed of light can be given. The phase front of a plane TEM1 wave propagates with the velocity *c* from point A to the point C (triangle ABC in Fig. 2.8) along the distance Δs for a time Δt. For the same time interval Δt, the constant phase point B has to travel over the distance Δz. Hence, the phase velocity in the waveguide must be greater than *c*:

$$\Delta t = \frac{\Delta s}{c} = \frac{\Delta z}{v_P} \quad \text{and} \quad v_P = \frac{c}{\sin\theta} . \tag{2.60}$$

Further, for the same period of time Δt, the superpositioned wave proceeds the distance $\Delta s \cdot \cos\theta$, which gives the group velocity $v_G = c \cdot \cos\theta$, obviously lower than *c*.

2.2.7 Propagating modes

It is very useful to determine which modes can propagate along the waveguide depending on the waveguide cross section and the wave frequency [11,20]. In Fig. 2.9 the normalized cutoff wavelength as a function of the ratio *b/a* is shown. For a given ratio *b/a* a line parallel to the λ_c/a axis should be drawn in the graph. Then, parallel to the b/a axis, a line for λ/a has to be also assigned to the graph. The propagating modes are all modes that are below the crossing point of those two lines.

As an example, it will be shown which modes can propagate along the standard WR340 at 2.45 GHz. The inner transversal dimensions of WR340 are a = 86 mm and b = 43 mm and the free space wavelength at 2.45 GHz is λ = 122.4 mm. Hence, the needed ratios are: b/a = 0.5 and λ/a = 1.42 (dashed lines in Fig. 2.9) and it is obvious that the only propagating mode is the fundamental TE_{10} mode (only this mode is below the crossing point C).

From Fig. 2.9 it can be also concluded that the dominant TE_{10} mode has the lowest cut off frequency (the highest cut off wavelength $\lambda_c = 2a$) and for b/a = 0.5 the next mode TE_{20} can propagate first at frequencies two times higher than f_c. So, there is a safe monomode operation range $\lambda_c = a \ldots 2a$ for b/a = 0.5 (framed area in Fig. 2.9) and because of that the practically so called standard waveguides have the ratio b/a = 0.5.

2.2.8 EM power in waveguides

Due to the fact that in both TE and TM modes there is only one longitudinal field component, the EM wave in the waveguide carries the EM power only in the z axial direction. The power propagating along the waveguide is equal to the flux of the Poynting vector through the waveguide cross section [12]:

$$\langle S_z \rangle = \frac{1}{2}|E_t| \cdot |H_t| = \frac{1}{2Z_{c,w}}|E_t|^2 = \frac{1}{2}Z_{c,w}|H_t|^2, \tag{2.61}$$

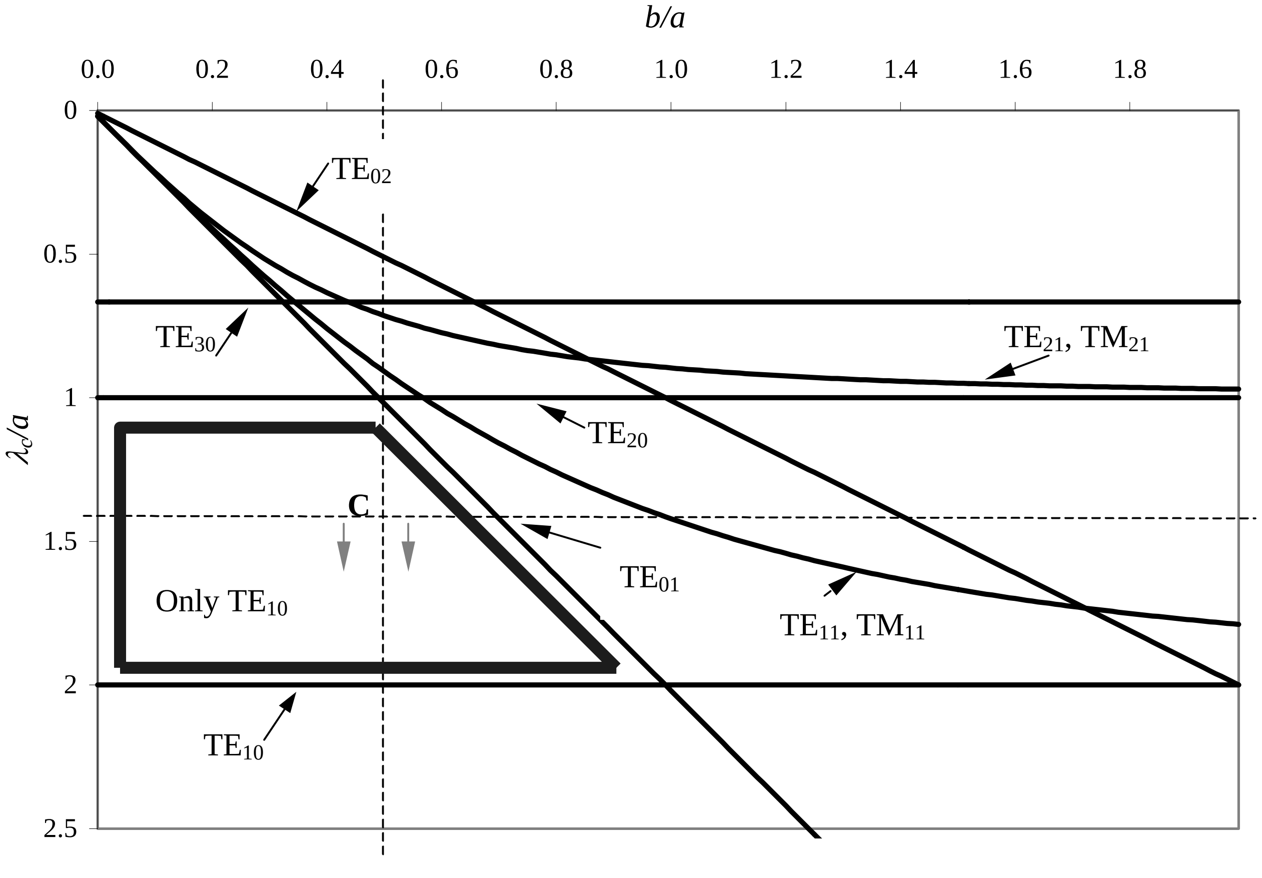

Figure 2.9 Cutoff wavelength as a function of transversal waveguide dimensions

where the subscripts *t* and *w* stand for transversal and waveguide, respectively. Hence, the averaged power carried by an EM wave along the waveguide is:

$$P_{aver} = \int_s \langle S_z \rangle ds = \frac{1}{2Z_{c,w}} \int_s |E_t|^2 ds = \frac{1}{2} Z_{c,w} \int_s |H_t|^2 ds, \tag{2.62}$$

through the cross section area $s = a \cdot b$.

For TE$_{mn}$ waves where *m* and *n* are non zero the averaged power can be calculated as:

$$P_{aver,TEmn} = \frac{1}{2} Z_{c,TE} \int_0^a \int_0^b \left(|H_x|^2 + |H_y|^2 \right) dxdy = \frac{ab}{8} Z_c \left(\frac{f}{f_c} \right)^2 \sqrt{1 - \left(\frac{f_c}{f} \right)^2} H_0^{\,2}, \tag{2.63}$$

and for TE$_{m0}$ or TE$_{0n}$ modes it is $P_{aver} = 2P_{aver,TEmn}$.

The average power of TM modes is:

$$P_{aver,TM} = \frac{1}{2Z_{c,TM}} \int_0^a \int_0^b \left(|E_x|^2 + |E_y|^2 \right) dxdy = \frac{ab}{8Z_c} \left(\frac{f}{f_c} \right)^2 \sqrt{1 - \left(\frac{f_c}{f} \right)^2} E_0^{\,2}. \tag{2.64}$$

The maximum peak power that can be transferred by a waveguide is limited by dielectric breakdown. This peak power can be determined by calculating the Poynting vector as a function of the maximum E field [21]. For the fundamental TE$_{10}$ mode it is given by:

$$P_{\max,TE_{10}} = \frac{ab}{4Z_{TE_{10}}} |E_{\max}|^2, \tag{2.65}$$

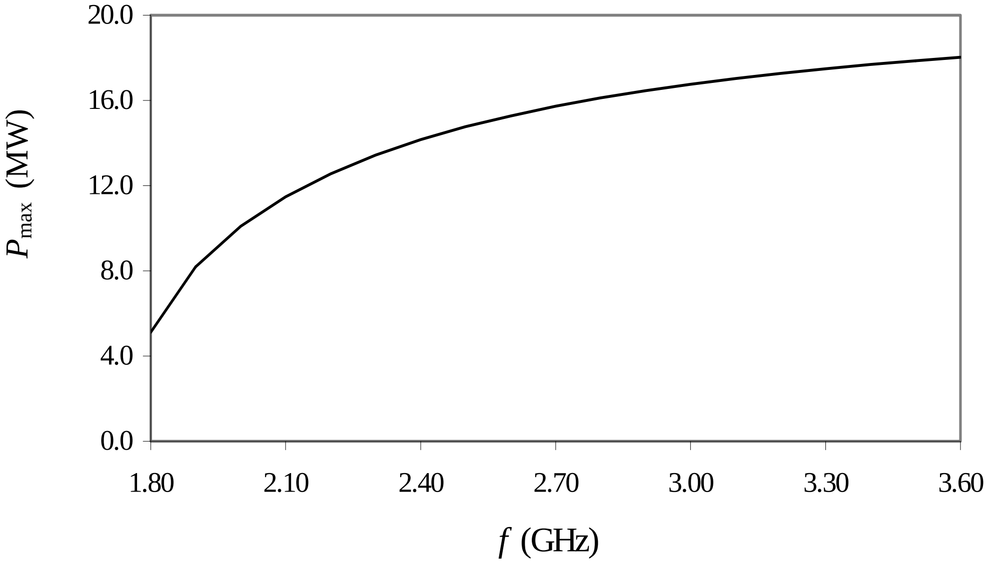

Figure 2.10 Theoretical maximum peak power of TE$_{10}$ mode in air filled WR340 standard with perfectly conducting walls

where $E_{\max}$ is a breakdown electric field for the dielectric, which fills the waveguide.

The maximum power capability versus frequency of the fundamental TE_{10} mode in a waveguide with a = 86 mm and b = 43 mm (standard WR340), filled with dry air at normal temperature and pressure ($E_{\max} = 2.9 \cdot 10^6$ V/m [20]), was calculated using the equation 2.65 and it is shown in Fig. 2.10. However, this is the theoretical value, and in practice the losses in the waveguide walls must be taken into account for deriving the realistic maximum power handling capability.

2.2.9 Losses in rectangular waveguides and attenuation constant

In practice waveguides are manufactured from materials with high but finite conductivity and with ohmic losses in the waveguide walls. To determine these power losses P_l it will be assumed that the EM field distribution inside the waveguide is the same as for the ideal case of infinitely conducting walls. Under this assumption, the surface current density on the inner waveguide walls can be determined as:

$$\vec{j}_{s1} = \vec{n}_1 \times \vec{H}\Big|_{x=0} , \tag{2.66}$$

$$\vec{j}_{s2} = \vec{n}_2 \times \vec{H}\Big|_{x=a} , \tag{2.67}$$

$$\vec{j}_{s3} = \vec{n}_3 \times \vec{H}(x) \text{ and} \tag{2.68}$$

$$\vec{j}_{s4} = \vec{n}_4 \times \vec{H}(x) , \tag{2.69}$$

where $\vec{n}_1$, $\vec{n}_2$, $\vec{n}_3$ and $\vec{n}_4$ are unit normal vectors on the s_1, s_2, s_3 and s_4 inner wall surfaces, respectively (see Fig. 2.11).

After the following integration:

$$P_l = \frac{R_s}{2}\left[\int_0^b \left(\left|\vec{j}_{s1}\right| + \left|\vec{j}_{s2}\right|\right) dy\Delta z + \int_0^a \left(\left|\vec{j}_{s3}\right| + \left|\vec{j}_{s4}\right|\right) dx\Delta z\right], \tag{2.70}$$

the attenuation constant can be given as [12]:

$$\alpha = \frac{\frac{\Delta P_l}{\Delta z}}{2P_{aver}} = \frac{R_s}{Z_c b}\frac{1 + 2\frac{b}{a}\left(\frac{f_c}{f}\right)^2}{\sqrt{1 - \left(\frac{f_c}{f}\right)^2}} . \tag{2.71}$$

The attenuation constants of WR340 made from silver (Ag), copper (Cu), aluminium (Al), brass and stainless steel are shown in Fig. 2.12. For frequencies near the cut-off frequency, the attenuation is very high. With increasing frequency it drops very fast to a minimum and with further frequency increasing it increases slowly. The difference at 2.45 GHz between Ag and Al is only $\Delta\alpha$ = 0.004 dB/m. Differences between Ag and Cu are negligible. Waveguides

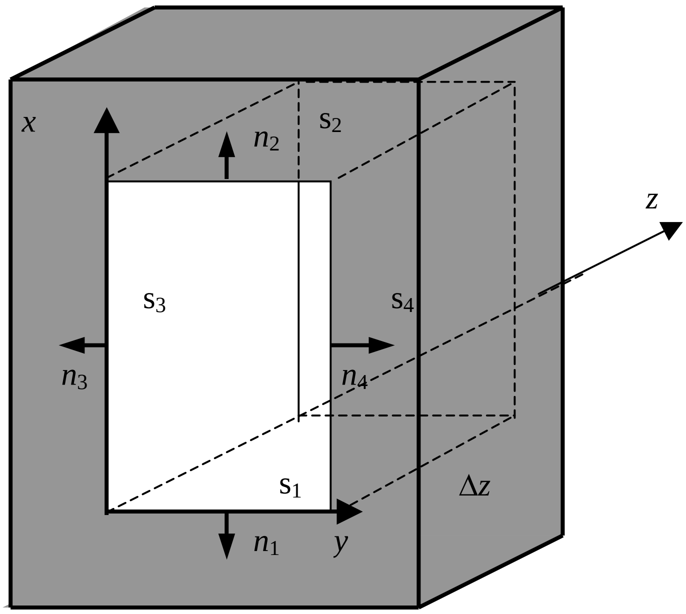

Figure 2.11 Calculation of the waveguide attenuation constant

made from brass or steel have the highest α. Hence, using Al as waveguide material, instead of Cu or even more expensive Ag (even if the silver is used only as a thin layer on the inner waveguide walls), the material costs can be reduced without a significant reduction of power efficiency.

In Fig. 2.13 the attenuation constant of WR340 made from aluminium versus frequency, but for different *b/a* ratio is shown. For constant *a*, α increases with decreasing *b*. So, even though *b* does not play any role in the calculations of f_c, k_z and $\lambda_{g,z}$, of the TE_{10} mode, it should not be taken arbitrary. In practice, this ratio is usually *b/a* = 0.5, because of the almost minimum attenuation in this case (Fig. 2.13) and to avoid the excitation of the parasitic TE_{01} mode.

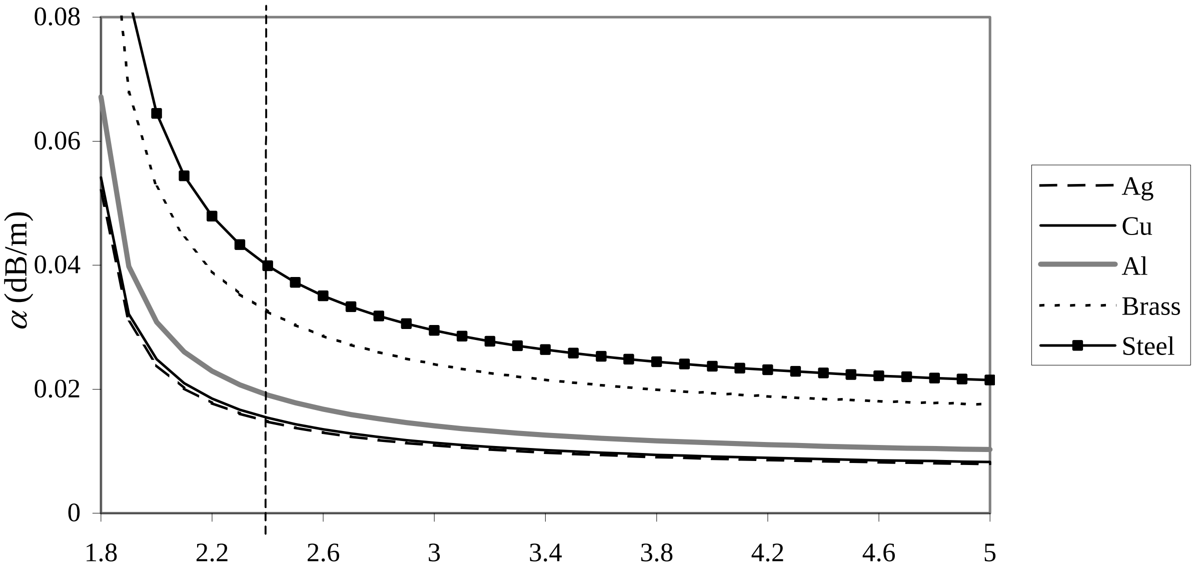

Figure 2.12 Attenuation constant of WR340 versus frequency for different waveguide walls materials

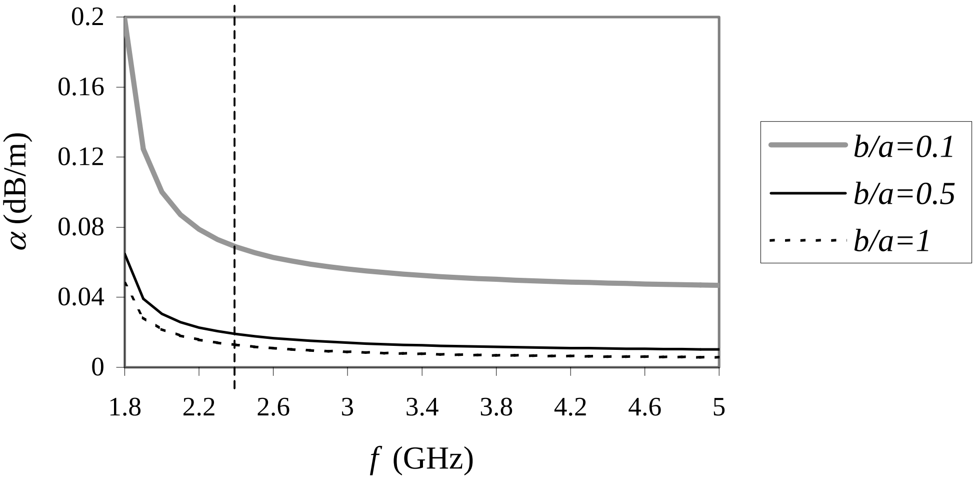

Figure 2.13 Attenuation constant of WR340 made from Al versus frequency for different *b*/*a* ratios

2.2.10 Fundamental TE_{10} mode

For the case of TE waves, as it has been mentioned before, one of the mode numbers can be zero. Then, the simplest TE waves, which can propagate through the waveguide, are

TE_{10} mode	
Mode numbers	$m=1$, $n=0$
Wave number	$k=\frac{\pi}{a}$
Wave number in *z* direction	$k_z=\pi\sqrt{\frac{4}{\lambda^2}-\frac{1}{a^2}}$
Cut off frequency	$f_c=\frac{c}{2a}$
Cut off wavelength	$\lambda_c=2a$
Waveguide wavelength	$\lambda_g=\frac{\lambda}{\sqrt{1-\left(\frac{\lambda}{2a}\right)^2}}$
Characteristic impedance	$Z_{TE_{10}}=\frac{Z_c}{\sqrt{1-\left(\frac{\lambda}{2a}\right)^2}}$
Maximum power	$P_{\max}=\frac{ab}{4Z_{TE_{10}}}\left\|E_{x,\max}\right\|^2$
Attenuation constant	$\alpha=\frac{R_s}{Z_c b}\frac{1+\frac{b}{2a^3}\lambda^2}{\sqrt{1-\left(\frac{\lambda}{2a}\right)^2}}$

Table 2.2 The parameters of the fundamental TE_{10} wave

the TE_{10} or TE_{01} waves and they are called the fundamental or dominant modes. The parameters of the TE_{10} mode are given in Tab. 2.2 and the field components in Tab. 2.3.

TE_{10} mode	
Electric field *x* component	$E_x = 0$
Electric field *y* component	$E_y = -jk_z \frac{a}{\pi} Z_{TE_{10}} H_0 \sin(\frac{\pi}{a} x) \cdot e^{-jk_z z}$
Electric field *z* component	$E_z = 0$
Magnetic field *x* component	$H_x = jk_z \frac{a}{\pi} H_0 \sin(\frac{\pi}{a} x) \cdot e^{-jk_z z}$
Magnetic field *y* component	$H_y = 0$
Magnetic field *z* component	$H_z = H_0 \cos(\frac{\pi}{a} x) \cdot e^{-ik_z z}$

Table 2.3 Field components of the fundamental TE_{10} mode

The field distributions are shown in Fig. 2.14 and Fig. 2.15. The waveguide cross sections in middle *xy*, *xz* and *xz* planes (planes 1, 2 and 3, respectively) are presented in Fig. 2.14 a.

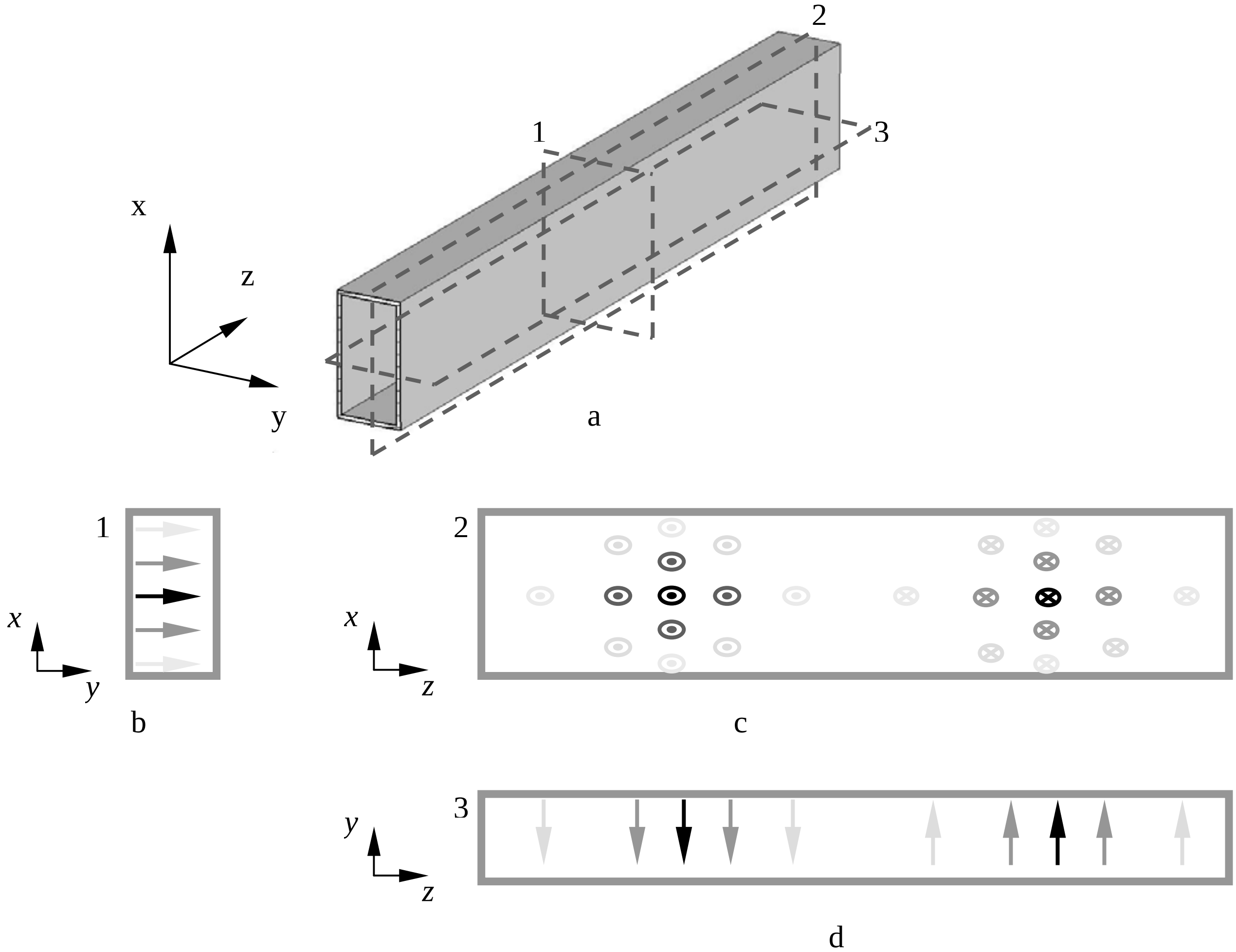

Figure 2.14 Waveguide cross sections and E field patterns for the TE_{10} mode

In addition, the E field patterns are shown in Fig. 2.14 b, c and d. Fading color marks the field intensity. The circles with a dot in the center present that the field flows from the picture plane and the circles with a cross in the center present that the field is oriented to the picture plane. The H field distribution is also depicted in Fig. 2.15 a, b and c, for the same cross sections as for E field in Fig. 14.

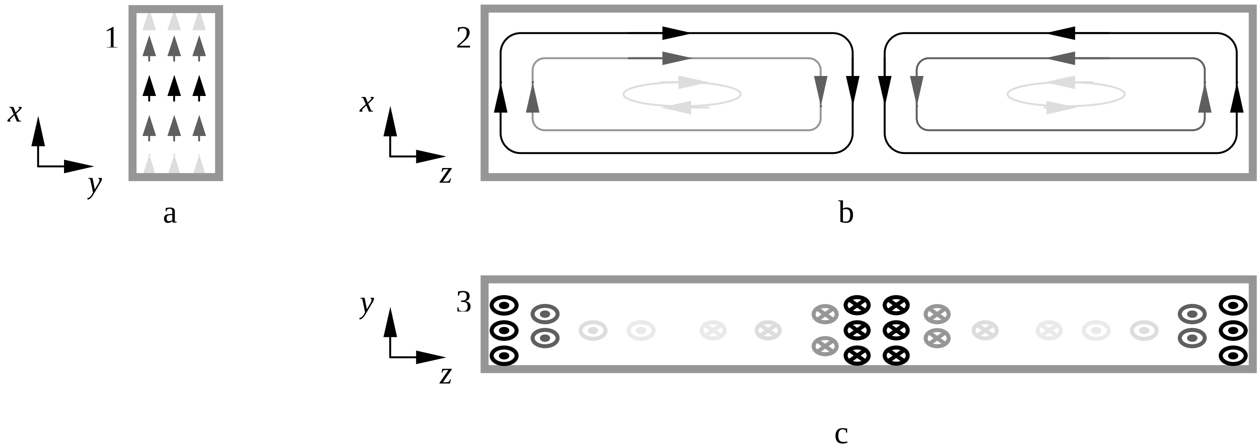

Figure 2.15 H field distribution patterns for the TE_{10} mode

2.2.11 WR340 waveguide standard

Now, the standard WR340 made from aluminium at the ISM frequency 2.45 GHz frequency is presented in more details in Tab 2.4. The power that is lost as heat in the waveguide walls P_l can be given in percentage as:

(2.72) $$P_l(\%) = \frac{P\big|_{z=0} - P\big|_{z=1m}}{P\big|_{z=0}} \cdot 100 = \left(1 - e^{-2\alpha}\right) \cdot 100$$

for 1 m long waveguide section.

WR340 from Al at 2.45 GHz	
Mode numbers	m=1, n=0
Inner transverse dimensions	a = 0.086 m, b = 0.043 m
Free space wavelength	λ = 0.1224 m
Wave number	k = 36.51 m^{-1}
Wave number in z direction	k_z = 36.05 m^{-1}
Group velocity	v_G = $2.1 \cdot 10^8$ m/s
Cut off frequency	f_c = 1.74 GHz
Cut off wavelength	λ_c = 0.172 m
Waveguide wavelength	$\lambda_{g,z}$ = 0.1742
Characteristic impedance	Z_{TE10} = 536.61 Ω
Attenuation constant	α = 0.018 dB/m

Table 2.4 WR340 Al waveguide parameters at 2.45 GHz

Further, in Fig. 2.16 the normalized losses due to the heating in the waveguide walls (ohmic losses) for different waveguide wall materials per 1 m length are depicted and compared.

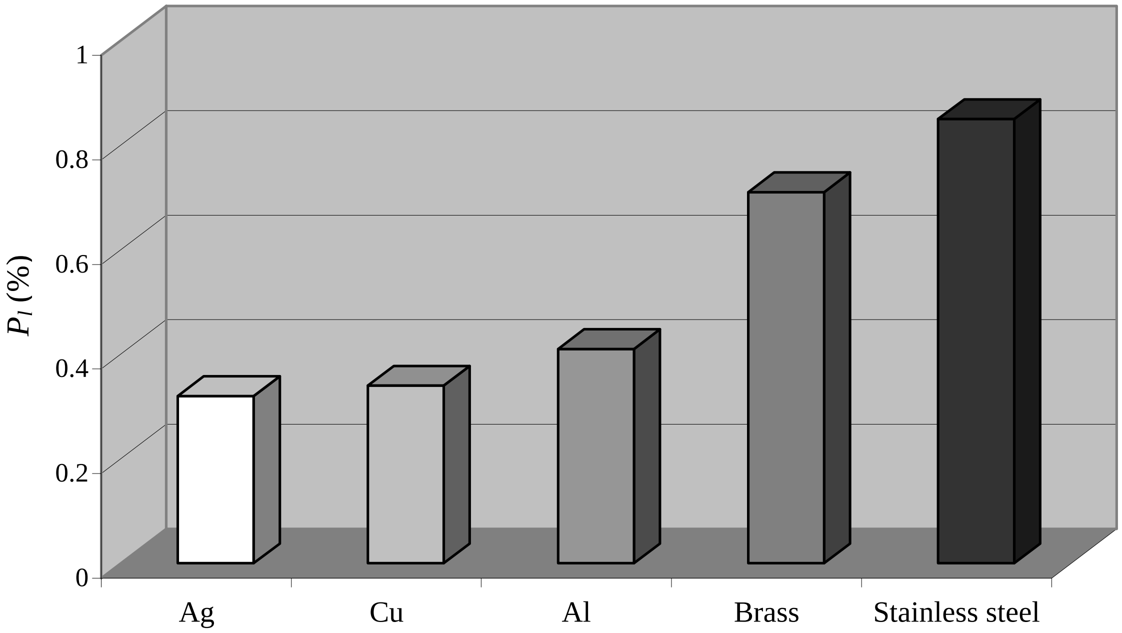

Figure 2.16 Normalized power losses in 1 m long WR340 section

2.3 Waveguides as Transmission Lines

In the following section it will be shown that waveguides for microwaves can be advantageously investigated using the transmission line theory, especially the problems of waveguide discontinuities, like slots in the walls. Because of that, the transmission lines (TL) and the TL theory describing this topic will be introduced shortly. After that, the TL simulations of waveguides will be presented and explained.

2.3.1 Transmission lines

A transmission line is a continuous system of two or more conductors with a dielectric between them, which is capable of guiding and directing the EM energy from one place to another. If the dimension of such devices, which is parallel to the propagation direction, is comparable with the wavelength of the propagating waves, the instantaneous values of the sinusoidal time-harmonic waves, such as voltage and current waves, will vary from point to point and will depend on the longitudinal coordinate in the propagation direction. To define and to describe such systems some new parameters beside the voltages and currents are needed and a new specific theoretical approach, the so called TL theory, must be applied for these problems [18].

The common transmission line of two perfectly conducting wires that are parallel to the *z* direction and its equivalent circuit of a Δz long section are presented in Fig. 2.1. For such transmission lines the E field (full line) and H field (dashed line) are transversal to the *z* direction and a TEM wave propagates along the line. The L', R', G' and C' are circuit parameters infinitesimally distributed along the line and they are defined as inductance per length unit, resistance per length unit, conductance per length unit and capacitance per length unit, respectively. As it can be seen, the voltage *V* and the current *I* are functions of *z*. Using the equivalent circuit from fig. 2.17 the equations which interconnect *V* and *I* can be written as [13,22]:

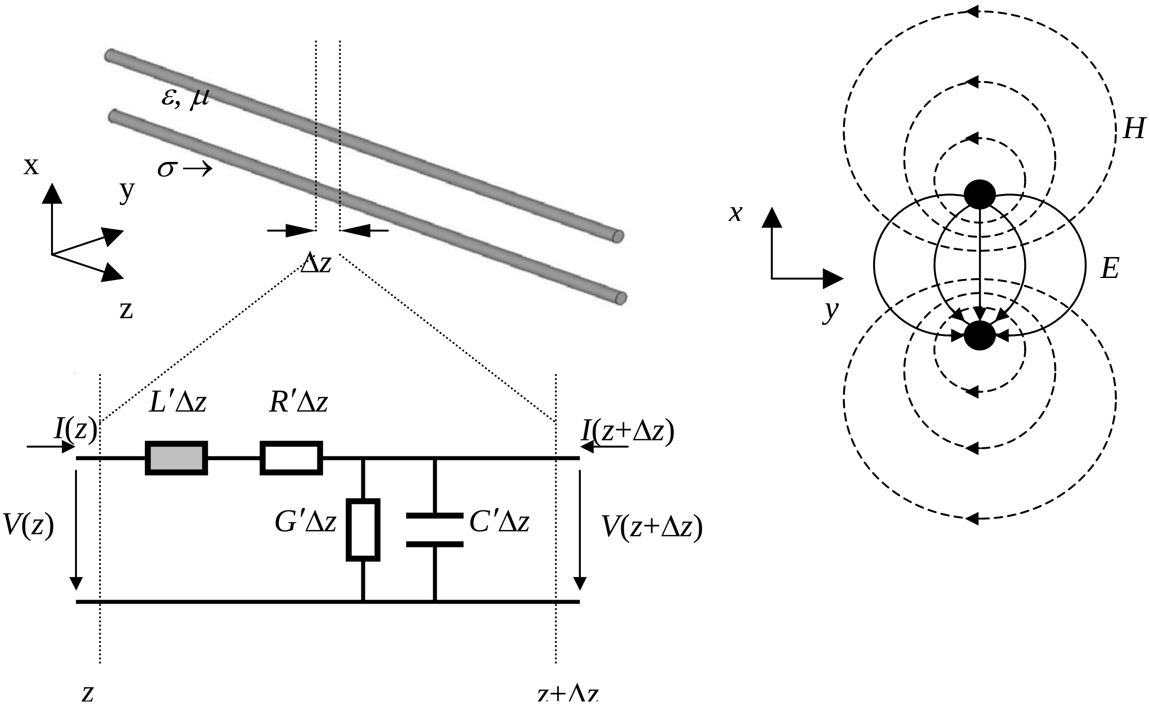

Figure 2.17 Transmission line, TEM wave field lines and equivalent circuit

(2.73) $$-\frac{dV(z)}{dz} = \left(R' + j\omega L'\right)I(z) \text{ and}$$

(2.74) $$-\frac{dI(z)}{dz} = (G' + j\omega C')V(z)\,,$$

where ω is the angular frequency of the voltage and current signals.

After z differentiation of equations 2.73 and 2.74, the wave equations for voltage and current waves on the transmission line are obtained:

(2.75) $$\frac{d^2V(z)}{dz^2} - \gamma^2 V(z) = 0 \text{ and}$$

(2.76) $$\frac{d^2I(z)}{dz^2} - \gamma^2 I(z) = 0\,,$$

where γ is the complex propagation constant, given by:

(2.77) $$\gamma = \sqrt{\left(R' + j\omega L'\right)\left(G' + j\omega C'\right)}\,.$$

The equations 2.75 and 2.76 are known as telegrapher's equations and they are equal to the one-dimensional scalar Helmholtz's equations 2.18 and 2.19. Hence, similar as for longitudinal waveguide E_z and H_z components, the solution of equations 2.75 and 2.76 can be given in the form of traveling voltage and current waves:

(2.78) $$V = V_1 e^{-\gamma z} + V_2 e^{\gamma z}\,,$$

(2.79) $$I = \frac{V_1}{Z_c} e^{-\gamma z} - \frac{V_2}{Z_c} e^{\gamma z}\,,$$

where V_1 and V_2 are amplitudes of in +z and in –z direction traveling voltage waves respectively. The ratio between voltage and current in an infinite transmission line is the characteristic impedance Z_c and it is defined as:

(2.80) $$Z_c = \sqrt{\frac{R' + j\omega L'}{G' + j\omega C'}}\,.$$

The total average power flow at point z is defined as:

(2.81) $$P_{av} = \frac{1}{2}\Re\left[V\left(z\right)\cdot I(z)^*\right] = \frac{1}{2}\frac{V_1^2 - V_2^2}{Z_c} = P_{av,1} - P_{av,2}\,,$$

where * denotes a conjugate complex value and $P_{\mathrm{av},1}$ and $P_{\mathrm{av},2}$ are the total average power carried by waves propagating in +z and –z directions, respectively.

The real and imaginary parts of $\gamma = \alpha + j\beta$ represent the attenuation and phase constant, respectively, and can be defined in terms of L', R', G' and C' as:

(2.82) $$\alpha = \omega\sqrt{\frac{1}{2}L'C'\left[\sqrt{\left(1+\frac{R'^2}{\omega^2 L'^2}\right)\left(1+\frac{G'^2}{\omega^2 C'^2}\right)}-1+\frac{R'}{\omega L'}\frac{G'}{\omega C'}\right]}$$ and

(2.83) $$\beta = \omega\sqrt{\frac{1}{2}L'C'\left[\sqrt{\left(1+\frac{R'^2}{\omega^2 L'^2}\right)\left(1+\frac{G'^2}{\omega^2 C'^2}\right)}+1-\frac{R'}{\omega L'}\frac{G'}{\omega C'}\right]}.$$

In practical realizations of transmission lines, the conductors have finite conductivity and the ohmic losses in the conductors will cause attenuation along the line, which can be important for longer transmission line sections. Dielectric losses in the material between the conductors should be also considered and can be included in *G´*.

2.3.2 Lossless transmission line

For a lossless transmission line with perfect conductors ($R' = G' = \alpha = 0$) the propagation constant is imaginary:

(2.84) $$\gamma = j\beta = j\omega\sqrt{L'C'}\ .$$

In this ideal case the characteristic impedance becomes $Z_c = \sqrt{\frac{L'}{C'}}$. Also the phase velocity and the wavelength can be defined as $v_P = \frac{\omega}{\beta} = \frac{1}{\sqrt{L'C'}}$ and $\lambda = \frac{v_P}{f}$.

If the lossless transmission line is closed with an arbitrary load impedance $Z_L = Z(z+l)$ (see Fig. 2.18), the impedance $Z_{in} = Z(z)$, which is seen from the generator at a distance *l* away from the load can be derived using following transformation [11]:

(2.85) $$Z_{in} = Z_c\,\frac{Z_L + jZ_c\tan(\beta l)}{Z_c + jZ_L\tan(\beta l)}$$

which is an important relation in TL theory. Using this equation one can give the answers on questions like, how the load can influence the transmission line properties and especially how it affects the efficiency of EM power transfer along the line.

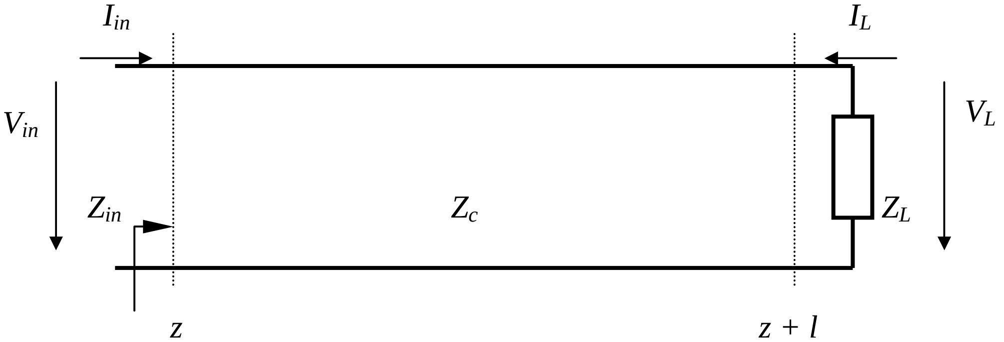

Figure 2.18 Transmission line terminated with an arbitrary load impedance Z_L

Knowing the voltage $V_L = V(z+l)$ and current $I_L = I(z+l)$ at the load impedance Z_L, the voltage $V_{in} = V(z)$ and the current $I_{in} = I(z)$ at the input point z can be calculated as:

(2.86) $$V_{in} = V_L\left[\cos(\beta l) - j\frac{Z_c}{Z_L}\sin(\beta l)\right] \text{ and}$$

(2.87) $$I_{in} = I_L\left[\cos(\beta l) - j\frac{Z_L}{Z_c}\sin(\beta l)\right].$$

2.3.3 *Termination with characteristic impedance – matched lossless TL*

From the relation 2.85 it is obvious that if the transmission line is terminated with the characteristic impedance, then everywhere along the line the impedance seen from the generator is Z_c, independent on distance l. This is the case of the matched transmission line and all available EM power is transferred to the load. The input voltage can be expressed as $V_{in} = V_1 e^{-j\beta z}$, because the amplitude V_1 and the distance l are chosen arbitrary, which presents only the forward propagating wave (+z direction). There is no reflection from the load backward to the generator $V_2 = V_r = 0$ and the reflection losses are zero $P_{av,2} = P_r = 0$. For a propagating wave the matched load is not a disturbance and it acts as an infinite transmission line section.

2.3.4 Short circuited lossless TL

For a short circuited line $Z_L = 0$ and Z_{in} can be estimated using (see equ. 2.85):

(2.88) $$Z_{in} = jZ_c\tan(\beta l).$$

At the distance of $l = \frac{\lambda}{4}$ from the load Z_{in} is transformed to an infinite value and a the admittance Y_{in} at this point is zero, as for the open circuit. So, the shorted $\frac{\lambda}{4}$ (lambda fourth) section after a parallel admittance will not change the input impedance at all. The Z_{in} of a shorted section in the range $0 < l < \frac{\lambda}{4}$ acts as an inductive reactance (positive imaginary value) and can be used for a compensation of pure capacitance on the transmission line. For $\frac{\lambda}{4} < l < \frac{\lambda}{2}$ the Z_{in} acts as capacitive reactance (negative imaginary value) and with this kind of shorted section a pure inductance can be compensated.

Along the shorted section there are only standing voltage and current waves and the EM energy oscillates along the line and no EM energy transfer is possible. The signals are totally reflected from the short, their amplitudes are equal to the direct signal amplitudes and their superpositions with the direct signals give standing waves. This can be shown using $V_L = 0$ for the shorted transmission line and relation 2.87, which yields in $V_{in} = jZ_c I_L \sin(\beta l)$ for the voltage and in $I_{in} = I_L\cos(\beta l)$ for the current. The functions *sin* and *cos* describe the standing wave oscillations along the transmission line.

2.3.5 Open lossless transmission line

In the case of an open transmission line $Z_L = \infty$, $I_L = 0$ and the relation for Z_{in} transforms into:

(2.89) $$Z_{in} = -jZ_c \cot(\beta l).$$

Signals are totally reflected from the open line back to the generator and superimpose with the direct signals and build up standing wave. The voltage and current of an open transmission line oscillate along the *z* coordinate are governed by standing wave functions. At the input point *z* they are $V_{in} = V_L \cos(\beta l)$ and $I_{in} = j\frac{V_L}{Z_c}\cos(\beta l)$.

2.3.6 Lossless TL loaded with arbitrary impedance- reflection coefficient

If the transmission line is terminated with an impedance different from the characteristic impedance, then a part of the propagating EM energy will be reflected back and a part of it will be transferred to the load, which can be considered as reflection loss. Hence, along the transmission line there will be two waves with different amplitudes, a direct one propagating forward to the load in +z direction with an amplitude V_d and the reflected one propagating backward from the load to the generator in –*z* direction with an amplitude V_r. The sum of these two waves defines the total wave:

(2.90) $$V = V_d e^{-j\beta z} + V_r e^{j\beta z}.$$

As a measure for reflection and mismatch the reflection coefficient, can be defined as the ratio between direct and reflected amplitudes at the load [11,22]:

(2.91) $$r = \frac{V_{d,L}}{V_{r,L}} = \frac{Z_L - Z_c}{Z_L + Z_c}.$$

At the input point *z* the reflection coefficient is:

(2.92) $$r_{in} = \frac{V_{d,in}}{V_{r,in}} = re^{-2j\beta l} = \frac{Z_{in} - Z_c}{Z_{in} + Z_c},$$

A common measure for reflection is also the Voltage Standing Wave Ratio (*VSWR*), which is the ratio between the maximum and minimum of the standing wave voltage [11]:

(2.93) $$VSWR = \frac{V_{\max}}{V_{\min}} = \frac{1 + r_{in}}{1 - r_{in}}.$$

In practice it is very useful to express the input reflection coefficient as a function of the normalized input impedance z_{in}, which is defined as:

(2.94) $$z_{in} = \frac{Z_{in}}{Z_c} = \frac{z_L + j\tan(\beta l)}{1 + jz_L\tan(\beta l)},$$

where $z_L = \frac{Z_L}{Z_c}$. Now the relation for the reflection coefficient is:

(2.95) $$r_{in} = \frac{z_{in} - 1}{z_{in} + 1}.$$

For the previous case of a matched line and zero reflections, $r = 0$ and $z_{in} = 1$ and this can be used as an input matching condition. Hence, using the normalized impedance is advantageous over using the normal impedance in practical calculations.

For transmission lines with parallel elements it is more convenient to perform the calculations with the normalized admittance $y_{in} = \frac{Z_c}{Z_{in}} = \frac{1}{z_{in}}$ than with the normalized impedance z_{in}.

The input reflection coefficient in this case is:

$$r_{in} = \frac{1 - y_{in}}{1 + y_{in}}. \tag{2.96}$$

Starting from the definition of the total average power (equ. 2.81) and using the reflection coefficient concept, the power transported to the load can be calculated as:

$$P_{av} = \frac{1}{2}\left(\frac{|V_d|^2}{Z_c} - \frac{|V_r|^2}{Z_c}\right) = P_{in}\left(1 - |r_{in}|^2\right), \tag{2.97}$$

where P_{in} is the available power at the input. Or, in other words, the reflection loss is $P_r = P_{in} \cdot |r_{in}|^2$ and the square of the reflection coefficient modulus defines the reflection losses.

2.3.7 Waveguides as transmission lines

In section 2.2 it has been shown that in waveguides, the EM fields can be described by two different types of modes, TE and TM. Waveguide modes are mathematical functions, which are the solutions of the wave equations and given boundary conditions and physically

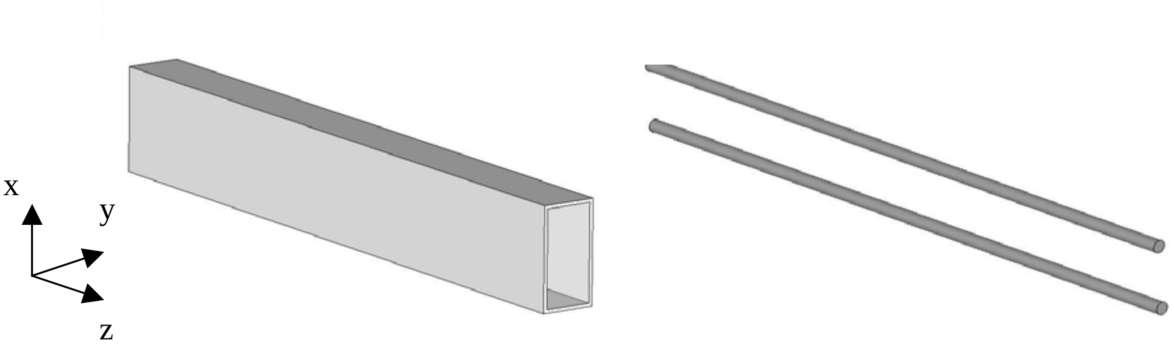

TE$_{10}$ waveguide

$$E_y = f_t(x,y) f_a(z) = f_t(x) E_0 e^{-\gamma z}$$

$$\gamma = j\beta = j\omega\sqrt{\varepsilon\mu}\sqrt{1 - \left(\frac{\lambda}{2a}\right)^2}$$

$$Z_c = \sqrt{\frac{\mu}{\varepsilon}} \frac{1}{\sqrt{1 - \left(\frac{\lambda}{2a}\right)^2}}$$

Two-conductors transmission line

$$V = V_0 e^{-\gamma z}$$

$$\gamma = j\beta = j\sqrt{L'C'}$$

$$Z_c = \sqrt{\frac{L'}{C'}}$$

Figure 2.19 Transmission line simulations of lossless waveguides they present the different wave types. The sets of equations 2.50-2.53 and 2.55-2.58 show that the EM field components in waveguides can be expressed by two types of functions [19]. The first type of functions are the transversal functions $f_t(x,y)$ dependent only on the cross-sectional coordinates transverse to the propagation direction. The second functions type can be denoted as amplitude function $f_a(z)$, which depends only on the longitudinal coordinate parallel to the direction of propagation.

For metallic rectangular waveguides with uniform transversal shape, which have been presented in section 2.2, the modes can be completely characterized by amplitude functions. This makes the transmission line theory applicable for waveguide problems, because the transmission line like behaviour of the mode amplitudes and the EM fields can be described in terms of the voltage and current on an appropriate transmission line. Knowing the transversal mode functions, the characteristic impedance and the propagation constant of the equivalent transmission line, one can characterize the waveguide completely and give the expressions for its EM field components. This useful approach is depicted in Fig. 2.19 for lossless transmission.

2.3.8 Two port network presentation of waveguides – S parameters

After introducing the transmission line theory as a tool for solving the problems of microwave waveguides, it is helpful to use the network theory to describe the EM fields and waves also. The concept of normalized impedance, admittance and reflection coefficient in the transmission line approach gives the basic idea of using the networks to determine the reflection and transmission in the waveguides.

A section of the waveguide in which only the fundamental mode exists is given with its equivalent two port presentation in Fig. 2.20.

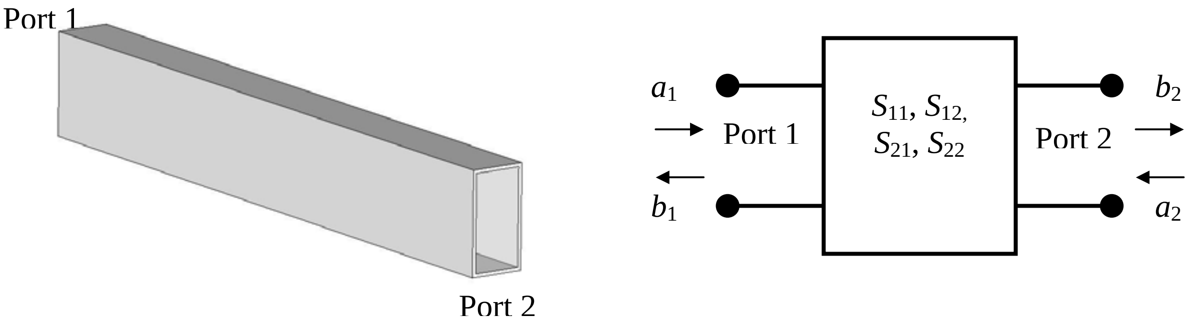

Figure 2.20 Two port S parameter presentation of a waveguide section

At the left side of the waveguide section (z = 0, port 1) the complex amplitudes of the normalized voltages of the inward and outward waves, which propagate in +z and –z direction respectively, are denoted by a_1 and b_1. At the right end of the waveguide section ($z = l$, port 2) the complex amplitudes of the normalized inward and outward voltage waves are denoted by a_2 and b_2 and they are oriented in –z and + z direction, respectively. Now, this waveguide section can be described in terms of relations between the normalized voltages, i.e. it can be characterized using the, so called, scattering (S) parameters of the equivalent two port network.

The S parameters of a two port are defined in matrix form as follows [22,23]:

(2.98)
$$\begin{bmatrix} b_1 \\ b_2 \end{bmatrix} = \begin{bmatrix} S_{11}S_{12} \\ S_{21}S_{22} \end{bmatrix} \cdot \begin{bmatrix} a_1 \\ a_2 \end{bmatrix}.$$

To explain the physical meaning of the S parameters it is better to use the following form derived from 2.98:

(2.99) $$S_{11} = \frac{b_1}{a_1}\Big|_{port\,2\,matched},$$

(2.100) $$S_{12} = \frac{b_1}{a_2}\Big|_{port\,1\,matched},$$

(2.101) $$S_{21} = \frac{b_2}{a_1}\Big|_{port\,2\,matched} \text{ and}$$

(2.102) $$S_{22} = \frac{b_2}{a_2}\Big|_{port\,1\,matched}.$$

Now, it is obvious that S_{11} represents the reflection at port 1 and S_{22} gives the reflections at the port 2 of the two port section. They are equal to the corresponding reflection coefficients:

(2.103) $S_{11} = r_1$ and

(2.104) $S_{22} = r_2$.

The parameters S_{21} and S_{12} determine the transmissions from the port 1 to the port 2 and vice versa, respectively. They can be denoted as transmission coefficients.

According to relations 2.95 and 2.103 the normalized impedance of a transmission line section equivalent to the waveguide can be calculated by measuring the S_{11} parameter at this point:

(2.105) $$z = \frac{1+S_{11}}{1-S_{11}}.$$

Further, measuring the S_{11} parameter the transmitted power along the waveguide section between port 1 and port 2 can be calculated as:

(2.106) $$P_t = P_{in}\left(1-\left|S_{11}\right|^2\right),$$

where P_{in} is the available power at the port 1. This relation clears the significance of the S_{11} parameter in the design of highly power efficient microwave systems, which can be realized by a minimization of the S_{11}.

2.3.9 S_{11} parameter of series impedance and parallel admittance

For a waveguide section, which can be transformed in a series impedance, the two port equivalent network gives a very simple (see Fig 2.21 a) relation with the S_{11} parameter:

(2.107) $$z = \frac{2S_{11}}{1-S_{11}}.$$

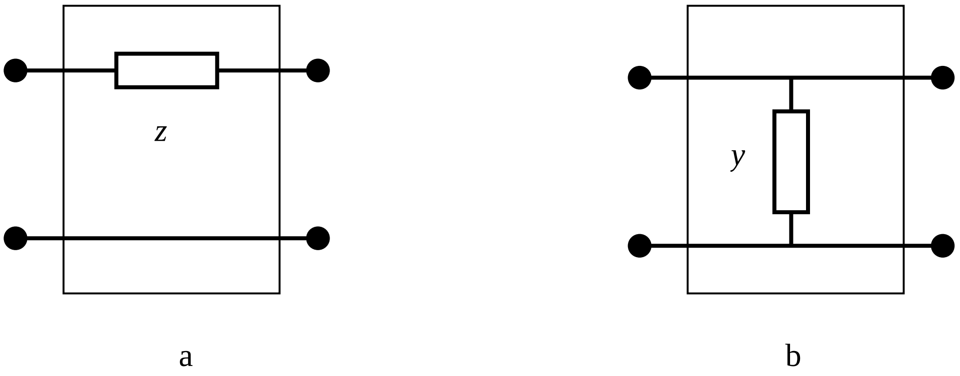

Figure 2.21 a) Series impedance and b) parallel admittance as two port networks

In the case of a parallel admittance (Fig. 2.21 b), the measured reflection at the input port can be used to calculate the normalized admittance as:

(2.108) $$y = \frac{-2S_{11}}{1+S_{11}} .$$

The complete S parameter matrix of the circuit elements presented in Fig. 2.21 are given with [11,20]:

(2.109) $$S = \begin{pmatrix} \frac{z}{z+2} & \frac{2}{z+2} \\ \frac{2}{z+2} & \frac{z}{z+2} \end{pmatrix}$$ for a series impedance z and

(2.110) $$S = \begin{pmatrix} \frac{-y}{y+2} & \frac{2}{y+2} \\ \frac{2}{y+2} & \frac{-y}{y+2} \end{pmatrix}$$ for a shunt admittance y.

Using the relations 2.107 and 2.108 and knowing the reflection coefficients of waveguide discontinuities, e.g. such like slots in the walls of antenna waveguides, these can be easily implemented in transmission line simulations of the waveguides.

2.4 Coupling of High Power Microwaves Sources to Waveguides

In this section the techniques of coupling between high power microwave sources and waveguides as microwave power transmission systems are presented. The principles of EM energy coupling to the waveguides are given, for low power applications and for common practical coupling systems for high power microwaves, which are considered in more details, with descriptions of each high power microwave component.

2.4.1 Principle of coupling to waveguides

To excite a desired wave type in a waveguide, first the frequency has to be higher than the cut-off frequency. Further, the coupling has to be appropriate for the excitation of the desired mode also. That means, the coupling mechanism has to generate an EM field in the waveguide, which can be transformed into the desired wave type in the shortest possible distance from the coupling point.

The simplest way to excite the dominant TE_{10} mode is to use a tiny wire antenna [12]. In the case of coupling with a coaxial cable, this is the inner conductor of the coaxial cable. This antenna has to be placed parallel to the E field vector in the waveguide and at the point

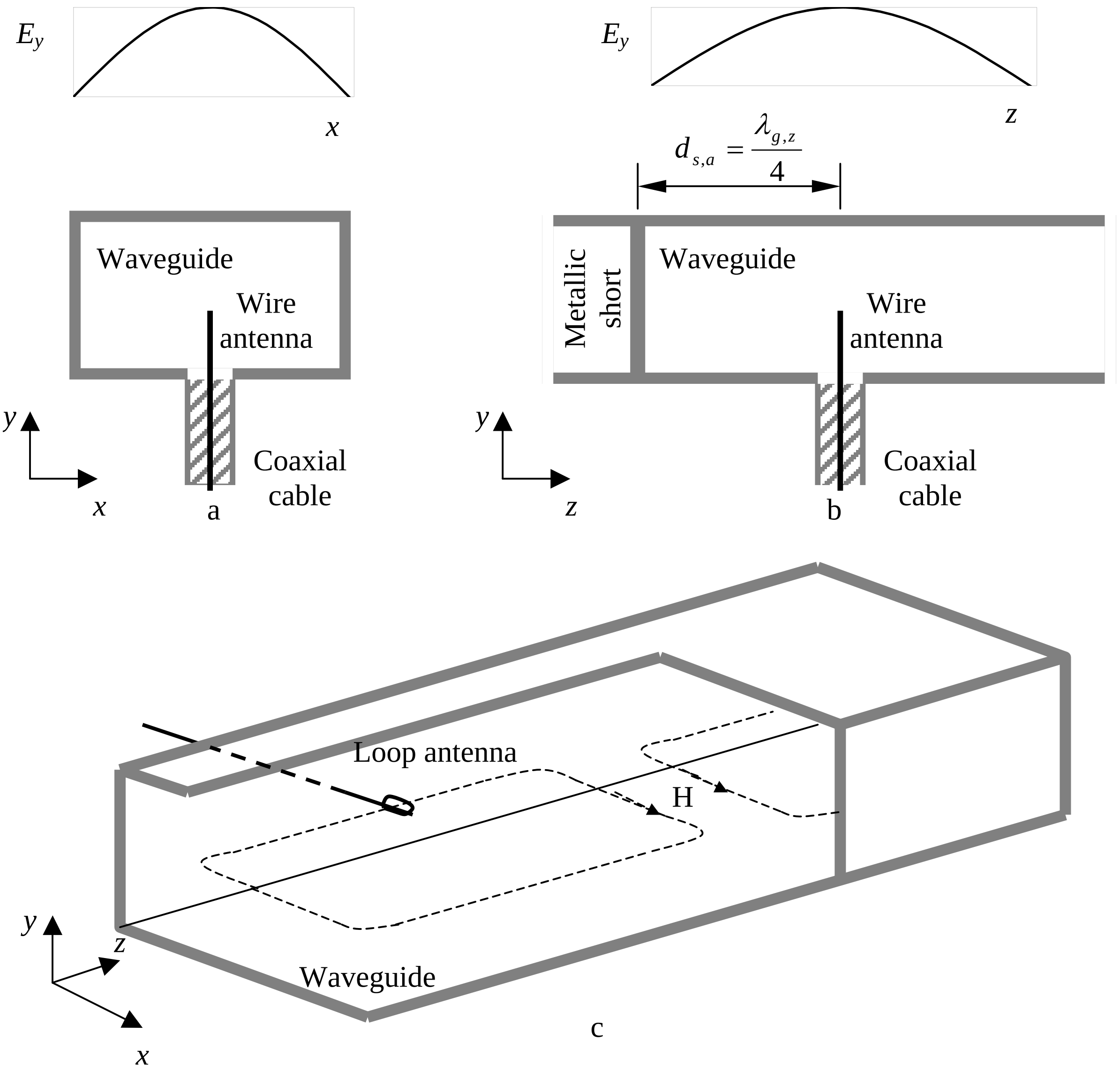

Figure 2.22 Principles of EM energy coupling to the TE_{10} waveguide mode

of the maximum E field, i.e. the distance $d_{s,a}$ between a metallic short and the coupling antenna should be one quarter of the waveguide wavelength (Fig. 2.22 a and b).

Another also simple technique is to use a loop antenna, which transfers the EM energy into the waveguide by means of H field coupling (Fig. 2.22 c).

The EM field near the wire antenna and loop antenna has a very complicated structure, because it has to satisfy the boundary conditions for given geometries in Fig. 2.15. Hence, these types of excitation present the ideal cases and in practice they cause an excitation of evanescent higher modes also, which decreases the efficiency of the coupling.

There are several techniques to suppress these undesired modes and to optimize the coupling. That can be done by optimization of the antenna geometry keeping the distance $d_{s,a}$ between the short end and the antenna constant, or by changing the distance $d_{s,a}$ for a given antenna geometry. Further, by using the tuning posts to match the antenna impedance to the waveguide characteristic impedance, the coupling can be also optimized.

As an example, an optimized coaxial cable to waveguide transition is presented in Fig. 2.23. Optimization has been done numerically using the CST Microwave Studio program. The antenna height h_a and the lower antenna part radius r_a have been varied to reduce the $|S_{11}|$ parameter at the coaxial cable to a level below –20 dB, i.e. to minimize the reflections from the waveguide and to find an optimum coupling for a given $d_{s,a}$. This optimized antenna has been used in low power measurements on nonresonant slotted waveguide energy feeding systems (sec. 5.1).

2.4.2 High power microwave coupling to waveguides

The above direct coupling techniques are common in low power applications, as it has been already mentioned. For systems with high power microwave sources, the coupling is indirect and more complex, due to the protection of the high power microwave generators from undesired and dangerous reflections, which can occur in the transmission systems. So, in the latter case, if the coupling is not at optimum, some additional components are needed between the microwave source and the waveguide systems, to hinder the damaging of the generator by reflections from the waveguide. These waveguide components are today standard parts in high power microwave transfer systems, in spite of the fact that their costs contribute significantly to the overall system costs.

The block diagram of a typical high power microwave coupling into a waveguide is depicted in Fig. 2.24. The 2.45 GHz microwave source is a magnetron which is broadly used

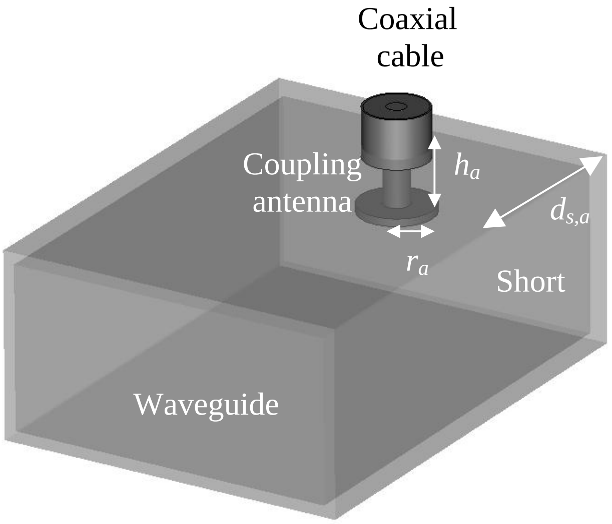

Figure 2.23 An optimized coaxial cable to waveguide transition

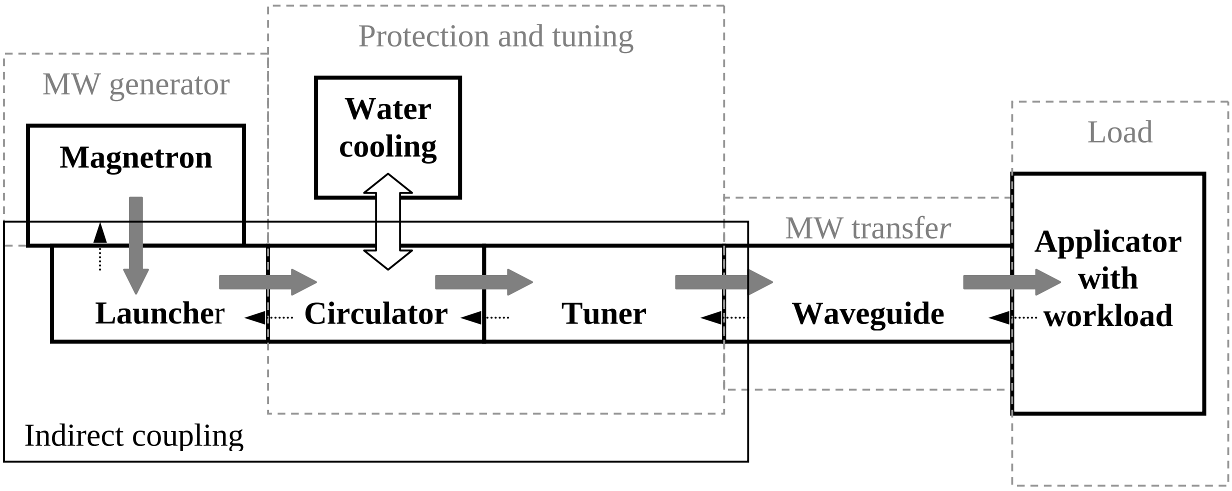

Figure 2.24 Block diagram of a typical high power microwave coupling system

in industrial installations and is used in every kitchen microwave oven as well. The magnetrons are usually directly connected to the waveguide launchers. Behind them in the coupling chain, circulators serve as protectors for undesirable reflections. Tuners are waveguide components which fine tune and optimize the coupling for different loads at the waveguide energy transfer system end.

The main flow of microwave (MW) power from the generator to the load is denoted with gray arrows. Black small arrows present the places where reflections occur. The functional blocks of the system are presented with grey dashed lines, the microwave components are separated with bold line and the components of indirect coupling between the microwave source and the waveguide are grouped with normal line.

2.4.3 High power microwave source – magnetron

To explain the coupling of high power microwaves into the waveguide and to find methods to optimize this coupling, it is advisable first to present the utilized high power microwave generator.

At the frequency of 2.45 GHz magnetrons are commonly used as sources in high power microwave material processing technology. For material processing applications at higher frequencies, i.e. in the millimeter wave range above 30 GHz, gyrotron tubes must be used as high power generators and there is an intensive research reported in this field [1,24]. However, the main difficulties in gyrotron material processing applications are the very high generator cost and an industrial up scale of research systems. Hence, here we will focus on magnetron generators.

Magnetrons are crossed-field high power vacuum electron tubes that convert DC energy into microwave energy using an electronic potential energy conversion process [25]. These devices are diode type vacuum tubes. Because the B field plays the role of a grid, this tubes are called M type devices.

The principles of magnetron operation can be explained using the Fig. 2.25. The magnetron consists of an electron emitting cathode and a concentric cylindrical hollow anode incorporating resonant cavities, which dimensions together with the spaces at the ends of the anode determine the operating microwave frequency of the tube . Between the electrodes high voltage is applied, usually in the kV range, which causes the existence of a static radial E field in the space between the electrodes. The magnetic field is provided axially, parallel to the anode and cathode axes, usually by a permanent magnet. The induction *B* is perpendicular to

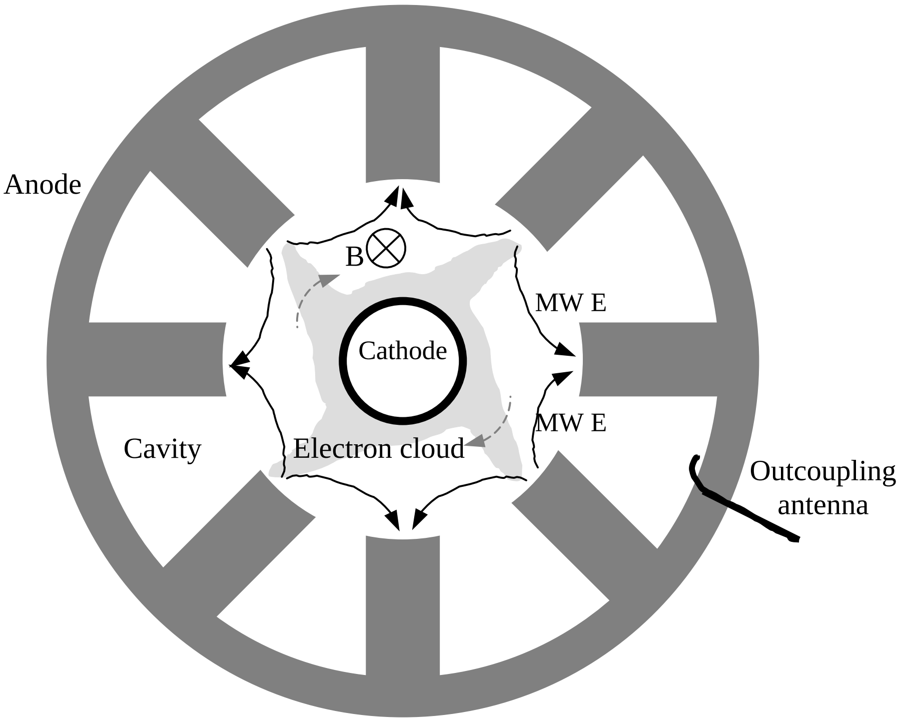

Figure 2.25 Principle cross section of a magnetron vacuum electron tube

the *E* field. This crossed field structure forces the electrons to travel on a quasi circular path around the cathode. However, the resonant structure of the cavities in the anode block causes the presence of an alternating *E* field at the microwave (MW) frequency in the interaction space between the cavities (black arrows in Fig. 2.25) [26]. This *E* field couples the neighboring cavities in one resonant circuit, building a standing wave. For the case that the fields in neighboring cavities oscillate with a phase difference of π, the magnetron works in the most efficient π-mode. One of the cavities can be used for outcoupling the MW power from the device by a loop antenna. The microwave electric field effects the electrons motion and causes an acceleration of some electrons and a decelaration of other electrons. So, the electrons are focused and make an electron cloud with spokes (gray in Fig. 2.25) rotating in the clockwise direction around the cathode. In addition, the microwave electric field cause the force, which moves the electrons with appropriate phase closer to the anode, converting their potential energy into the microwave field energy. In this way, the energy of the applied DC power can be converted into microwave energy.

The magnetron device has been invented by Albert Hull in the year of 1921. They have been further developed for applications in radar systems before and during the Second World War [16]. Since then, different types of magnetron tubes have been developed according to the wide range of different applications [25]. In radar systems pulsed magnetrons with power levels up to several MW and in a frequency range up to several tens of GHz are used. Continuous wave (CW) magnetrons are also developed, with power levels of a few hundred watts for frequency tunable devices, and up to several tens of kW in fixed frequency tubes. The fixed frequency CW magnetrons are common microwave sources in industrial microwave heating systems, as well as in kitchen microwave ovens.

Because of their large mass production, kitchen oven magnetrons are low cost devices, which is their main advantage over other high power microwave generators. They operate in a narrow frequency band of typical ± 10 MHz around the central ISM 2.45 GHz frequency. This magnetron type usually produces microwaves of 700 W nominal power, but there are

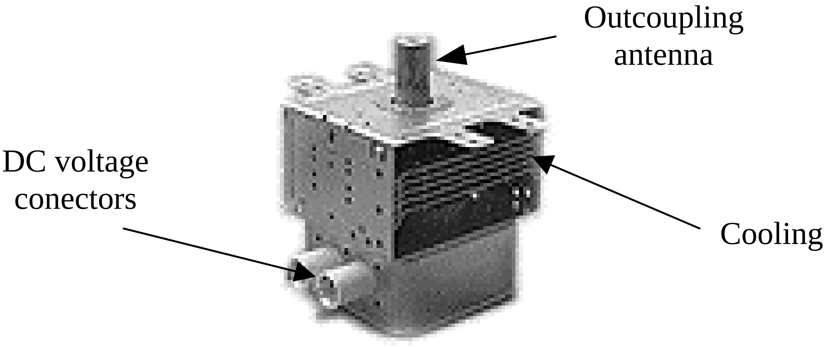

Figure 2.26 A photograph of a kitchen oven magnetron

also tubes with power levels up to a few kW on the market. A photograph of this magnetron type is shown in Fig. 2.26. The device is usually mounted on the launcher, which is a waveguide section with the appropriate positioned hole in the broad wall for the insertion of the magnetron outcoupling antenna. Kitchen oven magnetrons are relatively easy to couple into the system from Fig. 2.24. and they can be air cooled, which makes them advantageous for multi-fed microwave applicators, in comparison to other magnetron tubes producing higher MW power, but which need the water cooling and more complicated mounting in the system.

The performances of each type of magnetron tube, such as central operating frequency and nominal microwave power, are more or less dependent on the load (see Fig. 2.24). By changing the dimensions, material properties and positions of the workload in the applicator, the reflections toward the microwave generator will be changed also, which will affect the frequency and the power characteristics of the magnetron (load pulling). This is more critical for magnetrons at higher power levels and for single-mode applicators. The requirement for stable operation is a load with *VSWR* less than 3 (reflected power < 25%) [16]. To stabilize the magnetron generators and to protect them from reflections, circulators and tuners could be used in an indirect coupling system (Fig. 2.24).

2.4.4 Circulator

A waveguide circulator is a nonreciprocal ferrite device that contains three or more ports for junctions with three or more waveguides [16]. That is, for the three port device, which is usually called the Y-junction circulator, the microwave energy can flow only in one direction around the circle of waveguide junctions (Fig. 2.27), i.e. it flows from port 1 to port 2, from port 2 to port 3 and from port 3 to port 1. In a reciprocal device the same fraction of energy that flows from port 1 to port 2 would occur to energy flowing the opposite direction, from port 2 to port 1.

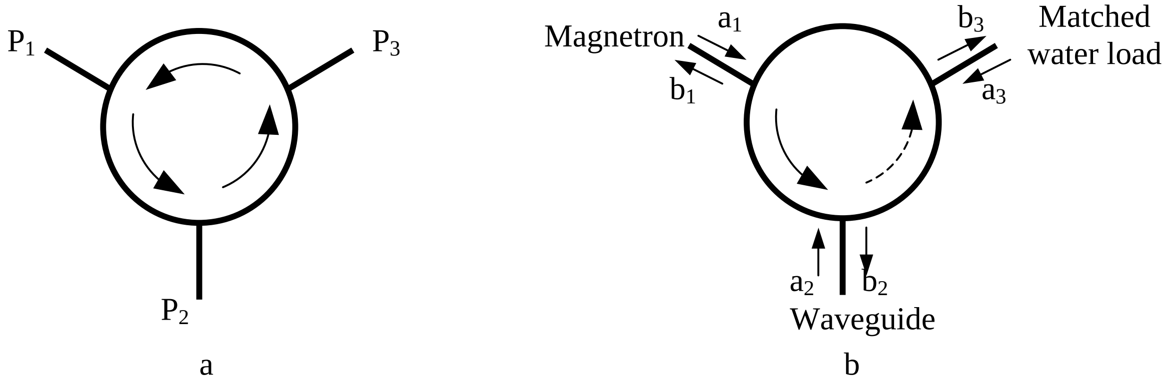

Figure 2.27 A Y-junction microwave circulator

The ferrite material (a sophisticated mixture including iron oxides and yttrium) is inserted at the center of a three waveguide ports junction. Strong permanent magnets provide a bias H field being perpendicular to the junction plane and parallel to the E field in the junction. In this strong H field the ferrite has different μ interacting with differently polarized microwave fields. That results in different phase lengths between the opposite directions of propagation around the ring and in a nonreciprocal behavior of the device.

As shown in Fig. 2.27 b, if port 3 is terminated with a broadband matched load, usually a water load, the circulator becomes an isolator or iso-circulator. In this case the power reflected from port 2 is absorbed in the water load at port 3 instead of going back to port 1. For the ideal iso-circulator from the Fig. 2.27 b, the S parameter matrix is:

$$\begin{bmatrix} b_1 \\ b_2 \\ b_3 \end{bmatrix} = \begin{bmatrix} 0 & 0 & 0 \\ 1 & 0 & 0 \\ 0 & S_{32} & 0 \end{bmatrix} \begin{bmatrix} a_1 \\ a_2 \\ a_3 \end{bmatrix}. \tag{2.111}$$

Due to the high heat dissipation in the ferrite, circulators have to be cooled. The water flowing through the load can be also used for ferrite cooling. That means, an additional cooling system, which keeps water to flow during the system working time, must be provided. This results in further energy consumption and in an increasing of overall processing costs. Adding the costs of the circulator component itself, results in the main disadvantage of indirect high power microwave coupling.

2.4.5 Tuner

For a fine tuning of the waveguides, i.e. for a fine compensation of the load mismatch and for an additional minimization of reflections, adjustable waveguide components called tuners can be used. The tuning is realized by inserting a set of three or more screws into the broad waveguide wall along the central line (Fig. 2.28). The inserted screws can be described by pure reactive admittance, which is a function of the screw insertion and screw diameter [16]. Realizing a susceptance having the opposite sign compared to the load susceptance, the load mismatch can be compensated. Distances between neighboring screws are usually equal to $\lambda_g/8$, making every compensation admittance realizable. However, in that case, only two screws should be inserted at one time, because the alternate screws have opposite effects and cancel each other. Insertion of the screws is limited to the half of the waveguide height, because of the undesirable resonant behavior of screws inserted up to $b/2$.

The main disadvantage of the multiscrew tuners is a high probability of arcing at places where the screws are inserted in the waveguide, especially at higher microwave power. So, tuners should be used in microwave applicators only for the generator protection which are highly sensitive to load variations, as monomode applicators, and up to certain power levels (few kW at 2.45 GHz), even though they are not so expensive as circulators.

Figure 2.28 A photograph of a waveguide tuner with 3 stubs

2.4.6 Direct coupling

However, by proper design of the EM energy transfer systems, direct coupling can be achieved also in high power microwave systems and the system costs can be reduced, since standard microwave components, as tuners and circulators, and components needed for cooling are not required.

Direct coupling is especially provided for multimode applicators, which are less sensitive on workloads characteristics than monomode applicators. Further, using multi-feed systems with several magnetrons of moderate power, for example using the costly advantageous kitchen oven magnetrons, instead of microwave generators with very high power, the danger of strong reflections from the load can be decreased. Multi-feed systems have an additional advantage, they increase the uniformity of the field inside the multimode applicator.

For direct coupling of the magnetrons to waveguides, the minimization of reflections in the waveguides is essential. Hence, a waveguide $|S_{11}|$ parameter below the 0.1 or -20 dB in the frequency band of the magnetron source can be stated as a main goal for an optimization of direct coupling. A photograph of a directly coupled kitchen oven type magnetron to the waveguide is given in Fig. 2.29.

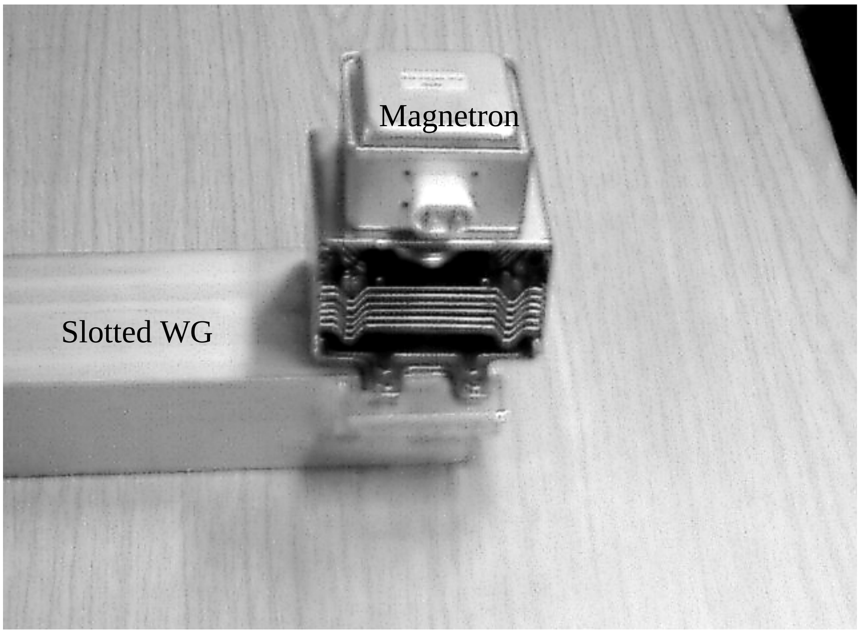

Figure 2.29 A photograph of a magnetron directly coupled to a waveguide

3. Waveguide Slots as EM Radiators

Slots in the waveguide wall can radiate EM energy from the waveguide and a multi slotted waveguide can be considered as an antenna array. Hence, for proper design of a slotted waveguide radiator and for achieving the defined optimization goals for the microwave power feeding system using slotted waveguides in a microwave applicator, the antenna theory and some important parameters of antennas and antenna arrays should be firstly introduced. Further, different types of radiating waveguide slots and their characteristics will be presented in this chapter. Design parameters for the slot types that are used in the design of slotted waveguide feeding elements are presented in this work and are numerically investigated in details. The virtual numerical models for these slot parameters calculations and the results of numerical slot simulations are given in the last chapter of this section.

3.1 Antennas and Antenna Arrays Parameters

3.1.1 Antenna parameters

As devices that transmit or receive electromagnetic waves, antennas have found applications in different fields such as communications, radars, navigation, research and science, medicine and industry [27]. According to the wide range of applications, different antenna types have been designed and developed, for different frequency bands and at different power levels. Despite of these large differences in antenna realizations, only a few principle antenna types can be defined considering the ways in which the irradiation/receiving of EM energy from/in an antenna can be modelled by laws of electromagnetics [28]. This leads to definitions of some general antenna parameters for description of all antenna types. These antenna parameters can be also used for investigation of slotted waveguide feeds for microwave applicators and they will be introduced in following.

From Maxwell’s equations (sec. 2.1) it can be seen that time varying currents in conductors cause the excitation of time varying electric and magnetic fields in the space around the conductor and they can propagate through the space as EM waves. By this, the so called loop and wire principle antenna types are defined. EM waves can be also excited using apertures in waveguides or in transmission lines and in this case the electric field across the apertures can be considered as a wave source defining another principle antenna named aperture antenna. Slotted waveguides naturally belong to this second antenna type. All general antenna parameters of both principle antenna groups can be derived investigating the EM fields on and around the antennas [23,29]. So, it is convenient to begin with the study of electric and magnetic fields produced by an antenna. In this work the antennas will be treated as transmitting devices, because the slotted waveguides radiators should be used as microwave power transfer systems from generator to the applicator, i.e. they should radiate the EM energy coming from the magnetron source to the load. However, the characteristics of an antenna are the same in both, transmitting or receiving applications.

3.1.2 Antenna radiation pattern

In the antenna theory the electromagnetic fields are usually given rather in spherical coordinates than in cartesian coordinates and in Fig. 3.1 a spherical coordinate system is introduced. The EM field radiated from the antenna can be separated in two field types: near field and far field. This field separation is done using approximations of the total radiation field for different distant regions from the antenna. The condition for the distance r, which defines the near field in the vicinity of the antenna, is [30,31]:

$$r \ll \frac{1}{k} = \frac{\lambda}{2\pi}, \tag{3.1}$$

where k and λ are the wave number and the wavelength of the EM wave in the free space, respectively. In this region the electric and magnetic fields are in phase quadrature, the Pointing vector is purely imaginary and there is no power flow but an EM energy oscillation around the antenna. Hence, the near field is also referred as the induction field. For the ISM frequency at 2.45 GHz (as used for the HEPHAISTOS microwave applicator) the near field condition becomes $r \ll 2$ cm.

In the far field zone the E and H fields are in phase, they are θ and φ oriented respectively, which gives the real radial component of the Pointing vector (Fig. 3.1) and the linear EM wave carrying the EM energy in radial direction. Because of that the far field is sometimes referred as radiation field also. The far field conditions can be summarized as follows [23]:

$$r \gg \frac{\lambda}{2\pi},\ \ r \gg L \ \text{ and } \ r > \frac{2L^2}{\lambda}, \tag{3.2}$$

where L is the antenna dimension along the antenna axis (longitudinal antenna dimension).

The parameter that describes the spatial distribution of electric and magnetic fields far from the antenna is the antenna radiation pattern. The radiation pattern gives the dependence

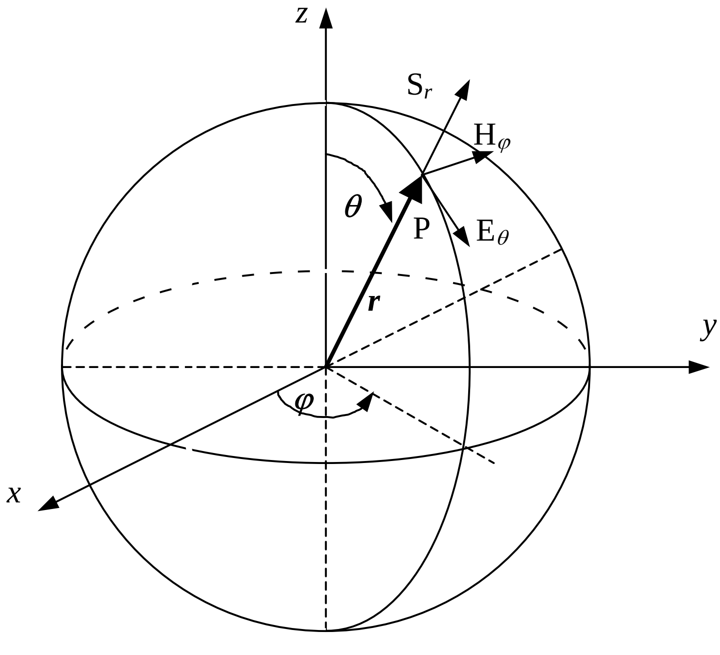

Figure 3.1 Spherical coordinate system

of the normalized electric and magnetic field magnitudes in spherical coordinates θ and φ at far distance r from the antenna (point P in Fig. 3.1). It can be defined such [30]:

(3.3) $$C(\theta,\varphi)=\left.\frac{\left|\vec{E}(\theta,\varphi)\right|}{\left|\vec{E}(\theta,\varphi)\right|_{\max}}\right|_{\substack{r=const\\ r\to\infty}}=\left.\frac{\left|\vec{H}(\theta,\varphi)\right|}{\left|\vec{H}(\theta,\varphi)\right|_{\max}}\right|_{\substack{r=const\\ r\to\infty}},$$

where the subscript max denotes the maxima of the field magnitudes. Using this normalization with maximum values the radiation pattern becomes independent on the radial coordinate r. The radiation patterns are usually presented graphically by polar diagrams in two planes as functions of only one coordinate, i.e. of θ or φ. The polar diagrams are the cross sections of the spherical surface defined by radiation pattern (equ. 3.1) in any plane that includes the origin. Commonly the yz plane (meridian plane for $\varphi=\frac{\pi}{2}$) is chosen for the normalized field magnitude presentation over the θ coordinate in the range from 0 to π. The other principle plane is the xy plane (equatorial plane for $\theta=\frac{\pi}{2}$) in which the normalized magnitudes of the fields are graphically presented as functions of φ.

It is useful to give some comments on radiation patterns and to derive some parameters from the radiation characteristics of the antenna. In practice many antennas can focus the EM radiation in one spatial direction range and they show the property of directivity. Other antennas have a constant radiation pattern over the entire angle range and they are known as omni directional antennas. The hypothetical antenna that radiates equally in all directions does not exist in reality, but it is used in definitions of some antenna parameters as comparative isotropic radiator. So, when the antenna shows directive properties and its pattern has one principle lobe in a specific range of the angles θ and φ, one can speak about the antenna beam [28,32]. The antenna main beam can be described by a parameter called antenna beamwidth and it is related to the angle range in which the radiation is stronger than one half of the beam maximum (half or 3 dB beamwidth) or one tenth of the beam maximum (tenth or 10 dB beamwidth).

Now, the design goal of uniform radiation along the energy feeding element (chap. 1) can be expressed using the antenna beamwidth definition as a very broad 10 dB beamwidth of the slotted waveguide in the cross section of its principle plane containing the waveguide axis.

3.1.3 Antenna gain and directivity

The spatial radiation characteristics of an antenna can be described using the spatial characteristics of radiated EM power also. The average power carried by an EM wave in the radiation field zone can be calculated from the radial component of the Poynting vector:

(3.4) $$S_r=\frac{1}{2}E_\theta\cdot H_\varphi^*\ \text{and}$$

(3.5) $$P_{av}=\iint_s S_r\,ds,$$

where * denotes the conjugate complex value and s is a spherical surface of radius r satisfying the far field condition (relations 3.2) and with the antenna being in the center. So, the EM average power at a far distance r is a function of θ and φ and it can vary with different directions giving the directive property of the antenna. Comparing the radiation power density of a real antenna in θ, φ direction to the power density of an isotropic radiator, a parameter called antenna gain G can be defined as [28,33]:

$$G(\theta,\varphi)=\frac{S_r(\theta,\varphi)}{S_i}=\frac{S_r(\theta,\varphi)}{\frac{P_r}{4\pi r^2}}, \tag{3.6}$$

where S_i is the power density of an isotropic radiator and P_r is the total radiated power from the antenna. The maximum gain describes the possibility of the antenna to direct the EM radiation in a certain direction and defines the so called antenna directivity parameter:

$$D=\frac{S_{r\max}}{\frac{P_r}{4\pi r^2}} \text{ or in dB } D_{\log}=10\log D. \tag{3.7}$$

For a slotted waveguide energy feeding system of a material processing applictor the directivity has to be low giving the desired uniformity of the radiated EM field.

3.1.4 Antenna efficiency

For a perfect antenna, which isotropically radiates in all directions the ratio between G and D is 1. A technical antenna that radiates non-isotropically has an efficiency η lower than unity:

$$\eta=\frac{G}{D}. \tag{3.8}$$

A transmitting antenna can be described as a transducer between the transmission line and a generator at one side and the free propagation space at other side [27]. Therefore, the antenna can be presented as an equivalent two port network connected to the transmission line as it is shown in Fig. 3.2. This equivalent circuit gives a picture of losses in the antenna and serves to define the antenna input impedance. Generally, the antenna input impedance is a complex value Z_a. The real part of Z_a contains a term R_L corresponding to the conductor losses in the conducting parts of the antenna and a term connected to the radiation power, named radiation resistance R_r.

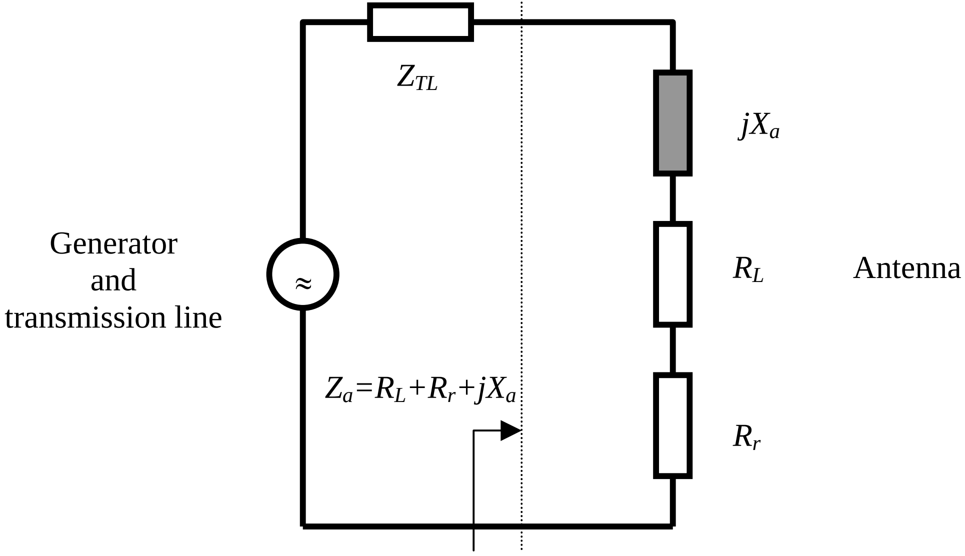

Figure 3.2 Transmitting antenna equivalent circuit

Using the equivalent circuit from Fig. 3.2 the antenna efficiency can be calculated also as:

$$\eta = \frac{R_r}{R_L + R_r}. \tag{3.9}$$

For a highly efficient antenna $R_L << R_r$ should be valid. From the last relation the importance of the antenna radiation resistance parameter can be highlighted.

The radiation resistance R_r can be defined as the value of a hypothetical resistor which dissipates a power equal to the power radiated by the antenna fed by the same current I, so:

$$R_r = \frac{2\iint_s S_r ds}{I^2}, \tag{3.10}$$

using the equ. 3.5 for the radiated power. At a fixed frequency the antenna resistance is a function of the antenna geometry.

3.1.5 Antenna matching

In addition, for the radiating antenna one of the main design challenges is the antenna matching. From Fig. 3.2 the condition for maximum power transfer from the transmitter to the antenna is given by:

$$Z_a = Z_{TL}^*, \tag{3.11}$$

where* denotes conjugate complex value. Hence, for highly efficient antennas the input impedance should be matched to the impedance of the feeding transmission line.

It is desirable to have a good matching in a broad frequency band to cover the band of interest by only one antenna system. This requires to ensure the stability of the antenna input impedance in a given frequency band. Usually there is an additional matching circuit or device implemented between the transmission line and the antenna for this task, such as waveguide tuners (sec. 2.4) in high power microwave transfer systems. However, by proper optimization of the antenna geometry parameters a good matching in the desired frequency band can be achieved without a matching circuit, providing a direct coupling.

A parameter that describes the antenna frequency response is the antenna bandwidth. The antenna bandwidth can be defined as frequency band in which the reflections are lower than a specific level (usually –10 dB) limiting the reflection losses in the system. In the present design the antenna matching is defined as less than -20 dB at the 2.45 GHz magnetron frequency. An additional advantage of magnetron sources is that they are narrow band devices making slotted waveguides, which are relatively narrow band antennas, appropriate for energy feeding systems in 2.45 GHz microwave applicators.

3.1.6 Antenna polarization

Due to the fact that in practice antennas have been made to transmit and receive only a specified type of EM waves, the antenna polarization is also an important antenna parameter. It is determined by the polarization of the radiated wave in the radiation field zone (see sec. 2.1). That means, linearly polarized slotted waveguide antennas radiate linearly polarized EM waves and can effectively receive only waves with the same polarization. Hence, using differently polarized antennas, which are closely placed in space, undesirable coupling between them can be significantly reduced. This is used for decreasing the unacceptably high levels of the so called mutual coupling between neighbouring slotted waveguide feeds for the HEPHAISTOS applicator (see section 4.3).

3.1.7 Antenna arrays

The optimization of an antenna, according to the desired matching and radiation characteristics, is limited by physical factors such as antenna geometry and antenna size. To overcome these limitations, same or different antennas can be grouped in so called antenna arrays with which the design goals can be achieved. Antenna arrays are especially advantageous in realization of high gain antennas with complex radiation patterns.

The antenna array field in the radiation field zone can be obtained by the vector sum (superposition) of the radiated fields from the individual radiating elements. These elements can be located along one dimension forming a basic linear antenna array (Fig. 3.3). The far field approximation can be introduced (relation 3.2), which gives the following for the power pattern of the antenna array made from equispaced, same type element radiators:

$$P_{array}(\theta,\varphi) = P_{el}(\theta,\varphi)\left|\sum_{n=1}^{N} a_n e^{j[(n-1)kd\cos\theta - \psi_n]}\right|^2 , \tag{3.12}$$

where $P_{el}(\theta,\varphi)$ is the power pattern of the radiator element, N is the number of antenna elements in the array, a_n is the amplitude of the n-th element, ψ_n is a phase difference between the first and n-th element in the array with $\psi_1 = 0$, k is the wave number in free space and d is the distance between the neighbouring elements. Relation 3.12 shows that the array pattern can be expressed as a multiplication of the pattern of an individual element with a factor, which depends on array properties such as the number of elements, their amplitudes and phases and their spacing. So, one can define an additional parameter for the antenna array as:

$$F_a(\theta) = \left|\sum_{n=1}^{N} a_n e^{j[(n-1)kd\cos\theta - \psi_n]}\right|^2 , \tag{3.13}$$

which is usually called the array factor [23].

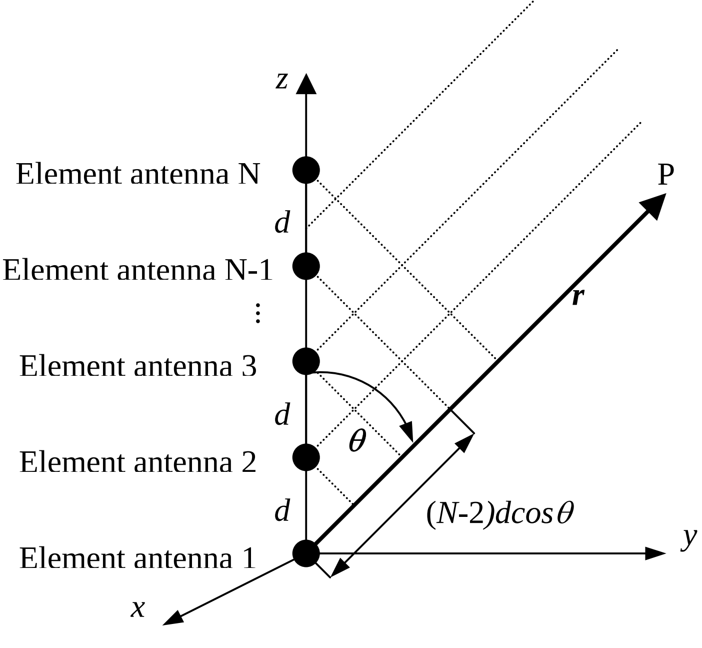

Figure 3.3 Linear antenna array of *N* elementary radiators

The phase contributions from each radiator element have been taken in equ. 3.13 as factor $(n-1)kd\cos\theta$, which represents the phase difference between the fields radiated from the array elements at the far field point P. This factor is determined by the far field approximation which states, that all lines connecting the element antennas and point P are parallel (Fig. 3.3). In addition, for the field amplitudes dependence on the distance between the element antennas and point P, this approximation assumes that $r_1 = r_2 = r_3 = \ldots = r_N = r$ and gives the ratio $1/r$ which is already implemented in the first term of the power pattern of an individual element $P_{el}(\theta,\varphi)$ in equ.3.12.

Using the general linear antenna array presented in Fig. 3.3, end fire and broadside array types can be defined. For the end fire arrays the main antenna beam is parallel to the array axis (z axis in Fig. 3.3) and for broadside array it is perpendicular to the array axis (for example y axis in Fig. 3.3).

Hence, the slotted waveguide antenna feeding systems for material processing applicators can be considered as linear broadside arrays.

3.2 Slot antennas

Slot antennas are one of the basic types of EM energy radiators. They can be realized by a linear array of slots in a waveguide, presenting a slotted waveguide antenna and as such they will be introduced in the following section. Using the duality principle in electromagnetics, slot antennas can be described by their complementary dipole antennas pair. At first, the consideration of the electromagnetic equivalent of the Babinet's principle and a short description of dipole antennas are described in this section. Then the radiating slots in the waveguide walls and their parameters will be presented and an overview of research on waveguide slots will be given.

3.2.1 Duality principle

A slot in an infinite conducting plane fed by a voltage connected to two opposite points at the centre of the slot (Fig. 3.5 a) presents one of the simplest antenna types. Calculating the far field of such antennas, it can be shown that these fields are the same as the radiating fields of an other basic radiator, called dipole antenna, except that the electric and magnetic fields are interchanged. Hence, the dipole antenna and the slot antenna are an example of a complementary antenna pair. This duality principle in electromagnetic theory is a result of the symmetry of Maxwell's equations. It is an electromagnetic equivalent of Babinet's principle in optics [27,28], well known as Booker's extension of Babinet's principle. Using the general complementary screens in Fig. 3.5 b) this duality principle can be expressed by the statement that the sum of the EM field behind a plane screen 1 and of the EM field behind the complementary screen 2 is equal to the original EM field in absence of any screens (1 and 2).

The duality principle leads to the following relation between the impedances of complementary dipole and slot antennas:

$$Z_{dipole} \cdot Z_{slot} = \frac{Z_c^2}{4}, \tag{3.14}$$

where Z_c is the wave impedance. From last relation it is easy to calculate the antenna impedance knowing the impedance of the complementary antenna.

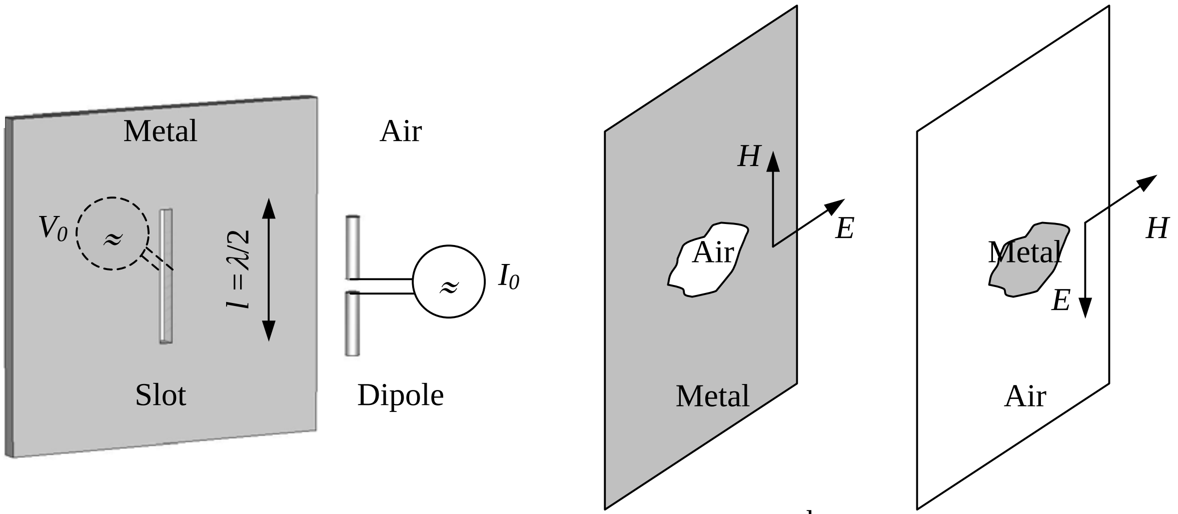

a b

Figure 3.5 Duality principle in electromagnetics: a) a complementary $\lambda/2$ antenna pair and b) general complementary screens

Some important parameters of slot and dipole antennas which are $\lambda/2$ long are given in Tab. 3.1, where V_0 and I_0 are the amplitudes of voltage and current applied to the slot and dipole antenna respectively. For the case that $V_0 = Z_c \cdot I_0$, it can be seen from the Tab. 3.1 that P_{av} is 4 times larger for the slot in an infinite conducting plane than for the dipole. This is due to the image of the slot in the conducting plane.

	Half wavelength slot	Half wavelength dipole
E far field	$E_\theta = \frac{jV_0 e^{-jkr}}{\pi r}\left[\frac{\cos\left(\frac{\pi}{2}\cos\theta\right)}{\sin\theta}\right]$	$E_\theta = \frac{jZ_c I_0 e^{-jkr}}{\pi r}\left[\frac{\cos\left(\frac{\pi}{2}\cos\theta\right)}{\sin\theta}\right]$
Average power density	$P_{av} = \frac{V_0^2}{2\pi^2 r^2 Z_c}\left[\frac{\cos\left(\frac{\pi}{2}\cos\theta\right)}{\sin\theta}\right]^2$	$P_{av} = \frac{Z_c I_0^2}{8\pi^2 r^2}\left[\frac{\cos\left(\frac{\pi}{2}\cos\theta\right)}{\sin\theta}\right]^2$
Radiation resistance (Ω)	486.1	73.1
Antenna reactance (Ω)	-*j* 836	*j* 42.5
Directivity	1.64	1.64
Polarization	Linear and perpendicular to the slot axis	Linear and perpendicular to the dipole axis

Table 3.1 Comparison of complementary antennas

3.2.2 Slots in the waveguide walls

A slot in a waveguide wall cuts and disturbs the currents flowing in the inner waveguide wall, which causes the radiation of EM energy from the waveguide. This can be explained using the following relation, which is derived directly from the law of conservation of the electric charge and from Maxwell's relation 2.4:

$$div\vec{j}_c = -\frac{\partial}{\partial t} div\vec{D}. \tag{3.15}$$

From the last relation it is obvious that an interruption of the currents in the inner waveguide wall results in an induced electric field, which has the character of a displacement current and can be considered as a radiating field. Stronger interruption of currents causes stronger radiation from the slot. So, the current distribution in the inner waveguide wall plays an important role in the design of slotted waveguide antennas. A current flow pattern for the fundamental TE_{10} mode is given in Fig. 3.6. Using the relations 2.60 – 2.63 (see Fig. 2.10) and the relations for the magnetic field components of the TE_{10} mode from Tab. 2.3, the distribution of the surface current j_s yields in following analytical expressions:

$$j_{sy} = -H_0 e^{-jk_z z}\Big|_{x=0} \text{ and} \tag{3.16}$$

$$j_{sy} = -H_0 e^{-jk_z z}\Big|_{x=a} \tag{3.17}$$

for the currents in the inner narrow waveguide wall (parallel to the *yz* plane). From these relations it can be seen that the surface currents in the narrow waveguide walls flow parallel to the *y* axis and they are constants over the transverse waveguide dimensions, i.e. they are functions only of the longitudinal z coordinate. Because slots made along the current paths do not affect the currents and cause negligible radiation, radiating slots in the narrow waveguide walls should be made in directions, which are not parallel to the *y* axis. Hence, the radiating slots in the narrow waveguide walls are longitudinal and inclined slots (Fig. 3.6).

For the broad waveguide walls (parallel to the *xz* plane) the inner current components can be calculated as:

$$j_{sx} = -H_0 \cos(\frac{\pi x}{a}) e^{-jk_z z} \text{ and} \tag{3.18}$$

$$j_{sz} = -jk_z \frac{a}{\pi} H_0 \sin(\frac{\pi x}{a}) e^{-jk_z z}. \tag{3.19}$$

The surface currents near the edges of the broad waveguide walls ($x \approx 0$ or $x \approx a$) have only components parallel to the transverse *x* axis (Fig. 3.7). However, near the central wall line ($x \approx \frac{a}{2}$) the currents have only a longitudinal z component. Hence, longitudinal slots along the central broad wall line disturb no currents and these slots represent a nonradiating slot type. These slots can be used for inserting coaxial probes for measurements in the waveguides. Very close to the central line only the transversal slots radiate strongly and they should be used as centred radiating slot types.

Longitudinal slots in the broad wall near the wall edges will radiate very effectively. Slots with more complex shape, for example, banana shaped slots which cut orthogonally the current paths, could be used for efficient radiation in the range between the broad wall central line and the region near the wall edges.

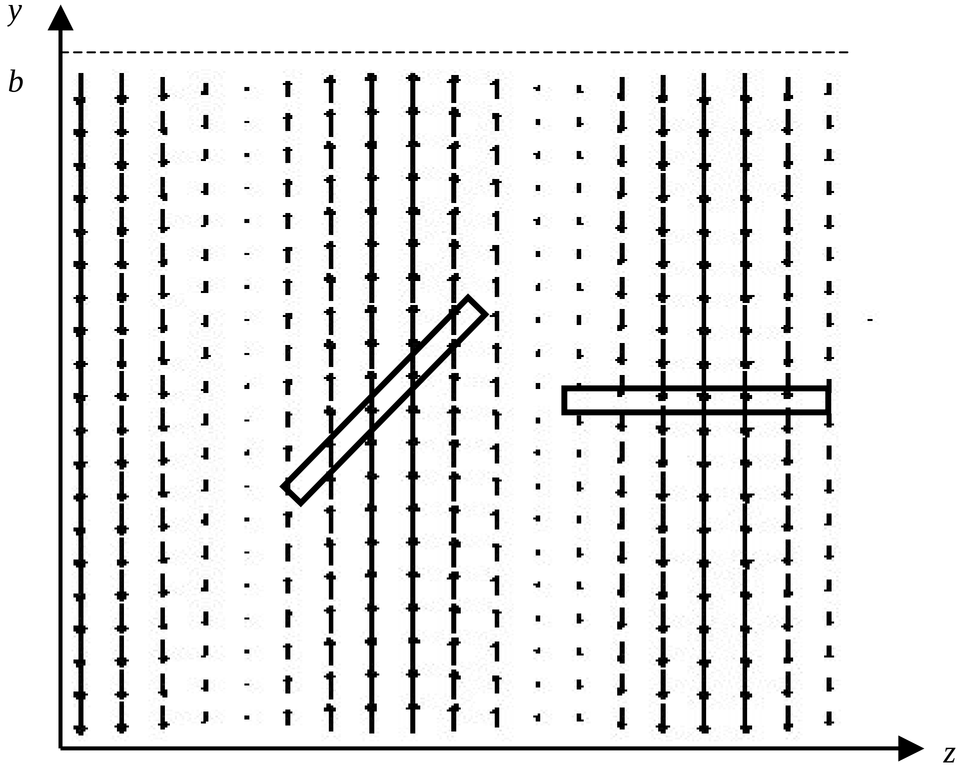

Figure 3.6 Current distribution for the TE_{10} mode in the inner narrow waveguide wall and radiating slot types

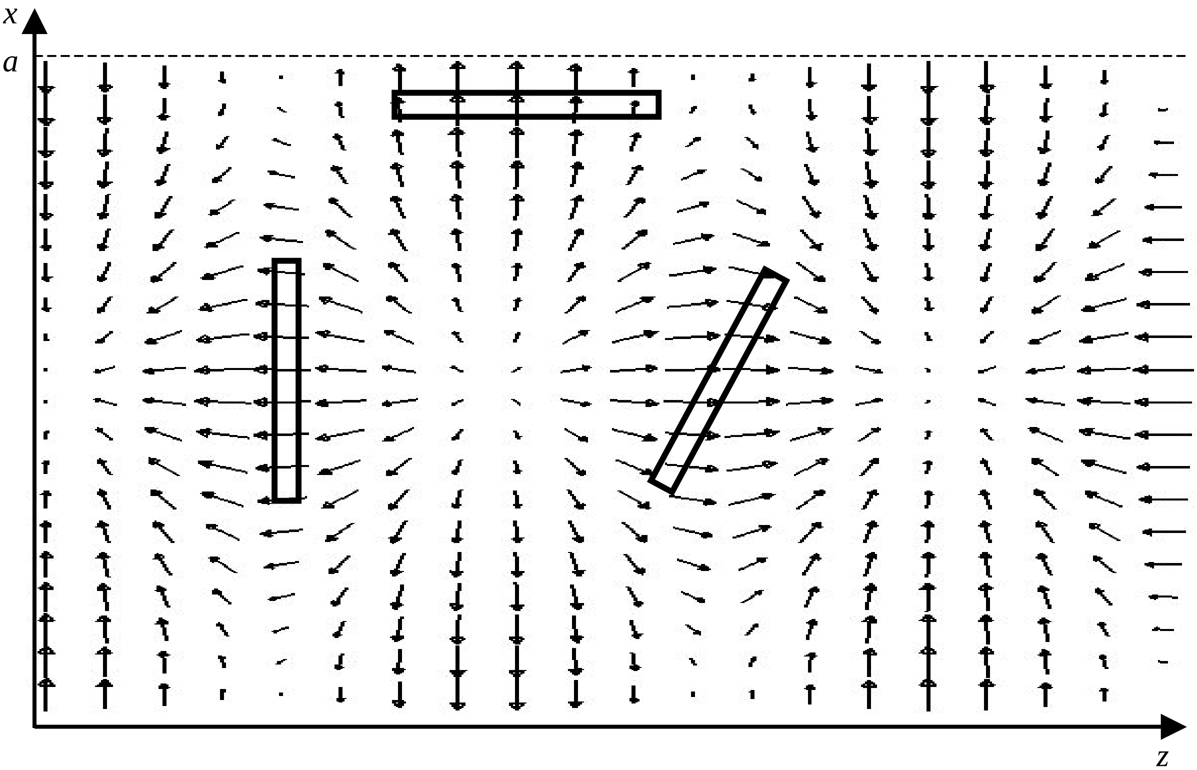

Figure 3.7 Current distribution for the TE_{10} mode in the inner broad waveguide wall and commonly used radiating slots

Each slot type represents a discontinuity in the waveguide and can be described using the concept of equivalent circuit elements. Calculating the equivalent impedance or admittance of the slot in the waveguide wall and connecting them properly to the transmission line representation of the waveguide (sec. 2.3), the behavior of the waveguide slots can be investigated and determined. So, the goal in slot design is to determine its equivalent impedance or admittance.

3.2.3 Waveguide wall slots research review

Stevenson was the first who has calculated the slot impedance for various slot types in his famous paper ‘Theory of slots in rectangular waveguides’ [34]. He derived the equations for narrow longitudinal, transversal and inclined slots in the broad waveguide wall and for inclined slots in the narrow waveguide wall (Fig. 3.8). However, in his work he made some assumptions, such as: the waveguide walls are infinitely thin, the slots radiate only outside the waveguide, the slots are ideally rectangular, the field on the slot is perpendicular to the slot’s longer dimension, i.e. the slot is narrow with width w which is much less than the slot length l, $w << l$, and that all slots have resonant length ($l \approx \frac{\lambda}{2}$). Some of these assumptions are more critical and the derived expressions 3.20 – 3.22 give accurate results only for slots near the central line in the broad waveguide wall, which are practically poor radiators and have no significant practical importance. The relations 3.20 – 3.23 are not sufficient for a serious design. But, the closed form of the Stevenson’s equations has the advantage of a very easy estimation of slot impedances r or slot admittances g and they are very popular in textbooks on this topic [28,35,36]. For purpose of comparison to the later numerically calculated slot impedances, they are given here as:

(3.20) $$g = \frac{480}{73\pi}\frac{\lambda_g}{\lambda}\frac{a}{b}\cos^2(\frac{\pi\lambda}{2\lambda_g})\sin^2(\frac{\pi d}{a})$$ for a longitudinal slot in the broad wall, (3.21) $$r=\frac{480}{73}\frac{\lambda_g^3}{4\pi^2\lambda ab}\cos^2\left(\frac{\pi\lambda}{4a}\right)\cos^2\left(\frac{\pi d}{a}\right)$$ for a transversal slot in the broad wall,

(3.22) $$r=0.131\frac{\lambda^3}{\lambda_g ab}\left[I(\theta)\sin\theta+\frac{\lambda_g}{2a}J(\theta)\cos\theta\right]^2$$ for a centered inclined slot in the broad waveguide wall and

(3.23) $$g=\frac{30}{73\pi}\frac{\lambda_g\lambda}{a^3b}\left[\frac{\cos^2\theta\cos\left(\frac{\pi\lambda}{2\lambda_g}\cos\theta\right)}{1-\frac{\lambda^2}{\lambda_g^2}\cos^2\theta}\right]^2$$ for a centered inclined slot in the narrow wall,

where *a* and *b* are the waveguide inner transversal dimensions, λ and λ_g are the wavelengths in free space and in the waveguide, respectively, *d* is the displacement (offset) from the central line of the broad waveguide wall, θ is the angle of inclination and $I(\theta)$ and $J(\theta)$ are functions which can be found in the literature [34]. The relations 3.20 – 3.23 have been derived later by Silver also [28].

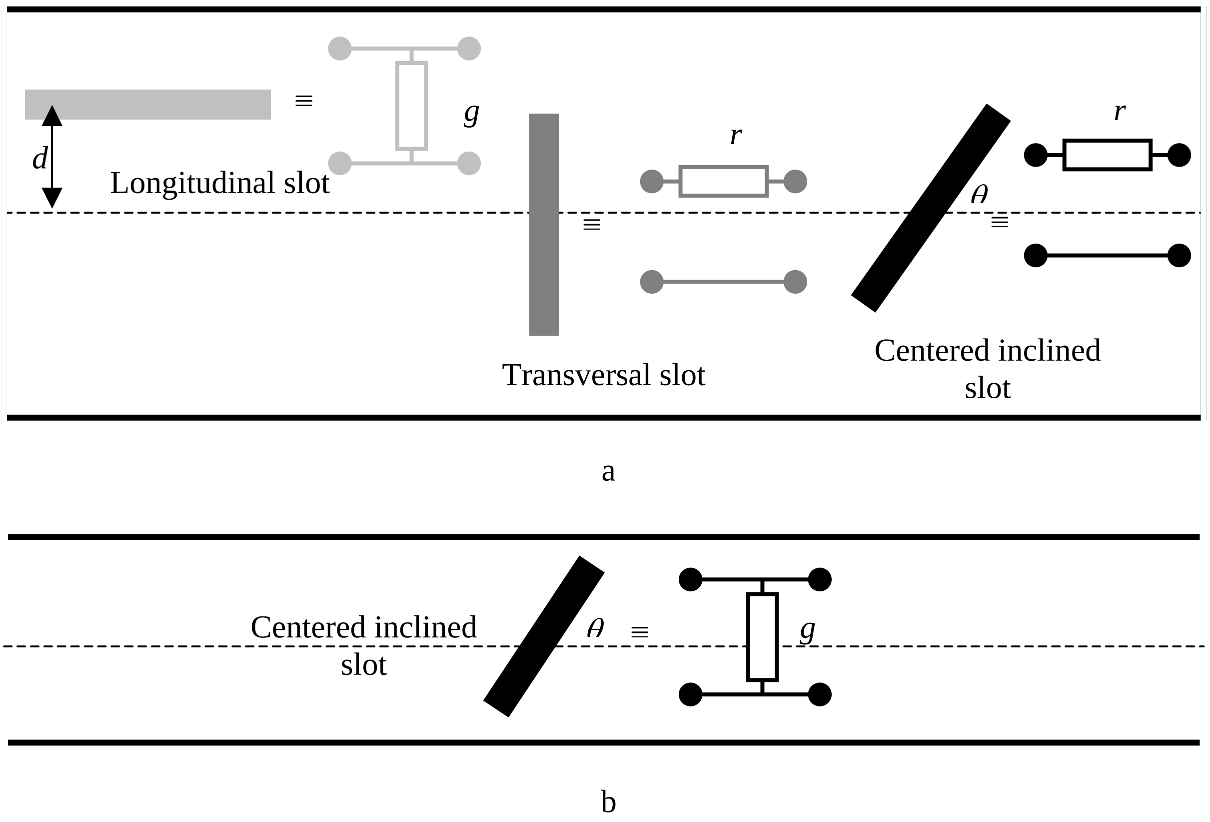

Figure 3.8 Stevenson’s equivalent circuits for various slot types a) in the broad waveguide wall and b) in the narrow waveguide wall

The most critical assumptions of Stevenson are that the waveguide walls are infinitely thin and that of the half wavelength resonating length of the slots. Hence, the Stevenson's relations assume that all slot lengths are equal to $\lambda/2$ and that they do not predict the slot lengths and slot reactances, which gives incorrect results for slots with medium and higher offsets from the central waveguide line.

Several authors have proved this experimentally. In 1951 Stegan [37,38] performed a series of experiments on longitudinal slots in the broad waveguide wall. He used round ended narrow slots of various offsets and lengths and achieved a standard against the theory can be judged. He found out that the resonant slot length, contrary to Stevenson's assumption, was dependent on the slot displacement from the central wall line. Hence, using Stevenson's equations for slots with higher offsets will result in larger errors in the design.

Working in parallel with Stegan, Oliner [39] developed the first theory for longitudinal slots that permits the calculation of the imaginary parts of slot impedance or slot admittance. However, Oliner had to add some adjustments to his theoretical calculations to correct the results according to the measurements of Stegan. First, he assumed zero wall thickness, but Stegan measured on a waveguide which walls had a finite thickness. Second, Oliner considered in his theory perfect rectangular slots, opposite to Stegan's rounded slots. After he adjusted his equations, Oliner concluded that his square ended slot in an infinitely thin waveguide wall should be 4 percent shorter than the actual Stegan's slot, to fit the measured data. Oliner's equations for the equivalent slot impedance or admittance are more reliable than Stevenson's equations, but at the same time they are more complicated and also insufficient for today's design requirements [40]. So, they have more theoretical than practical importance.

The next theoretical contribution to the theory of waveguide slots has been made by Khac [41]. Using the method of moments he solved an integral equation obtaining the electric field in the slot. Knowing this field he could calculate the reflections from the slot and find the equivalent slot admittance. Khac's results were in better agreement with Stegan's experimental standards than Oliner's results, but he faced the same problems as Oliner. Khac also assumed perfect rectangular slots and infinitely thin waveguide walls, and he also had to adjust his parameters to bring the theoretical results closer to the measurements, but not better than 2 percent.

As an extension of Oliner's work, Yee developed the theory for calculation of the resonant slot length as a function of the slot offset from the center of the waveguide using the variational method [42]. He considered the longitudinal rectangular slot in the broad waveguide wall with non zero thickness. He presented a semi-empirical equation for the resonant length of a slot with round ends for practical applications:

$$l_{res,round} = l_{res,rect} + \frac{3(1-\frac{\pi}{4})w}{2}, \tag{3.24}$$

where $l_{res,round}$ and $l_{res,rect}$ are the resonant lengths of the rounded and rectangular slots respectively and w is the slot width.

Using the available theoretical and experimental data Elliott gave in 1978 an iterative design procedure for slotted waveguide structures based on two practical equations [43]. He considered the mutual coupling between the slots in the slot array and its influence on the resonant length of the slot. With his colleagues he improved the theory of waveguide slots and presented a successful design procedure for basic types of slotted waveguide antennas [38].

Further improvements in the analysis of waveguide slots have been made by Josefsson [44]. He used the method of moments with entire basis function for calculation of the longitudinal slot aperture field, considering a finite wall thickness. Computed resonant slot lengths compare very well with measured results. He also investigated transversal slots in the broad waveguide wall and numerically calculated the normalized slot impedance versus slot length and frequency [45]. An improved technique for calculations of transversal slot parameters has been reported by Park et al. [46].

Using the method of moment analysis, LC equivalent circuit models for transversal and longitudinal rectangular waveguide slots were also obtained [47]. These equivalent circuit models are then used for investigation of slots in slot arrays over the frequency bands of interest.

However, other numerical methods have been also reported for investigations of waveguide slots. Using the FDTD method Ren et al. presented a full wave analysis of slots in the broad waveguide wall [48]. Modeling the conventional types of slots in FDTD simulations the slots have been characterized by their equivalent impedances and admittances in the X band, which is important for telecommunications applications. The virtual models for calculations included the finite wall thickness and the rounded slot ends into the considerations. Very good agreement with the famous Stegan's standards, which has been obtained, validated and proved this approach. Additionally, numerical simulations have been already used for a successful design of SW components for MW applicators [49,50]. Because of that, the numerical approach based on the use of commercial finite integral time domain method software has been chosen for the characterisation of slots in this PhD thesis.

3.3 Numerical investigations on waveguide slots at 2.45 GHz

3.3.1 Numerical models

Numerical simulations of different waveguide slot types are performed with the CST Microwave Studio 3-D electromagnetic simulator software [51]. Using the finite integral time domain method (FITD) MWS software overcomes the problems of numerical modeling of curved structures [13,51]. Additionally, it is a proven reliable numerical tool for designing antenna structures and it has been well evaluated for the modeling of MW applicators also [52].

The characterization of various slots is crucial to select an appropriate slot type for the slotted waveguide feeding system design. Numerical models have been made to calculate the normalized impedances and admittances of the various slots types (Fig. 3.9). Further, using this numerical method, all other important parameters, such as electric fields in the slots and radiation characteristics of the different slot types (polarizations of the radiated fields), can be determined.

The virtual model consists of one slot made in the broad wall of a WR 340 waveguide section radiating into the free space, with TE_{10} mode excitation at one end and open waveguide at the other end. The waveguide section is one waveguide wavelength long and the slot is positioned in the middle of the WR340 section. The waveguide walls are perfectly conducting and 2 mm thick. Using Absorbing Boundary Conditions (ABC) to model the matched waveguide (all reflections from the open waveguide end are absorbed with the ABC) it could be achieved that only the reflections from the slot are present at the input port. From the simulated S_{11} parameter the normalized slot admittance y and normalized slot impedance z were calculated by the well known formulas 2.106 for a shunt element and 2.107 for a serial element, respectively.

3.3.2 Conventional longitudinal slots

First the longitudinal rectangular slot has been investigated, which is presented with its grid for the numerical calculations in Fig. 3.10. In the slot aperture region the grid is finer assuring reliable numerical results. This type of slot can be described as a parallel admittance

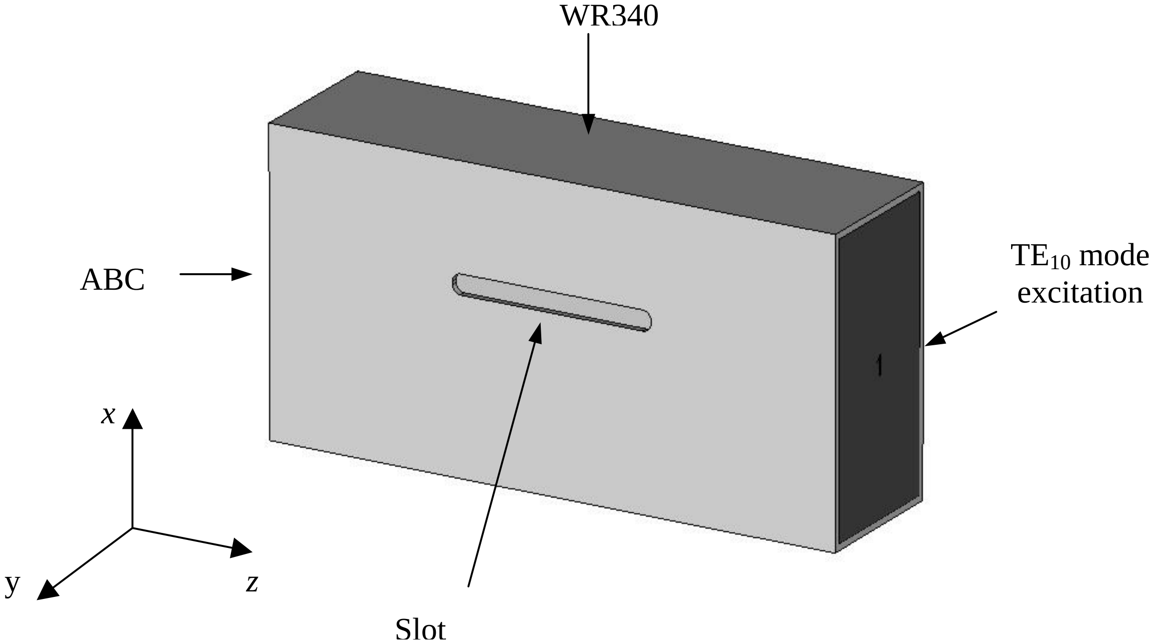

Figure 3.9 Model for numerical calculations of the slot normalized admittance

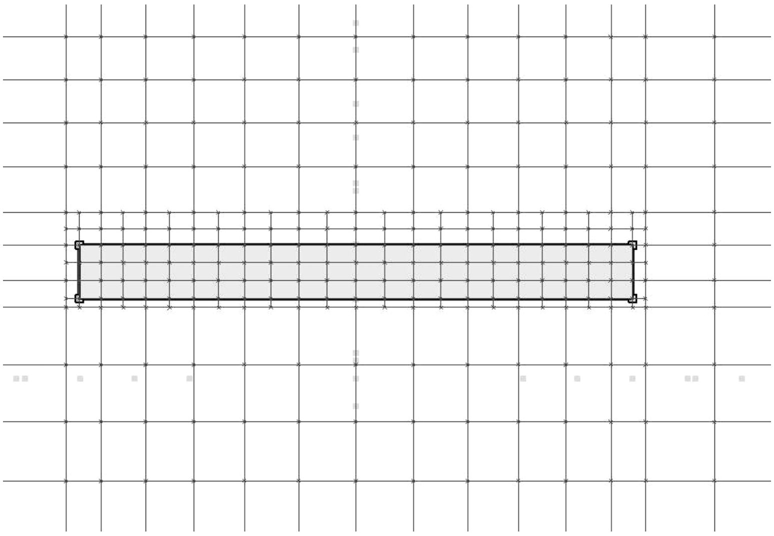

Figure 3.10 Rectangular longitudinal slot and its grid for numerical simulations

y (Fig. 3.8) in the transmission line model of the waveguide. For the calculations of y the slot offset d has been varied from 4 mm to 18 mm (measured from the central line of the broad waveguide wall). For each offset value, the S_{11} parameter has been simulated and the normalized slot admittance of the rectangular longitudinal slot has been obtained, which determines the amount of radiated EM power from the waveguide.

In these numerical calculations of y as a function of d, the model from Fig. 3.9 was used, with slots, which are, l = 61 mm long ($\lambda/2 \approx 61$ mm is nearly the resonant length at 2.45 GHz) and 6 mm wide. This ratio $w \approx \frac{l}{10}$ between the slot width and the slot length allows that the slots can be considered as narrow type and ensures a pure linear polarization of the radiated field.

In practice the slots are made with rounded ends in order to improve high power operation and manufacturability. This important slot type has been also numerically investi-

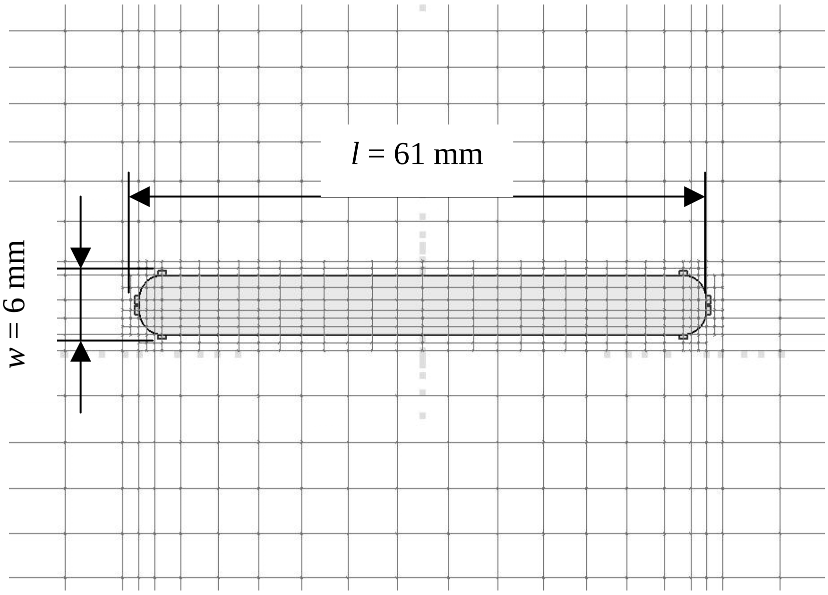

Figure 3.11 Practical longitudinal slot with round ends and modelling grid for simulations

gated. The longitudinal narrow slot with rounded ends is presented in Fig 3.11. The total length of the slot is, like in the previous case of the rectangular slot, equal to 61 mm (near the resonant length), with the same width of 6 mm. The effective length of this slot type is shorter than the rectangular one, which should affect the resonant behavior of the slot and its normalized admittance y (especially the imaginary part of y). The mesh in the numerical model is correspondingly finer at the rounded slot ends than in the slot aperture region.

Additionally to the investigation of the dependence of the slot admittance on the slot offset, the variation of y with slot width and slot length has been also numerically simulated. For the constant slot displacement of d = 10 mm from the central line, the normalized slot admittances were numerically obtained for the slot widths of w = 4 mm and w = 8 mm and for the slot lengths l = 59 mm and l = 63 mm.

These first presented slot types are very common in slotted waveguide design [35, 36,38,53] and could be defined as conventional slot types. However, as it has been already mentioned before, they cut the inner waveguide wall currents very efficiently only for higher values of the displacements d. As a more efficient alternative in the lower and medium offset range, a new slot type is introduced here, with curved shapes, which should strongly interrupt the inner wall currents giving stronger radiation from the waveguide [54,55].

3.3.3 Novel curved shaped slot type

If one wants to provide strong radiation of EM energy from the waveguide by cutting a slot in the waveguide wall, one has to ensure that the slot disturbs the inner wall currents strongly, i.e. one has to ensure that the slot is positioned perpendicularly to the current paths. From Fig. 3.7 it can be seen that for the lower and medium offset range, this can be done using banana like shaped slots, which cut the currents orthogonally. This new curved shaped slot is presented in Fig. 3.12. In the same figure it is shown that the new slot type cuts the

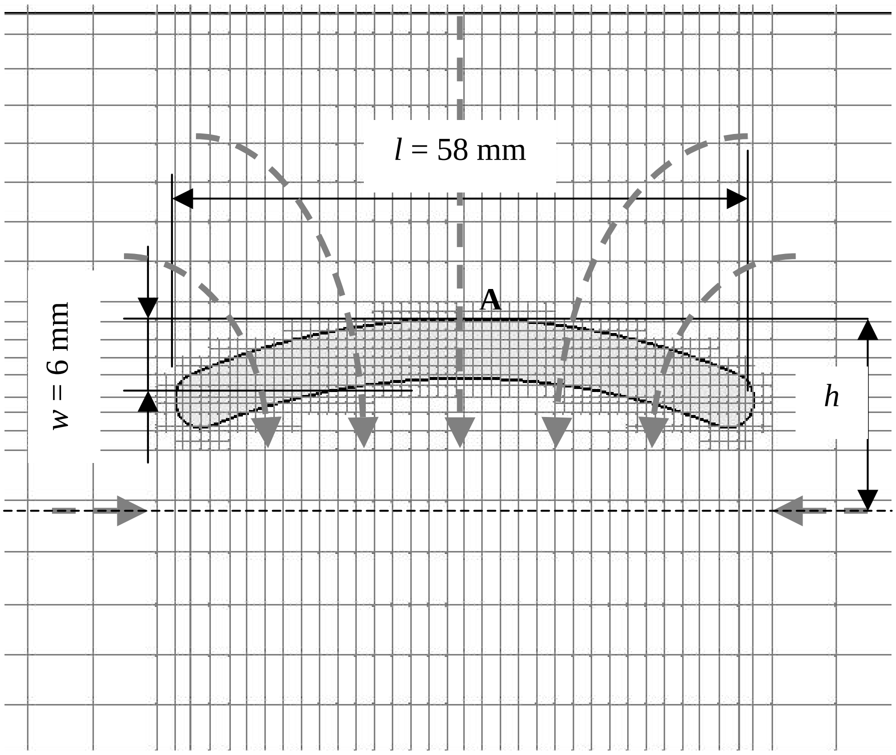

Figure 3.12 New banana shaped slot cuts the inner waveguide wall currents orthogonally

inner waveguide wall currents orthogonally. The slot width remains 6 mm. The slot length in longitudinal dimension is a bit less than 61 mm (58 mm) so that the slot arc length is nearly 61 mm long.

The slot displacement in the considered case is defined as a distance *h* in mm from the central wall line to the longitudinal line which contains the top slot point A (Fig. 3.12), minus 3 mm (one half of the slot width *w*), i.e. *d* in mm can be estimated using $d = h - 3$.

3.3.4 Centered transversal slots

As radiators of EM fields with linear polarization, which is parallel to the waveguide axis and orthogonal to the polarization of the longitudinal slots, transversal slots in the broad waveguide wall have been also numerically simulated. In figures 3.13 and 3.14 the rectangular and round ended centered narrow transversal slots with their numerical models grids are shown. These slot types can be represented as serial impedances in transmission line simulations of the waveguide. Hence, in the investigations of transversal slots, the numerically calculated S_{11} parameters are used for estimation of the normalized slot impedance *z*.

However, in these simulations, the slot offset was kept constant to zero (slots are centered) and *z* is determined as a function of the slot lengths, which varied from 32 mm to 63 mm. This is due to the fact that centered transversal slots with lengths near the resonant length disturb the inner wall currents very strongly (Fig. 3.7). That results in a very high value of their normalized resistance (real part of *z* is larger than 1) and they cannot be matched to the characteristic waveguide impedance. So, they have no practical importance.

Another alternative way to overcome this problem is to use non-centered slots, with displacements from the central line. But, in that case, the available offset parameter range is very small ($d < \frac{a - \frac{\lambda}{2}}{2}$) and already with d = 12 mm the slot touches the waveguide edge. Additionally, also for displacements around 10 mm, the real parts of the normalized slot resistances *r* are still undesirably high and it would be practically impossible to achieve the input matching condition ($z_{in} = 1$). Because of these disadvantages resonant transversal slots with offset were not further considered.

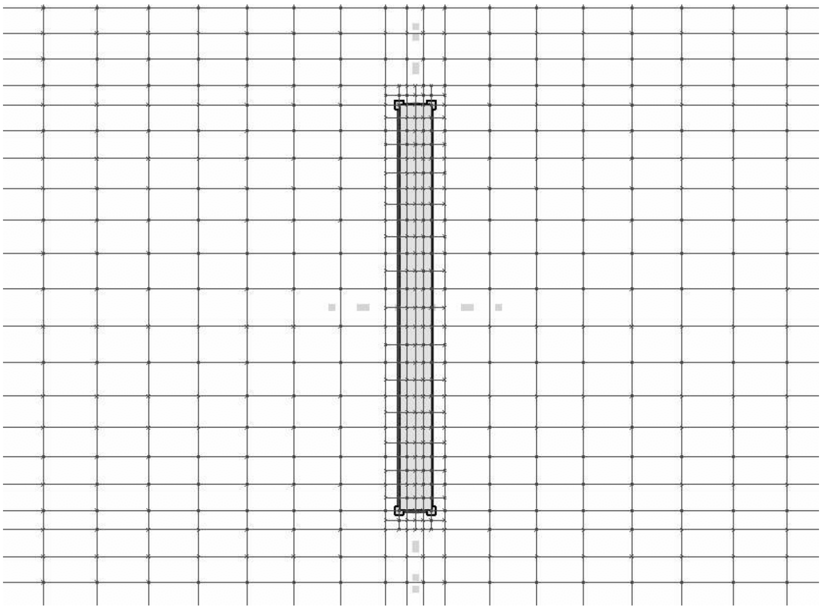

Figure 3.13 Rectangular transversal slot and its grid for numerical simulations

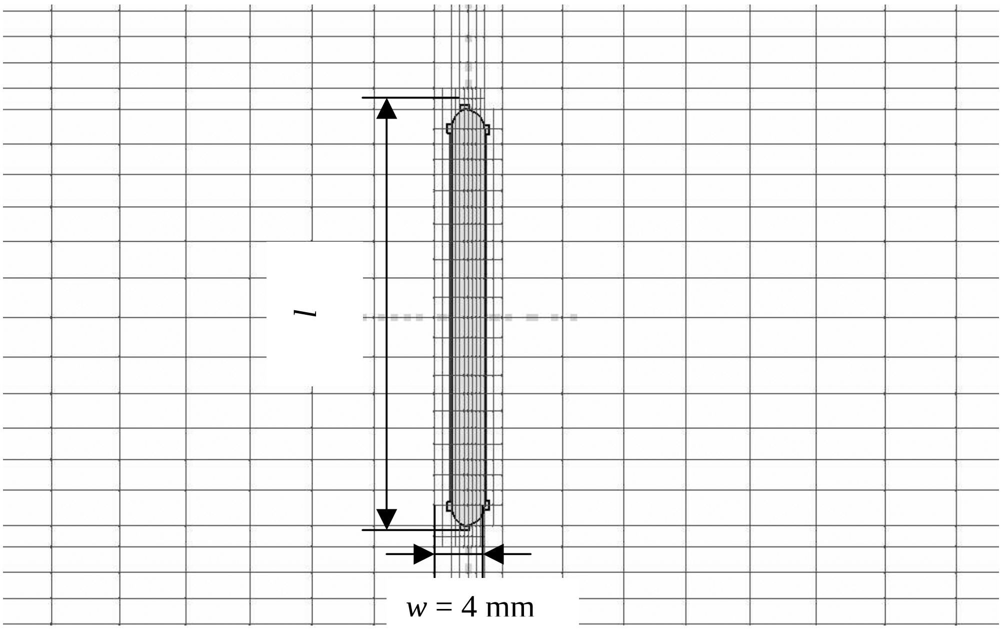

Figure 3.14 Transversal slot with rounded ends and its grid for numerical simulations

By the proposed variation of the slot length one can realize the desirable normalized slot resistances and match the slots to the characteristic waveguide mode impedance. However, this approach has the disadvantage that a nonresonant slot length will probably give very high undesirable normalized slot reactance. So, there will be a high reactive term in the sum of all normalized slot impedances, which should be compensated in the matching process.

The slot width for both transversal slot types is constant, *w* = 4 mm in all numerical simulations of the normalized slot impedances as function of the slot length. To obtain the dependence of the normalized slot impedances on the slot width, centered rectangular slots

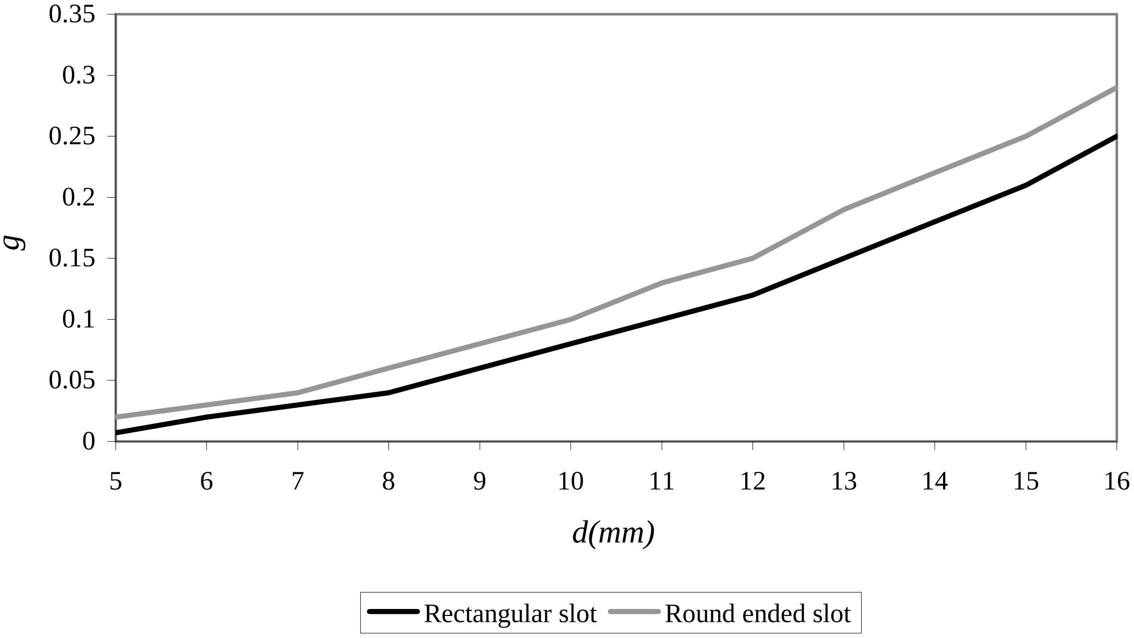

Figure 3.15 Normalized conductance of longitudinal slots vs. slot offset at 2.45GHz

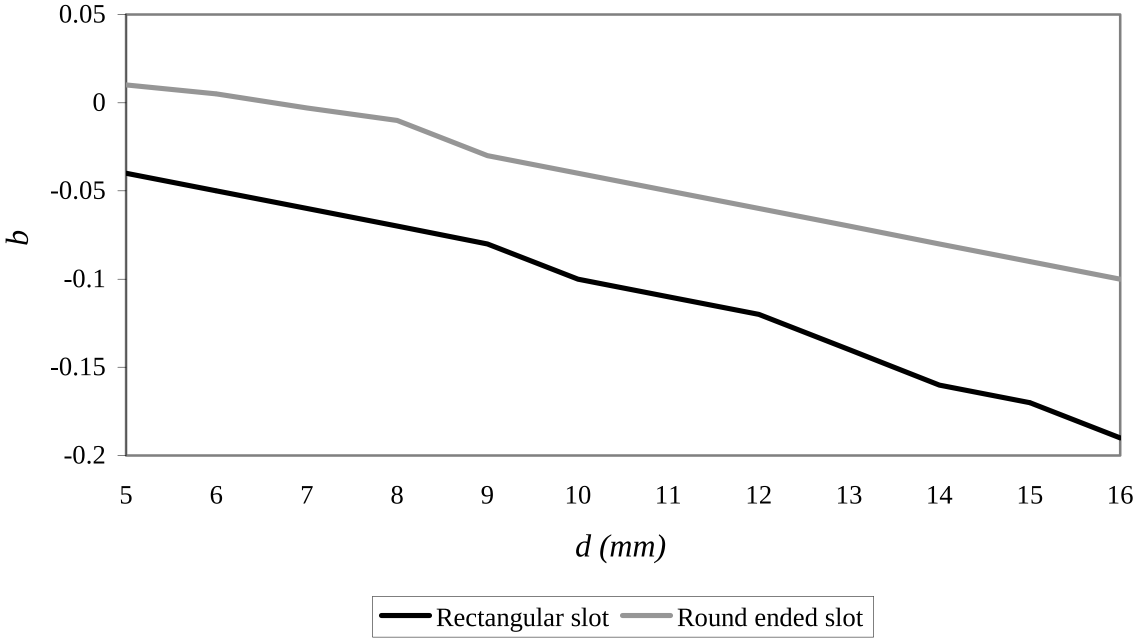

Figure 3.16 Normalized susceptance of longitudinal slots vs. slot offset at 2.45 GHz

with different slot width (w = 6 mm and w = 8 mm), at a constant slot length, have been also numerically investigated.

3.3.5 Results of the numerical calculations

In Figs. 3.15 and 3.16 the numerically obtained results of the normalized slot admittances for the rectangular and round ended longitudinal slots are presented.

The normalized slot conductances g of these conventional slot types are depicted and compared in Fig. 3.15. The slots with rounded ends cause a bit stronger EM radiation from the waveguide than the slots with square ends. This is more obvious for higher slot offsets, as it can be seen from Fig. 3.15. The difference between the values of g for the conventional slots can be explained by the difference in slot lengths of the considered two slot types. The effective slot length of the slots with round ends is closer to the resonant one, than the slot length of the rectangular slots, which results in higher g and stronger EM fields.

In Fig. 3.16 the calculated normalized slot susceptance b of both longitudinal slot types is given. The rounded slots show lower values for b than the square ends slots. This also leads to the conclusion that the length of the round ended slots is closer to the resonant slot length at 2.45 GHz, than the effective length of the rectangular slots. Hence, for the chosen slot length of 61 mm the rounded slots are the better choice for the design of slotted waveguide antennas. However, by shortening of the length of the rectangular longitudinal slot to the resonant length, the radiated power of this slot type can be increased.

The results of numerical simulations of the novel banana shaped slot type are given in Figs. 3.17 and 3.18. The real part of the calculated normalized slot conductance is compared with the normalized conductance of the rounded conventional slot in Fig. 3.17. As it has been expected, in the lower and middle offset ranges, for d up to nearly 20 mm, the new banana like shaped slots cut the inner wall currents more orthogonally and give higher values of g, than the conventional type. Further, as it has been also predicted, in the higher offset range above 20 mm, the conventional slots radiate more EM energy from the waveguide, because they disturb the inner wall currents more efficiently.

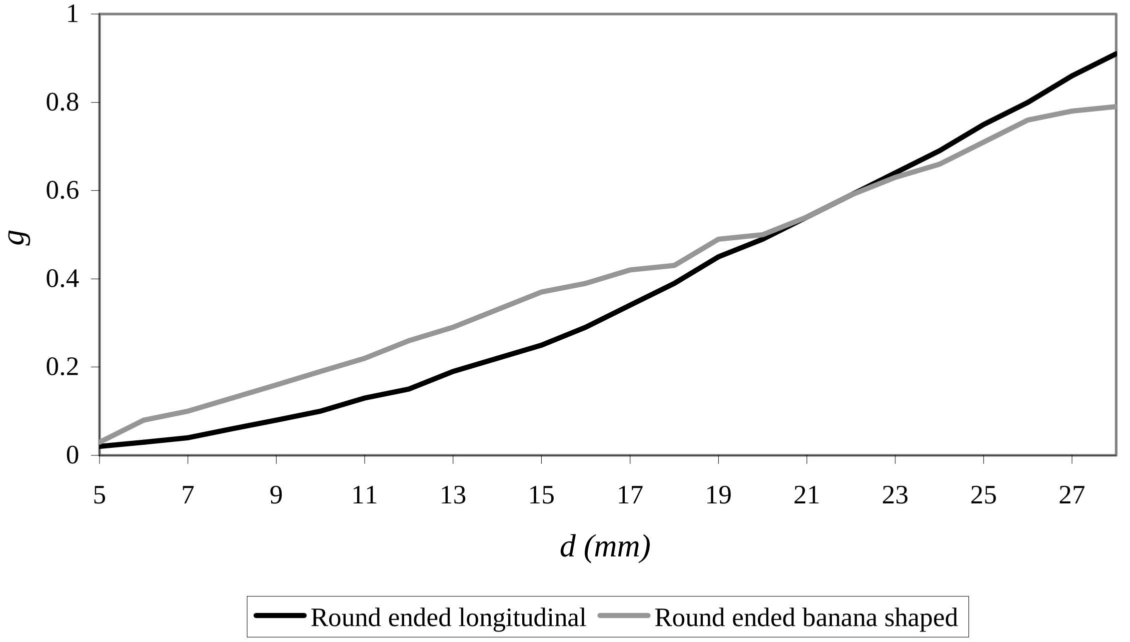

Figure 3.17 Normalized conductance of longitudinal rectangular and new banana shaped slots at 2.45 GHz

In Fig. 3.18 the imaginary parts of the obtained slot admittances are compared. For small offsets, near the central line, there is no significant difference in the magnitude of the normalized slot susceptance between new and conventional slots. Also in the middle offset range this difference remains small, but the susceptances have the opposite sign. For displacements over 20 mm, the conventional slot shows clearly lower values of *b*, which is more desirable for the design of slotted waveguide antennas.

From Figs. 3.17 and 3.18 it can be concluded that the new banana shaped slots are more efficient EM radiators at small and medium offsets, than the conventional slots. But, they also have some disadvantages in comparison to the conventional ones. First, the small values of *g*, which are necessary in the design of slotted waveguides with a greater number of slots, are not feasible with the novel slots, because even near the waveguide central line, they cause certain EM radiation. Second, very high *g* values (over 0.7) cannot be achieved using the novel slots. In other words, the conventional rounded slots provide a wider range of normalized slot admittances than the banana like shaped slots, for the same offset range from 5mm to 28 mm (Fig. 3.17). That makes them more flexibile for the SW design. Further, the practical fabrication of the novel slots is more complicated than for the round ended longitudinal slots. Hence, they can be recommended only for the design of a slotted waveguide with a low number of slots (shorter slotted waveguide section). In this case, the slots should be very effective radiators of EM energy and should have higher values for *g* and lower values for *b*. This makes the novel slot type advantageous over the conventional one, because in the lower and medium offset range they have exactly these desirable characteristics. The conventional slots in the higher displacement range have high values of *g*, but at the same time, they have unwanted high values of *b*.

The variation of the slot admittance with different slot widths for a constant slot length, and vice versa, for the conventional round ended slot are given in the tables 3.2 and 3.3. For constant *l* = 61 mm and for slot offsets of 6 mm, 10 mm and 14 mm, the real and imaginary parts of the numerically calculated *y* are given for 3 different slot widths *w*. It is

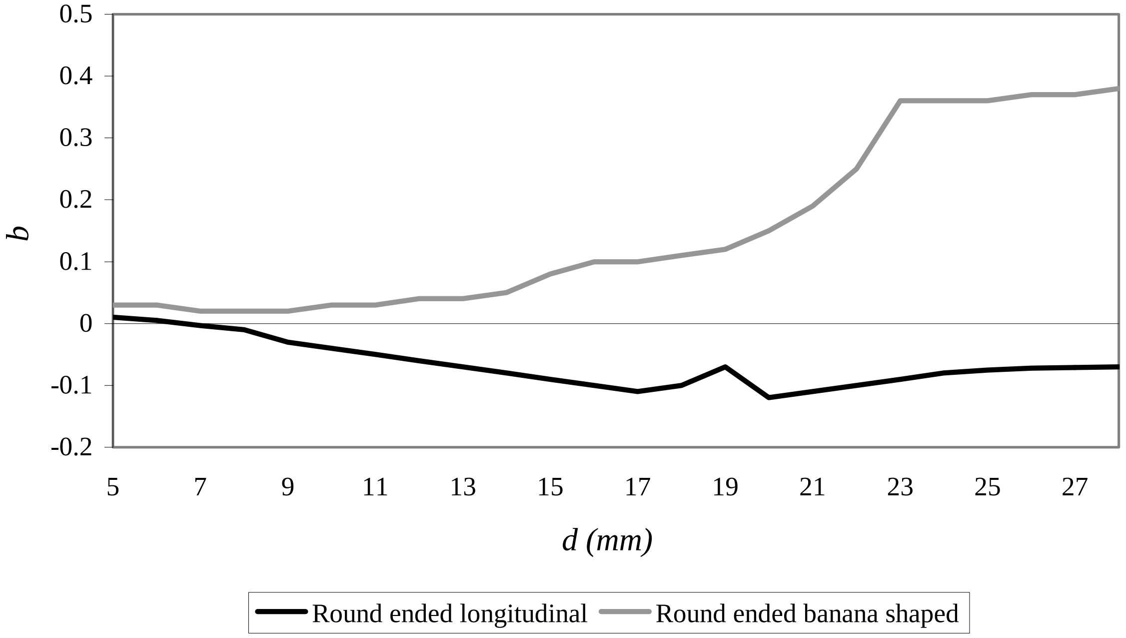

Figure 3.18 Normalized slot susceptance for longitudinal and new banana shaped slots at 2.45 GHz

obvious that the changes of the slot width do not affect the normalized slot conductances (*g* remains constant for *d* = 6 mm and *d* = 10 mm). In the case of the normalized slot susceptance, the slot width *w* changes cause maximum variation of *b* up to $\Delta b_{max} = 0.03$, which is also a very small amount. That means, the slot width of the narrow slots, plays a minor role as a design parameter for slotted waveguides.

In Tab. 3.3 the real and imaginary parts of the normalized slot admittance as functions of the slot lengths, for 3 different offsets 6 mm, 10 mm and 14 mm and for constant slot width of 6 mm are presented. Opposite to the previous case of the insensitivity of *y* on *w*, the slot length *l* affects both, *g* and *b*, and represents a very important parameter in the design process of slotted waveguide antennas. The highest normalized conductances are for the shortest slot at all 3 displacements, and the difference Δg for different slot lengths rises with higher offsets ($\Delta g_{max} = 0.05$ for *d* = 14 mm). However, the largest difference of the *b* values, $\Delta b_{max} = 0.08$, is for the smallest offset *d* = 6 mm. This is an effect of the strong influence of the slot length on the slot resonant behavior. From Tab. 3.3 it can be also seen that for the lower offset range, the slot length of 61 mm is closest to the resonance and for medium and higher slot offsets, this is the slot length of 59 mm.

	Offset 6 mm		Offset 10 mm		Offset 14 mm	
	g = Re(*y*)	*b* = Im(*y*)	*g* = Re(*y*)	*b* = Im(*y*)	*g* = Re(*y*)	*b* = Im(*y*)
w = 4 mm	0.03	0.007	0.1	-0.03	0.23	-0.06
w = 6 mm	0.03	0.005	0.1	-0.04	0.22	-0.08
w = 8 mm	0.03	-0.008	0.1	-0.04	0.21	-0.09

Table 3.2 Normalized slot admittance of longitudinal round ended slot for different slot widths

	Offset 6 mm		Offset 10 mm		Offset 14 mm	
	g = Re(y)	b = Im(y)	g = Re(y)	b = Im(y)	g = Re(y)	b = Im(y)
l = 59 mm	0.05	0.013	0.14	0.005	0.27	0.02
l = 61 mm	0.03	0.005	0.1	-0.04	0.22	-0.08
l = 63 mm	0.02	-0.01	0.06	0.06	0.14	-0.12

Table 3.3 Normalized slot admittance of longitudinal round ended slot for different slot lengths

The numerically obtained values for the normalized slot conductance g of conventional slots are compared with the theoretical results of Stevenson (equ. 3.20) and Oliner [39] in Fig. 3.19. It is shown that the well known Stevenson's formula gives correct results only for small slot displacements and even for medium offsets values it leads to errors. The results obtained using Oliner's calculations for rectangular 61 mm long slots (without 4 % length correction) are close to the FITD simulations results for the same slot type (black lines with points and small squares) only for offsets up to 12 mm. However, with 4% length correction the Oliner's formulas give results that are much closer to the numerically obtained

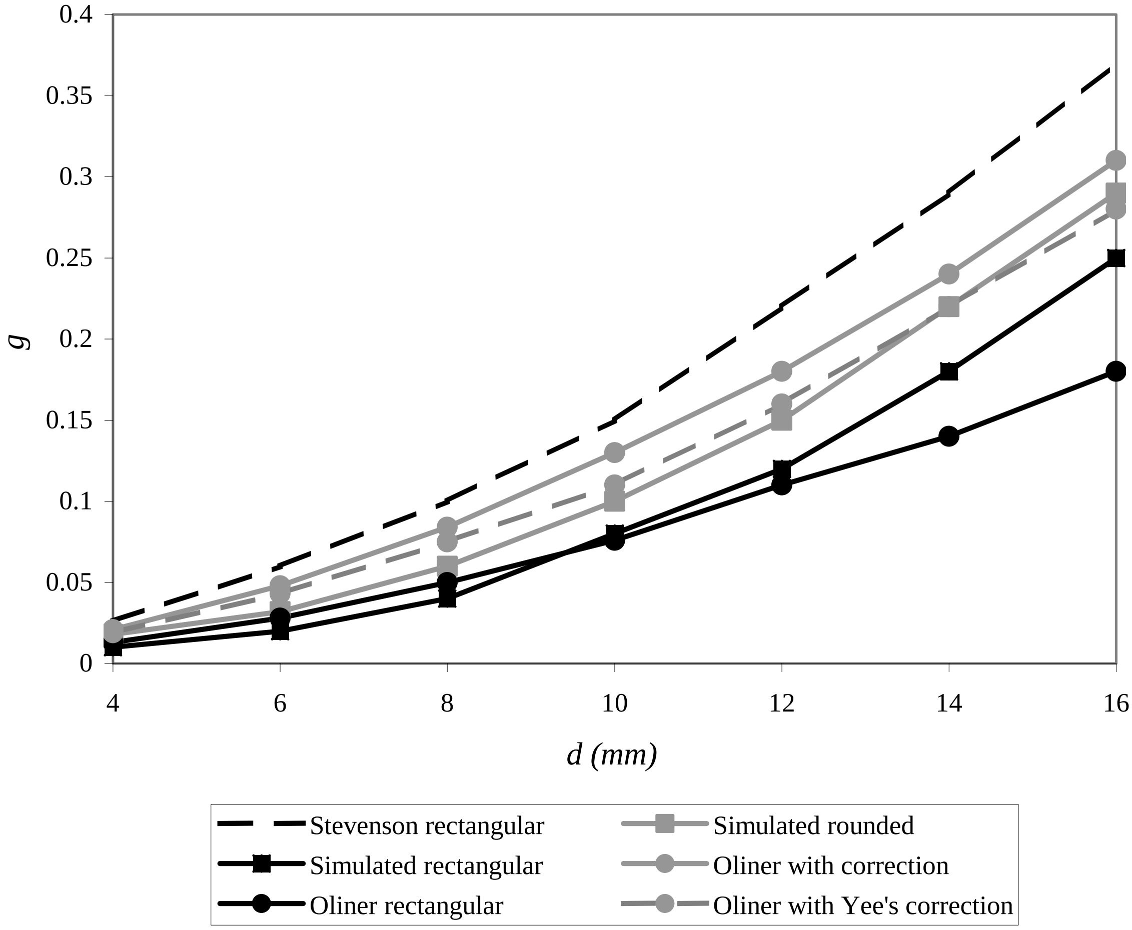

Figure 3.19 Comparison of calculated normalized conductances of slots

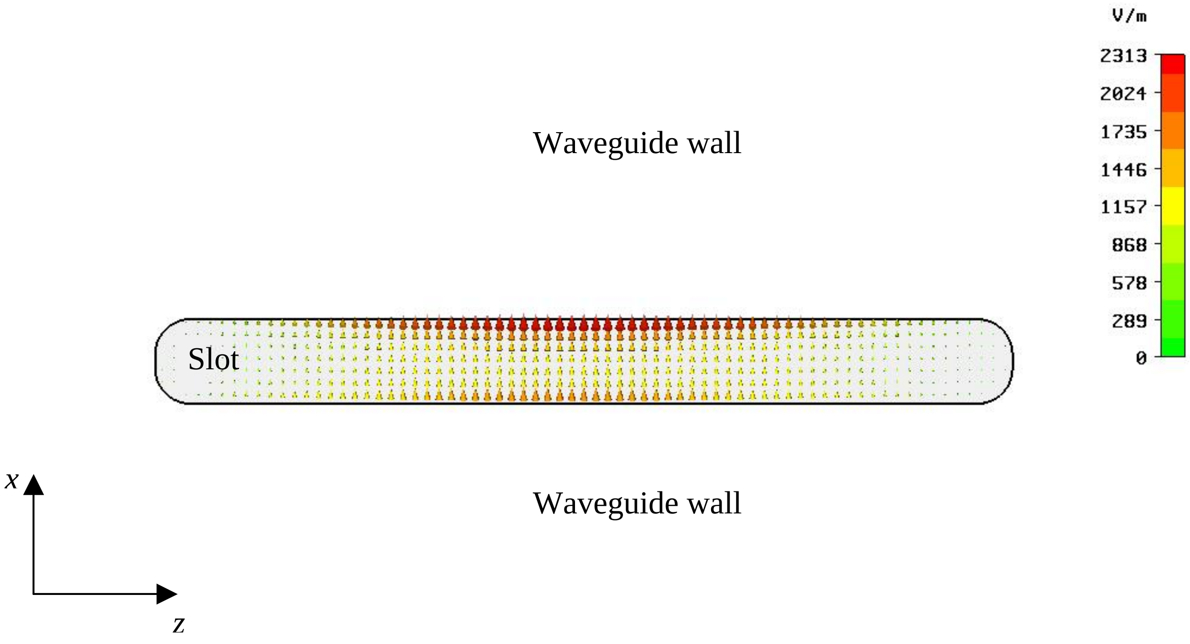

Figure 3.20 Electric field in the middle *xz* plane of a longitudinal slot with round ends

results for the round ended slots (grey lines with points and small squares). This is in agreement with Oliner's assumption that his theory has to be corrected for calculations of realistic round ended slots (sec. 3.2). Further, Yee's correction of Oliner's calculations (equ. 3.24) leads to results, which are in excellent agreement with the numerical simulations. Hence, the good agreement between the results of the numerical calculations performed with CST MWS and the results of Oliner's theoretical approach, confirmed that Oliner's formulas

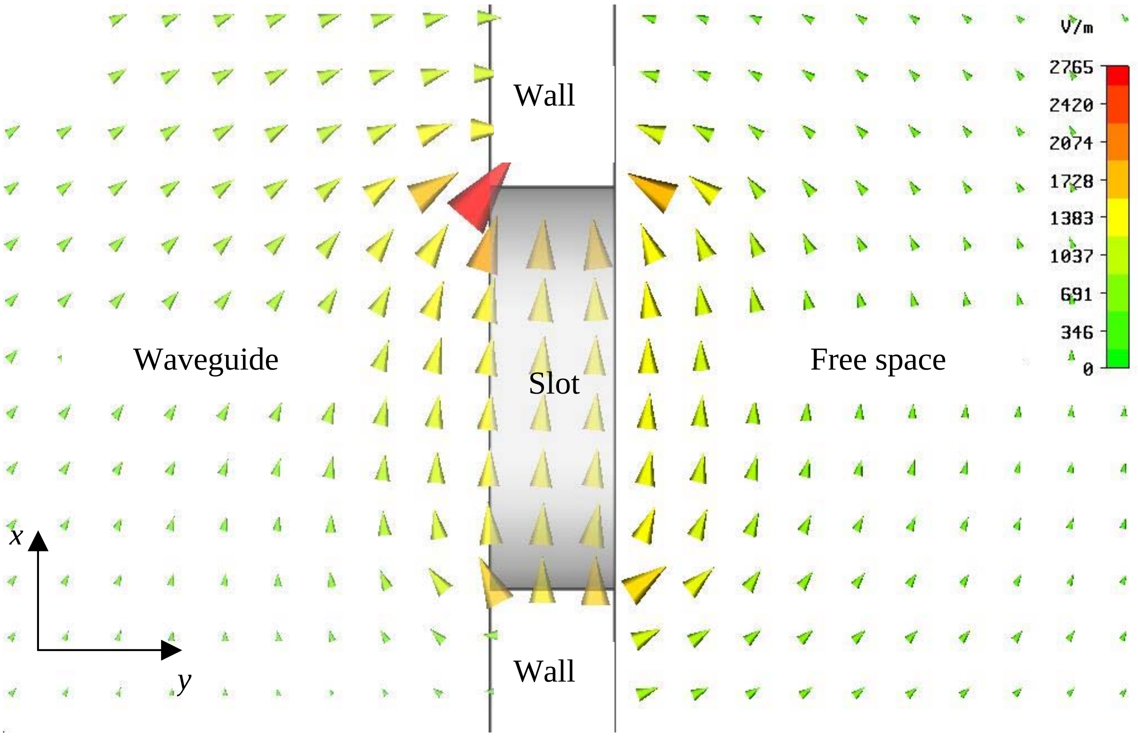

Figure 3.21 Electric field in the middle *xy* plane of a longitudinal slot with round ends

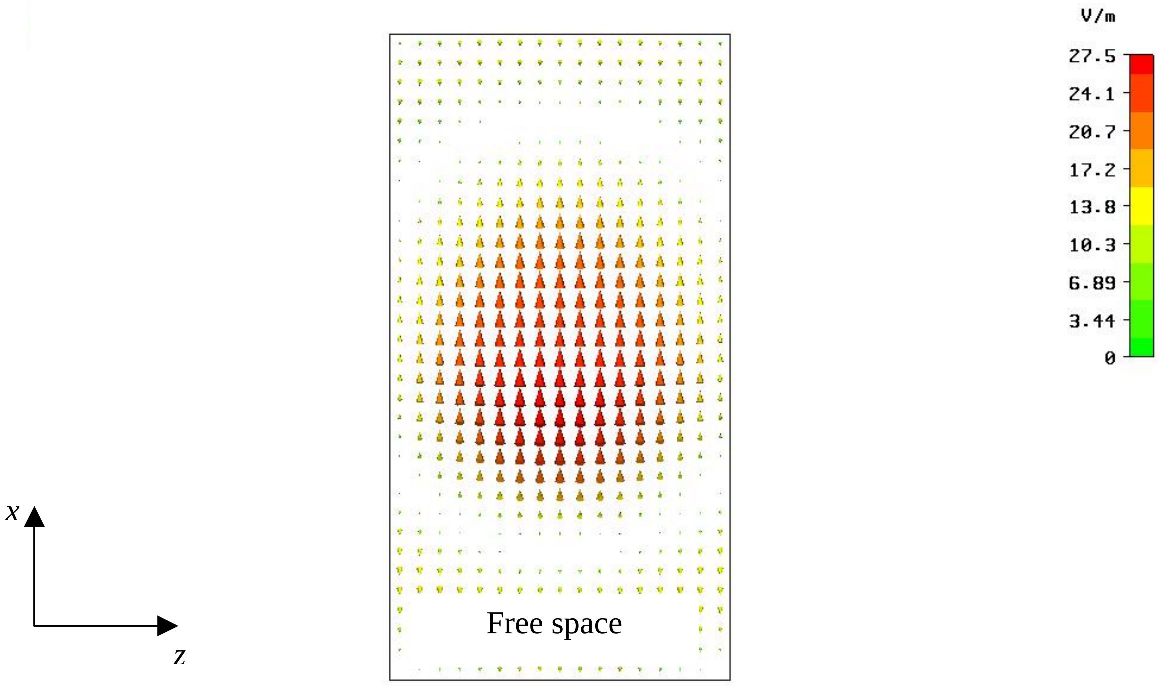

Figure 3.22 Radiated electric field in the *xz* plane at a distance of λ from the rounded longitudinal slot

with corrections are the better choice for slotted waveguide design than the Stevenson's one. In addition, this proves the idea to use full wave 3-D FITD simulations for the estimation of normalized slot impedances and admittances that are important slot parameters for the design of slotted waveguide feeding elements.

The numerically simulated electric field patterns for the conventional and new banana slot types are depicted in Figs. 3.21 – 3.26. As it has been given in literature [34,44], the electric field in the slot is perpendicular to the slot axis (parallel to the *x* axis, Fig. 3.20) and it is sinusoidally dependent on the longitudinal slot dimension *y*.

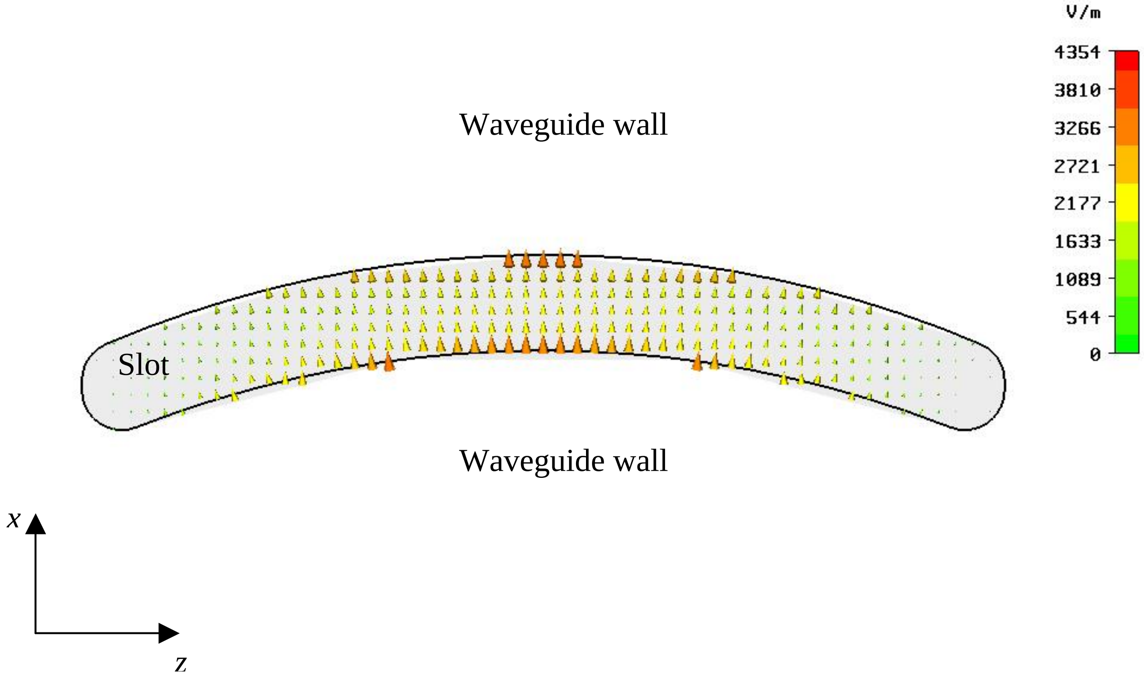

Figure 3.23 Electric field in the middle *xz* plane of the banana shaped slot with round ends

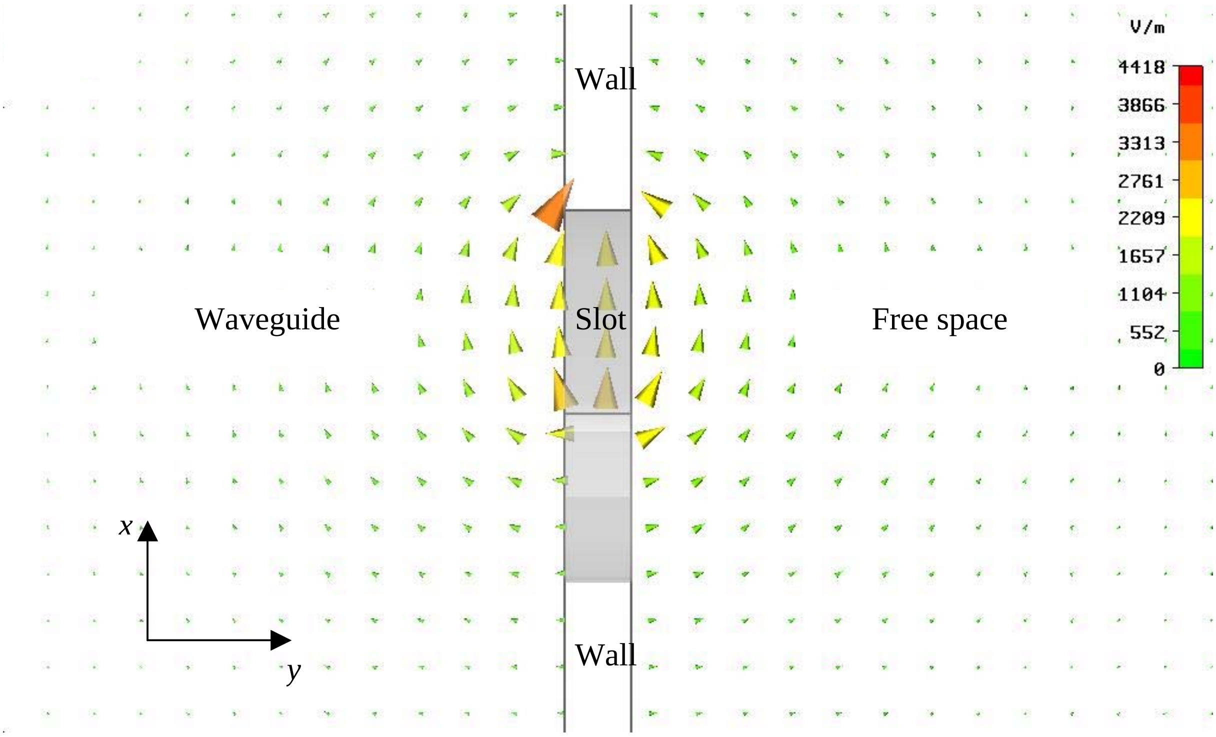

Figure 3.24 Electric field in the middle *xy* plane of the new banana shaped slot

However, the slot electric field is not constant along the *x* coordinate, even for the small slot width of 6 mm, and it has an asymmetrical distribution across the slot. This is due to the fact that the inner waveguide wall currents are dependent on the *x* dimension (Fig. 3.7) and the upper slot edge disturbs more the currents than the lower slot edge resulting in the slot E field pattern given in Fig. 3.20.

The transversal (to the slot axis) character of the slot electric field can be seen also in

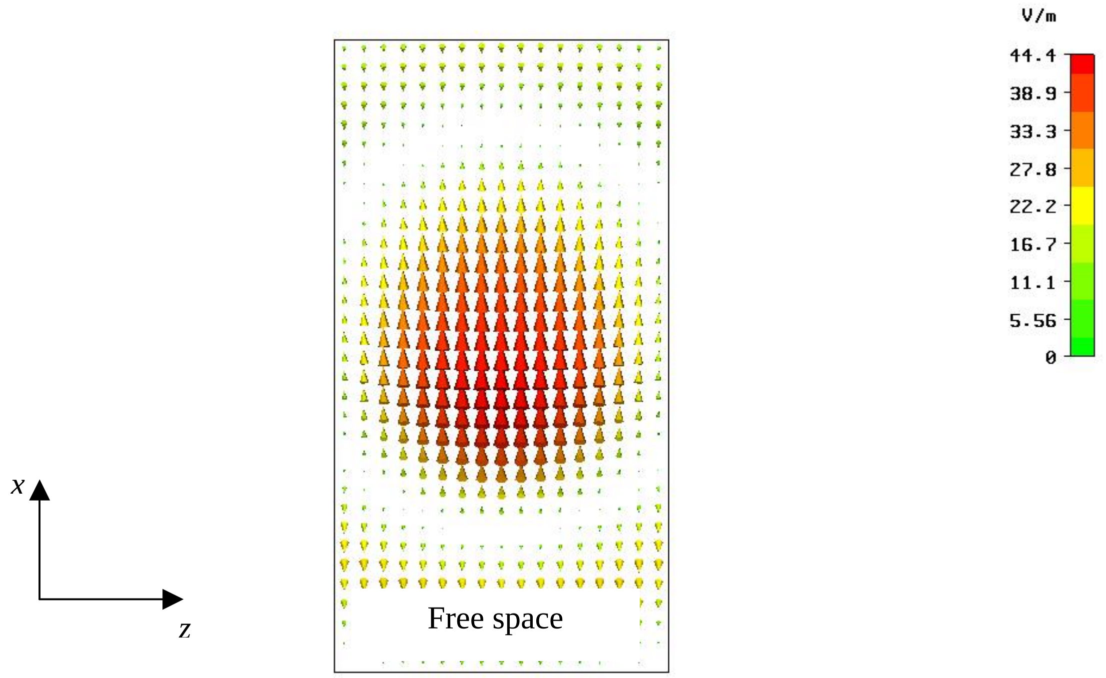

Figure 3.25 Radiated electric field in the *xz* plane at a distance of λ from the banana shaped slot

Fig. 3.21, for the middle *xy* plane of the slot. A stronger concentration of the E field is around the inner upper slot edge. This distribution of the E field in the slot cause a linear polarization of the radiated field that is orthogonal to the longer slot axis (Fig. 3.22). Hence, an array of identical slots in the waveguide wall acts as a linearly polarized antenna, with polarization perpendicular to the antenna axis [28,38].

For the new slot type, the electric field patterns in the slot and in the free space at a distance of λ from the slot are given in Figs. 3.23 – 3.25. The new type slot is at equal offset as the conventional one. The *E* field has also a maximum in the middle of the slot, but there are other smaller local maxima along the slot (*E* is not sinusoidally dependent on the *z* coordinate). This is because, the slot cuts the inner wall currents effectively not only in the slot center region, but also along the slot. Stronger interruption of the currents results in stronger radiation (field scales in Fig. 3.22 and Fig. 3.25). The polarization of the radiated field remains linear and transversal to the longer slot dimension, which makes this slot type applicable also for the design of a slotted waveguide antenna.

The results of the numerical inspection of centered transversal slots are given in the following. The calculated normalized slot resistances and normalized slot reactances for slots that are 4 mm wide are presented in Figs. 3.26 and 3.27. The resonant behavior of the slot length parameter can be seen near the 58 mm length in both figures. Undesirable very high values for the *r* near the resonance are due to the central position (zero displacement) of the slots in the waveguide wall. They disturb very strongly the inner waveguide wall current along the central line. Hence, the centered transversal slots with resonant length are not appropriate for the design of slotted waveguide EM radiators. Instead of them, shorter slots of this type with lengths between 32 mm and 52 mm, can be used for this application.

The variations of the normalized slot impedance *z* with the slot width, for 3 different slot lengths, are presented in Tab. 3.4. The slot width of the centered transversal slots influence both, the normalized slot resistance *r* and normalized slot reactance *x*, very strongly. Although *r* rises for wider slots, it is recommended to use narrower slots with *w* = 4mm, because of the lowest *x* values for these slots. Taking the wider slots (*w* = 6 mm and *w* = 8 mm), for which the normalized slot reactance values are higher, it would be more difficult to achieve the matching condition in the slot array design.

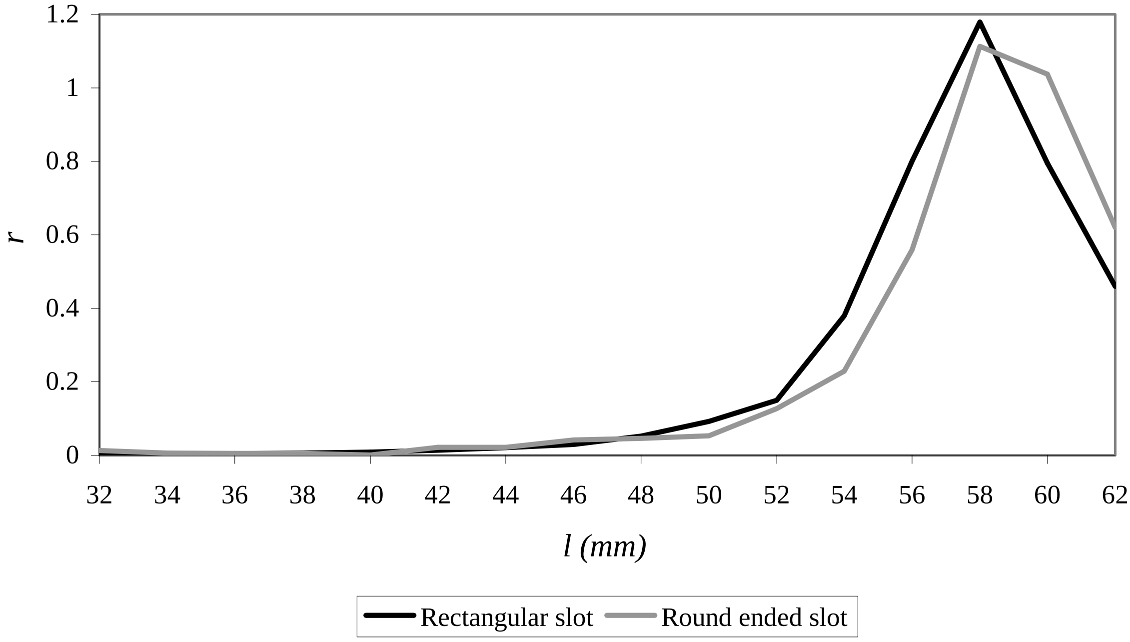

Figure 3.26 Normalized resistance of the transversal slots vs. slot offset at 2.45GHz

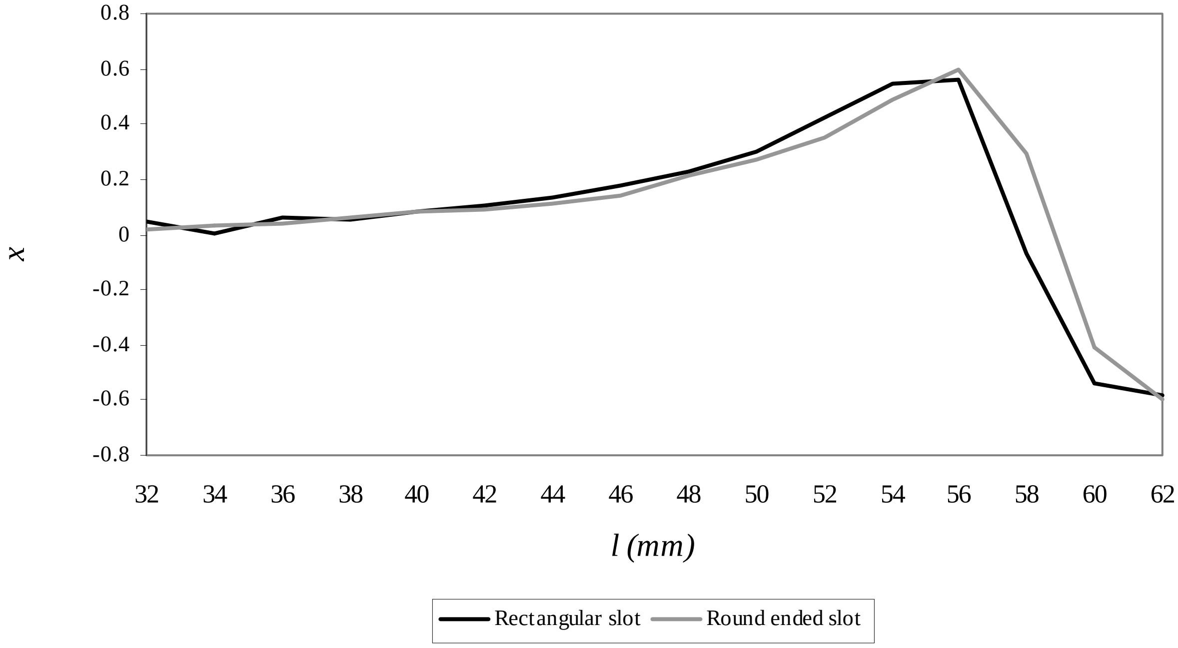

Figure 3.27 Normalized reactance of the transversal slots vs. slot offset at 2.45GHz

The electric field patterns for the case of the centered transversal slot with l = 50 mm and w = 4 mm are shown in figures 3.28 – 3.30. The E field is also orthogonal to the slot axis and has sinusoidal dependence on the x coordinate, which is obvious from Figs. 3.28 and 2.29. Contrary to the longitudinal slot case, the electric field in the centered transversal slot is almost constant over z coordinate. This slot field distribution causes a polarization of the radiation field that is parallel to the waveguide axis (z direction, Fig. 3.30).

	Length 44 mm		Length 50 mm		Offset 54 mm	
	r = Re(z)	x = Im(z)	r = Re(z)	x = Im(z)	r = Re(z)	x = Im(z)
w = 4 mm	0.022	0.11	0.053	0.27	0.23	0.49
w = 6 mm	0.033	0.16	0.11	0.36	0.45	0.59
w = 8 mm	0.044	0.21	0.17	0.45	0.65	0.61

Table 3.4 Normalized slot impedance of centered transversal slot for different slot widths

3.3.6 Appropriate slot types for the design of slotted waveguide feeding elements

The requirements for the slot properties that are appropriate for the design of slotted waveguide feeding elements, are summarized as follows:

- the slots should have a normalized slot resistance or normalized slot conductance in the broad range of 0.01 to 0.4;

- the slots should have very low values of the normalized slot reactive components (reactance and susceptance);

- the electric field in the slot should cause a linear polarization of the radiated field and

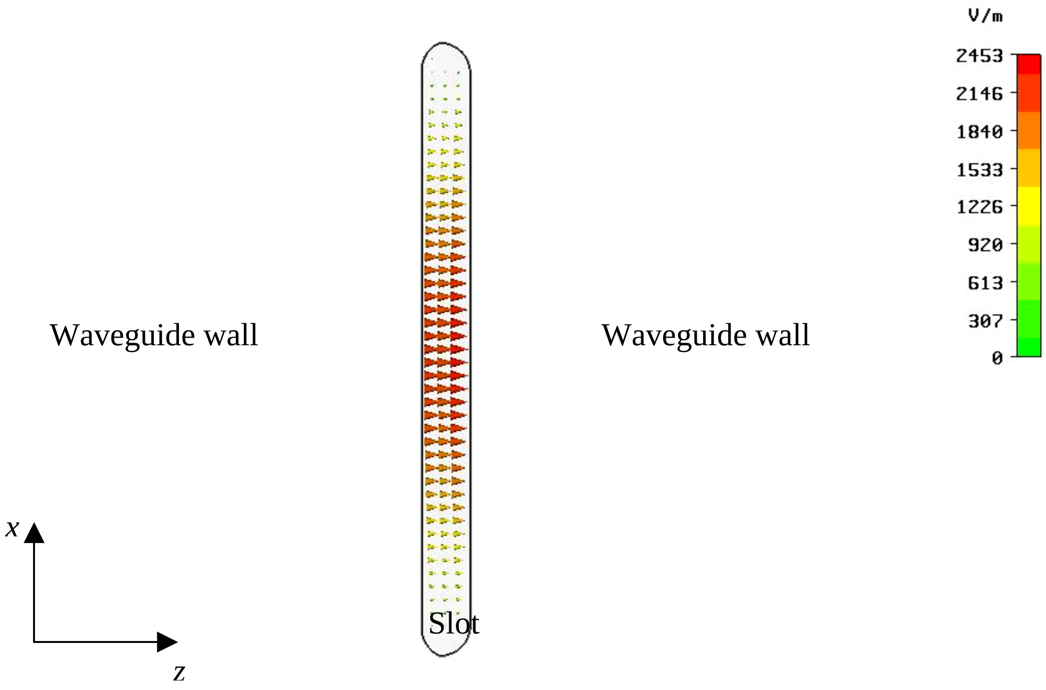

Figure 3.28 Electric field in the middle *xz* plane of the transversal slot with round ends

- easy manufacturing and low fabrication costs.

Hence, using the above requirements, the round ended longitudinal slot in the broad waveguide wall with l = 61 mm, w = 6 mm and different slot offset has been selected for the slotted waveguide antenna with a polarization, which is perpendicular to the waveguide axis. For the slotted waveguide radiator with a polarization that is parallel to the waveguide axis, the 4 mm wide centered transversal slots with l in the range of 32 mm – 52 mm have been chosen for this application.

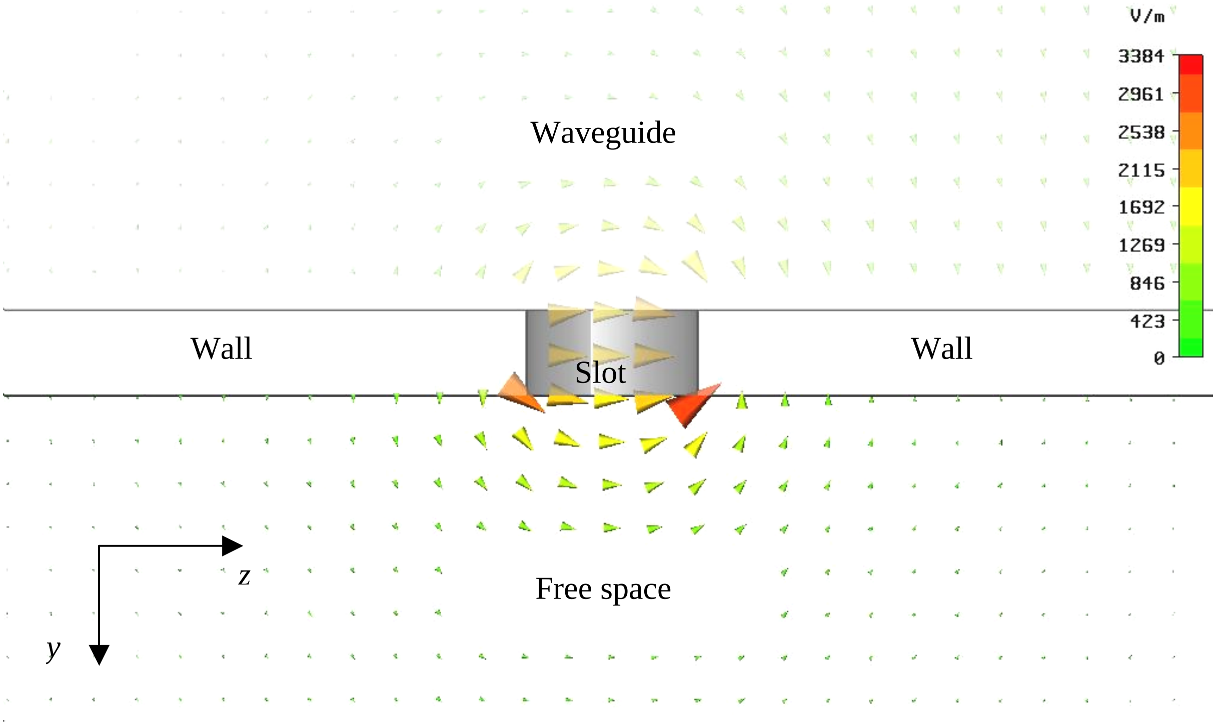

Figure 3.29 Electric field in the middle *yz* plane of the transversal slot with round ends

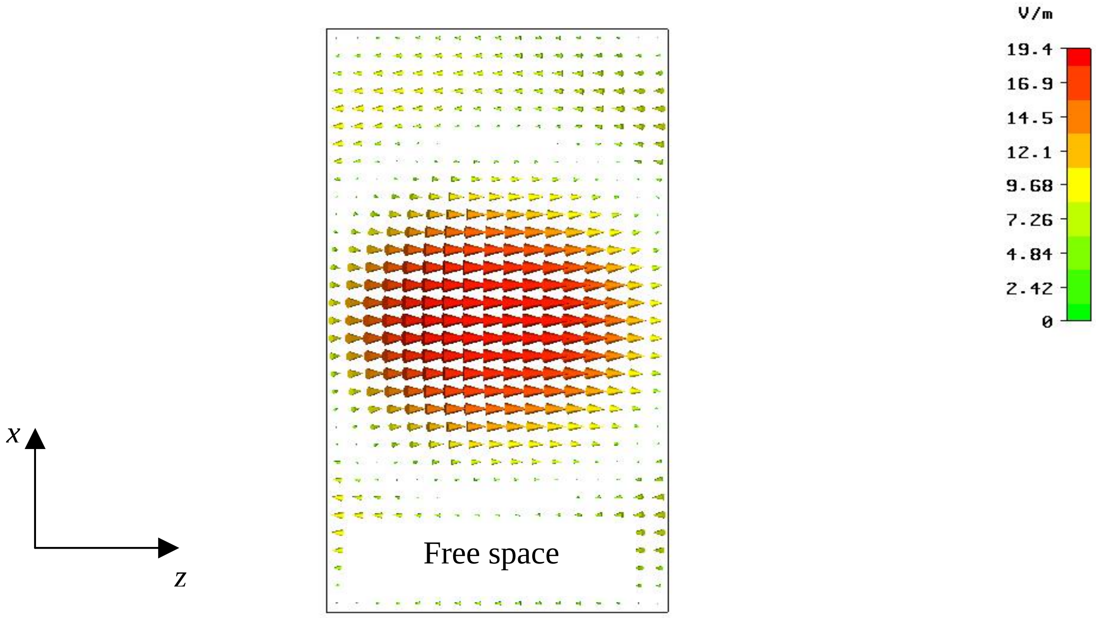

Figure 3.30 Radiated electric field in the *xz* plane at a distance of λ from the transversal slot

4. SLOTTED WAVEGUIDE MW POWER FEEDING SYSTEMS

In this chapter slotted waveguide EM energy feeding systems for microwave applicators are described. At first the parameters and characteristics of two different types of slotted waveguide antennas are given. Further, the resonant or standing wave slotted waveguides and the conventional procedures for their design are shortly explained and analyzed in the second subsection of the chapter. Finally, the nonresonant or traveling wave slotted waveguides, a novel design procedure for them and numerical investigations on this topic are presented in more details in the last subsection of the chapter.

4.1 Slotted Waveguide Antennas

4.1.1 Parameters and types of slotted waveguides

In the previous chapter slots in the waveguide walls have been presented as basic EM energy radiators. Using a number of the same type of slots in the waveguide wall an antenna array can be made that is advantageous over just one slot radiator. That means, the radiation characteristics of the elementary antenna slot in a slotted waveguide array can be combined and estimated to achieve stronger EM radiation with an improved EM field distribution in the radiation zone, than in the single slot case. The slotted waveguide array can be linear, which presents an one dimensional array, or it can be a planar slotted waveguide array that is two dimensional with more slotted waveguides coupled and grouped side-by-side. Planar slotted waveguide antennas found broad applications in the field of telecommunications (satellite communications), in which their simplicity of mounting and their high directivity are advantageous over other antennas. However, in this work, the research is focused on linear, one dimensional slotted waveguide arrays. They are more appropriate for directly fed high power feeding element applications, especially for the present hexagonal applicators with multiple feeding system. Additionally, they are more flexible and simpler for the design than the planar slotted waveguide arrays.

There are two basic goals in the design of slotted waveguide array antennas: first, to achieve a desired radiation pattern and second, to realize a maximum radiation of the available microwave power from the microwave source into the applicator. The main slot array parameters that can be used to get the above design aims are the slot position parameters, such as the distance between the centers of the neighboring slots D, as well as the distance between the last slot center and the waveguide shorted end that is here denoted by D_s. The slot geometry parameters which determine the amount of radiation from each slot (like the slot offset d or the slot length l) are also crucial for the SW feed design.

The distance between the neighboring slots D is a very important parameter, because it defines the phase difference between the EM fields in the slots, which affects the entire radiation characteristics of the antenna. The distance from the last slot to the waveguide end D_s also sets the phase of the slot fields. Hence, using appropriate values for the parameters D and D_s, the slots can be placed at certain positions giving zero phase difference of the slot fields or they can be equispaced but having a non zero phase difference of the fields along the slots.

These two different cases of the principle slot positioning along the waveguide give the reason to distinguish two basic slotted waveguide types – a resonating or standing wave slotted waveguide and a nonresonating or traveling wave slotted waveguide.

For the case of the resonating horizontally polarized slotted waveguide (Fig. 4.1 a) with centred transversal slots in the broad wall, the distances D and D_s are equal to the lengths of the λ_g and $\lambda_g/2$ respectively. This resonant distribution of the centred transversal slots is defined by the fact that the standing wave in the waveguide causes also the standing wave character of the inner waveguide wall currents patterns. Hence, the slots are positioned at those places, where the maxima of the z axis parallel standing wave currents are. The slot fields are in phase ($\Delta\varphi = k_z D = \frac{2\pi}{\lambda_g}\lambda_g = 2\pi$).

For a waveguide with longitudinal slots in the broad wall (Fig. 4.1 b), which are mutually at the opposite sides to the central line giving an additional phase shift of π in the neighboring slot fields, the resonating mutual slot distances are $D = \lambda_g/2$ and $D_s = \lambda_g/4$ [56,57]. This is the case of the standing wave slotted waveguide antenna with vertical polarization and the slots are positioned at the places of the maxima of the standing wave currents that are parallel to the x axis (orthogonal to the longitudinal slots). The equiphased radiation from the slots is obvious ($\Delta\varphi = k_z D + \pi = \frac{2\pi}{\lambda_g}\frac{\lambda_g}{2} + \pi = 2\pi$).

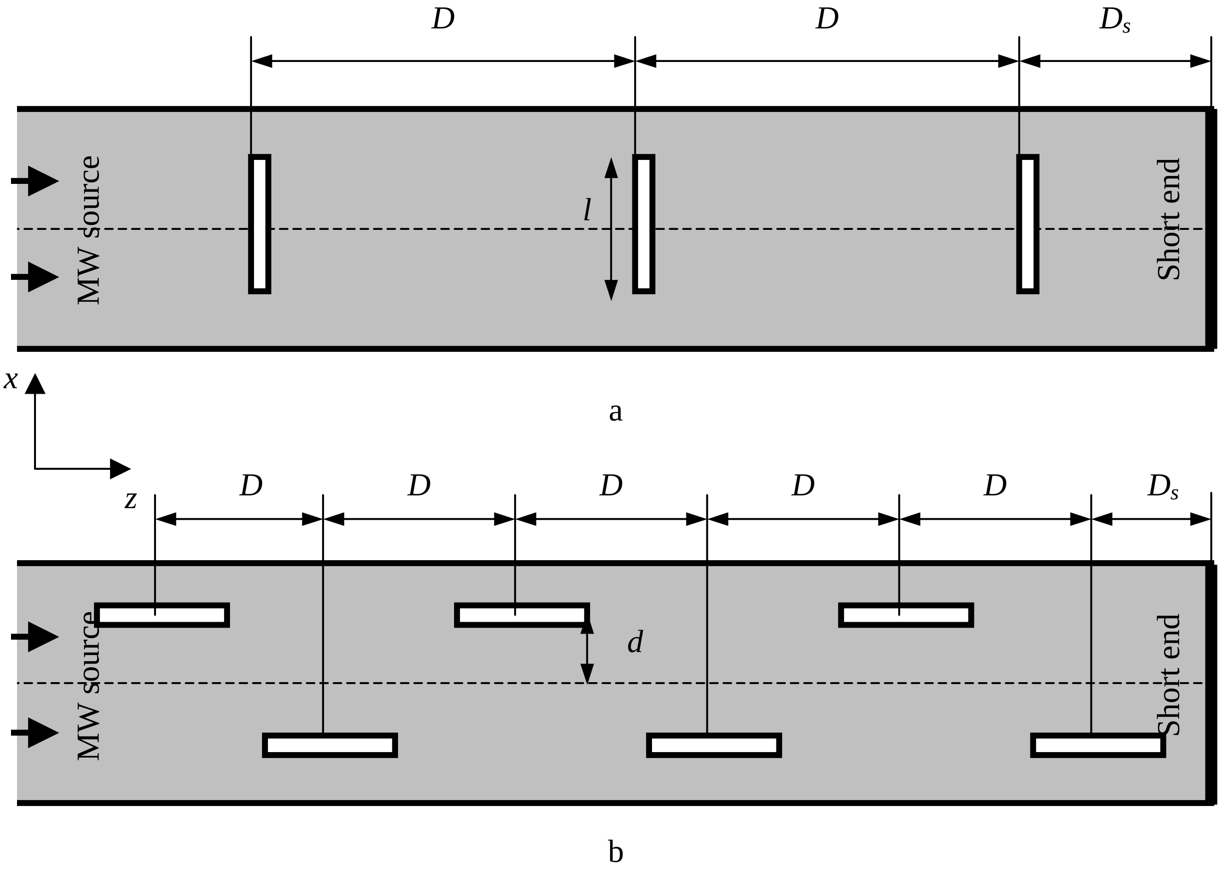

Figure 4.1 Slotted waveguide parameters for a) horizontally polarized and for b) vertically polarized slotted waveguides

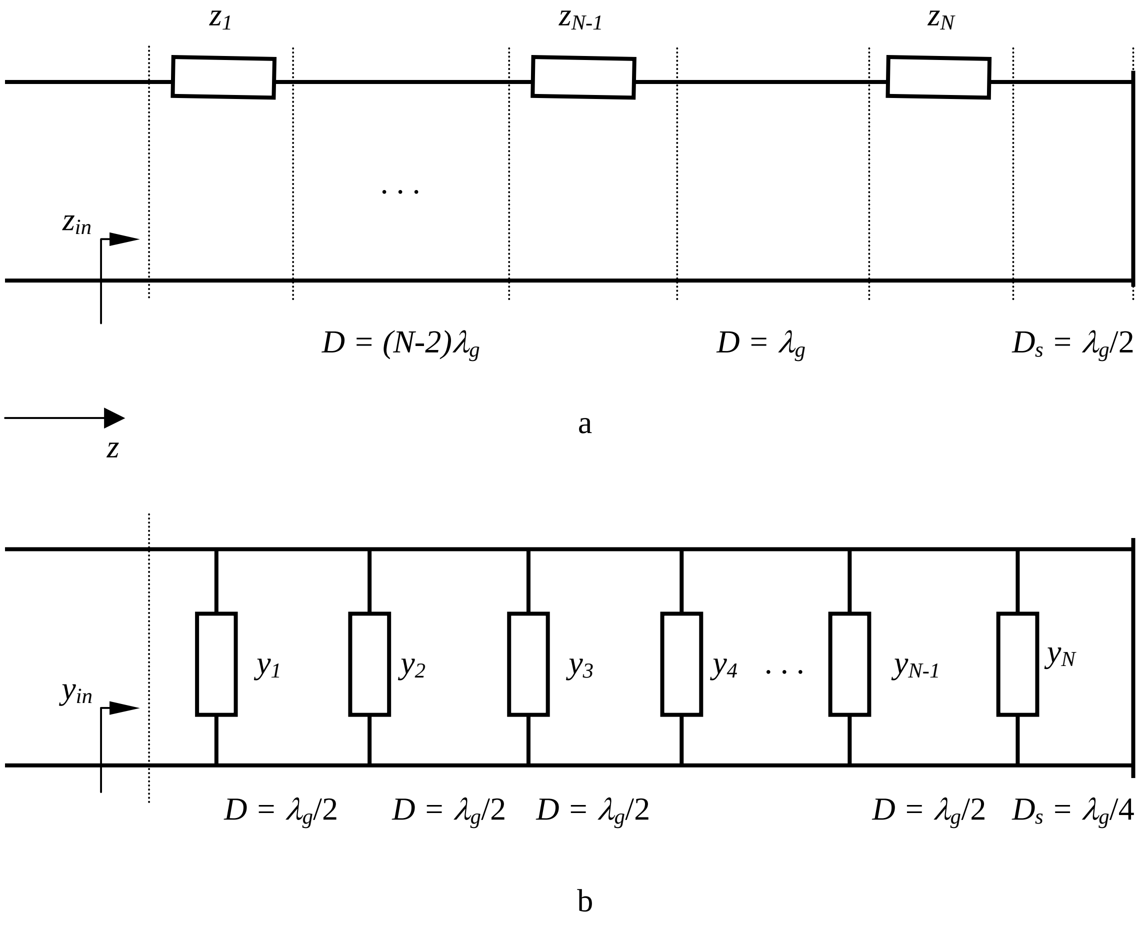

Figure 4.2 Equivalent transmission line circuit of a) horizontally polarized and b) vertically polarized resonant slotted waveguides

The transmission line representations of the standing wave slotted waveguides are shown in Fig. 4.2. It should be noticed that in the transmission line slotted waveguide simulations there are less parameters to be considered in the design process than in the waveguide theory approach. The slot length and slot offset parameters are already included in the normalized slot impedances and admittances and except for the distance between the slot centers, these are the only parameters that govern the behavior of a SW antenna. Hence, the transmission line theory is very useful in calculations of the input normalized impedance or admittance, which determine the reflections at the input of the slotted waveguide (equ. 2.95).

4.1.2 Matching conditions

For an estimation of z_{in} one can use the equation 2.94, which for $l = D = \lambda_g$ gives the following:

(4.1)
$$\tan(\beta l) = \tan(\frac{2\pi}{\lambda_g}\lambda_g) = 0 \text{ and}$$

(4.2)
$$z_{in} = \sum_{n=1}^{N} z_n + z_s ,$$

where z_n is the normalized slot impedance of the n-th slot and z_s is the normalized impedance of the shorted waveguide section, which is seen from the last slot (length of the shorted section equals the distance $D_s = \lambda_g/2$). Using equ. 2.88 it is easy to find that $z_s = 0$ and equ. 4.2 gives that the normalized input impedance is the sum of the normalized slots impedances z_n for $n = 1..N$ only, i.e. $z_{in} = \sum_{n=1}^{N} z_n$.

The relation $y_{in} = \frac{1}{z_{in}}$ and the same equation 2.94 for z_{in} can be used to calculate the y_{in} of a resonating slotted waveguide with longitudinal slots (figures 4.1 b and 4.2 b). The product βl is equal to 2π also in this case, giving a zero value for $\tan(\beta l)$:

(4.3)
$$\tan(\beta l) = \tan(\frac{2\pi}{\lambda_g}\frac{\lambda_g}{2} + \pi) = 0 ,$$

because of the fact that $D = \lambda_g/2$ and neighbouring slots are at opposite sides of the central line. This leads to the following simple formula for the normalized input standing wave slotted waveguide admittance:

(4.4)
$$y_{in} = \sum_{n=1}^{N} y_n + y_s$$

and similar as in the previous case, y_n is the normalized slot admittance of the n-th slot and y_s is the normalized admittance of the shorted waveguide section, calculated at the distance D_s from the short. Setting $D_s = \lambda_g/4$ and using again equ. 2.88 it is obvious that $z_s = \infty$ and $y_s = \frac{1}{z_s} = 0$. So, the equ. 4.4 is reduced to the simple relation [35]:

(4.5)
$$y_{in} = \sum_{n=1}^{N} y_n .$$

The derived relations for the normalized input slot impedance and admittance can be now used for a computation of the reflections from the slotted waveguide at the input port (see the equ. 2.95). Additionally, the matching conditions for zero reflections can be defined in the following forms:

(4.6)
$$\sum_{n=1}^{N} z_n = 1 \text{ and}$$

(4.7)
$$\sum_{n=1}^{N} y_n = 1 .$$

In the case of the nonresonating slotted waveguides the distances between the neighboring slots and between the last slot and waveguide short end do not equal the resonant lengths that are defined above (Fig. 4.3). In nonresonating slotted waveguides the phase difference between the neighboring slots EM fields is not 2π, i.e. the slots radiate with some phase shift that is constant for a constant D. This type of slotted waveguide is more general than the resonant one and it gives greater flexibility in the design procedure, especially in an

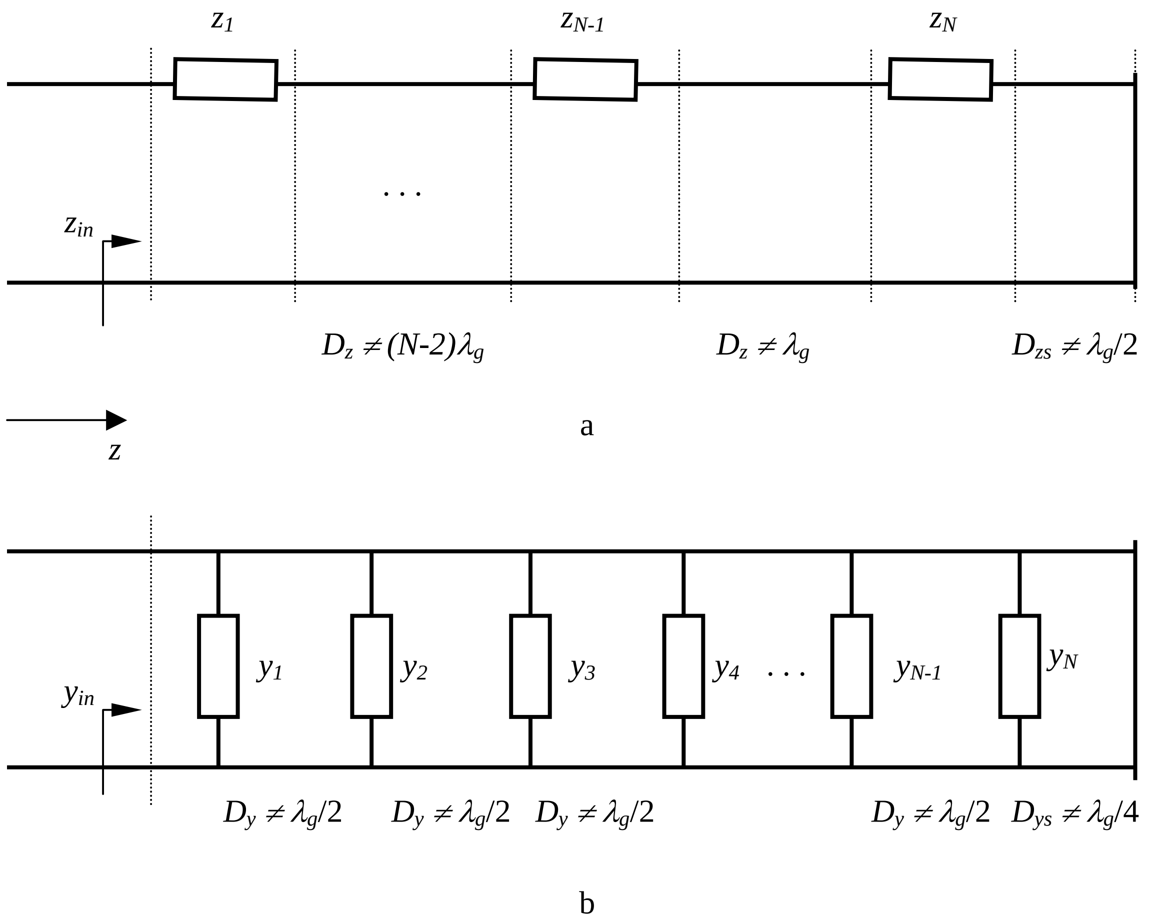

Figure 4.3 Equivalent transmission line circuit of a) horizontally polarized and b) vertically polarized nonresonant slotted waveguides

estimation of the number of slots in the waveguide wall and the distance between them. So, the distance D can be used for the realization of the appropriate phase shift that gives the desired radiation characteristics of the slotted waveguide antenna according the specific application (see equ. 3.12).

Further, if there are no reflections from the waveguide end, or there are only weak reflected waves, then only a direct wave travels along the waveguide, which is an example of the so called traveling wave antenna.

The transmission line circuits for the nonresonant slotted waveguide are presented in Fig. 4.3. Because of the nonresonant lengths of the transmission line sections between the slots, the factor $\tan(\beta l)$ is not zero and it must be taken into account using the relation 2.94. Hence, instead of the above equations 4.6 and 4.7, the relations for the matching conditions are calculated using the following formulas:

(4.8) $$z_{n,in} = \frac{z_{n+1,in} + j\tan(\beta D_z)}{1 + jz_{n+1,in}\tan(\beta D_z)}$$ and

(4.9) $$y_{n,in} = \frac{y_{n+1,in} + j\tan(\beta D_y)}{1 + jy_{n+1,in}\tan(\beta D_y)},$$

where n = 1,..,N-1, $z_{N,in} = z_N + z_s$ and $y_{N,in} = y_N + y_s$, which results in:

(4.10)
$$z_{in} = \frac{z_{1,in} + j\tan(\beta D_z)}{1 + jz_{1,in}\tan(\beta D_z)} = 1 \text{ and}$$

(4.11)
$$y_{in} = \frac{y_{1,in} + j\tan(\beta D_y)}{1 + jy_{1,in}\tan(\beta D_y)} = 1.$$

As it has been mentioned already, the distances D_z, D_y, D_{zs} and D_{ys} can now be chosen according the application requirements and are not predefined parameters. They can be used in optimization processes for antenna matching and for realization of a desired radiation pattern.

4.1.3 Slotted waveguide array factor

The slots in the waveguide wall are excited by a traveling fundamental mode wave in the waveguide [36]. Because of that, the slot array radiation must also depend on the characteristics of this waveguide fundamental mode. This can be implemented in the calculation of the slotted waveguide array factor (equ. 3.13) by defining an additional term that contains the information of the fundamental waveguide mode, such as the product βD. So, the array factor can now be described by:

(4.12)
$$F_a(\theta) = \left| \sum_{n=1}^{N} a_n e^{j[(n-1)kD\cos\theta + \beta D + \Delta\varphi]} \right|^2,$$

where a_n, k and θ are the same values as in the relation 3.12.

4.2 Resonant Slotted Waveguides

In order to explain the need for a new design technique for the SW feeding elements, this section is focused on the analysis of conventional designs for vertically and horizontally polarized antennas, highlighting the difficulties of this standing wave SW approach.

4.2.1 Analysis of the standard design procedure for vertically polarized SWs

The first step in the design of slot arrays is to determine the excitation amplitudes a_n of the individual slots to achieve the required antenna performance. That means, the calculation of values for a_n are governed by the input matching condition (equ. 4.7) and a desired radiation pattern (equ. 4.12). The average radiated power from the n-th slot is proportional to the square of the excitation slot amplitude a_n. For vertically polarized slotted waveguides it can be given by:

$$p_n = \Re(V^2 y_n) = V^2 g_n \propto a_n^2 , \tag{4.13}$$

where V is the peak voltage across the equivalent circuit from Fig. 4.2. Hence, the excitation amplitudes a_n are proportional to $\sqrt{g_n}$, which can be stated as [35]:

$$g_n = C a_n^2 , \tag{4.14}$$

where C is a constant that has to be determined. Using the last relation, the input matching condition 4.7 becomes:

$$C \sum_{n=1}^{N} a_n^2 = 1 . \tag{4.15}$$

After finding the excitation amplitudes according to relation 4.12, the normalized slot conductance parameters g_n are finally calculated by 4.14. Further, the proper slot offsets from the central longitudinal line d_n can be estimated using one of the curves g_n vs. d_n from Fig. 3.19. In standard design procedures for standing wave slotted waveguides that can be found in many antenna textbooks [28,35,38,53], Stevenson's relation is chosen for calculation of d_n from given g_n. However, the experimentally and numerically proved inaccuracy of Stevenson's formula leads to nonsatisfactory results of the design. Because of that, here it is recommended to use numerical calculations or to perform experiments to determine the proper g_n vs. d_n curves. This can be shown using the following examples of resonant slotted waveguide design.

The parameters of conventional longitudinal round ended slots should be calculated for a nearly 1m long resonant slotted waveguide energy feeding element with vertical polarization. The resonant distances between the slots in this case are defined by $D = \lambda_g/2 \approx 0.087$ mm and $D_s = \lambda_g/4 \approx 0.043$ mm. The maximum number of slots, which can be used along the waveguide, is determined by D and D_s and it is $N = 10$ for the 1 m long waveguide section. Exactly, the length of the waveguide L is estimated to be the resonant one with $L = 5\frac{\lambda_g}{2} = 0.958\,\text{m}$. Assuming a constant value for the excitation amplitude $a_n = \frac{1}{\sqrt{N}} = 0.316$, the needed values for the $g_n = 0.1$ can be found by equations 4.14. and

4.15. That presents the simplest case of equal average power radiation from the slots along the waveguide. Now, using the curves from Fig. 3.19, the slot offset parameters are estimated to be d_n = 8 mm and d_n = 10 mm, for the cases of Stevenson's formula and CST MWS numerically obtained results respectively. The offset d_n = 8 mm gives in Stevenson's formula 3.20 the normalized slot conductance g_n = 0.1001 and zero normalized slot susceptance, which according the equations 4.5 and 2.95 results in y_{in} = 1.001 and in almost zero reflection $|S_{11}|$ = 0.0005 (-66 dB) at the input port. However, the same offset of 8 mm in numerical simulations gives the value of $y_n = 0.065 - j0.042$ that determines the input normalized admittance $y_{in} = 0.65 - j0.42$ and the reflection $|S_{11}|$ = 0.233 (-12.7 dB), using the same analytical relations 4.5 and 2.95. This discrepancy in the obtained results for the reflections of the slots with same offset is due to the error that Stevenson's relation produces. Additionally, the performed numerical simulations and the corrected Oliner formula (Fig. 3.19) suggest to use slots with 10 mm offset, because their normalized slot admittance is $y_{in} = 0.1065 - j0.065$ giving for the reflection $|S_{11}|$ = 0.196 (-14.2 dB).

To prove that, the numerical models for both cases have been made and the simulations of the S_{11} parameter (reflection) in the 0.958 m long slotted waveguide have been performed using the MWS software (Fig. 4.4). Indeed, the obtained results have shown that for the case of d_n = 10 mm the calculated $|S_{11}|$ parameter was –1 dB lower than for d_n = 8 mm (Fig. 4.5). This proves that the simulated g_n vs. d_n curve is more accurate than Stevenson's relations and they are the right choice for a slotted waveguide design, giving the better matching and lower reflections into the slotted waveguide.

But these reflections levels are still not satisfying the design requirement of $|S_{11}| < 0.1$. This is due to the fact that the imaginary part of the normalized slot admittance b_n is not zero in both cases. Hence, the matching condition 4.7 cannot be fulfilled without a compensation of the non zero slot susceptances. In order to compensate the b_{in}, only the slot lengths could be varied to achieve the resonant slot length (and to decrease b_n), because the distance between the last slot and the short is a constant that is set to $\lambda_g/4$ and it cannot be changed to

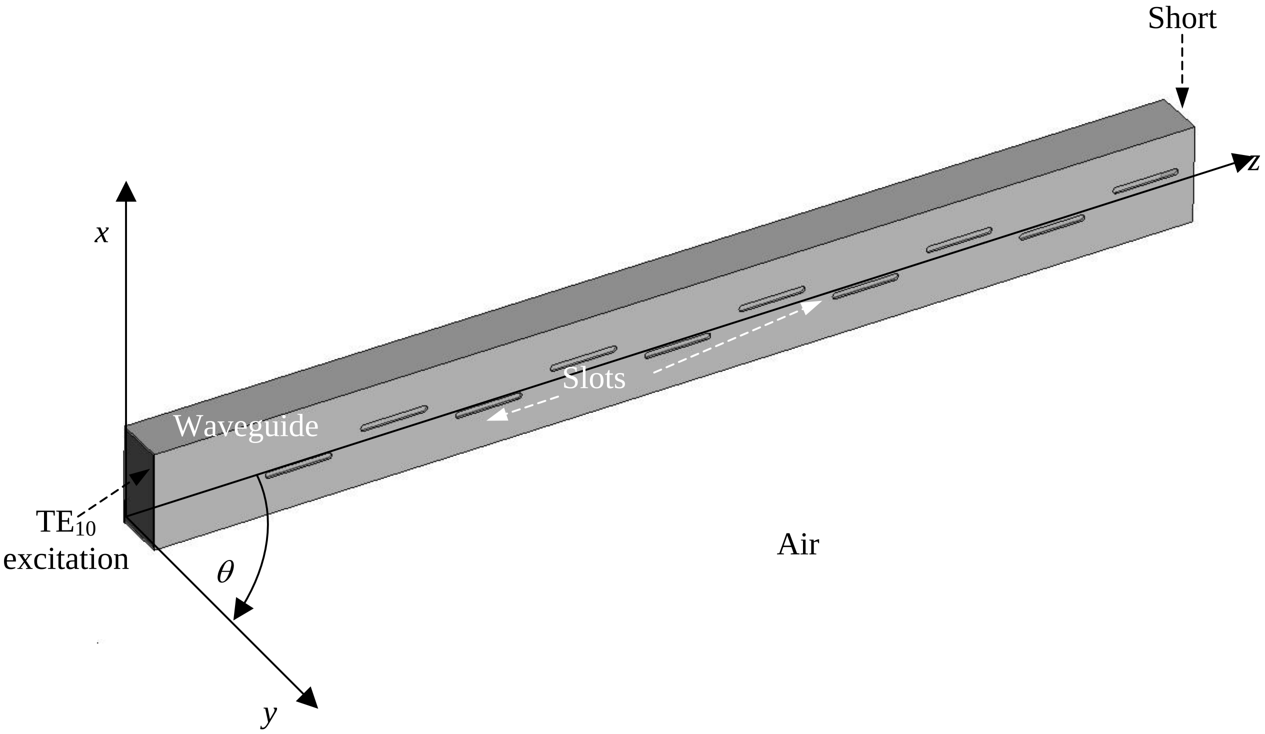

Figure 4.4 Slotted waveguide model for numerical calculations of the reflections and the radiation characteristics

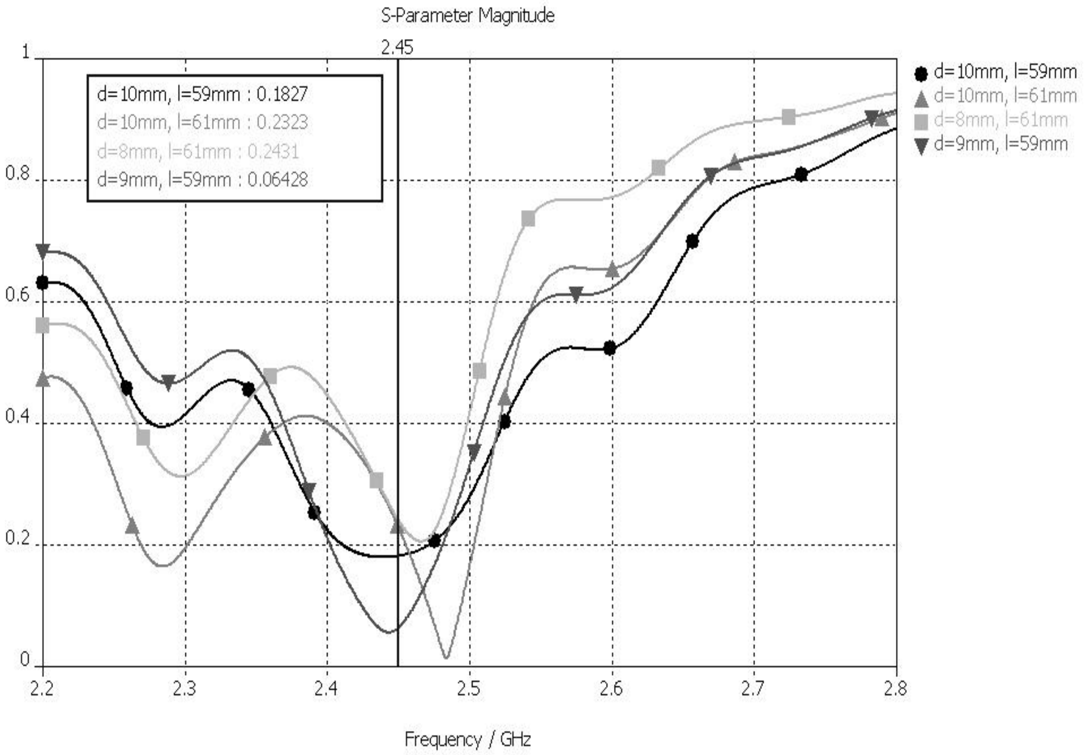

Figure 4.5 Numerically calculated $|S_{11}|$ for the vertically polarized resonant slotted waveguide examples with different slot parameters

realize the desired compensating susceptance $b_s = -b_{in}$. Shortening the slots from l = 61 mm to 59 mm for 10 mm displacement from the center line, the imaginary part of the normalized slot admittances are decreased to the value of $b_n = 0.005$, but at the same time, the real part of y_n is increased to 0.14 and the reflections remain at a level of –15 dB. Hence, the offset should

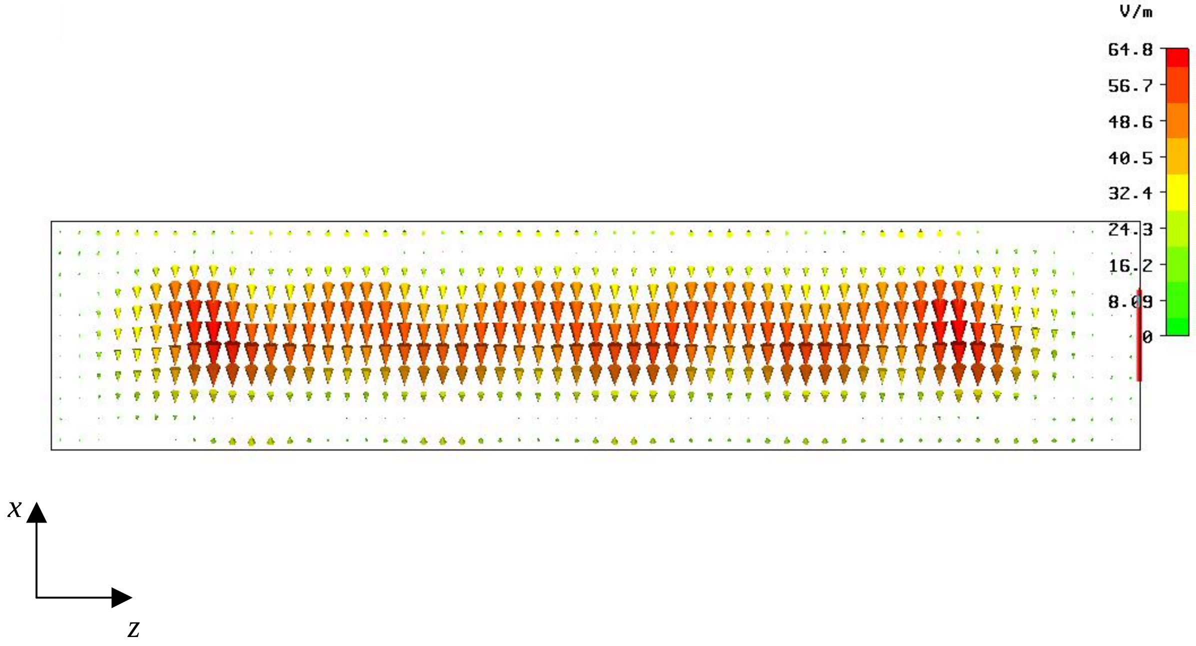

Figure 4.6 E field distribution pattern in the xz plane at a distance of λ from a longitudinal slot with 10 mm offset from the center line

be decreased to $d_n = 9$ mm (lower value $g_n = 0.11$) and the slot lengths should be shortened to the resonant length for this offset (almost zero susceptance, $b_n = 0.003$). Simulations of the waveguide with these slots prove the lower reflection level in the slotted waveguide, i.e. a level of –24 dB ($|S_{11}| = 0.064$) was numerically obtained at 2.45 GHz. All these results of the S_{11} parameter simulations are summarized in Fig. 4.5.

The near field radiation distributions of the vertically polarized standing wave slotted waveguides have been also numerically simulated. A typical pattern of the E field distribution in the *xz* (θ) plane at a distance of λ from the slotted waveguide wall in the free space is shown in Fig. 4.6. The vertical polarization of the radiated field is obvious. Additionally, a relatively homogeneous radiation in the near field region along the longitudinal *z* axis is observed. However, this slot distribution does not produce a desired constant radiation pattern in the θ plane at distances longer than 4λ, which will be presented in the following.

Using the equation 3.12, one can calculate the array factor using the following relation:

$$F_a(\theta) = \frac{1}{N} \cdot \left\{ \left[\sum_{n=1}^{N} \cos(\alpha_n \cos\theta) \right]^2 + \left[\sum_{n=1}^{N} \sin(\alpha_n \cos\theta) \right]^2 \right\}, \tag{4.16}$$

where $\alpha_n = (n-1)kD = (n-1)\pi \frac{\lambda_g}{\lambda}$ has been introduced for abreviation. The calculated function $F_a(\theta)$ for the θ range from 0 to 180° is presented in Fig. 4.7 and it is obvious that this a_n distribution results in a very sharp EM radiation pattern which is undesirable for energy feeding element applications. The similar narrow radiated field pattern is obtained also in the numerical simulation for the *yz* plane and $x = 0$ (Fig. 4.8).

Using the novel slots presented in the previous chapter, only the antenna input matching can be improved. The banana shaped slots with offsets of $d_n = 6$ mm have $y_n = 0.08 - j0.03$,

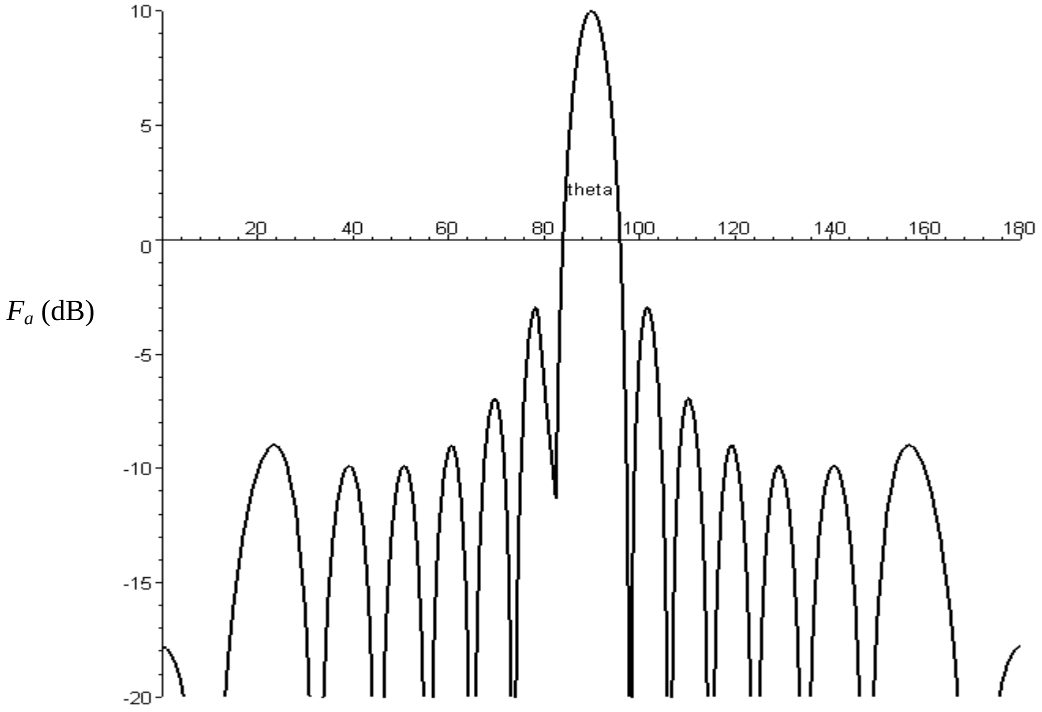

Figure 4.7 Calculated array factor for the vertically polarized resonant slotted waveguide example using relation 4.16

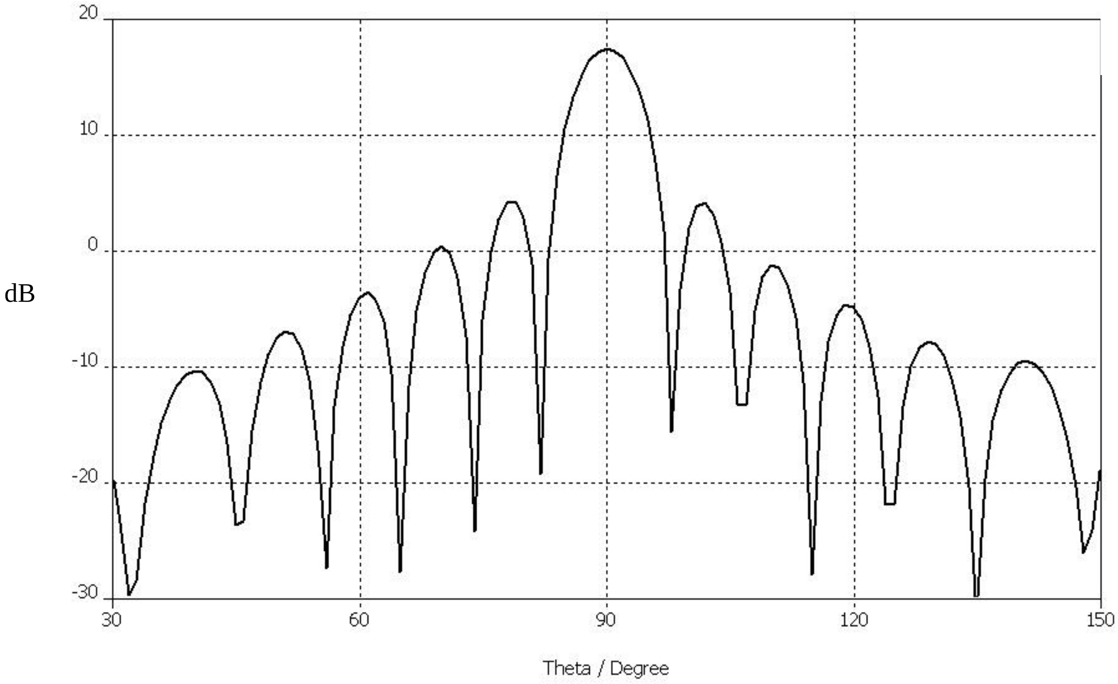

Figure 4.8 Numerically obtained radiation characteristics for the vertically polarized resonant SW array using MWS software

which results in lower reflection ($|S_{11}| = 0.197$) than for the conventional longitudinal slots with the same length $l = 61$ mm (Fig. 4.5). However, because of their very similar radiation characteristics as for the conventional slots, the radiation characteristics cannot significantly differ from the patterns shown in Fig. 4.6, which is nondesirable.

The standard design procedure that relies on Stevenson's formula and which was described in the previous example of the resonant slotted waveguide with conventional longitudinal slots, obviously needs experimental optimization and fine tuning of the slots offsets and slot lengths in order to achieve the defined design goals. First, the matching condition is not achieved and second, the radiation characteristics is not acceptable for the foreseen application. For the input matching problem and for the maximum power transfer one should use the accurate numerically calculated values for the normalized slot admittances in the slot displacements estimation process. Further, Elliott's design [38] that is based on an iterative procedure and slot parameter measurements could be also used instead the standard procedure explained above. Additional advantage of this approach is that the mutual coupling between the slots is already taken into account. However, this requires an additional precise and sophisticated experimental work to estimate the normalized slot admittances, which makes the design process more time consuming. Further, in the case of longitudinal slots, the mutual coupling is weak and it can be neglected in practice. The second problem with the very narrow radiation pattern can be solved using other distributions for the slot exciting amplitudes a_n, which should give broader radiation characteristics also in the *yz* plane.

Hence, there is a need for a new simple and effective design approach, which should be more general and flexible giving the possibility to achieve total power transfer from the microwave source into the applicator and a desired homogeneous radiation characteristics. This need is more obvious for the case of the horizontally polarized standing wave slotted waveguide that is presented in the following subsection.

4.2.2 Analysis of the standard design procedure for horizontally polarized SWs

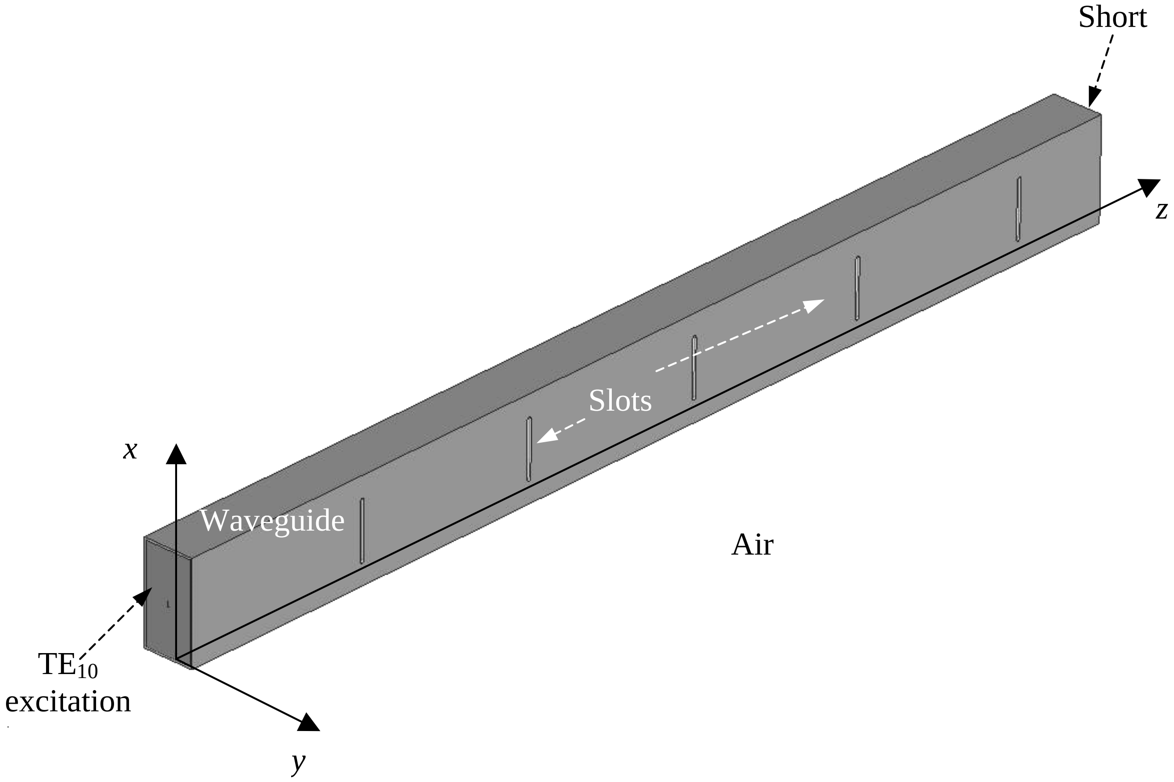

Figure 4.9 Slotted waveguide virtual model with transversal slots for numerical calculations of the reflections and the radiation characteristics

For the horizontally polarized standing wave slotted waveguides with centered transversal slots in the broad waveguide wall, the distances between the slots are defined to be $D = \lambda_g$ and $D_s = \lambda_q/2$. These distances determine the number of slots $N = 5$ in the $L = 0.958$ m long wave-

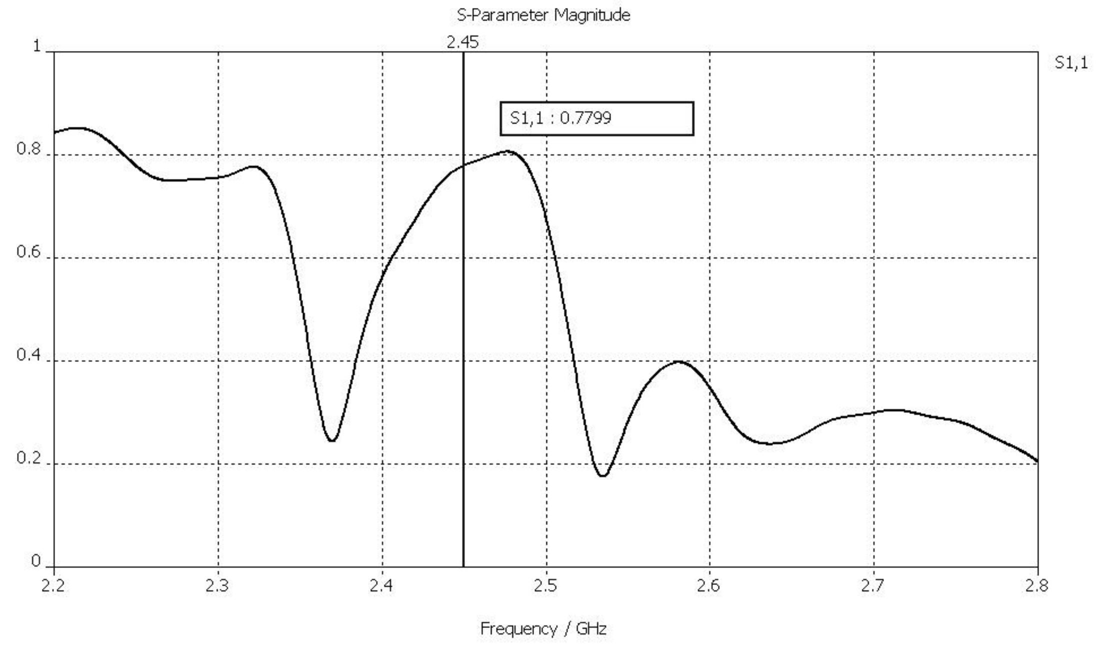

Figure 4.10 Numerically calculated $|S_{11}|$ parameter for the horizontally polarized SW

guide section. But, in this case, Stevenson's relation 3.21 cannot be used in the calculation of the slot properties, because it assumes that the slots are resonant and this is not the case (the slot length has to be obtained). Further, it gives only values for the slot offsets, but this slot parameter is fixed to zero displacement from the central line. Here should be mentioned that resonant waveguide means that a standing wave is present in the waveguide and the resonant slot is related to the resonant length of the slot (imaginary part of the slot impedance is zero). Resonant centered transversal slots radiate very strongly, their normalized slot resistance is already larger than 1 and they cannot be matched to the characteristic waveguide mode impedance.

The results of the numerical calculations of z will be used now for the estimation of the nonresonant transversal slot lengths (see Fig. 3.26 and 3.27). Using the similar simple excitation amplitude distribution $a_n = \frac{1}{\sqrt{N}} = 0.447$, the normalized slot impedance can be estimated by equations 4.6 and 4.15 to have the value $z_n = Ca_n^2 = 0.2$. The numerically calculated curves r_n vs l and x_n vs l give for the slot length l = 54 mm the value $z_n = 0.23 + j0.49$. This results in $z_{in} = 1.1 + j2.45$ and in very high reflections losses $|S_{11}| = 0.75$ (-2.4 dB), according to the relations 4.6 and 2.94 respectively. The slots are far from resonance and they have high values for the normalized slot reactances ($x_n = 0.49$), which should be compensated. Changing the slot width w the normalized reactances x_n would be varied only slightly, which is not enough for achieving the matching condition. The waveguide short is set to the resonant distance and it also cannot be used for the antenna matching. Hence, standing wave slotted waveguides with centered transversal slots are not appropriate for a direct and efficient transfer of the MW power from the magnetron generators into the applicator.

The near field pattern that is simulated and depicted in Fig. 4.11 shows the horizontal polarization, but also an inhomogeneous field distribution along the z axis.

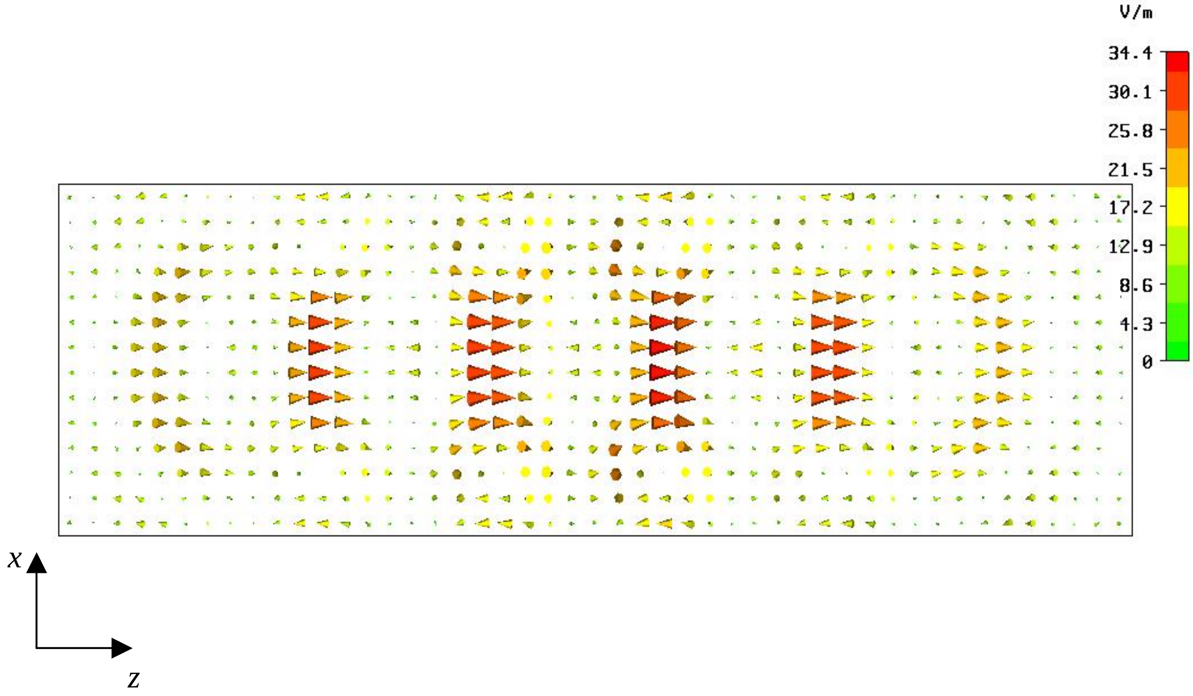

Figure 4.11 E field distribution pattern in the xz plane at a distance of λ from the transversal slot

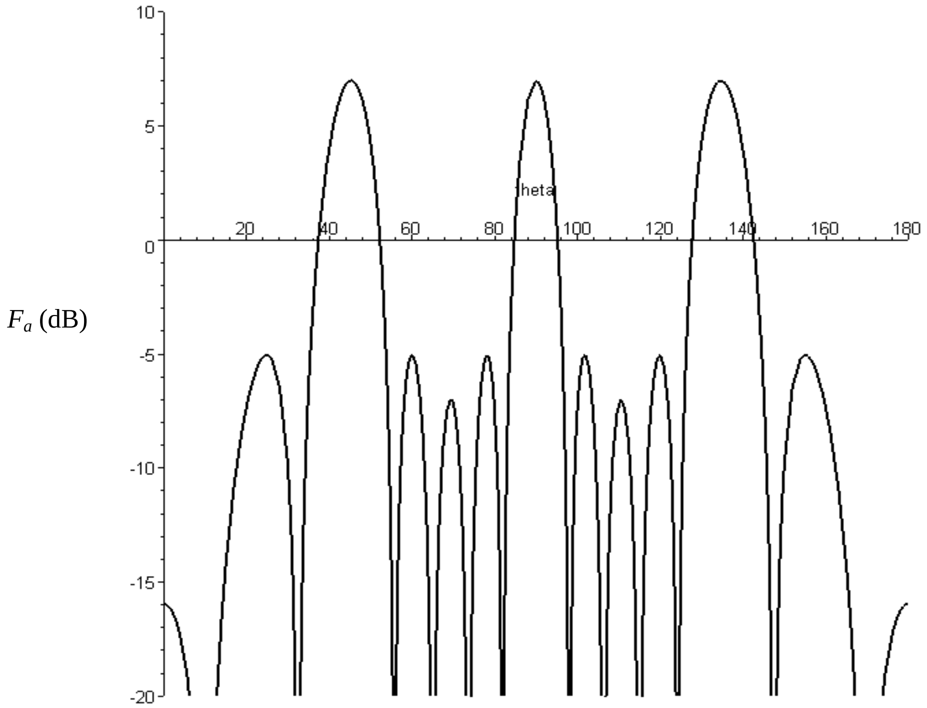

Figure 4.12 Calculated array factor for the horizontally polarized resonant slotted waveguide example using the relation 4.16

Further, horizontally polarized slotted waveguides have a sharp radiated field pattern due to the simple excitation amplitude distribution, as in the last case. The calculated array factor (equ. 4.16) and the numerical simulations prove this undesirable nonhomogenous radiation along the waveguide axis. They are presented in Figures 4.12 and 4.13.

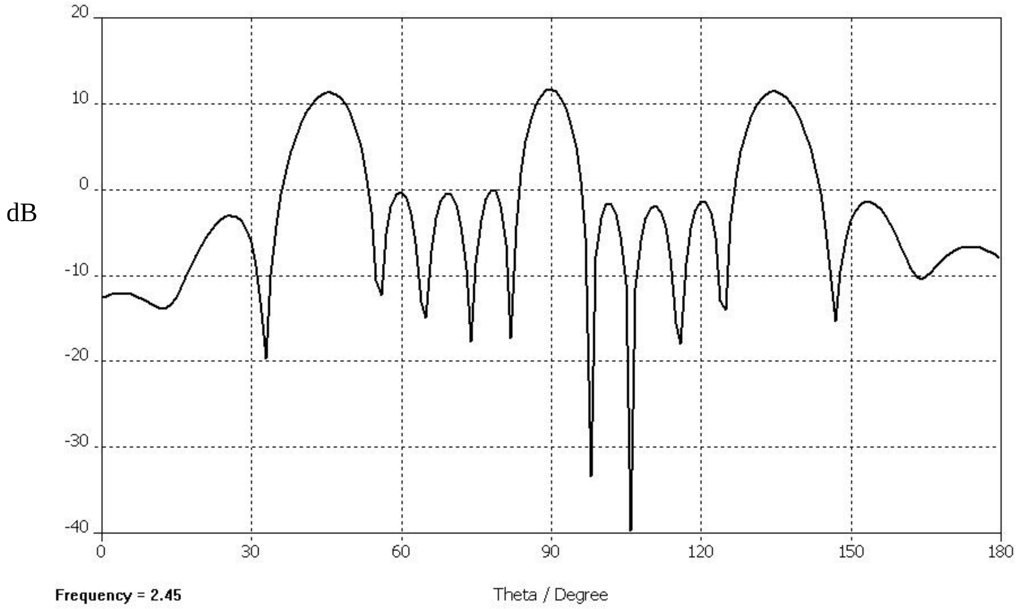

Figure 4.13 Numerically obtained radiation characteristics for the horizontally polarized resonant SW array using MWS software

The difficulties and challenges of the standard design procedure for standing wave slotted waveguides shown in this section ask for a new approach in order to fulfill the defined design requirements. The demand of total MW power transfer requires the minimization of the reflections inside the slotted waveguide energy feeding system, which can be defined also as avoiding the standing wave character of the fundamental mode in the slotted waveguide. This leads to the idea to use nonresonant (traveling wave) slotted waveguides for energy feeding system applications. An additional argument for this is the higher flexibility. The parameters as distances between the slots and distance between the last slot and the waveguide end can be changed to fulfill both requirements, a desired low reflections level into the feeding waveguide and a wanted constant radiation along the waveguide.

This approach with a nonresonant slotted waveguide has been investigated and will be presented in the following section. The proper design and the optimization process for vertically and horizontally polarized slotted waveguide radiators are explained there in more details.

4.3 Nonresonant Slotted Waveguides

To avoid standing waves inside the antenna waveguides (to minimize reflections), nonresonant traveling wave SWs are chosen for the energy feeding parts, instead of resonant standing wave SWs, which are recommended in the literature for this application [35]. In a resonant SW some part of the MW energy is always captured in the oscillating standing wave inside the SW and can not be transferred into the MW applicator. The traveling wave SWs show an additional advantage over the SWs with resonant slot spacing, i.e. they provide broader frequency bandwidths for low reflections [58]. This is very important in high power microwave applications with magnetrons, which have their intrinsic line width due to phase noise. Further, in resonant SWs the positions of the slots along the waveguide are already given by definition and this parameter can not be used in an optimization procedure of the antenna radiation pattern. Hence, nonresonant TW slotted waveguide types with two different and mutually orthogonal polarizations have been investigated and designed according to the application of energy feeding systems for industrial microwave ovens.

4.3.1 New synthesis procedure for vertically polarized SWs (longitudinal slots)

At first, a novel synthesis method for a vertically polarized traveling wave slotted waveguide feed will be presented. It is supposed that along the waveguide only the fundamental mode wave is propagating from the microwave source, which is close to one waveguide end, towards the opposite waveguide end, i.e. there are no, or there are only negligible, reflections from the waveguide end backward to the microwave source. This traveling fundamental waveguide mode is attenuated along the propagation, because of the presence of the radiating slots in the broad waveguide wall. The attenuation can be modeled by an exponential function (equ. 2.78) and for the case of a single direct wave it can be stated as:

$$V = V_0 e^{-\gamma z}, \tag{4.17}$$

where $\gamma = \alpha + j\beta$ and V_0 have been already defined. That means, the active power carrying in the traveling fundamental mode wave is exponentially attenuated along the propagation:

$$p = p_{in} e^{-2\alpha z}, \tag{4.18}$$

where p_{in} is the available power at the first slot (Fig. 4.14).

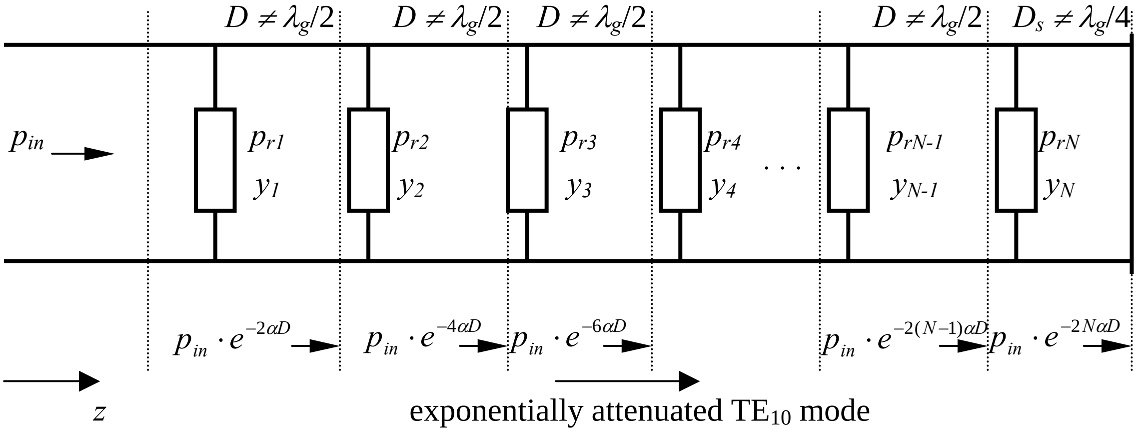

Figure 4.14. Equivalent transmission line circuit of the vertically polarized nonresonant SW

In Fig. 4.14 the radiated power from the n-th slot in the array is denoted by p_{rn} and the microwave power that is available at the n-th slot is represented by the relation $p_{in} \cdot e^{-2(n-1)\alpha D}$. So, the slots radiate some amount of the power from the slotted waveguide and the available power in the traveling waveguide mode exponentially decreases from slot to slot, which can be written as:

(4.19) $$p_{in} = \sum_{n=1}^{N} p_{rn} + p_e \text{ and}$$

(4.20) $$p_{in} - \sum_{n=1}^{M} p_{rn} = p_{in} \cdot e^{-2(M-1)\alpha D},$$

where p_e is power that remains after the last slot and which reaches the waveguide end. N is the number of slots in the array and M is a number from 1 to N, which stands for the M-th slot. The equation 4.19 can be found in the literature [21], but equ. 4.20 takes the exponential attenuation function into account.

The main goal in the design procedure is to estimate the slot parameters according to the defined design requirements. In other words, the appropriate normalized slot conductances have to be obtained in this process. Hence, using the relations between the available and the radiated power that are governed by the desired normalized slot conductances, one can write the following relation [21]:

(4.21) $$p_{r1} = g_1 \cdot p_{in},\ p_{r2} = g_2 \cdot (p_{in} - p_{r2}), \dots,\ p_{rN} = g_N \cdot (p_{in} - \sum_{n=1}^{N-1} p_{rn}).$$

Now, setting the power after the last slot to be a very small part of the input power:

(4.22) $$p_e = \xi \cdot p_{in},$$

where ξ can be any constant that satisfies $\xi \approx 0$, and using the equations 4.10 and 4.21, the relation 4.19 can be rewritten as:

(4.23) $$1 - \xi = \frac{\sum_{n=1}^{N} p_{rn}}{p_{in}} = \frac{\sum_{n=1}^{N} g_n (p_{in} - \sum_{k=1}^{n-1} p_{rk})}{p_{in}} = \sum_{n=1}^{N} g_n \cdot e^{-2(n-1)\alpha D}.$$

This equation can be related to the requirement of total microwave power transfer and to the input matching condition, because it states that almost all available input power is radiated through the slots from the waveguide into the applicator.

Additionally, the demand for uniform radiation along the waveguide should be also implemented into the calculations. The simplest distribution of radiated powers from slot to slot was used for the first design:

(4.24) $$p_{r1} = p_{r2} = \dots = p_{rN},$$

which means that the slots should radiate equally. This results in the following formula:

(4.25) $$g_1 = g_2 \cdot e^{-2\alpha D} = \cdots = g_N \cdot e^{-2(N-1)\alpha D}.$$

From the last relation it is obvious that the normalized slot conductances g_n should increase from slot to slot in the direction of the fundamental waveguide mode propagation in order to compensate the attenuation of the available power. Equation 4.25 defines therefore a slot offset distribution pattern that gives increasing slot displacements from slot to slot along the z direction of propagation (Fig. 4.14).

Combining the relations 4.23 and 4.25 the slot design equation can be derived as:

$$1-\xi = N \cdot g_N \cdot e^{-2(N-1)\alpha D}. \tag{4.26}$$

The equation 4.26 presents also the antenna efficiency η, and one can write:

$$\eta = 1-\xi. \tag{4.27}$$

The attenuation constant α and the normalized conductance of the N-th slot g_N can be estimated using the last relation 4.26 and the fact that $g_1 = \frac{1-\xi}{N}$ (see equ. 4.23 – 4.24). So, from 4.26 and for chosen g_N, α can be determined to satisfy above relation for the first normalized slot conductance g_1. In this way, the slots will radiate equally and the reflections back from the slotted waveguide will be minimized.

4.3.2 Linearization of the exponential attenuation function

However, the exponential increase of the normalized slot conductances and of the slot offsets could result in a very large difference in the slot offsets values. This can lead further to the situation where the slot displacement are too high (over $a/2$) or to low (near 0) and cannot be practically realized. To avoid this a linearization of the exponential attenuation function has been performed. After the linearization the normalized slot conductances g_n and slot displacements d_n should linearly increase, which is a more appropriate slot distribution for homogeneous radiation along the slotted waveguide. Hence, the linearization of the exponential attenuation function of the traveling fundamental TE_{10} mode in the waveguide has been done taking only the linear term from the series $e^x = \sum_{n=0}^{\infty} \frac{x^n}{n!}$, such as:

$$e^{-\alpha z} \approx 1-\alpha z. \tag{4.28}$$

The linearization (relation 4.28) affects the equations 4.25 and 4.26, which yield in the set of the following slot calculation formulas:

$$g_1 = g_2 \cdot (1-2\alpha D) = \cdots = g_N \cdot \left[1-2(N-1)\alpha D\right] \text{ and} \tag{4.29}$$

$$1-\xi = N \cdot g_N \cdot \left[1-2(N-1)\alpha D\right], \tag{4.30}$$

respectively.

The eqs. 4.29 and 4.30 can be taken as the set of design relations for vertically polarized nonresonant slotted waveguides.

4.3.3 Design example of a nonresonant vertically polarized SW

The parameters of a slotted waveguide feed that is nearly 1 m long, should be calculated for the HEPHAISTOS industrial microwave applicator. The lengths l_n of the longitudinal conventional round ended slots is chosen to be near the first resonance, i.e.

$l_n = \frac{\lambda}{2} = 0.061$ m. All slots have the same small width of 6 mm. The distance D between the neighboring slot centers can be in the range that is defined by $l_n < D < \lambda_g/2$. To have a continuous radiation along the waveguide, which should improve the homogeneity of the radiation pattern, the distance D is set to the minimum value, i.e. $D = l_n = 0.061$ m. This determines the value of the number of slots to be $N = 14$.

The amount of reflections in the waveguide has been limited by the design requirement to 1% of the available microwave power, which can be used as value for the ξ parameter. Now, setting $\eta = 0.99$, $\xi = 0.01$, $g_N = 0.03$ and using the design relation 4.30, the value of the attenuation constant has been calculated to be $\alpha = 0.57$ Np/m, which gives $g_1 \approx 1/14$.

Further, the desired normalized slot conductances g_n have been calculated using the design equations 2.29 and 2.30. The obtained values are given in Tab. 4.2.

n	1	2	3	4	5	6	7	8	9	10	11	12	13	14
g_n	0.07	0.07	0.08	0.08	0.09	0.11	0.11	0.12	0.14	0.16	0.19	0.22	0.24	0.3

Table 4.2 Distribution of the normalized slot conductance

Now, having the values of the normalized slot conductances, the numerically calculated results for the normalized slot admittance (Fig. 3.19) were used to determine the transversal slot positions (offsets) d_n from the central line of the broad waveguide wall. The slot displacements increase linearly from slot to slot in the TE_{10} waveguide mode propagation direction, compensating the fundamental mode attenuation. This slot offset pattern fulfills:

(4.31) $$d_1 < d_2 < d_3 < \ldots < d_{13} < d_{14}.$$

Knowing the normalized slot admittances, the reflections at the input of the slotted waveguide can be also determined using the relations 2.93 and 2.95. In this first estimation of the input reflections, it has been supposed that the distance between the last slot and the waveguide short end D_s is equal the $\lambda_g/4$. That means, the normalized admittance of the shorted waveguide section at the position of the last slot is zero. In this case, the obtained value of the normalized input admittance is $y_{in} = 0.82 - j0.06$ and the level of the input reflection is around -20 dB, which provides a very good antenna input matching.

Additionally, the array factor F_a was also calculated for this particular slotted waveguide antenna array, and the result is shown in Fig. 4.15. For this calculation the following relation was used:

(4.32)

$$F_a(\theta) = \left\{ \left[\sum_{n=1}^{N} a_n \cos\left(\alpha_n \cos\theta + (n-1)(\beta D + \pi)\right) \right]^2 + \left[\sum_{n=1}^{N} a_n \sin\left(\alpha_n \cos\theta + (n-1)(\beta D + \pi)\right) \right]^2 \right\},$$

where a_n and α_n are the constants defined by 4.14 and 4.16. From Fig. 4.15 it can be seen that the requirement of equal slot radiation gives a more homogeneous radiation, than in the case

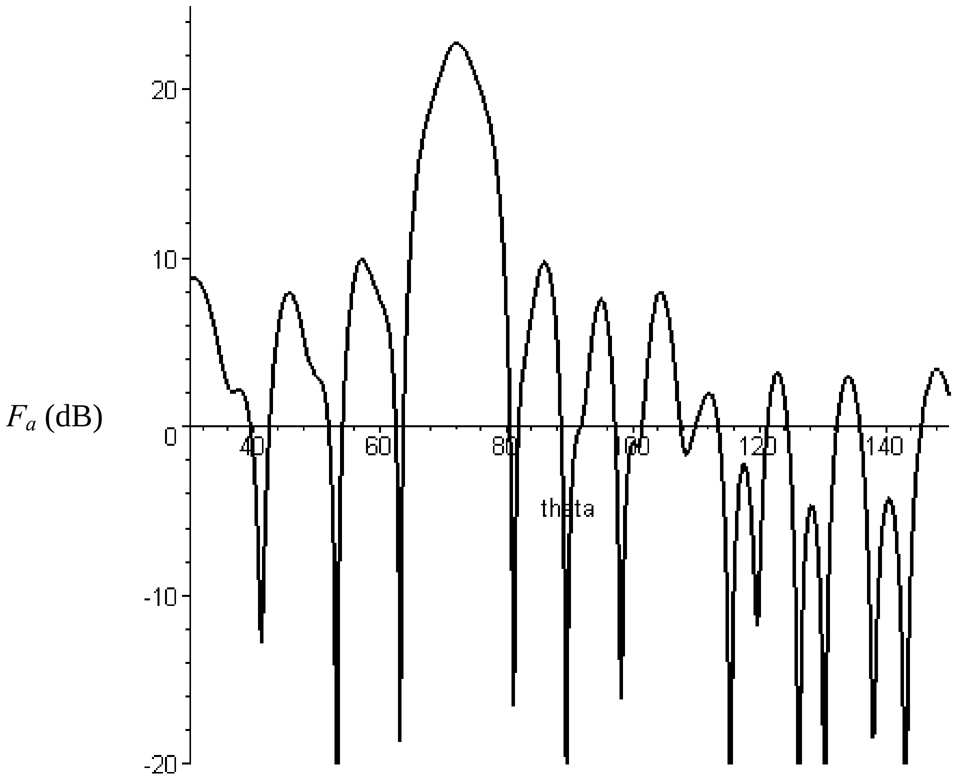

Figure 4.14 Calculated array factor F_a of the vertically polarized nonresonant slotted waveguide

of the standing wave slotted waveguide with the same slot radiation condition (Fig. 4.7).

This presented design has been further optimized by numerical simulation and by experimental measurements, in order to improve the antenna matching and the antenna radiation characteristics.

4.3.4 Numerical investigations on vertically polarized nonresonant SW feed

Numerical calculations on the vertically polarized slotted waveguide have been performed with CST Microwave Studio using the model that is shown in Fig.4.15. It consists of a standard WR340 waveguide with 14 longitudinal slots in the broad wall, as described in the last subsection. It is excitated by the fundamental TE_{10} waveguide mode at one end and has a short at the opposite waveguide end. The surrounding material is air, bounded by absorbing boundaries modeling the free space.

In the numerical calculations the reflection at the input port and the radiated fields of the synthesized SW array were obtained. This results have been compared to the results of the analytical calculations from the previous subsection. The simulations have been also used for an optimization of the slotted waveguide, i.e. the distance D_s has been varied to achieve a minimum for the reflections into the waveguide and to improve the radiation characteristics of the SW feed, simultaneously.

The numerically obtained level of reflections $|S_{11}| = 0.098$ differs from the calculated only by 1 %. This proves the validity of the design procedure. Further, in Fig. 4.16 the results of the simulated frequency dependance of the reflections of the slotted waveguide are shown. Here the distance D_s has been adjusted to the optimum value. The level of reflections at the frequency of 2.45 GHz is 2 dB lower than for the nonoptimized D_s value.

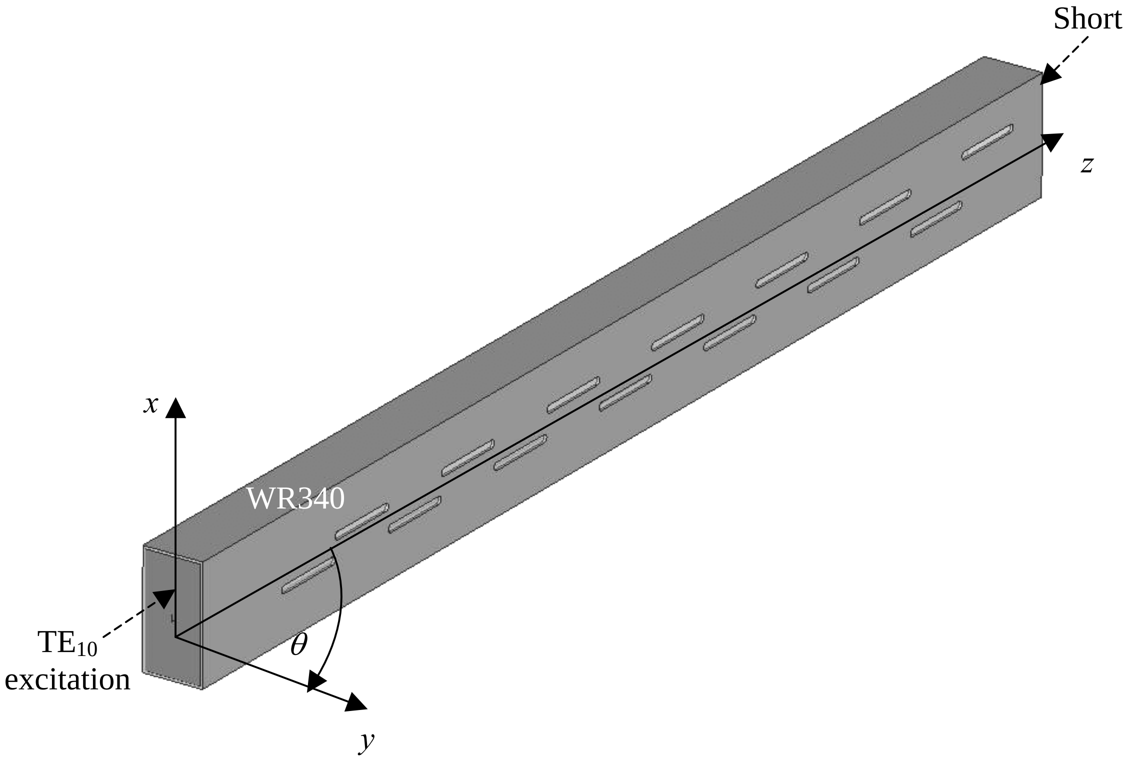

Figure 4.15 Model of vertically polarized slotted waveguide for numerical calculations

The instantaneous *E* field in the *xz* plane that is a wavelength away from the slots is shown in Fig. 4.17. The vertical polarization of the radiated field is obvious, like in the case of the standing wave slotted waveguide (Fig. 4.6). However, for the nonresonant slotted waveguide antenna a phase difference in the traveling field distribution along the *z* axis can be noticed as expected.

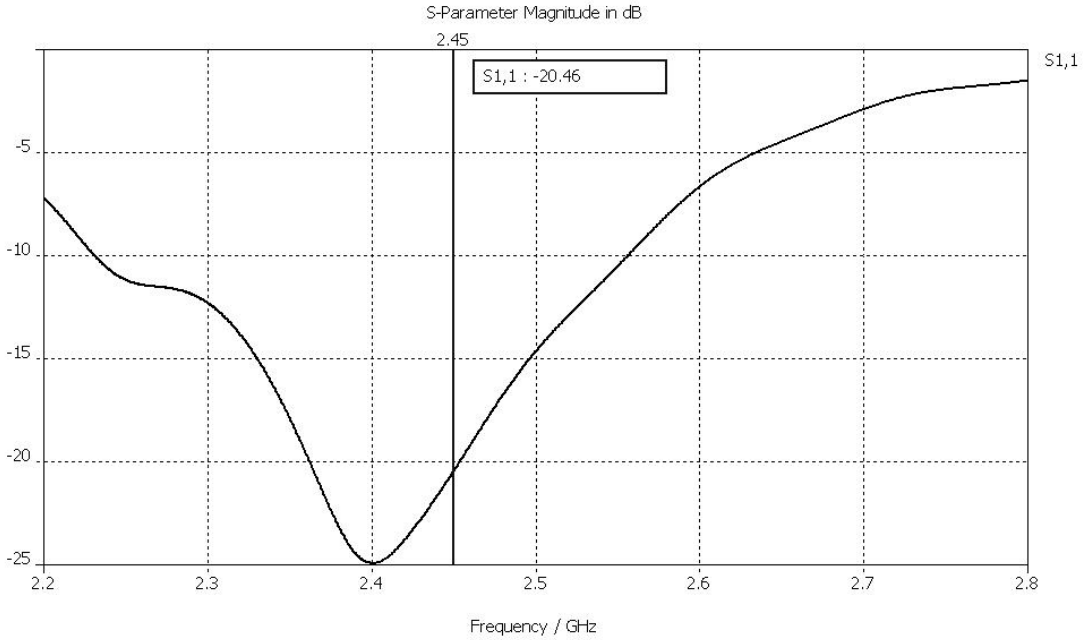

Figure 4.16 Numerically obtained $|S_{11}|$ parameter after optimization

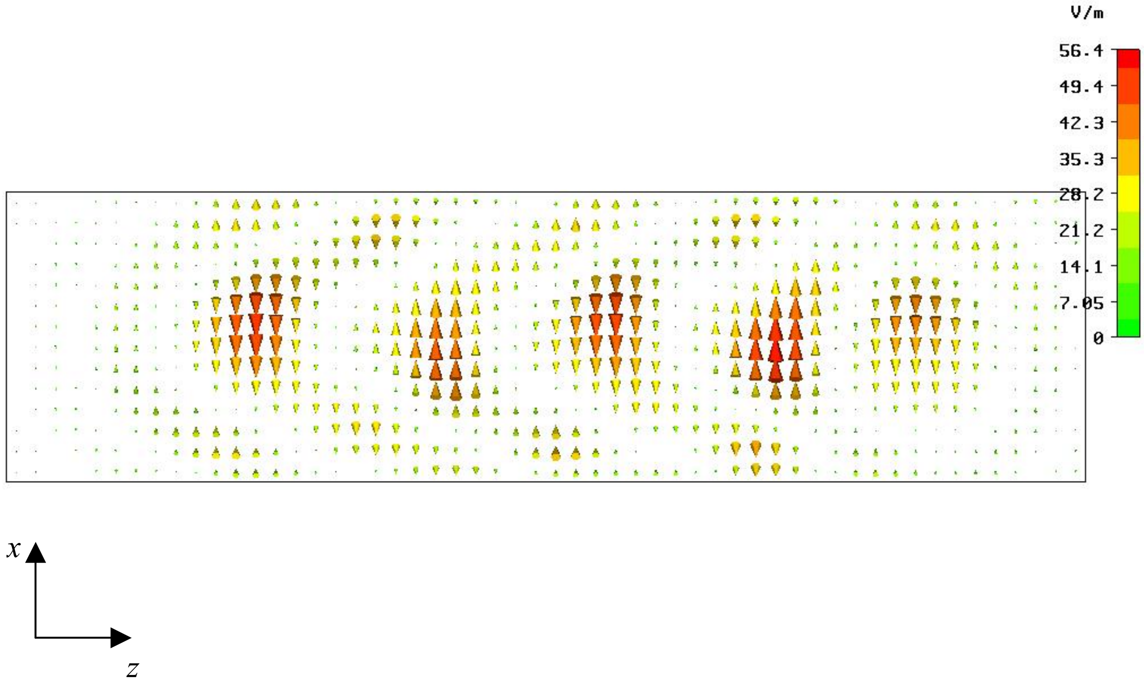

Figure 4.17 Instantaneous E field in the xz plane at a distance of λ from the longitudinal slots

The numerically calculated near E field amplitude pattern of the radiating field that is in the xz plane one wavelength away from the SW is presented in Fig. 4.18. Relatively uniform field distribution along the z direction of the waveguide axis can be seen.

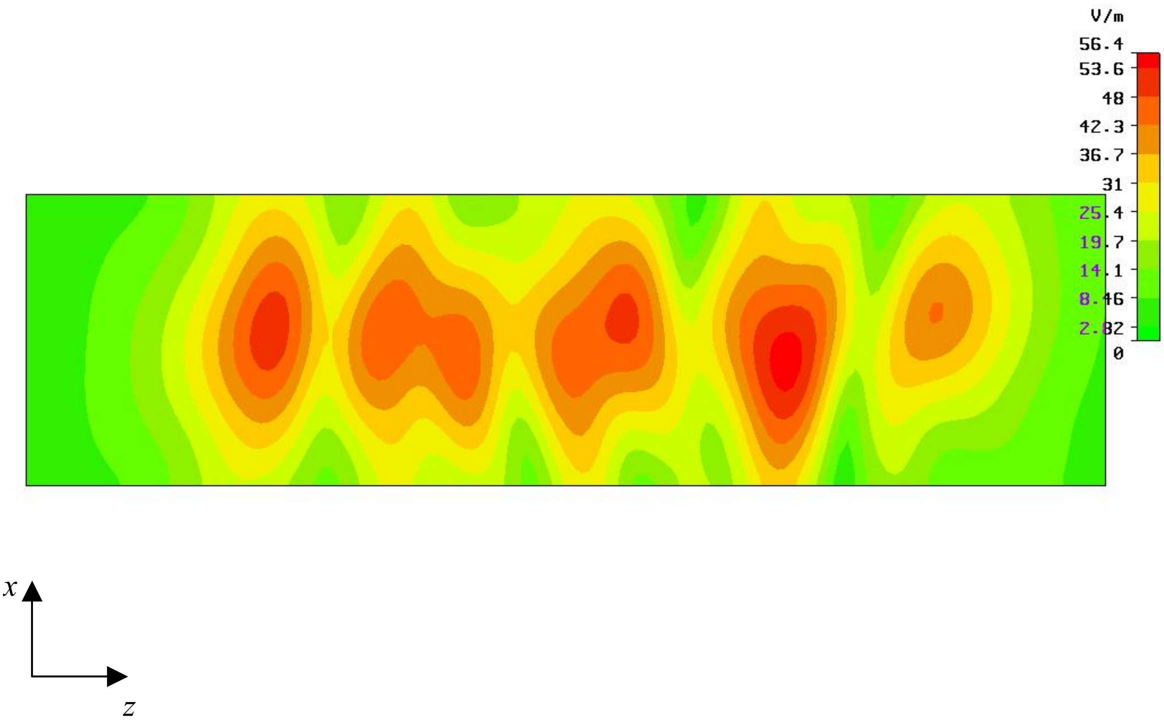

Figure 4.18 $|E|$ field distribution pattern in the xz plane at a distance of λ from the longitudinal slots

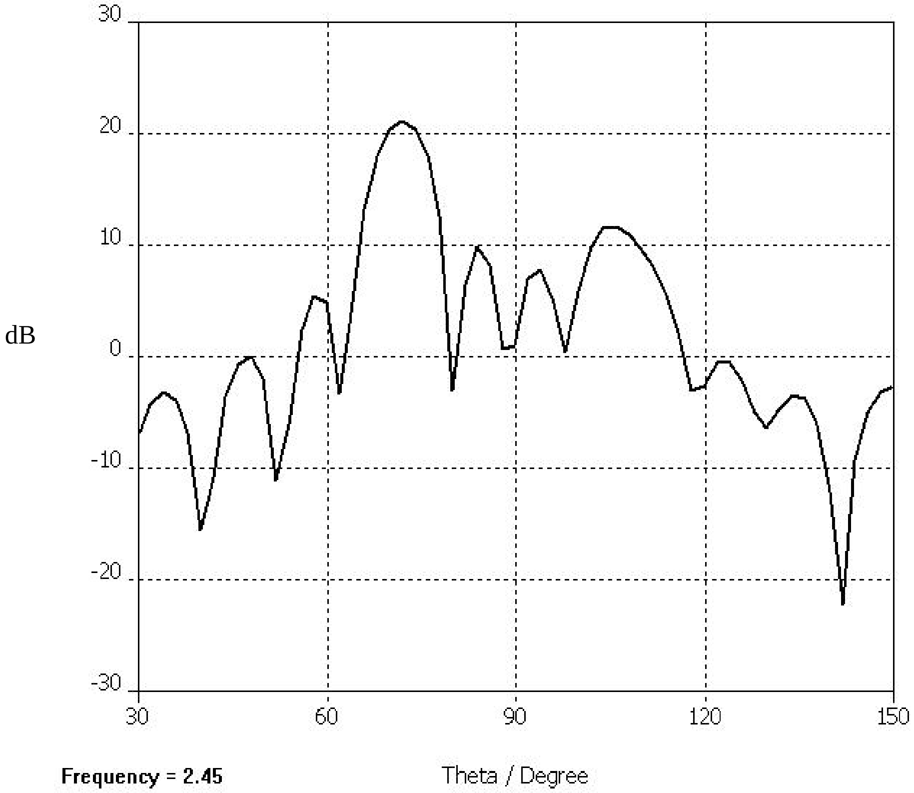

Figure 4.19 Numerically obtained radiation characteristics for the vertically polarized nonresonant SW array

The numerically obtained farfield pattern is in good agreement with the theoretical prediction (Fig. 4.14). In comparison to the farfield of the resonant slotted waveguide antenna with only one narrow main beam that is depicted in Fig. 4.8, in this case there are two beams in the θ range from 60 to 120 degrees.

4.3.5 New synthesis procedure for horizontally polarized SWs (transversal slots)

For a horizontally polarized traveling wave slotted waveguide with centered transversal slots in the broad waveguide wall a synthesis procedure has been performed that is similar as for a vertically polarized SW. Now, instead of the normalized slot conductance g_i in equ. 4.21, the normalized resistance r_i of the i-th transversal slot should be taken into account. This yields in the following relations:

$$(4.33) \qquad p_{r1} = r_1 \cdot p_{in}\,,\ p_{r2} = r_2 \cdot (p_{in} - p_{r2}),\ldots,\ p_{rN} = r_N \cdot (p_{in} - \sum_{n=1}^{N-1} p_{rn})\,.$$

Further, considering the relation 4.24 and after the same linearization approach (see 2. 4.28), the design formulas can be defined as:

$$(4.34) \qquad r_1 = r_2 \cdot (1 - 2\alpha D) = \cdots = r_N \cdot \left[1 - 2(N-1)\alpha D\right] \text{ and}$$

$$(4.35) \qquad 1 - \xi = N \cdot r_N \cdot \left[1 - 2(N-1)\alpha D\right],$$

where ξ, N, α and D are the same constants as in the case of a vertically polarized SW. Of course, here is also $r_1 = \frac{1-\xi}{N}$. Hence, choosing the appropriate value for r_N that satisfies the last relation for the r_1, using the design relations, the desired attenuation and the normalized slot resistances can be obtained for a given number of slots N and given distance D between them. To realize this distribution of the normalized slot resistances, the length of the centered transversal slots is taken as the design parameter. That means, for the slot radiating power distribution given by 4.33, the slot length will increase from slot to slot compensating the linearized exponential attenuation along the propagation. This will be proved in the following design example.

4.3.6 Design example of a nonresonant SW with horizontal polarization

For a nearly 1 m long waveguide section the design parameters have been set to $N = 16$, $D = 0.058$ mm, $\xi = 0.01$ and $r_N = 0.3$ giving an attenuation constant $\alpha = 0.46$ Np/m . The normalized slot resistances have been calculated using the relation 4.34 and they are given in Tab 4.3. The linear increasing of the normalized slot resistances is obvious. The value $r_1 = 0.06$ is in agreement with the desired value $r_1 = \frac{1-\xi}{N}$.

n	1	2	3	4	5	6	7	8	9	10	11	12	13	14	15	16
r_n	0.06	0.06	0.07	0.07	0.08	0.08	0.09	0.1	0.1	0.11	0.13	0.14	0.17	0.2	0.24	0.3

Table 4.3 Distribution of the normalized slot resistance

As in the previous case of the vertical polarization, having the values of the normalized slot conductances, the numerically calculated results for the normalized slot impedance (Fig. 3.26) were used to determine the slot lengths l_n. The obtained slot lengths increase linearly from slot to slot (4.36) in the TE_{10} waveguide mode propagation direction, compensating the fundamental mode attenuation.

(4.36) $$l_1 < l_2 < l_3 < \ldots < l_{15} < l_{16}.$$

Calculating the normalized slot impedances, the reflection at the input of the slotted waveguide can be also determined using the relations 2.93 and 2.94. In this first estimation of the input reflection, it has been supposed that the distance between the last slot and the waveguide short end D_s is equal to the $\lambda_g/2$. That means, the normalized impedance of the shorted waveguide section at the position of the last slot is zero. In this case, the obtained value of the normalized input admittance is $y_{in} = 0.85 + j0.07$ and the level of the input reflection is near -20 dB, which proves a very good antenna input matching.

The antenna array factor F_a was also calculated for this particular slotted waveguide feed, and the result is shown in Fig. 4.15. Because the slots are here centered, there is no alternating phase change as in the previous case and for the calculation of F_a the following relation was used:

(4.37)
$$F_a(\theta) = \left\{ \left[\sum_{n=1}^{N} a_n \cos\bigl(\alpha_n \cos\theta + (n-1)\beta D\bigr) \right]^2 + \left[\sum_{n=1}^{N} a_n \sin\bigl(\alpha_n \cos\theta + (n-1)\beta D\bigr) \right]^2 \right\},$$

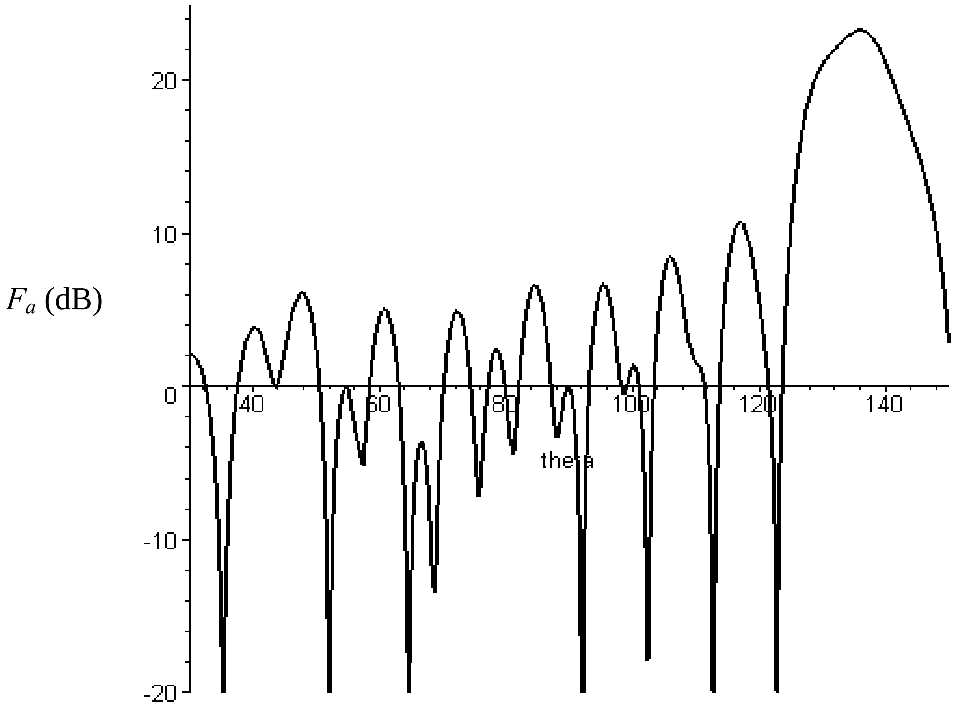

Figure 4.20 Calculated array factor for the horizontally polarized nonresonant SW example

where a_n and α_n are the constants defined by 4.14 and 4.16. From Fig. 4.15 it can be seen that the requirement of equal slot radiation does not give a homogeneous radiated field pattern. So, the simple slot radiation power distribution given by relation 4.33 is not appropriate for an energy feeding system design and it should be optimized.

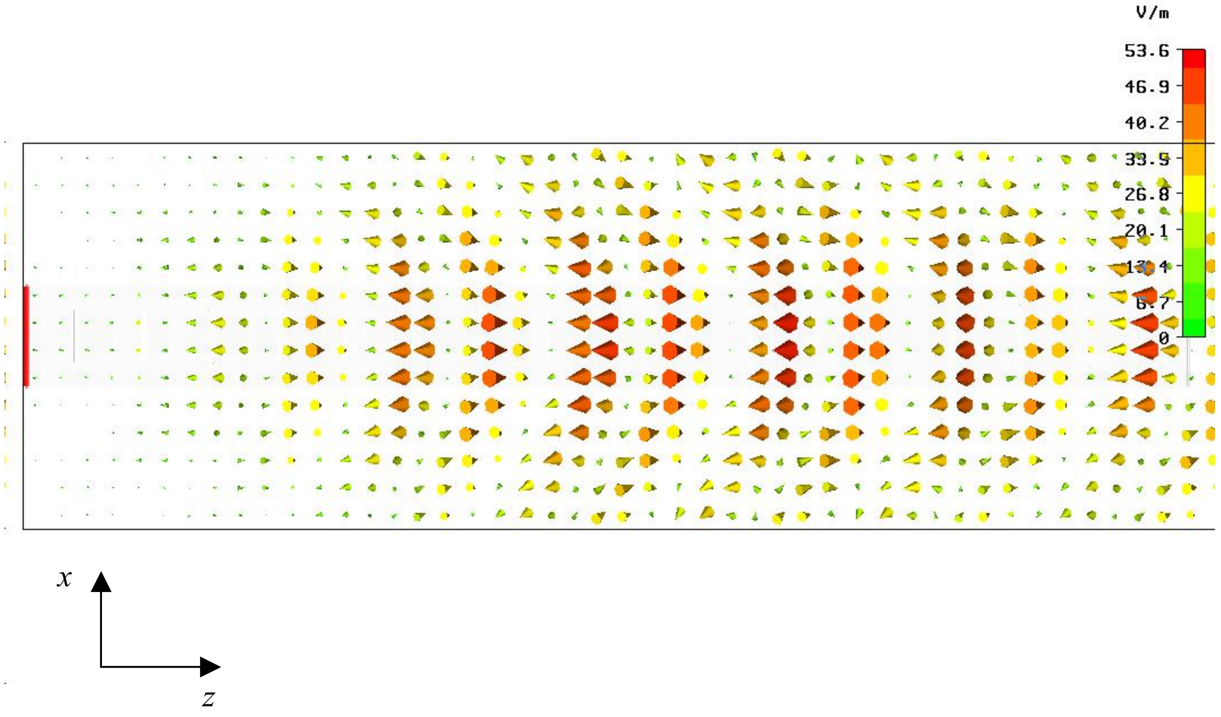

Figure 4.21 Simulated instantaneous E field in the xz plane at a distance of λ from the slots

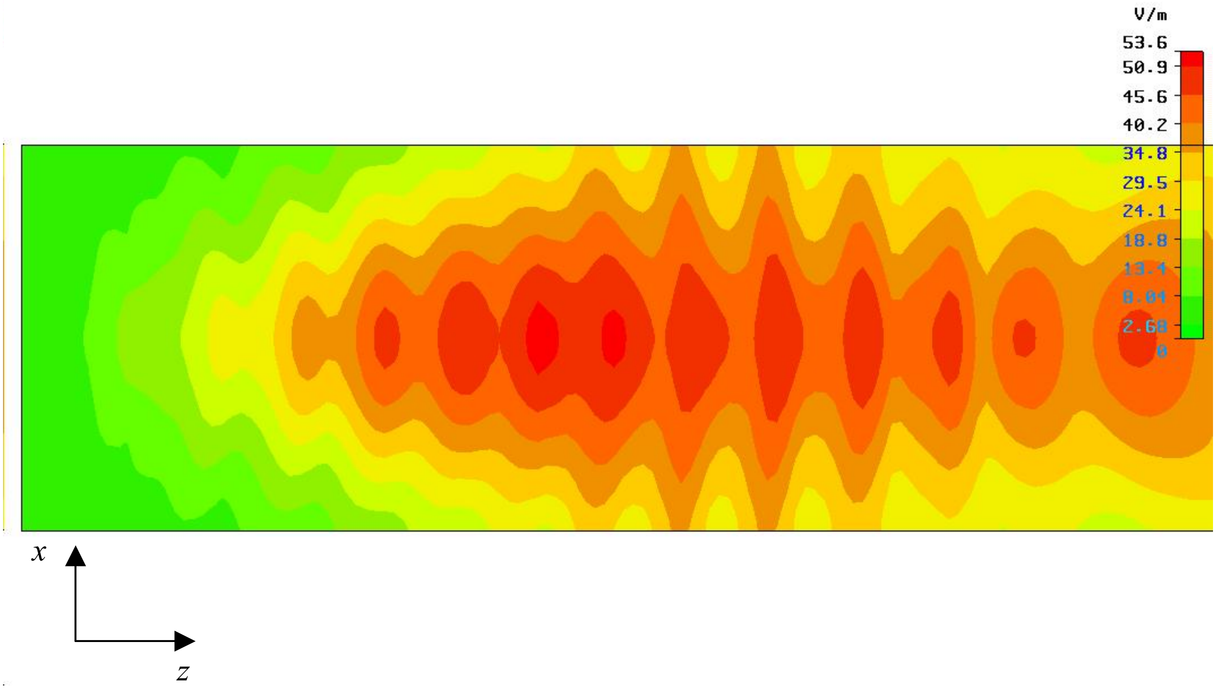

Figure 4.22 Simulated near |*E*| field pattern in the *xz* plane at a distance of λ from the slots

A model for numerical investigations has been made also. After performing the simulations a good antenna input matching ($|S_{11}|$ = -25 dB), a relatively uniform near EM field in the *z* direction of propagation and nonhomogeneous radiation characteristics have been proved (Fig. 4.21 - 4.24). Hence, an optimization of the radiation pattern is needed.

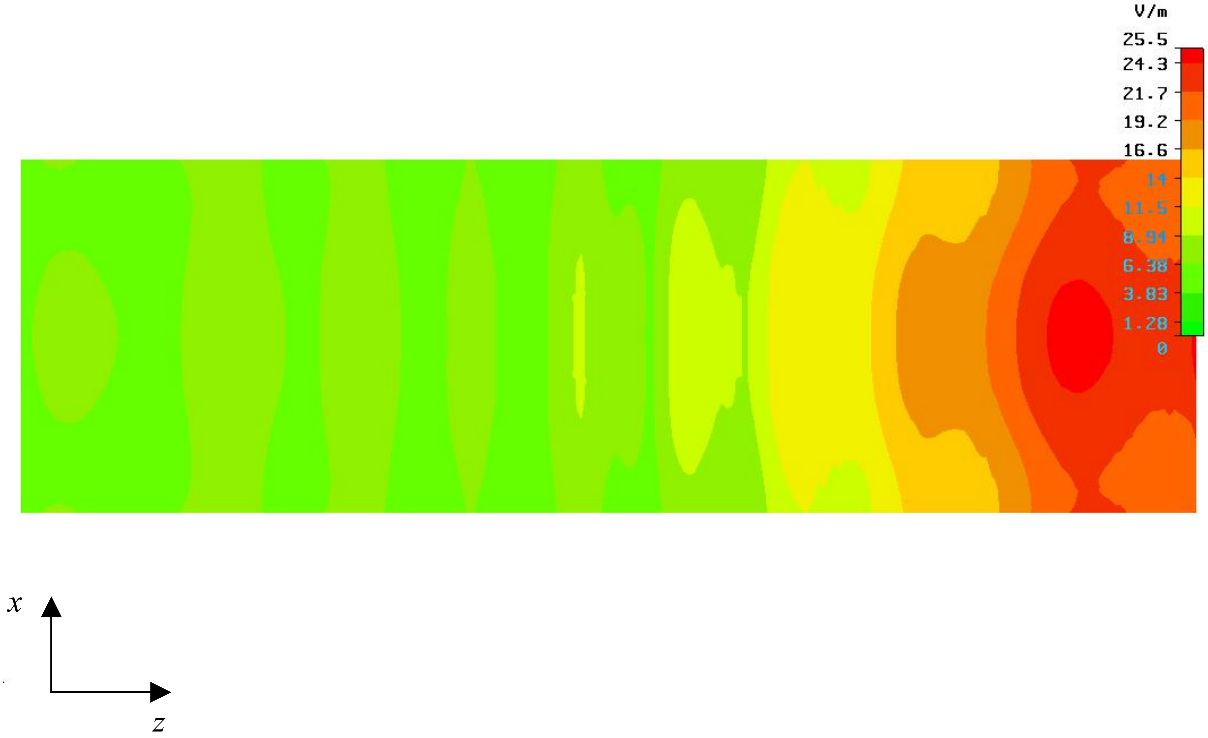

Figure 4.23 Simulated |*E*| field pattern in the *xz* plane at a distance of 4λ from the slots

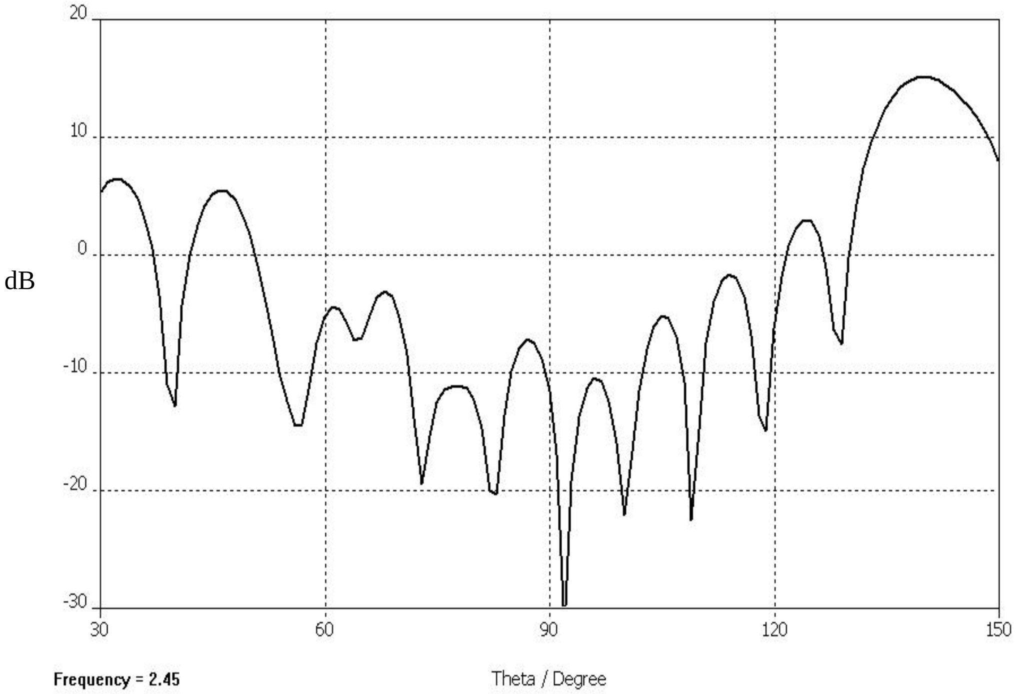

Figure 4.24 Numerically calculated radiation characteristic for the horizontally polarized nonresonant SW array

4.3.7 Radiation characteristics optimization

The desired uniform radiation has been achieved using an optimization method, similar to the method utilized in the calculation of diffraction gratings in optics [59]. The electric field, radiated from the n-th slot, in the far field point P can be determined as [60]:

$$E_{n,P} = \frac{1}{R} \int_{(n-1)D-\frac{w}{2}}^{(n-1)D+\frac{w}{2}} a_n \sin(\omega t - kR + kz\sin\theta - \beta z)dz, \tag{4.38}$$

where $n = 1,\ldots,N$, R is the distance from the center of the first slot to the point P, w is the slot width (small and constant), a_n is the E field amplitude of the n-th slot, k is the phase constant in the free space and β is the phase constant in the waveguide for the fundamental TE_{10} mode. The total field in the point P is the sum of all radiated fields from the slots:

$$E_{tot,P} = \sum_{n=1}^{N} E_{n,P} \tag{4.39}$$

and it is a function of the angle θ between the y axis (normal to the slot plane) and the direction of R (see Fig. 4.25). By determination of an appropriate set of amplitudes a_i, a relatively uniform distribution for the total field and a desired radiation pattern of the SW antenna can be achieved in the full θ angle range. Determination of the slot field amplitudes a_i leads to the calculation of the normalized slot resistances and to an estimation of the slot lengths.

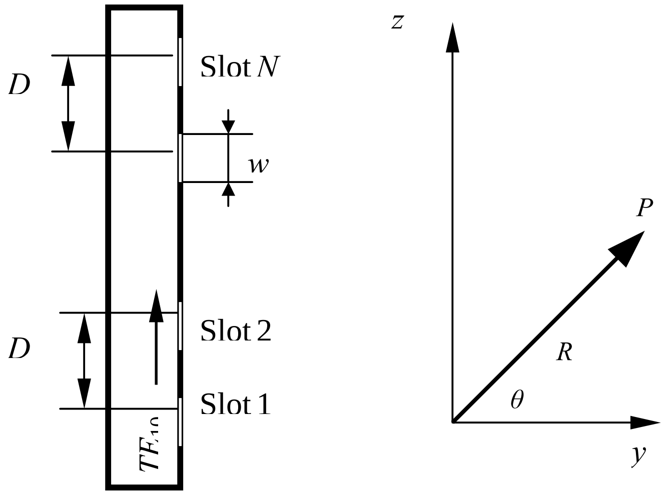

Figure 4.25 Calculation of the total E field in a far field point P

For the distribution function of the excitation amplitudes a_n in longitudinal z direction, the following function $f_{amp}(z)$ has been chosen:

(4.40)
$$f_{amp}(z) = \frac{1}{\left|\cos\left[z(k-\beta)\right]\right|}.$$

Hence, the excitation amplitudes have to satisfy the relations:

(4.41)
$$a_1 = a_2 \cdot \left|\cos\left[D(k-\beta)\right]\right| = \ldots = a_N \cdot \left|\cos\left[(N-1)D(k-\beta)\right]\right|.$$

The proposed function $f_{amp}(z)$ and distribution of excitation amplitudes should reduce the dependence of the E field on the phase difference k - β in the farfield zone. This can be observed as relatively flat radiation characteristics over a broad θ range shown in Fig. 4.26.

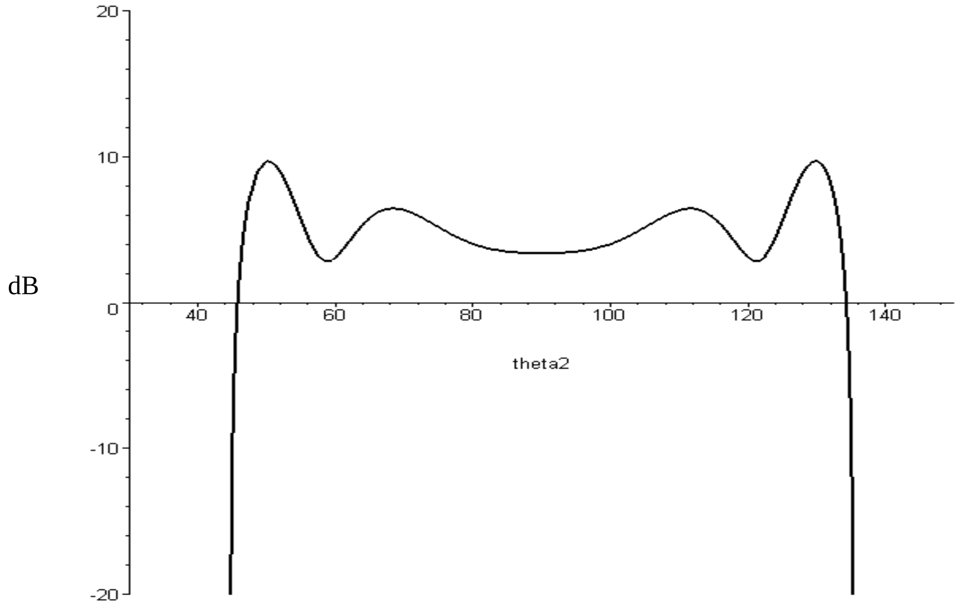

Figure 4.26 Calculated total E field using the a_n distribution of equ. 4.43

The curve in Fig. 4.26, which presents the normalized $E_{tot,P}$ field calculated in dB scale, has been obtained by implementing the a_n distribution (given in equ. 4.41) into equation 4.38 and then by adding the radiated fields using 4.39.

The square of the excitation amplitude defines the amount of the radiated power p_{rn} from the n-th slot giving the relations:

(4.42) $$p_{rn} \propto a_n^2 ,$$

for $n = 1 \ldots N$. Now, from the power governing equations 4.21, 4.23 and after the linearization of the exponential fundamental TE_{10} mode attenuation function and for the given a_n distribution (4.41 and 4.42), the first design formula can be written as:

(4.43) $$1-\xi = r_1 \cdot \left\{ 1 + \sum_{n=1}^{N-1} \frac{1}{\cos^2\left[nD(k-\beta)\right]} \right\}.$$

The relation 4.43 is for the calculation of the first normalized slot resistance r_1. Additionally, the design equations for the calculation of all the remaining normalized slot resistances r_n are defined as:

(4.44) $$r_n = \frac{r_1}{\left[1-2(n-1)\alpha D\right] \cdot \cos^2\left[(n-1)D(k-\beta)\right]},$$

for $n = 2 \ldots N$.

Setting the slotted waveguide feed parameter as $\xi = 0.01$, $N = 16$, $w = 0.004$ m and $D = 0.05$ m for the WR340 standard at 2.45 GHz, the values for the normalized slot resistances that are appropriate for both design requirement, a good input matching and a flat radiation pattern, have been calculated using 4.43 and 4.44. The obtained values of r_n are given in Tab. 4.3.

n	1	2	3	4	5	6	7	8	9	10	11	12	13	14	15	16
r_n	0.001	0.001	0.8	0.005	0.001	0.001	0.13	0.005	0.001	0.001	0.053	0.022	0.005	0.005	0.053	0.053

Table 4.3 Distribution of normalized slot resistance

Getting the values of the normalized slot resistances, the desired slot lengths can be estimated from Fig. 3.26 (numerically calculated results for the normalized slot resistance vs. transversal slot lengths). However, the proposed slot excitation distribution does not result in increasing slot lengths, as in the previous case of the non satisfying uniform radiation from slot to slot (equ. 4.24). So, now the lengths of the centered transversal slot differ from slot to slot, but not in an increasing or decreasing order :

(4.45) $$l_1 \neq l_2 \neq l_3 \neq \ldots \neq l_{15} \neq l_{16}.$$

Having the r_n and l_n distributions, analytical and numerical investigations have been firstly performed in order to verify the above presented design procedure. Calculating the input normalized impedance, a low reflection level of about – 20 dB has been obtained using the relations 2.93 and 2.94. After that, from the equ. 4.37 for the array factor $F_a(\theta)$, an opti-

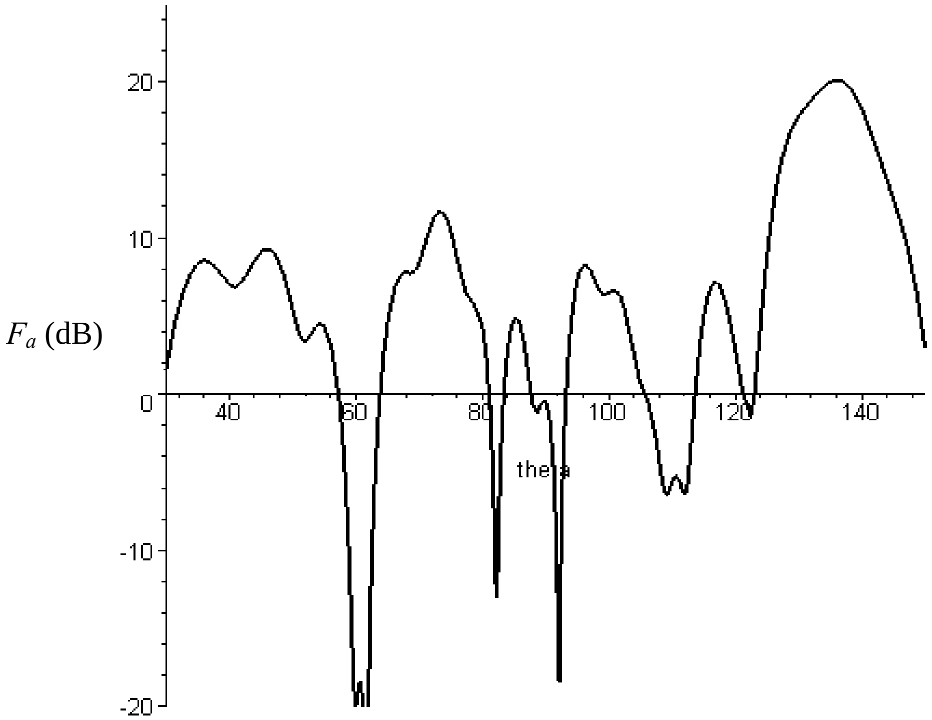

Figure 4.27 Optimized array factor for the example of horizontally polarized nonresonant SW

mization of the radiation characteristic of the slotted waveguide array has been proven (see Fig. 4.27).

For the numerical simulations the model presented in Fig. 4.28 has been used. A very low level of reflection ($|S_{11}|$ = - 20 dB at the design frequency of 2.45 GHz) has been obtained in the simulations.

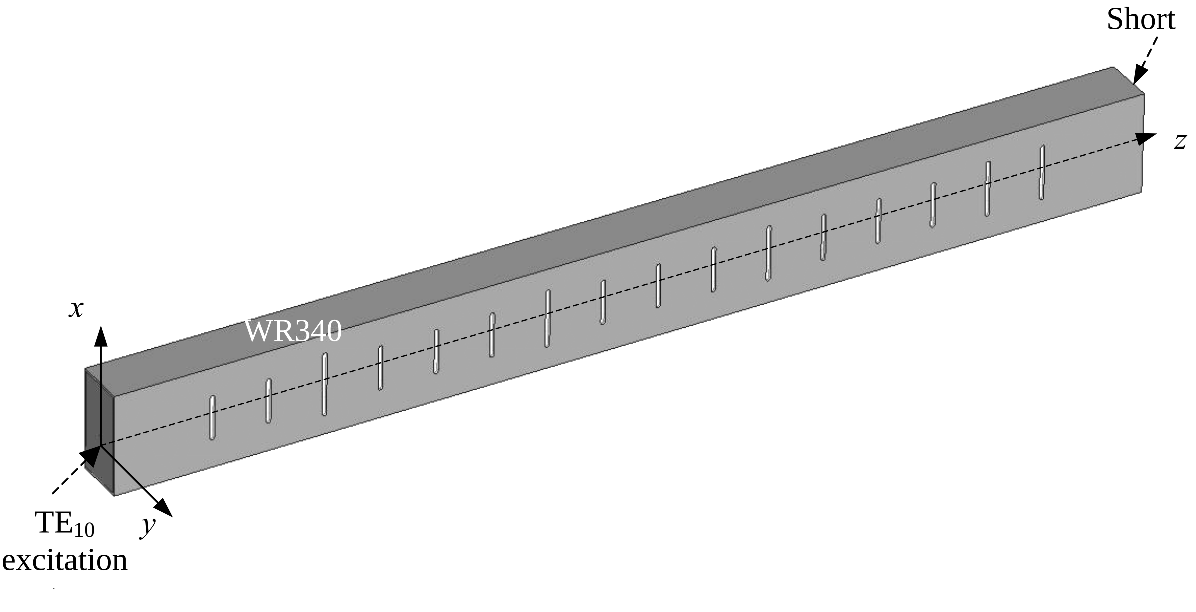

Figure 4.28 Model of horizontally polarized SW with optimized radiation pattern

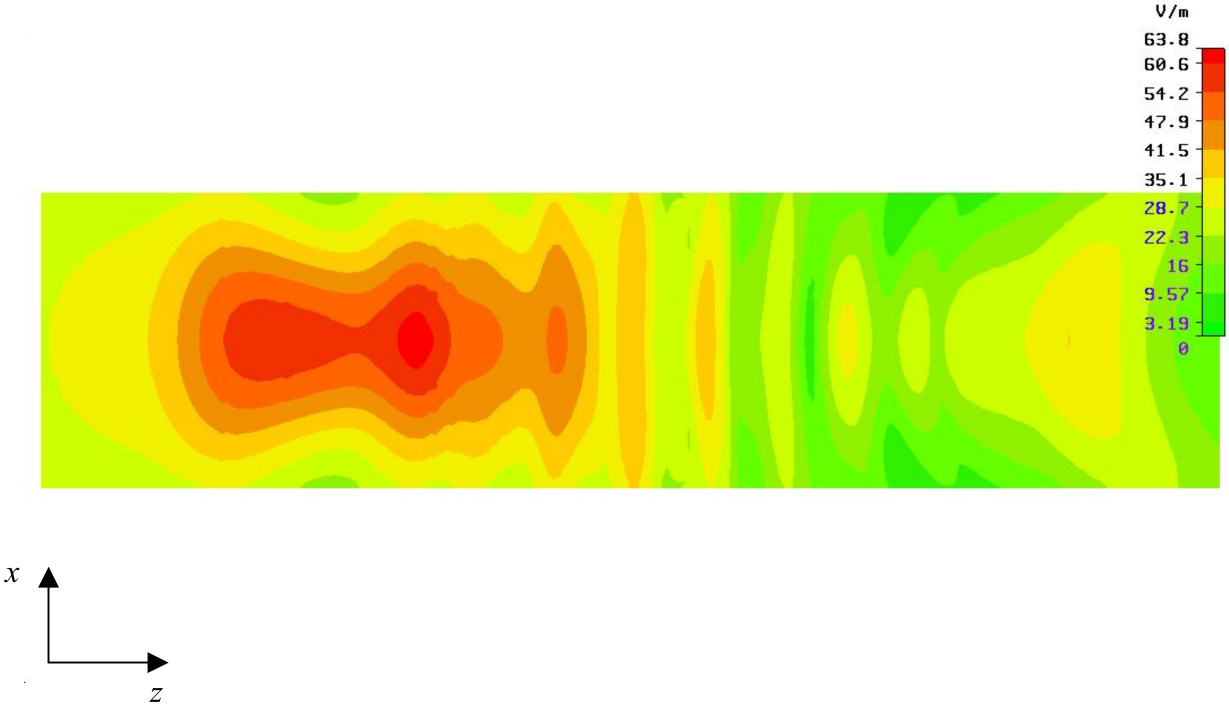

Figure 4.29 Simulated near |*E*| field pattern in the *xz* plane at a distance of λ from the slots

The expected non uniform EM near field in the *z* direction of propagation has been simulated and is depicted in Fig. 4.29. This is due to the calculated nonuniform slot excitations and the unequal slot power radiation. However, an optimized homogeneous radiation characteristic has been achieved (Figs. 4.30 and 4.31), which is the required characteristic of a slotted waveguide feed system for a microwave applicator.

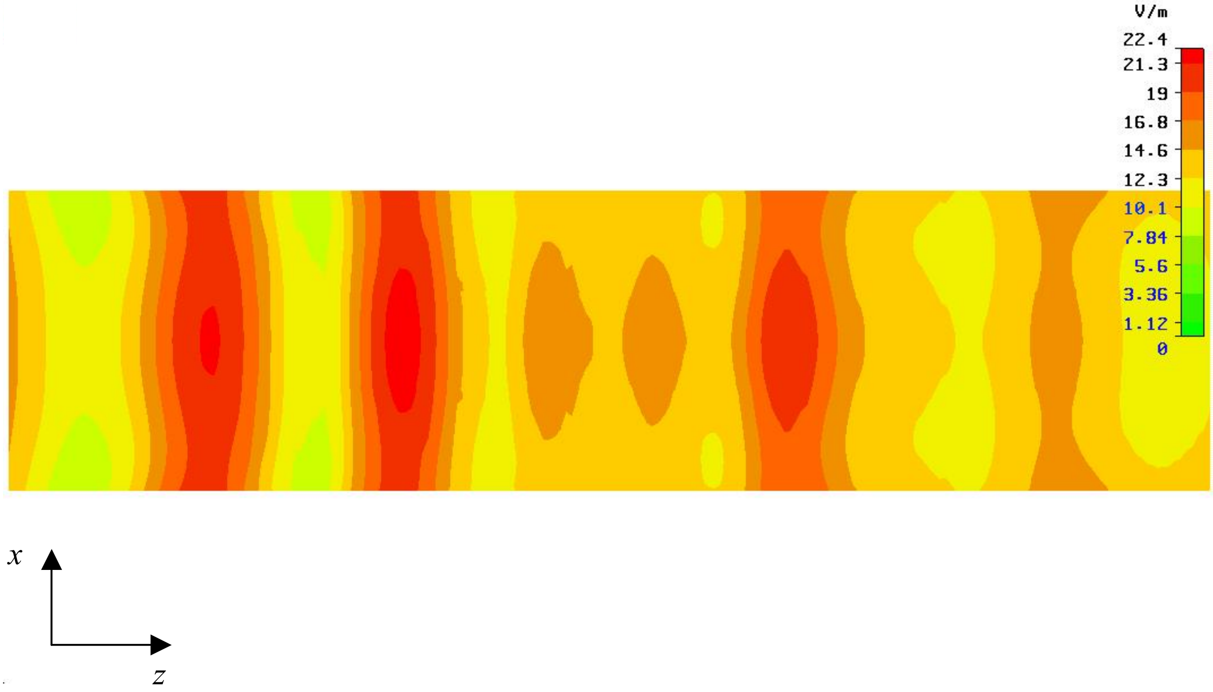

Figure 4.30 Simulated |*E*| field pattern in the *xz* plane at a distance of 4λ from the slots

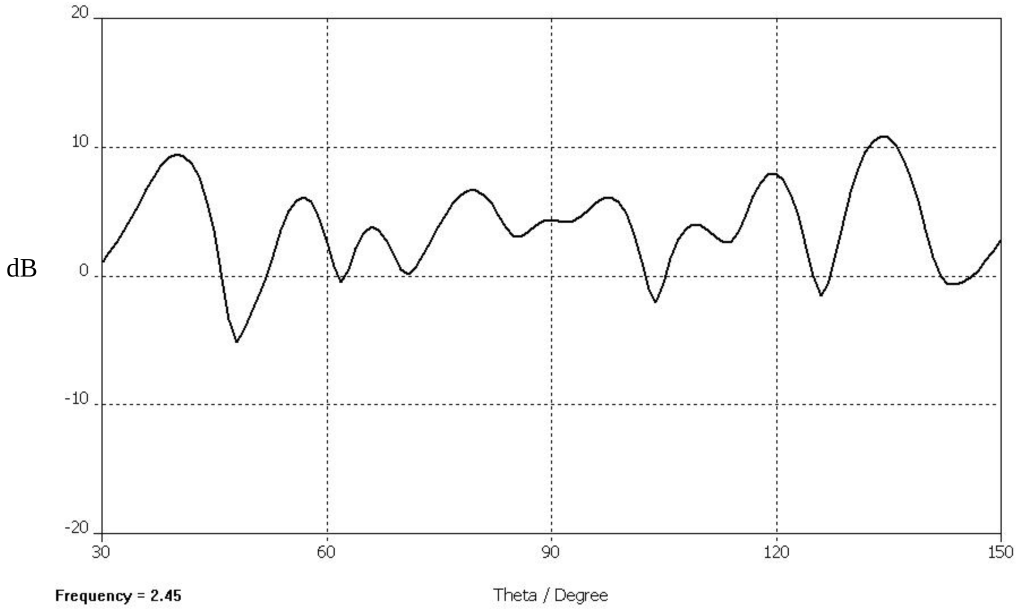

Figure 4.31 Numerically calculated optimized radiation pattern for the horizontally polarized nonresonant SW array

4.3.8 Conclusions related to the new SW design procedures

In this section new design procedures for transversally (vertically) and longitudinally (horizontally) polarized nonresonant SW feeds have been presented and discussed. Their main advantages over standing wave SWs, such as the broader matched bandwidth for low reflections and the possibility of using additional optimization parameters in the design process, have been shown and highlighted.

The new synthesis procedures are based on a linearization of the proposed exponential attenuation of the traveling fundamental waveguide mode. For the given excitation amplitude distributions, which are determined by the demand of uniform radiation, the design formulas for calculations of the normalized slot admittances and impedances have been derived. In the design processes the requirement of total MW power transfer from the SW feeding system to the microwave applicators has been also considered, setting the reflection losses to levels below 1 %.

First design verifications have been performed using numerical simulations of the analytically calculated slotted waveguides with the CST MWS software. The results of the simulations have shown a very good input antenna matching $|S_{11}|$ under -20 dB for both SW antennas.

Further, the numerically obtained radiation pattern of the vertically polarized SW feed (Fig. 4.19) proves the desired field uniformity.

However, the simple slot radiation power distribution given by equ. 4.24 does not result in a homogeneous radiation pattern in the case of the SW with centered transversal slots. Using an optimization method similar as for diffraction gratings in optics an appropriate excitation amplitude distribution function has been found giving the desired uniform radiation. A model based on this calculation has been made also and a nondirectional radiation pattern has been simulated, proving the chosen a_n distribution and the entire design procedure.

For a final verification of the designs described here, various experiments have been performed. The results of measurements will be presented in chapter 5.

5. EXPERIMENTAL VERIFICATIONS AND OPTIMIZATIONS

In this chapter the experimental measurements of the computationally designed and mechanically fabricated nonresonant SW feeds will be presented and described. For the verification of the numerically predicted very low levels of reflections in the SWs, so called ‘cold’ (low power) measurements of the feeds $|S_{11}|$ parameters have been performed with a vector network analyzer (VNA). The input antenna matching was tested for the cases that the SWs radiate into: the free space, a small laboratory scale applicator and the large industrial HEPHAISTOS oven. These measurements have been also used for additional fine optimizations of the nonresonant SWs. The mutual coupling between the SW feeds that have been mounted in the HEPHAISTOS system has been measured with the VNA proving the reduced cross coupling in the case having two orthogonally polarized feeding elements.

Tests in the high power operating range are also presented verifying the SW radiators stability and safety. Finally, the optimized SWs have been used as reliable power transfer devices in a set for different processes for carbon reinforced plastics with the HEPHAISTOS system.

5.1 Low Power Measurements

5.1.1 Experimental set up with VNA

For low power measurements of the reflections in the calculated SW feeds a VNA was used (Fig. 5.1). The set up consists of the AD R3860 VNA from ADVANTEST, a coaxial-to-

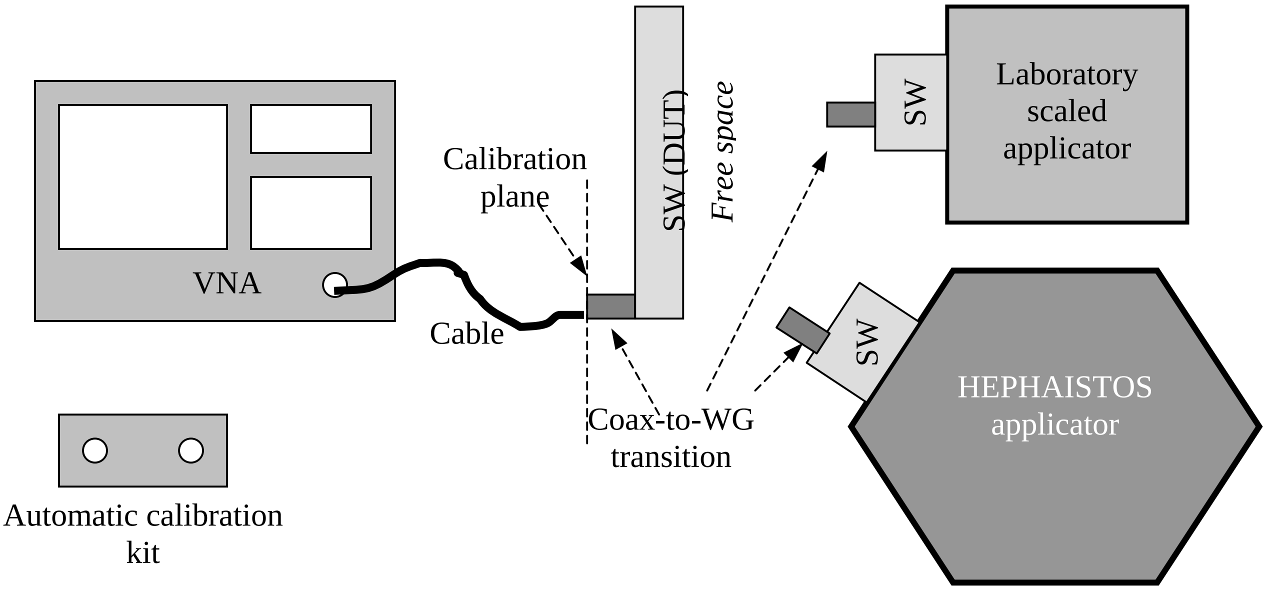

Figure 5.1 Experimental set up for cold measurements of the SWs reflections

waveguide transition that is optimized for the particular measurements and an automatic calibration device AD R17051. The SW feeds that were fabricated according to the application for industrial MW processing systems represent the devices under test (DUT) in the experimental set up. A set of high quality connecting cables is an important part of the set up. Additionally, the SW feeding systems can be connected to a small scale laboratory applicator or the large HEPHAISTOS applicator.

The coax-to-waveguide transition is directly placed at the position where the magnetron output antenna has to be mounted in the nonresonant SW feed. In that way, the reflections inside the SW feeds can be measured exactly at the location of the magnetron input in the SWs. In other words, the distance between the near waveguide short ended wall and the transition antenna is the same as the optimized distance between the magnetron output and the waveguide short. It should be mentioned here, that this distance is shorter than the $\lambda_g/4$ shorted waveguide section recommended by simple theory. Hence, the geometry of the transition antenna has been optimized using the CST MWS software in order to achieve negligible reflections at the coax input port at operating frequency of 2.45 GHz, for the given optimized magnetron position (sec. 2.4). In Fig. 5.2 a photograph of the transition antenna before and after the optimization is shown.

The calibration plane is at the input of the coax-to-waveguide transition (dashed line in Fig. 5.1). The reflections that arise inside the connecting coaxial cable and from the VNA input port were calibrated with the automatic calibration kit AD R17051. Using an automatic calibration device has the advantage that the measurements were accelerated in comparison to the time consuming calibration with open, short and load standards (OSL calibration).

5.1.2 Free space radiation measurements

The reflections inside the traveling wave SW feeding systems have been obtained measuring the S_{11} parameters of the feeds. First, the measurements of the SW antennas with sliding short at the waveguide end close to the last slot have been performed. In that way, the reflections have been additionally minimized after the insertion of the coax-to-waveguide transition and the optimized total lengths of the SW feeds were obtained.

The very low level of measured reflected power are shown in Figs. 5.3 and 5.4 for the transversally and longitudinally polarized SW radiators. Both antennas are very well matched to the bandwidth of typical kitchen oven magnetrons offering low cost direct coupling to the

Figure 5.2 Photograph of the transition antenna before and after the optimization

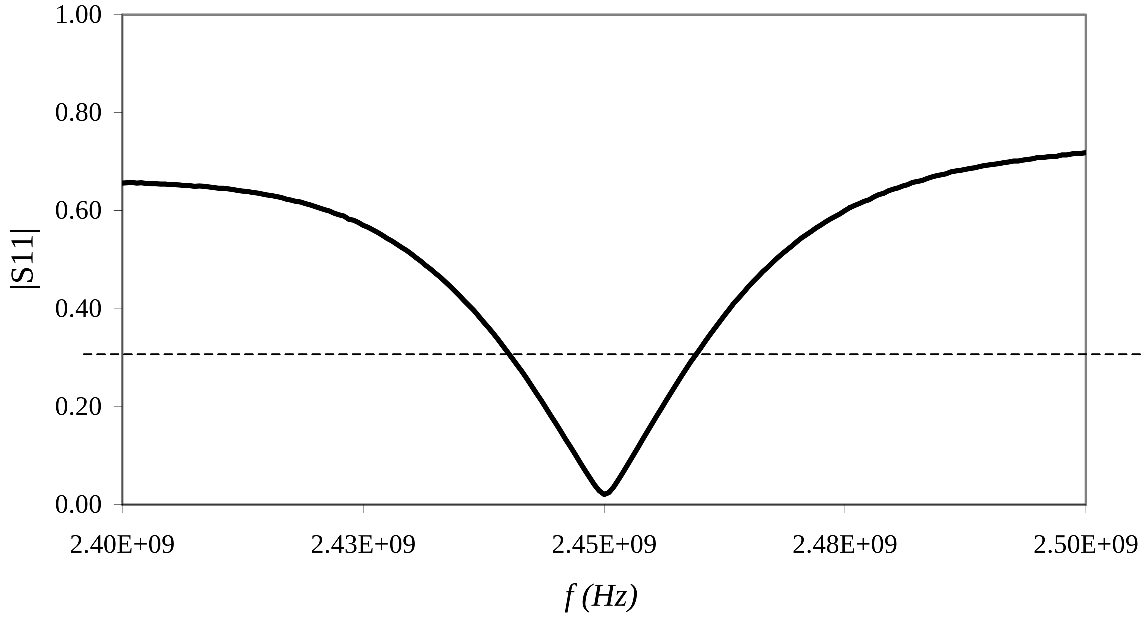

Figure 5.3 Measured $|S_{11}|$ parameter of the vertically polarized SW feed radiating into the free space

power MW sources. The power reflection losses are under 1 % at the design frequency of 2.45 GHz and less than 10 % in the whole magnetron frequency bandwidth range (2.45 ± 0.01 GHz).

5.1.3 Measurements on the laboratory applicator

A laboratory scaled applicator with dimensions 0.5 m x 0.5 m x 1m (Fig. 5.5 b) was fabricated for verification of the SW antennas input matching in the case that they are coupled

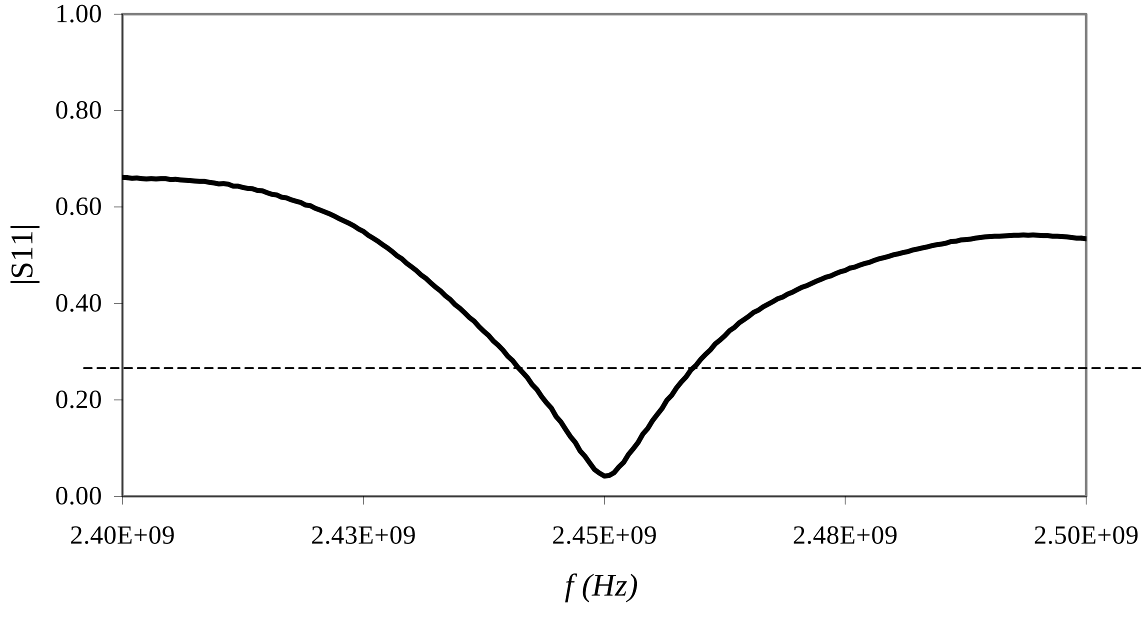

Figure 5.4 Measured $|S_{11}|$ parameter of the horizontally polarized SW feed radiating into the free space

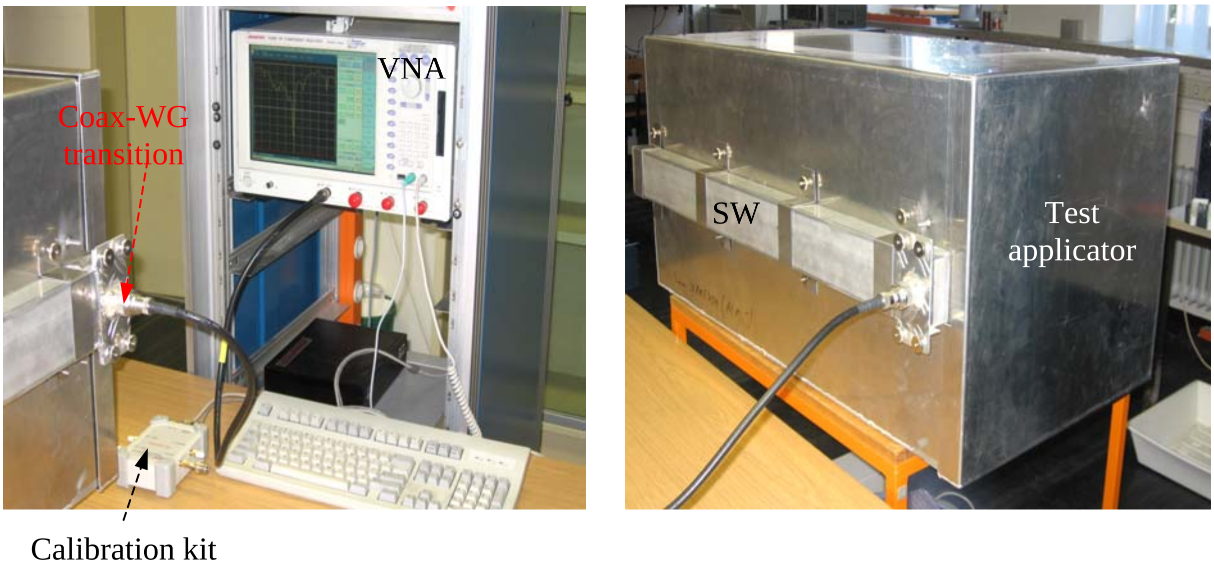

a) b)

Figure 5.5 Photograph of a) experimental set up and b) laboratory scaled applicator with mounted SW feed

to a MW cavity. The reflections (S_{11} parameter) inside the SW feeds have been measured with the VNA. Results for an empty and for a partially loaded applicator were obtained in these measurements. The water load is placed inside the applicator near the wall that is opposite to the SW feed. The reflections inside the SW antenna that radiate into the applicator loaded with 3 *l* of water are given in figures 5.6 – 5.7. The low level of reflection losses in the feeding parts has been verified at 2.45 GHz for both polarizations. However, the optimized power transfer was achieved only in a very narrow frequency band. These tests for the laboratory ca-

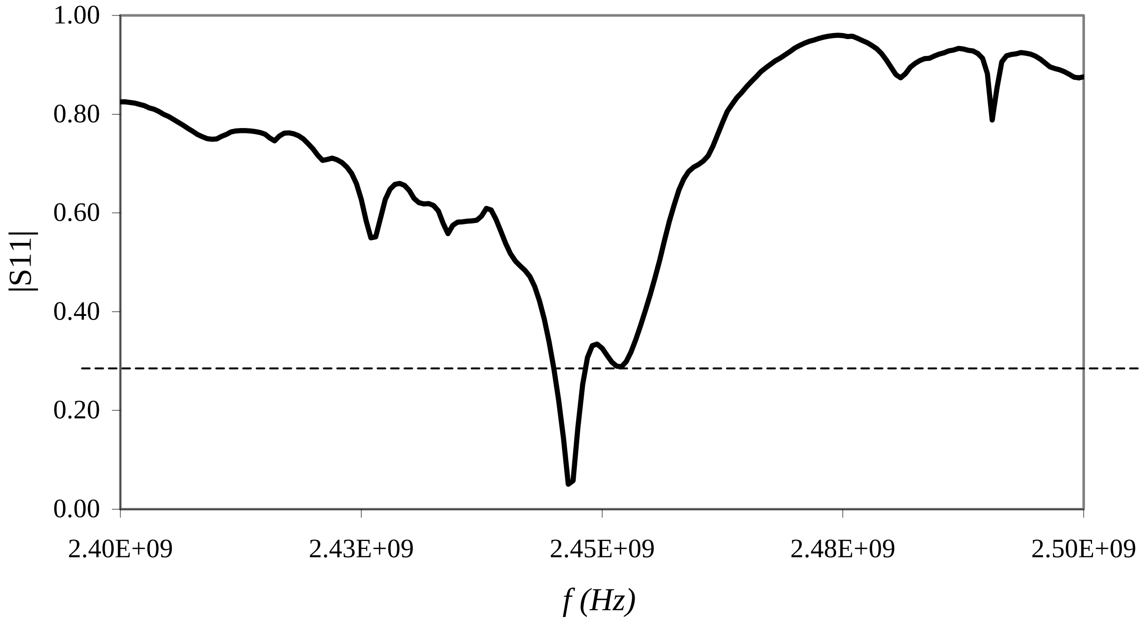

Figure 5.6 Measured $|S_{11}|$ parameter of the vertically polarized SW feed radiating into the laboratory applicator

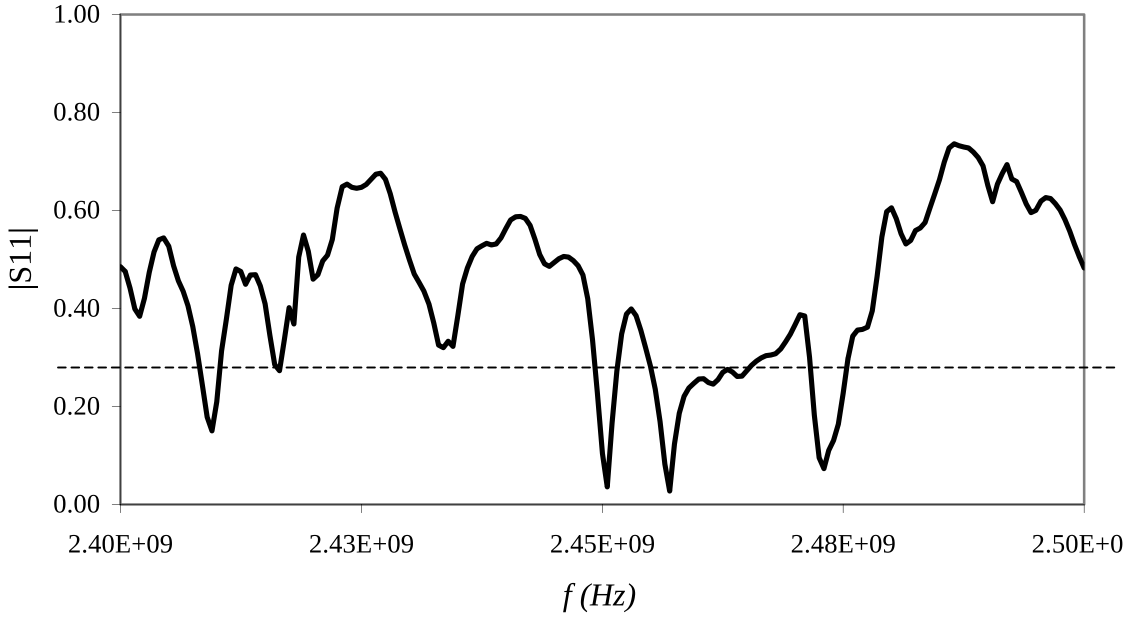

Figure 5.7 Measured $|S_{11}|$ parameter of the horizontally polarized SW feed radiating into the laboratory applicator

vity, have also shown that the obtained reflection curves depend on the placing of the load inside the MW oven.

5.1.4 Measurements on the HEPHAISTOS applicator

The most important tests of the designed SW feeding systems were for the case that they have been mounted to the large industrial HEPHAISTOS oven. The reflections inside the SW radiators were obtained in low power measurements with the VNA. The S_{11} parameters at

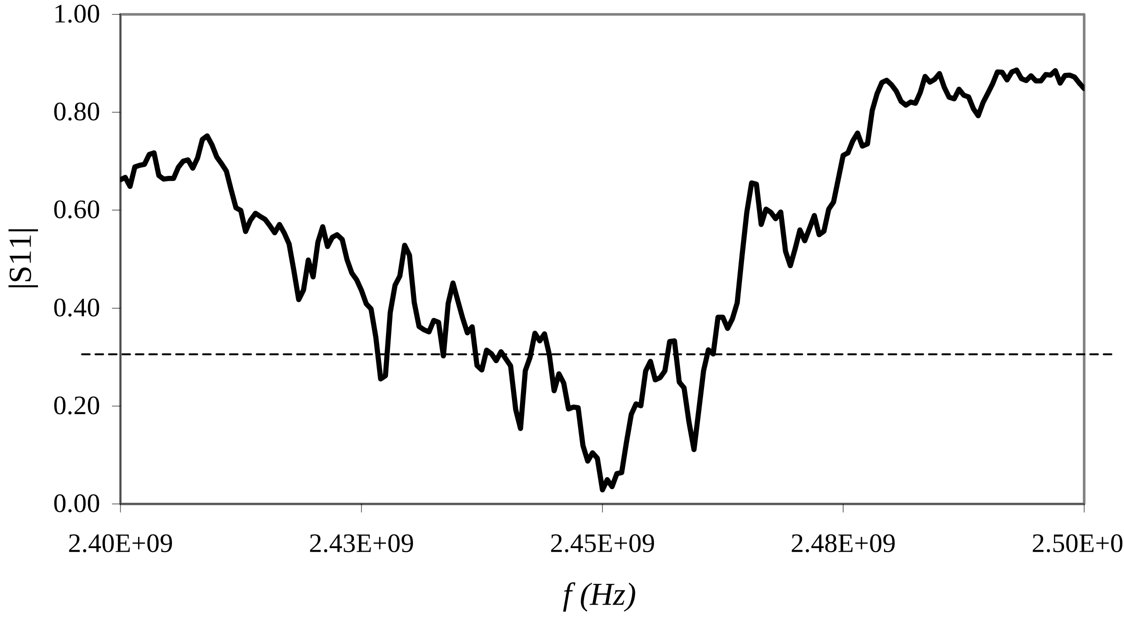

Figure 5.8 Typical measured $|S_{11}|$ parameter of the vertically polarized SW 1 feed radiating into the loaded HEPHAISTOS applicator

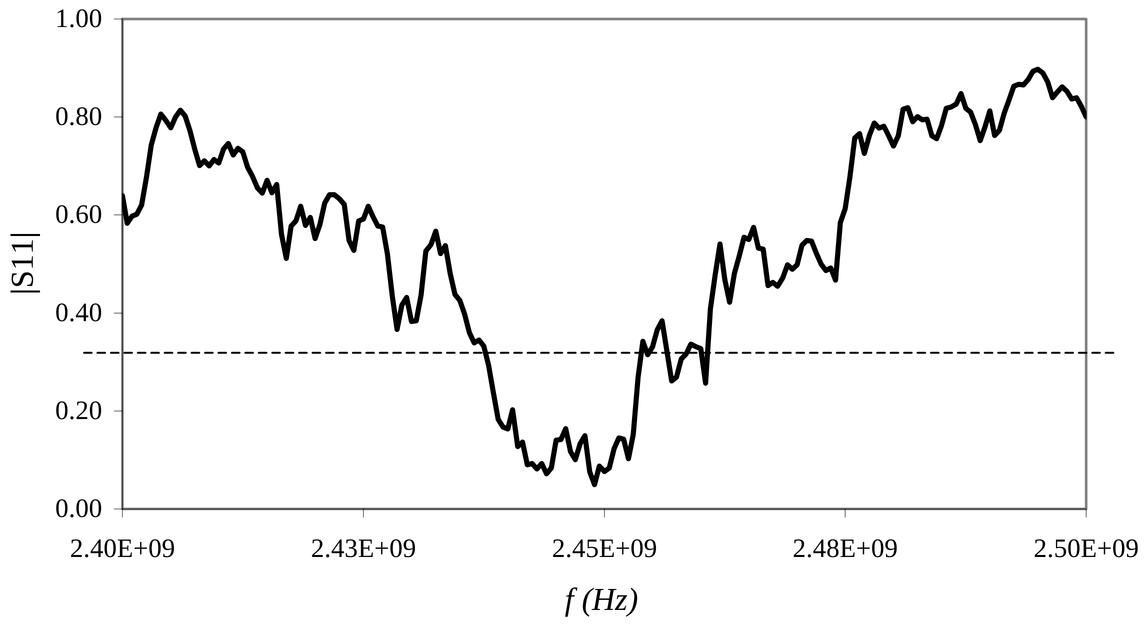

Figure 5.9 Typical measured $|S_{11}|$ parameter of the horizontally polarized SW 1 feed radiating into the loaded HEPHAISTOS applicator

the input of the coax-to-waveguide transition were measured for the feeds that have been placed at various positions at the oven. For these tests the load of 5 *l* water was placed centrally into the large oven.

In these cold tests the low levels of reflections and the very good input matching of the designed directly coupled feeding parts have been shown. In Figs. 5.8 and 5.9 broadband good input matching near the operating 2.45 GHz ISM frequency can be seen for both polari-

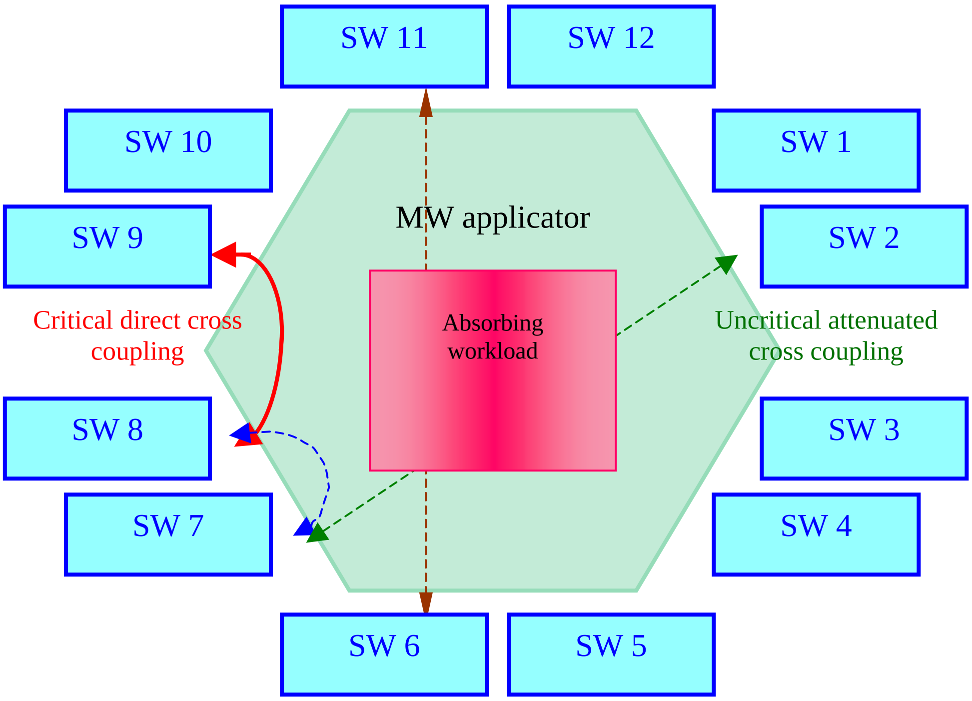

Figure 5.10 Measurements of the S_{12} parameters on the loaded HEPHAISTOS cavity

zations. In the larger HEPHAISTOS cavity the number of modes is much higher than in the smaller laboratory applicator giving a smoother $|S_{11}|$ curve (Fig. 5.7) compared to the sharp reflection results shown in Fig. 5.5. The presence of the many modes inside the MW applicator is indicated by the improved homogeneity of the EM field distribution in the oven.

5.1.5 Measurements of the mutual coupling

A good transmitting antenna is also a good receiving antenna, and it could happen that the radiated MW power from one SW feed can be received and coupled in an other SW feeding element of the multi-feed MW system. This mutually coupled MW power can be added to the reflected power inside the SW and it can cause damage at the high power MW source. So, it is very important to estimate the levels of cross coupling between the feeding elements in the MW applicator.

For the measurements of the mutual coupling between the SW antennas having the same and orthogonal polarizations, the S_{12} parameters have been obtained with the VNA. First, in the tests with SW feeds of equal polarization, the critical position of unwanted high mutual coupling have been found and highlighted (Fig. 5.10). The results presented in Fig. 5.11 show that the most critical case is for the neighbouring SW feeding systems, which are mounted at opposite sides of the same hexagon corner. This case of undesired direct coupling is marked by the red line (SW 8-SW 9 coupling) in Fig. 5.10. With the dashed lines the non direct and by load attenuated coupling paths are presented in the same figure, which are not critical for the system. The measured coupling of the corner SWs is given by the red curve in Fig. 5.11, showing the unacceptable cross coupling level that is higher than –20 dB.

Using different SW feeds with orthogonal polarizations for the neighbouring pair, the critical cross coupling between them was reduced to the negligible level of –30 dB at 2.45 GHz (fig. 5.12). This proves the idea to have the SW feeding elements with two different polarizations in the MW heating system. Hence, placing them in such order that SW feeds

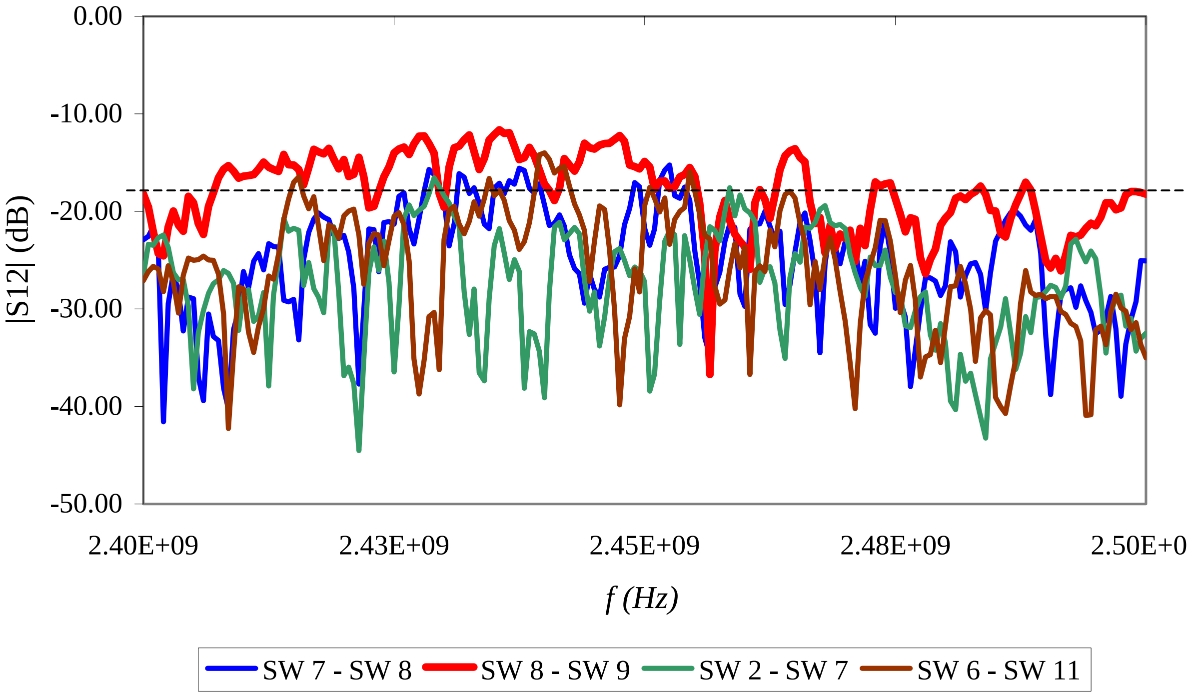

Figure 5.11 Measured $|S_{12}|$ parameter between pairs of vertically polarized SW feeds radiating into the loaded HEPHAISTOS applicator

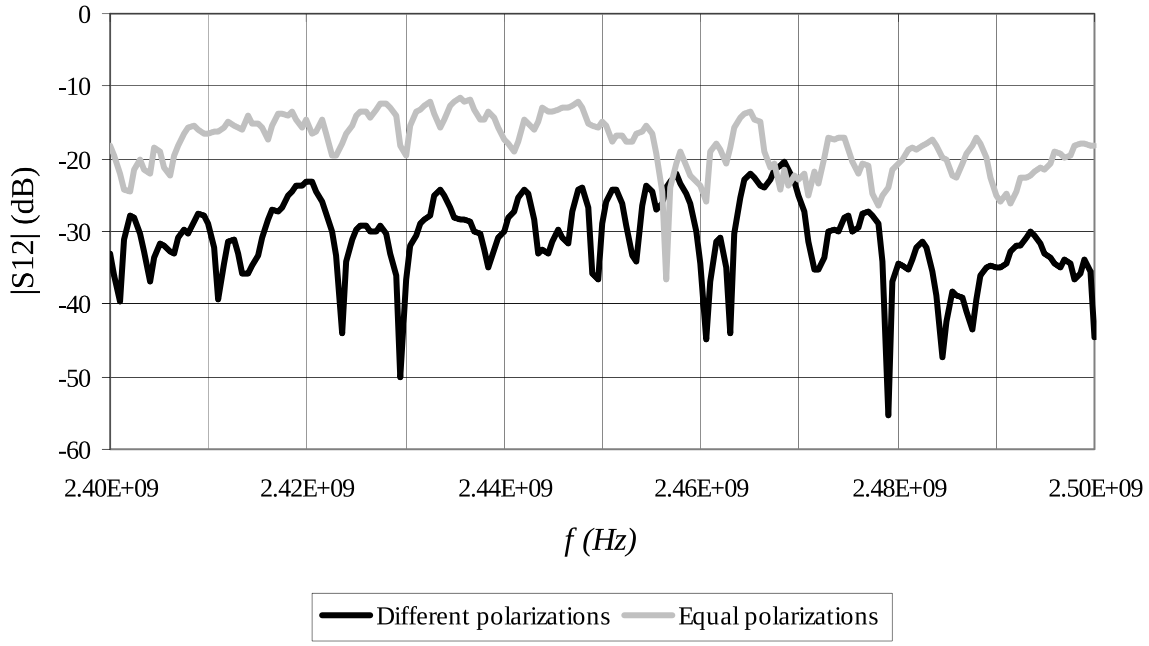

Figure 5.12 Measured $|S_{12}|$ parameter between the feeding pair SW 8 – SW 9 radiating into the loaded HEPHAISTOS applicator

with different polarizations are always at opposite sides of the HEPHAISTOS hexagon corners, the problem of the mutual coupling can be adequately solved.

5.1.6 Comparison of the experimentally and numerically obtained results

After the experimental optimizations of the SWs, new numerical simulations of them have been performed. Appropriate models of SWs (Fig. 5.13) have been made. These models

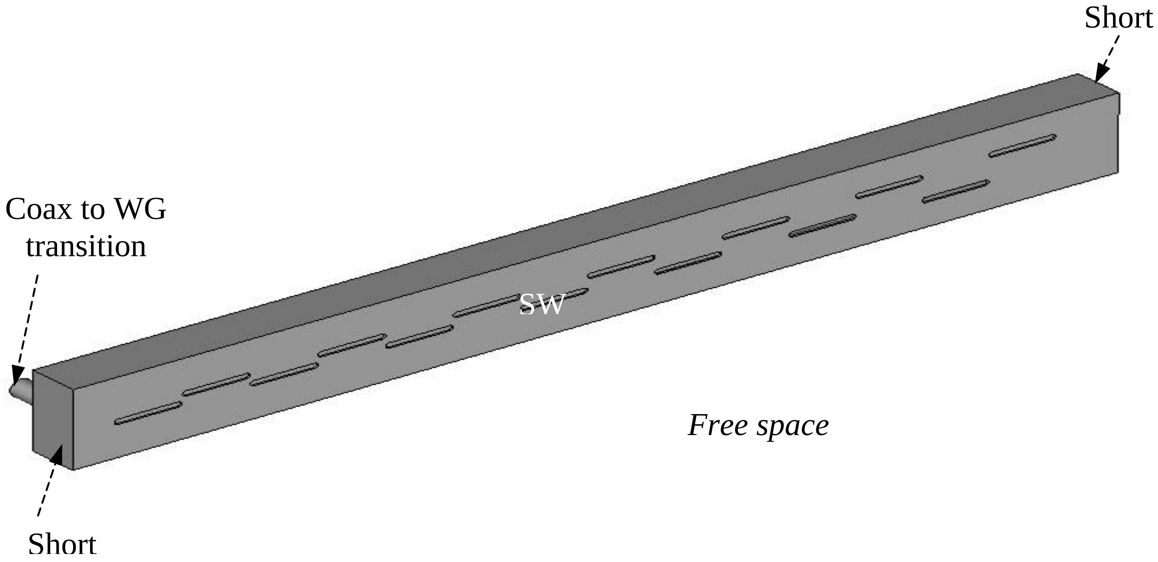

Figure 5.13 Model of the experimentally optimized SW

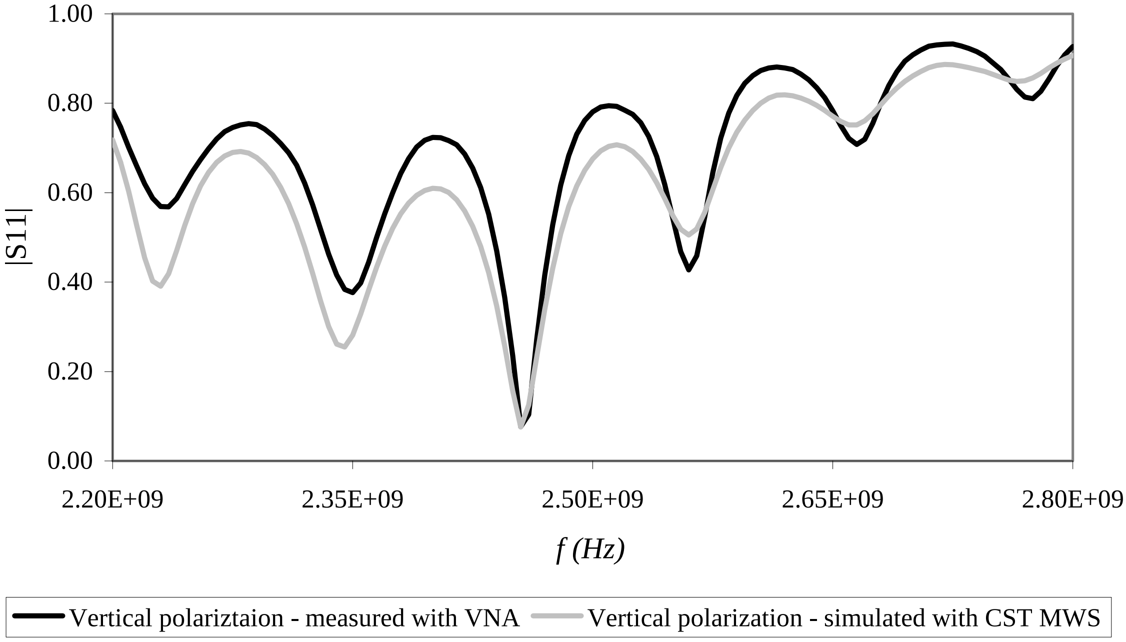

Figure 5.14 Comparison of the numerically and experimentally obtained results

include the coax-to-waveguide transition. The total length of the waveguide models has been adjusted according to the experimental optimizations and it equals to the optimized value.

Very good agreement between numerically obtained and measured reflection levels for the vertically polarized SW in a broader frequency range is presented in Fig. 5.14. The slight difference between these results are mainly due to the ideal boundary conditions in the numerical simulation models provided by CST MWS.

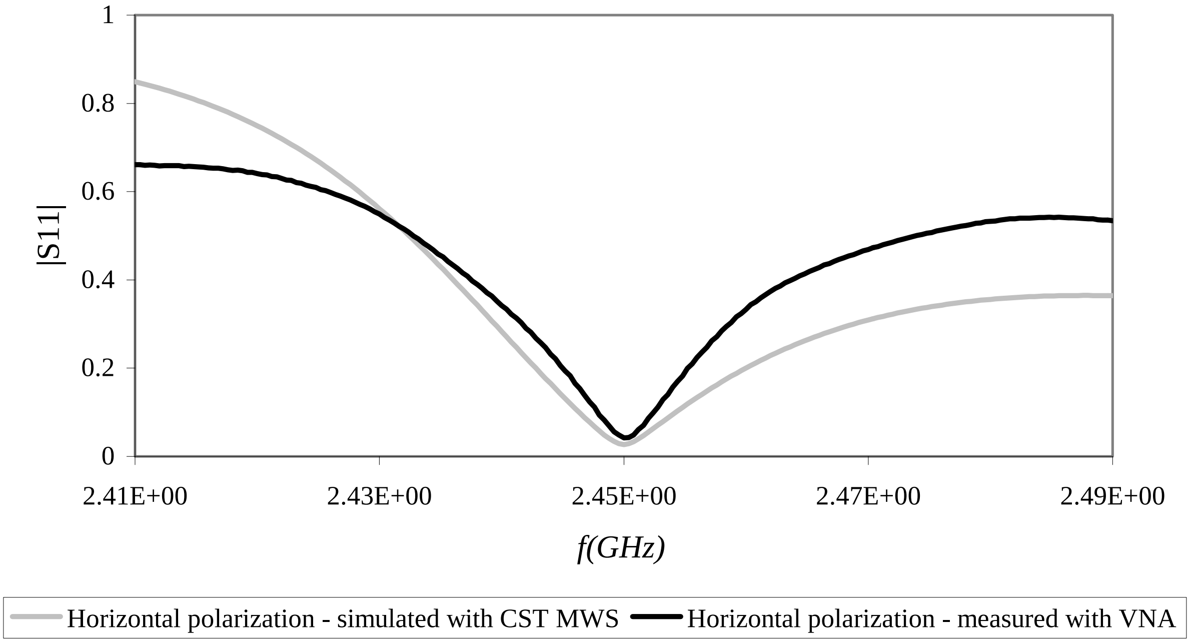

Figure 5.15 Comparison of the numerically and experimentally obtained results

The experimentally optimized horizontally polarized SW feed has been also numerically investigated. The relatively good agreement between the measured and simulated reflections inside the SW feed is shown in Fig. 5.15. The reflection minima are at 2.45 GHz for both curves, but the numerically calculated results show a little bit lower reflection in the frequency range of a typical magnetron bandwidth.

5.2 High Power Tests and Measurements

In the previous section the results of the cold measurements were presented verifying the optimized MW energy transfer through the SW feeds with both polarizations, transversal and longitudinal. The reflections inside the SW antennas and the cross coupling between the feeding elements have been successfully minimized. In the following section the high power tests that have been performed will be described and their results will be given. In these tests standard kitchen oven magnetrons served as high power MW sources, to which the SW radiators were directly connected. That means, the MW power range in the particular experiments was up to 0.7 kW, in the case of a single magnetron tube and up to nearly 16 kW (up to 24 magnetrons in two modules) for the case of the multi-fed HEPHAISTOS system. Modules are arranged in series and a distribution of magnetrons per modul is shown in Fig. 5.17.

5.2.1 Tests of reliability and safety

After the testing of the fabricated SW radiators in low power measurements with a VNA, they have been verified with respect to reliability and safety. The nonoptimized metallic MW components show high probability of arcing and failure in high power EM fields. Especially the slots in the waveguide wall are sensitive places for arcing and burning, because of the high EM field that exists among them. Further, nonoptimized strong reflection inside the feed can reach the directly coupled magnetron tube and damage it. Hence, these tests were very important, regarding the usability of the SWs for particular high MW power applications.

In an EM closed metallic chamber a test set up for the reliability verification was arranged. It consists of a kitchen oven magnetron tube, which is directly coupled to the tested SW antenna. The SW antenna radiates in a small cavity filled with a water load (Fig. 5.16) that absorbs the microwaves at 2.45 GHz well.

The magnetron was operating at its maximum power for 3 days (72 hours) without switching off. The SWs and the high power MW source itself have been monitored for arcing and burning. Additionally, a possible leaking of the MW radiation from the magnetron - WG junction and from the SW was monitored. The leaking radiation was measured with a radiation meter EMR-200, which is a device for isotropic measurements of EM fields. The standard limit value of the *E* field at 2.45 GHz is 61.4 V/m (CENELEC European standard for public areas).

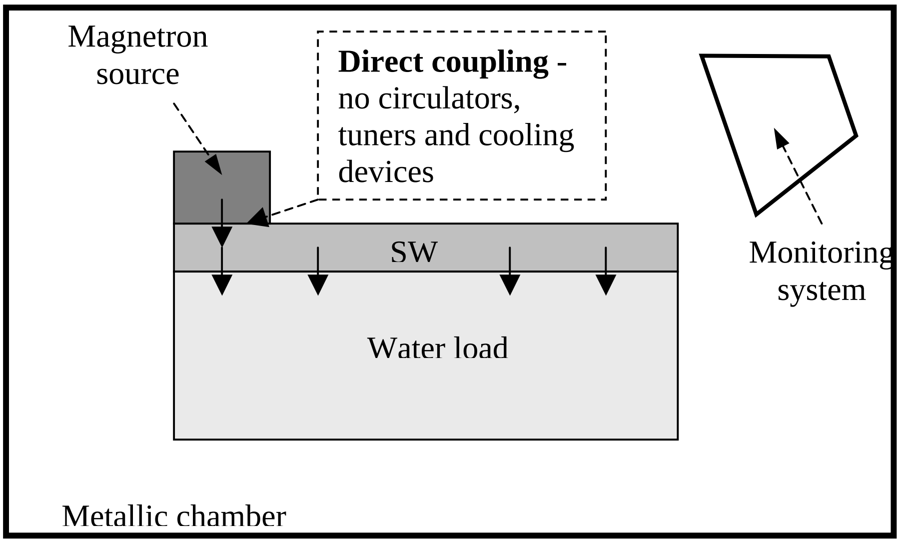

Figure 5.16 Schematic of a set up for reliability and safety tests

Tests have shown no arcs and damages inside the SW feeding elements or in the magnetron tube along the period of 72 hours. The measured leaking radiation inside the metallic chamber was under safe limits. These experiments verified the high reliability and safety of the designed SW feeding elements when operating in the high power range.

5.2.2 Measurements in the HEPHAISTOS oven with calorimeter

After mounting the SW antennas on the large industrial HEPHAISTOS applicator the leaking radiation was measured with the radiation meter device EMR-200. At a distance of nearly 3λ from the SWs the E field was measured. Safe radiation below 1/10 of the allowed limits of approximately 60 V/m has been proven for all feeding elements.

For the measurements of the absorbed power in the loaded cavity, a set up with a calorimeter device was prepared (Fig. 5.17). The principle of MW power measurement with a calorimeter lies in the measurements of the temperature difference in the flowing medium before and after it has been exposed to the MW field [61]. For a constant flow rate, the absorbed power p_{abs} can be calculated using the following formula:

$$p_{abs} = c_p \cdot \frac{\Delta m}{\Delta t} \cdot \Delta T \,, \tag{5.1}$$

where c_p is the specific heat capacity of the medium, $\Delta m/\Delta t$ is a constant flow rate and $\varDelta T$ is the temperature difference between the input and output ports in Fig. 5.17.

This type of calorimeter is appropriate for measurements in the higher power range (>1W), but it has a low sensitivity [61,62]. The main problem that causes the errors in these measurements is the thermal influence from the surrounding space. Hence, for highly precise measurements of the absorbed power inside the load, a good thermal isolation of the measured media is needed.

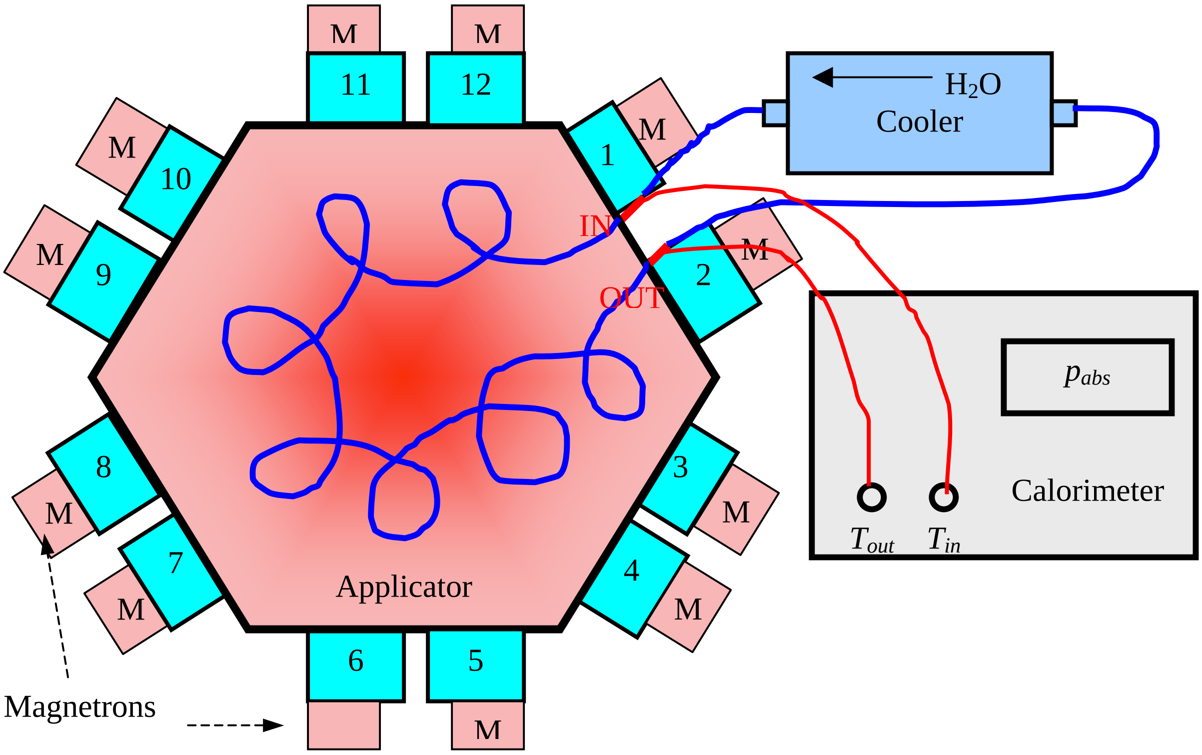

Figure 5.17 Scheme of the set up for the measurements of p_{abs} with a calorimeter

Figure 5.18 Measured Δp_{abs} distribution

Water has been used as the flowing medium in these experiments. A tiny plastic hose near 2 m long was inserted in the industrial MW oven and randomly scattered in its whole volume. The hose was filled with 1.3 l of cooled flowing water. The flow rate has been set to the value of the 2.6 l/min and it was maintained to be constant during the tests. The sensors for temperature measurements have been inserted directly in the hose at the positions where it enters in and comes out from the MW cavity. The hose was not thermally isolated from the surrounding environment. The measured values have been sampled in 30 values per minute giving the average absorbed power in a time period. The measurement uncertainty of the calorimeter is 5-10 %.

The differences Δp_{abs} from the average absorbed power for each of the 12 magnetrons of one HEPHAISTOS module are shown in Fig. 5.18. These results show that Δp_{abs} is under 10 % for all magnetrons except one (at position 10), which means a relatively good uniformity of MW energy feeding as function of the position of the SW antenna. From Fig. 5.18 it can be also seen that the highest absorbtion is for the positions 1, 2 and 10, which are closest to the temperature sensors. Further, the lowest absorbtion is for the SWs 5 and 6, which are most distant from the temperature sensors. This leads to the conclusion that a thermal isolation of the hose is essential for more accurate results.

5.2.3 Measurements on the HEPHAISTOS oven with infrared camera

Experiments with an infrared (IR) camera have been performed in order to verify the uniformity of heating and temperature distribution in the workload. A wood board load with dimensions of 1.4 m x 1.64 m x 0.2 m (Fig. 5.19) has been heated in the HEPHAISTOS-CA2 system. The temperature distribution on the surface of the wood board has been recorded with the IR camera during the heating period of approximately 10 min. Recorded data have been transfered to a PC and shown on a display. In this particular case of a wood board load with an average relative permittivity of $\varepsilon_r = 3.2$ and electric conductivity of $\sigma = 0.07\ \Omega^{-1}\text{m}^{-1}$, the temperature distribution is very well correlated to the EM field distribution in the MW applicator. The maximum measured temperature difference from the average temperature of 66°C was 6°C, and this difference is mainly due to the different wood structures in the board

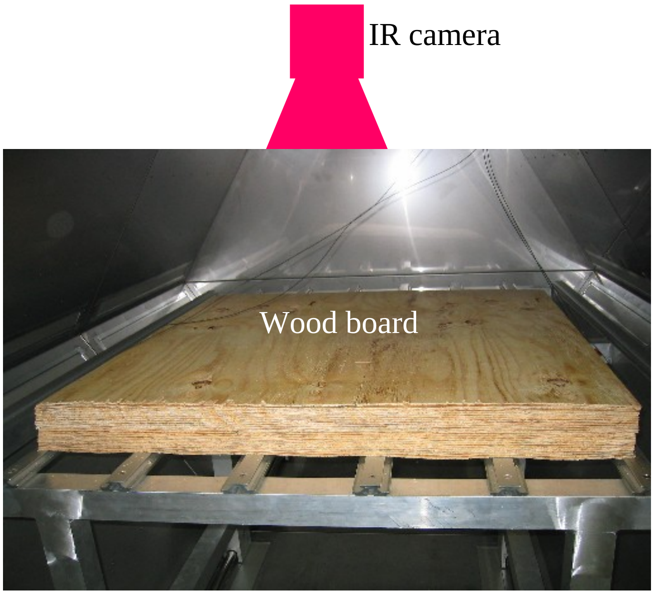

Figure 5.19 Photograph of a wood board load in the HEPHAISTOS-CA2 oven

with different microwave absorbing characteristics. Hence, the good temperature homogeneity during the heating process, which can be seen in Fig. 5.20, corresponds to the high uniformity of the EM field inside the MW oven. This is provided by the advanced hexagonal geometry of the HEPHAISTOS applicator. Further, these results of the measurements with IR camera show that the synthesized SW feeds radiate uniformly along the waveguide axis and support a desired homogeneous EM field distribution pattern in the hexagonal HEPHAISTOS system.

5.2.4 Tests for CFRP processing

Experiments on CFRP processing in the HEPHAISTOS-CA2 system equipped with the directly coupled vertically polarized SW feeds were very successful. The radiation field uniformity along the SW feeds assists a desired homogeneity of the EM field distribution

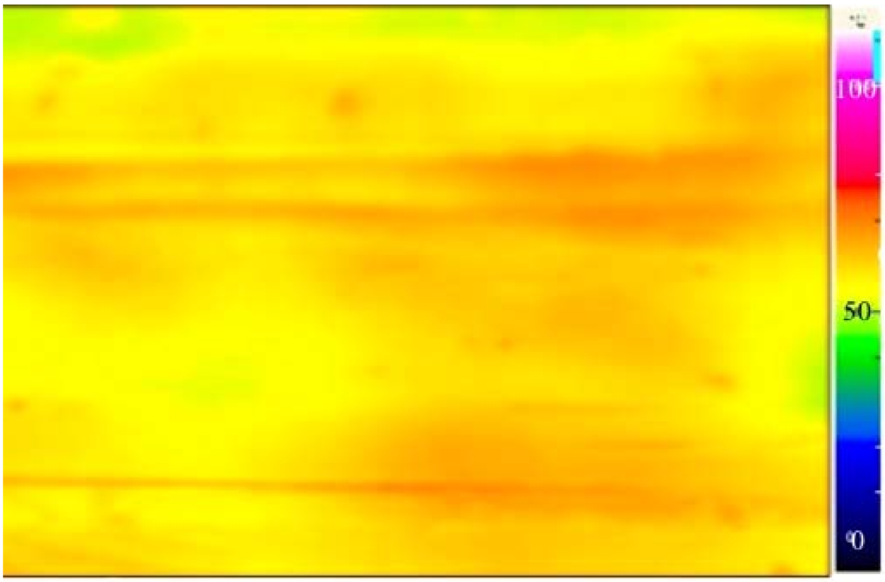

Figure 5.20 Measured temperature distribution of a wood board processed in the HEPHASITOS-CA2 system

inside the MW oven, which is provided by the hexagonal structure of the HEPHAISTOS applicators. The fabricated SW feeding systems with minimized reflections support a fast MW heating of the CFRP material also, save energy and hardware costs and remain cool. Additionally, no sparks or burnings occurred during the heating process. A CFRP presentation structure that have been processed inside the HEPHAISTOS-CA2 oven is shown in Fig. 5.21.

Figure 5.21 Photograph of a curved CFRP plate (1.26 m x 1.95 m) processed in the HEPHAISTOS-CA2 oven

6. SUMMARY, CONCLUSIONS AND OUTLOOK

6.1 Summary

MW processing of materials is presently being established in the field of industrial applications, offering advantages compared to the conventional heating technology such as, volumetric heating, reduction of cycle times and energy savings. In order to compete, industrial MW heating systems overcame the main problem of an insufficient field uniformity in MW applicators, as well as the technology challenges like an upscale of the oven volume, a high system efficiency and reduced hardware costs. Nonresonant SW feeding systems have been designed for supporting this demands. They offer an economical advantage using the direct coupling to the high power MW sources, provide an optimized MW power transfer and support an appropriate homogeneous EM field inside the applicator.

The first steps in the design process of the SWs antennas were numerical investigations on the waveguide slots that are presented in chapter 3. Using the commercial software package CST Microwave Studio various types of radiating slots were characterized. The normalized slot impedances and admittances have been numerically calculated as functions of different design parameters like slot length, width, displacement and shape. Based on these numerical slot investigations a selection of the appropriate slots for the SW feeds design has been performed. The longitudinal round-ended slot type with resonant $\lambda/2$ length has been chosen for the vertically (transversally to the waveguide axis) polarized SW radiator. The centered transversal round-ended slot with nonresonant length was selected for the SW antenna with horizontal (longitudinal) polarization. Comparing the results of the numerical calculations with the standard slot design formulas, which are recommended in the literature (Stevenson’s formulas), it has been shown that the proposed approach of the numerical simulations gives more accurate results. Additionally, it has the advantage that the slot geometries are not limited to the standard rectangular shapes having an infinite small thickness.

The numerical analysis of the standard resonant SW antenna design in industrial MW systems, which is given in chapter 4, showed that the nonresonant SWs are more convenient for feeding elements application. They have an additional design parameter, the distance between the slots, which can be used for optimization of the radiation pattern and for achieving a desired EM field pattern for the MW applicator. Further, the nonresonant SWs provide broader bandwidth of the input antenna matching than the resonant SWs, assuring minimized SW reflections in the operating frequency range of the kitchen oven magnetron source.

A new synthesis procedure for these nonresonant SW feeding systems was also described in chap. 4. The novel analytical calculations of the optimized SW feed parameters have been done using a linearization of the exponential attenuation function of the propagating fundamental TE_{10} waveguide mode. For the nonresonant SW antennas with two mutually orthogonal polarizations desired radiation characteristics were achieved also. However, in the case of the horizontally polarized SW feed, an additional optimization of the radiation field pattern was needed (method similar as for diffraction gratings in optics). It should be noted that the proposed advanced design of nonresonant SW radiators, as a more general case, can be easily used also for the design of resonant SW antennas, by setting the resonant $\lambda_g/2$ value for the distance between the slots.

After the numerical verifications of the new nonresonant SWs designs, measurements have been performed for an experimental optimization and for tests of the manufactured feeds (chapter 5). The measurements on the optimized SW feeding elements in the low power range with a VNA have shown very low level of reflections inside the SWs for both cases, radiation in the free space as well as for radiation in the loaded MW applicators (laboratory scaled and industry scaled HEPHAISTOS applicators). Negligible levels of the mutual coupling between the SW feeds in the multi-fed MW system having two different polarizations were also verified in these cold measurements. Directly coupled to the magnetron high power source the SWs were successfully tested for the reliability and safety in a metallic closed chamber in a non-stop operation time period of 72 hours. The measurements with a calorimeter and an IR camera verified the desired uniform radiation along the designed SW feeding systems. CFRP structure processing experiments in the HEPHAISTOS CA2 system equipped with the directly coupled nonresonant SW feeds were very successful.

6.2 Conclusions

In this dissertation it has been shown that:

1. Using the direct coupling to cheap kitchen oven magnetron sources, the proposed advanced SW feeding systems offer significant economical savings. The overall MW heating system costs have been reduced by the costs for standard MW components such as circulators, tuners as well as for cooling devices.

2. Optimized MW power transfer from the MW generator into the MW applicator has been achieved by minimization of the reflections inside the novel nonresonant SW feeds to levels below –20 dB.

3. The unwanted cross coupling between the SW feeding parts in the multi-fed HEPHAISTOS applicator has been suppressed to the negligible level of –30 dB using two different polarizations for adjacent feeds.

4. The designed SWs provide a desired radiation field uniformity along the SW antennas, supporting an appropriate homogeneous EM field distribution inside the HEPHAISTOS system.

5. The strong requirements for feeding systems for high power MW applications were completely fulfilled using a new general design procedure for nonresonant SW antennas, emphasizing the technical relevance of the SW design approach that has been presented in this thesis.

6.3 Outlook

In the future new optimizations of SW feeding systems appropriate for differently sized industrial 2.45 GHz HEPHAISTOS systems at high power levels (several kW per magnetron source) and high thermal demands will be performed. This will require further progressive computational investigations on the SW antennas in order to calculate the EM fields as well as the thermal interaction for cooling issues.

Additionally, measurements in the high power range, particularly with an improved calorimeter, will be needed for verifications of the desired high efficiency of high power MW systems.

BIBLIOGRAPHY

1. Y. V. Bykov, K. I. Rybakov and V. E. Semenov, *High-Temperature Microwave Processing of Materials*, Journal of Physics, D-Applied Physics, 34(13), 2001, R55-R75.

2. G. Link, L. Feher and M. Thumm, *Sintering of Advanced Ceramics Using a 30 GHz, 10 kW, CW Industrial Gyrotron*, IEEE Transactions on Plasma Science 27[2], 1999, pp 547-554.

3. L. Feher, G. Link and M. Thumm, *Comparison of microwave and millimeter-wave materials processing*, Proc of 25th Int. Conf. on Infrared and Millimeter Waves, Bejing, China, 2000, pp 475-476, IEEE Press., Liu, S. (Ed).

4. L. Feher, *Simulationsrechnungen zur verfahrentechnischen Anwendung von Millimeterwellen für die industrielle Materialprozesstechnik*, PhD thesis, Forschungszentrum Karlsruhe, FZKA-5885, 1997 (in German).

5. L. Feher and M. Thumm, *System Design Development for Microwave and Millimeterwave Material Processing*, Proc. of SPIE, Vol. 4720, 2002, pp 75-79.

6. M. Paulson, L. Feher and M. Thumm, *Parameter Optimization Modeling Using Stationary 1D-Electrothermal Model to Improve Temperature Homogeneity*, Journal of Microwave Power and Electromagnetic Energy, Vol. 39, No. 3-4, 2004, pp 141-151.

7. L. Feher, A. Flach, V. Nuss, P. Pozzo and T. Seitz, *HEPHAISTOS – A Novel 2.45 GHz Microwave System for Aerospace Composite Fabrication*, Proc. of 9th Int. Conf. on Microwave and High Frequency Heating, Loughborough, UK, 2003, pp 414-444.

8. L. Feher and M. Thumm, *Microwave Innovation for Industrial Composite Fabrication – the HEPHAISTOS Technology*, IEEE Transactions on Plasma Science, Vol. 32, No.1, Feb 2004, pp 73-79.

9. L. Feher, K. Drechsler, J. Filsinger and M. Thumm, *Development of the Industrial 2.45 GHz HEPHAISTOS CA2 Microwave Processing System for Composite Fabrication*, Proc. of 10th Int. Conf. on Microwave and High Frequency Heating, Modena, Italy, Sept 2005, pp 56-59.

10. L. Feher, M. Thumm and K. Drechsler, *Gigahertz and Nanotubes – Perspectives for Innovations with Novel Industrial Microwave Processing Technology*, Advanced Engineering Materials, 8, No. 1-2, 2006, pp 26-32.

11. K. Zhang and D. Li, *Electromagnetic Theory for Microwaves and Optoelectronics*, Springer-Verlag, Berlin Heidelberg, 1998.

12. J. Surutka, *Elektromagnetika,* Gradjevinska knjiga, Beograd, 1989 (in Serbian).

13. O. Dössel, *Electromagnetics and Numerical Calculation of Fields* (Lecture notes), University of Karlsruhe, Germany, 2003.

14. A. C. Metaxas, *Foundations of Electroheat,* John Wiley and Sons, 1996.

15. A. C. Metaxas and R. J. Meredith, *Industrial Microwave Heating*, IEE Power Engineering Series, 1983.

16. R. Meredith, *Engineers' Handbook of Industrial Microwave Heating,* Institution of Electrical Engineers, London, 1998.

17. R. A. Waldron, *Theory of Guided Electromagnetic Waves*, Van Nostrand Reinhold Company Ltd, 1970.

18. S. E. Adam, *Microwave Theory and Applications*, Prentice-Hall Inc, 1969.

19. N. Marcuvitz, *Waveguide Handbook*, McGraw-Hill Book Company, 1951.

20. M. Thumm, *High Power Microwave Engineering* (Lecture notes), University of Karlsruhe, Germany, 2004.

21. P. Bhartia and I. J. Bahl, *Millimeter Wave Engineering and Applications*, John Wiley and Sons, 1984.

22. G. Zimmer, *Hochfrequenztechnik*, Springer-Verlag, Berlin Heidelberg, 2000 (in German).

23. K. F. Lee, *Principles of Antenna Theory,* John Wiley and Sons, 1984.

24. S. Miyake and Y. Makino, *Application of Millimeter-Wave Heating to Materials Processing,* IEICE Trans. Electron., Vol. E86-C, No. 12 Dec. 2003.

25. J. C. Whitaker, *Power Vacuum Tubes – Handbook*, CRC Press, 1999.

26. J. Bretting, *Technische Röhren*, Hüthig Buch Verlag, Heidelberg, Germany, 1991 (in German).

27. E. A. Wolff, *Antenna Analysis*, Artech House, 1998.

28. S. Silver, *Microwave Antenna Theory and Design*, Peter Peregrinus Ltd, London, UK, 1984.

29. R. E. Collin and J. Zucker, *Antenna Theory*, McGraw-Hill, New York, 1969.

30. W. Wiesbeck, *Antennen und Antennensysteme* (Lecture notes), University of Karlsruhe, Germany, 2003 (in German).

31. H. Jasik, *Antennas Engineering Handbook*, McGraw-Hill, New York, 1961.

32. C. A. Balanis, *Antenna Theory: Analysis and Design*, Wiley, 1996.

33. J. D. Kraus, *Antennas*, 2nd Edition, McGraw-Hill Inc, 1988.

34. A. F. Stevenson, *Theory of Slots in Rectangular Wave-Guides*, Journal of Applied Physics, Vol. 19, Jan 1948, pp 24-38.

35. B. V. Chow Ting Chan and H. Reader, *Understanding Microwave Heating Cavities*, Artech House, Boston London, 2000.

36. K. Kark, *Antennen und Strahlungsfelder*, Vieweg, 2004 (in German).

37. R. J. Stegen, *Longitudinal Shunt Slots Characteristics*, Hughes Technical Memorandum, No. 261, Nov 1951.

38. R. S. Elliott, *Antenna Theory and Design*, Englewood Cliffs, Prentice-Hall, 1981.

39. A. A. Oliner, *The Impedance Properties of Narrow Radiating Slots in the Broad Face of Rectangular Waveguide*, IEEE Transactions on Antennas and Propagation, Jan 1957, pp 4-20.

40. G. J. Stern and R. S. Elliott, *Resonant Length of Longitudinal Slots and Validity of Circuit Representation: Theory and Experiment*, IEEE Transactions on Antennas and Propagation, Vol. AP-33, No. 11, Nov 1985, pp 1264-1271.

41. T. V. Khac and C. T. Carson, *Impedance Properties of a Longitudinal Slot Antenna in the Broad Face of a Rectangular Waveguide*, IEEE Transactions on Antennas and Propagation, Sept 1973, pp 708-710.

42. H. Y. Yee, *Impedance of a Narrow Longitudinal Shunt Slot in a Slotted Waveguide Array*, IEEE Transactions on Antennas and Propagation, July 1974, pp 589-592.

43. R. S. Elliott and L. A. Kurtz, *The Design of Small Slot Arrays*, IEEE Transactions on Antennas and Propagation, Vol. AP-26, No. 2, March 1978, pp 214-219.

44. L. G. Josefsson, *Analysis of Longitudinal Slots in Rectangular Waveguides*, IEEE Transactions on Antennas and Propagation, Vol. AP-35, No. 12, Dec 1987, pp 1351-1357.

45. L. Josefsson, *A Waveguide Transverse Slot Array Applications*, IEEE Transactions on Antennas and Propagation, Vol. 41, No. 7, July 1993, pp 845-850.

46. P. K. Park, G. J. Stern and R. S. Elliott, *An Improved Technique for the Evaluation of Transverse Slot Discontinuities in Rectangular Waveguide*, IEEE Transactions on Antennas and Propagation, Vol. AP-31, No. 1, Jan 1983, pp 148-154.

47. I. A. Eshrah et al., *Wideband Lumped Element Equivalent Circuit Model for Waveguides Slots and Applications*, IEEE MTT-S Digest, 2004, WE2B-4, pp 607-610.

48. W. Ren et al., *Full-Wave Analysis of Broad Wall Slots Characteristics in Rectangular Waveguides*, IEEE Transactions on Antennas and Propagation, Vol. 52, No. 9, Sept 2004, pp 2436-2444.

49. V. A. Mechenova and V. V. Yakovlev, *Efficient Optimization of S-Parameters of Systems and Components in Microwave Heating*, Proc. of 3rd World Cong. in Microwave and RF Applications, Sydney, Australia, 2002, pp M4A.24 – M4A.25.

50. J. W. Cresko and V. V. Yakovlev, *A Slotted Waveguide Applicator Design for Heating Fluids*, Proc. of 9th Int. Conf. on Microwave and High Frequency Heating, Loughborough, UK, 2003, pp 317-320.

51. *CST Microwave Studio – Advanced Topics* (Software manuals), Computer Simulation Technology, 2003.

52. V. V. Yakovlev, *Examination of Contemporary Electromagnetic Software Capable of Modeling Problems of Microwave Heating*, Advances in Microwave and Radio Frequency Processing, Springer Verlag, 2005.

53. A. Heilmann, *Antennen III*, Bibliographisches Institut, Mannheim, 1970 (in German).

54. S. Stanculovic, L. Feher and M. Thumm, *Optimization of Slotted Waveguides for 2.45 GHz Applicators Using New Slot Shape*, Proc. of Int. Symp. On Antennas, Nov. 2004, Nice, France, pp 392-393.

55. S. Stanculovic, L. Feher and M. Thumm, *Slotted Waveguides for 2.45 GHz Industrial Applicators*, Proc. of 6th Int. Conf. on Vacuum Electronics, Noordwijk, Holland, April 2005, pp 467-470.

56. L. Sikora and J. Womack, *The Art and Science of Manufacturing Waveguide Slot-Array Antennas*, Microwave Journal, June 1988, pp 157-162.

57. A. J. Sangster and A. H. I. McCormick, *Theoretical Design/Synthesis of Slotted Waveguide Array*, IEE Proc. Vol. 136, Pt. H, No. 1, Feb 1989, pp 39-46.

58. M. M. Brady, *Single Slotted-Waveguide Linear Arrays*, Advances in Microwaves, Academic Press, New York London, 1971, pp 131-173.

59. E. Hecht, *Optik*, Schaum Verlag, 1980, pp 175-176 (in German).

60. S. Stanculovic, L. Feher and M. Thumm, *Design of Nonresonant Slotted Waveguide Feeds for 2.45 GHz Industrial Microwave Heating Systems*, Proc. of 10th Int. Conf. on Microwave and High Frequency Heating, Modena, Italy, Sep 2005, pp 454-457.

61. M. Thumm, W. Wiesbeck and S. Kern, *Hochfrequenzmesstechnik*, Teubner, Stuttgart, 1997 (in German).

62. A. Fantom, *Radio Frequency and Microwave Power Measurement*, Peter Peregrinus Ltd., London, 1990.